UNIVERSITY OF Southampton

FACULTY OF MEDICINE

Human Development and Health

Characterization of parallel G-quadruplex formation by highly conserved G-rich motifs in *INS* intron 1

by

Ana Luísa Gonçalves das Lages

Thesis for the degree of Doctor of Philosophy

June 2018

UNIVERSITY OF SOUTHAMPTON

ABSTRACT

FACULTY OF MEDICINE

Human Development and Health

Thesis for the degree of Doctor of Philosophy

CHARACTERIZATION OF PARALLEL G-QUADRUPLEX FORMATION BY HIGHLY CONSERVED G-RICH MOTIFS IN *INS* INTRON 1

Ana Luísa Gonçalves das Lages

Individuals predisposed to type 1 diabetes (T1DM) carry an adenine allele at rs689, a T-to-A genetic variant located 6 nucleotides upstream of the 3' splice site of *INS* intron 1. The A allele disrupts the polypyrimidine tract (Py-tract) and impairs splicing, increasing intron retention (IR) levels in mature transcripts. Intron 1-containing messenger RNAs have an extended 5' untranslated region (5'UTR), introducing an upstream open reading frame (uORF) and curtailing translation. IR can be reduced using oligonucleotides complementary to an intronic segment flanked by G-rich sequences, mitigating the splicing defect. To investigate their potential to form G-quadruplex (G4), a G4-specific fluorescent probe, thioflavin T, was used to examine DNA and RNA G-tracts flanking the antisense target region, *in vitro*. Fluorescence intensity was shown to be specific for G4 structures in DNA and RNA. G4 formation was influenced by the adjacent target region in each direction and by concentrations of K+ and Mg2+. G4s were also detected in RNA transcribed in real time and their formation was influenced by mutations that affected intron 1 removal. To identify proteins binding to this intronic region, *in vitro* RNA transcripts containing the antisense target region were used in RNA pull-down assays with HeLa nuclear extracts, revealing heterogeneous nuclear ribonucleoproteins (hnRNPs) F and H1 binding to G-rich segments. The G-rich 5' UTRs of representative primate species were also cloned into a dual-luciferase-reporter system to establish primate-specific translation rates. Elimination of the Homoninae-specific uORF significantly increased luciferase translation, demonstrating its importance for *INS* gene expression. Overall, data obtained in this project has improved the understanding of the molecular mechanisms underlying the allele-specific expression of preproinsulin expression. These results may facilitate development of future preventative strategies for T1DM.

I. Table of Contents

II. List of Tables

III. List of Figures

IV. DECLARATION OF AUTHORSHIP

I, Ana Luísa Gonçalves das Lages declare that this thesis entitled Characterization of parallel G-quadruplex formation by highly conserved G-rich motifs in *INS* intron 1, and the work presented in it are my own and has been generated by me as the result of my own original research.

I confirm that:

1. This work was done wholly or mainly while in candidature for a research degree at this University;
2. Where any part of this thesis has previously been submitted for a degree or any other qualification at this University or any other institution, this has been clearly stated;
3. Where I have consulted the published work of others, this is always clearly attributed;
4. Where I have quoted from the work of others, the source is always given. With the exception of such quotations, this thesis is entirely my own work;
5. I have acknowledged all main sources of help;
6. Where the thesis is based on work done by myself jointly with others, I have made clear exactly what was done by others and what I have contributed myself;
7. Parts of this work have been published as:

Kralovicova J, Lages A, Patel A, Dhir A, Buratti E, Searle M, et al. Optimal antisense target reducing INS intron 1 retention is adjacent to a parallel G quadruplex. Nucleic Acids Res. 2014;42(12):8161–73

Signed:

Date:

V. Acknowledgements

The accomplishments in the present project result from the effort and contribution of several people, to whom I would like to leave my sincere appreciation.

First of all, I would like to acknowledge my funding organization, Diabetes UK, for providing unique opportunities to present my research and meet those involved in grant applications, students funded by the charity, and extraordinary people that have to live with type 1 diabetes and were so keen on understanding our research and share their life experiences as patients.

I would like to thank my supervisor, Dr Igor Vorechovsky, for his support, guidance and encouragement throughout the project, as well as revising my drafts and refining my presentations. I am grateful for the considerable time spent in meetings and all the constructive discussions regarding this project. To my supervisors, Professor John Holloway and Professor Chris Proud, for their availability to help and support, every single time.

I would like to thank Dr Mark Coldwell and Dr Joanne Cowan for sharing their knowledge in cell culture and helping with the studies of the effect of uORFs in translation. To Professor Douglas Black for the plasmids containing the cDNAs of hnRNPs F and H1.

A big thank you to all my friends. To the ones I left in Portugal who kept sending their words of motivation and encouragement; the never-ending conversations were breaths of fresh air in so many occasions. And to the ones I met in these last four years. We've spent many hours in countless lunches, trips, coffees, chats and laughs. You've always had the right words at the right time. I hope we can stay in touch, no matter where we all are.

At last but not the least, a very special thank you to my family. Adelina, Dionil and Nuno, you have been my foundation. You have always pushed me to do more, to accomplish more, and to never give up on anything. If it weren't for your many advices and words of wisdom, I would never have started this adventure, which made me grow up as a person. Isaura, António, Francisca and José, your kind words of encouragement, love and comprehension for your granddaughter were always a motivation to do better and keep going. Lurdes, thank you for the lovely holiday trips, the advices to remain calm and to always see the bright side of everything. You have always been much more than a godmother. Palmira, Pedro and José Manuel, for all the good laughs, lunches and chats. I would like to thank you for your support and motivation as well.

I can never thank you enough for your immense love, patience, guidance and support, fundamental throughout all the good and bad moments.

VI. Abbreviations

Abbreviation	Full designation
3'ss	3' splice site
3'UTR	3' untranslated region
5'ss	5' splice site
5'UTR	5' untranslated region
7-deaza-GTP	7-Deazaguanosine-5'-Triphosphate
APA	Alternative polyadenylation
AS	Alternative splicing
DIs	Detained introns
ESE	Exonic splicing enhancer
ESS	Exonic splicing silencer
G4	G-quadruplex
hnRNPs	Heterogeneous nuclear ribonucleoproteins
IDDM2	Insulin-Dependent Diabetes Mellitus locus 2
INS	Preproinsulin gene
IPTG	Isopropyl-β-D-thiogalactopyranoside
IR	Intron retention
ISE	Intronic splicing enhancer
ISS	Intronic splicing silencer
KCl	Potassium chloride
Licac	Lithium cacodylate
LiCl	Lithium chloride
NMD	Non-sense mediated decay
pIC	pICtest2
Pre-mRNA	Pre-messenger RNA

PTCs	Premature termination codons
Py-tract	Polypyrimidine tract
QGRS	Quadruplex forming G-rich sequences
q-RRM	quasi- RNA recognition motifs
RIs	Retained introns
RBPs	RNA-binding proteins
RIs	Retained Introns
RNA Pol II	RNA polymerase (Pol) II
RNPs	Ribonucleoproteins
RRMs	RNA recognition motifs
RT	Room temperature
SNP	Single nucleotide polymorphism
snRNPs	Small nuclear ribonucleoproteins
SR-rich protein	Serine/arginine-rich proteins
T1DM	Diabetes mellitus type 1
ThT	Thioflavin T
uORF	Upstream open reading frame

Chapter 1: Introduction

1.1 Gene Expression

Gene expression is the process through which a cell synthesizes functional biomolecules from its DNA. Differential expression of genes determines cell differentiation, i.e., the expression of a unique set of genes in each cell type accounts for the differences between muscle cells, skin cells, neurons or any other cell type (1). In the first step of gene expression, transcription, genes are copied into primary transcripts (precursor-messenger RNAs, pre-mRNAs), which have to be further processed into functional RNAs. By default, eukaryotic genes are silenced, since DNA is tightly bound to histones, one of the most evolutionary conserved protein families (1,2). Histones bind tightly to DNA via electrostatic interactions established between positively charged amino acids of proteins and negatively charged phosphate groups of DNA. About 146 base pairs of DNA fold around eight histone proteins into a structure called nucleosome (3). Chromatin is formed by tight coiling of 250 nm-wide fibers consisting of several nucleosomes (3,4). In order to alter the steady-state of a gene, chromatin structure is altered via histone modifications, which leads to decreased histone:DNA interactions and the overall structure gets opened. Interactions between DNA and histones are weakened by chemical modification processes on histones: methylation, acetylation, phosphorylation, ubiquitylation, sumoylation, ADP-ribosylation, deamination and proline isomerization (5).

In general, the compact chromatin structure resulting from nucleosome assembly hides regulatory binding sites, restricting access to DNA and downregulating processes like transcription, replication, recombination and repair (4,6,7). This physical barrier is actively overcome and gene processes initiated via interaction of DNA-binding factors to nucleosome-depleted regions (NDRs), like the binding of transcription factors to promoter regions (6). Activation of gene expression is associated and requires nucleosome organization and positioning which lead to chromatin structure opening and increase gene accessibility (4,6,7).

It is, therefore, logical that nucleosomes and their positioning within chromatin also influence gene expression regulation. Nucleosomes are generally located over the transcribed region of genes (suppressing their activation) or over non-genic regions (7,8). In general, enhancer, promoter and terminator regions of genes are depleted of nucleosomes (4,7,8). Most studies indicate that nucleosome positioning is determined by a combination of factors: DNA sequence, DNA-binding proteins, nucleosome remodelers and RNA pol II transcription machinery (7,8).

Once genes are accessible, many proteins, commonly named transcription factors (TFs), interact with the DNA, activating or repressing transcription. (1).

1.1.1 Genome complexity and coding capacity

Sequencing of the human genome increased our knowledge of the number of genes and encoded proteins (9,10). There is still much to uncover and a consensus regarding the number of human proteins and their encoding genes has not been reached yet (11). Recent data, obtained through the analysis of gene expression of 30 histologically normal human cell and tissue types showed the existence of 20687 proteins encoded by 17294 genes, including the evidence for the translation of 140 annotated pseudogenes and an annotated non-coding RNA that can be translated into five peptides (9). Using mass-spectrometry data, Kim and co-workers claim to have identified isoform-specific peptides for 2861 protein isoforms derived from 2450 genes (9). Thus, a single gene may encode different mRNAs, which in turn, are translated into several isoforms of the same protein (9,12,13). For example, the Fas receptor gene encodes isoforms involved in apoptosis. Two of these isoforms have opposite effects on apoptosis. The soluble isoform blocks the programmed cell death of tumour cell lines induced by the membrane-bound isoform of the protein (14,15). A second example is the synthesis of at least three protein isoforms from the *Drosophila fruitless* gene, where each isoform has a different function in male sexual behaviour (16).

1.1.2 Maturation of RNA

Expression of protein isoforms is predominantly regulated at the pre-mRNA maturation level. Eukaryotic pre-mRNAs contain intervening non-coding sequences known as introns that separate coding regions called exons (17). Maturation of pre-mRNA into mRNA (template for protein translation) involves three major processes: 5’ capping, splicing and 3’ cleavage/polyadenylation (18). Shortly after translation initiation, the 5’ end of pre-mRNA is blocked by the addition of a modified guanine, 7-methylguanosine, in a process termed 5’ capping (18). 3’ cleavage/polyadenylation is a post-transcriptional modification comprising the sequential endonucleotide cleavage and addition of poly(A)-rich sequences to the 3’ end of RNA transcripts (19). Splicing removes introns and joins exons together (12,13), which can occur after 3’ cleavage/polyadenylation (in short transcripts) or simultaneously during transcription, particularly in 5’ parts of genes with multiple exons (18).Usage of particular splice sites defines inclusion or exclusion of exons leading to different mRNAs being translated into protein isoforms that may have distinct functions, in a process called alternative splicing (AS) (20).

Although approximately 75% of the human genome is transcribed, not all transcripts are translated into proteins (21,22). These noncoding RNAs include ribosomal RNA (rRNA), transfer RNA (tRNA), small nuclear RNA (snRNA), small nucleolar RNA (snoRNA), microRNA, piwi-interacting RNA (piRNA)

and small interfering RNA (siRNA), and are expressed at different levels; 80-90% of total RNA in most cells corresponds to rRNA and the remaining 10% are non-coding RNAs (23). Most non-coding RNAs are processed by capping, splicing and polyadenylation (22). However, various non-coding RNAs are non-canonically processed, lacking 5' cap, poly(A) tail or both, or containing retained introns (RIs) or mutually exclusive exons, showing stable conformations and playing important cellular roles (22). mRNA is the third more abundant RNA, after tRNA (10-15%), representing 3 to 7% of total RNA, approximately two orders of magnitude more than remaining non-coding RNAs (23).

1.2 Pre-mRNA splicing

Production of different mRNAs from a single gene by splicing involves accurate recognition of introns and exons, followed by precise removal of introns from pre-mRNA and ligation of exons (24,25). Splicing requires conserved sequences within both introns and exons, that contain dinucleotides GU and AG at the 5' (donor) and 3' (acceptor) exon-intron junctions, respectively (24,26) (Figure 1).

The 5' splice site (5'ss) consensus motif is characterized by a 9 nt long sequence (MAG/GURAGU, where M denotes amino nucleotides, A or C, and R corresponds to purine nucleotides, A or G). The 3' splice site (3'ss) consensus sequences include three motifs: the YAG/G (where Y is a pyrimidine, C or T) motif at the intron-exon boundary, the branch-point (YNYURAY, with N representing any nucleotide) and the polypyrimidine tract (Py-tract). Altogether, these three distinct elements define a 3'ss region that may extend more than 100 nucleotides upstream of the 3'ss AG dinucleotide into the intron (24,26,27) (Figure 1).

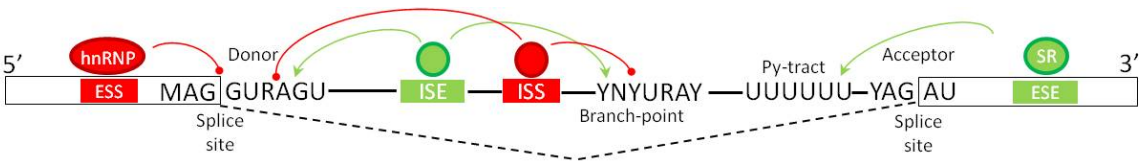

Figure 1 - Cis-acting elements involved in pre-mRNA splicing.
Schematic representation of consensus sequences of splice sites, branch-point and Py-tract. Exons are shown as boxes, intron as a line. Intronic and exonic splicing enhancer and silencer elements are denoted as green and red boxes, respectively. Corresponding trans-acting factors are represented by green and red circles and their effects are indicated by coloured arrows.

The 3’ and 5’ss are highly degenerate in eukaryotes and additional less conserved sequences present in exons and introns regulate this process, increasing the overall splicing accuracy and fidelity (24,28,29). These cis-acting regulatory sequences act by promoting or inhibiting recognition efficiency and are known as exonic or intronic splicing enhancers (ESE, ISE) or silencers (ESS, ISS), respectively (24,26). Although the role played by cis-acting elements varies according to the context they are inserted in, splicing enhancers tend to have dominant roles in constitutive splicing and silencers are usually more relevant in alternative splicing regulation (15,28,30–33). Both splicing enhancer/silencer regions are thought to interact with a number of trans-acting factors, such as serine/arginine (SR)-rich proteins or heterogeneous nuclear ribonucleoprotein (hnRNP) complexes (Figure 1) (24,26). However, structural properties of cis-acting factors involved in the assembly of ribonucleoproteins (RNPs) and how these motifs recruit and bind to proteins remain unclear (29,34,35).

RNPs are essential for gene expression and its regulation. The spliceosome is a large RNP responsible for pre-mRNA splicing, mainly constituted by uridine (U)-rich small nuclear RNPs (snRNPs) (35). Spliceosome assembly occurs in a dynamic and stepwise manner, starting with the interaction of U1 with the 5’ss (15,20). U2 auxiliary factor (U2AF) is recruited to the Py-tract and 3’ ss, resulting in the formation of the early (E) complex and the recruitment of the U2 snRNP to the branch-point (formation of A complex). The mature spliceosome (C complex), in which the two-step splicing process occurs, is then formed by the final association of U4-U5-U6 tri-snRNP (20).

The first step in splicing is a transesterification reaction (exchange of an esther R” group with an alcohol R’ group), where the binding of U1 and U2 to RNA brings the splice sites into proximity (36). The 2’-hydroxyl group of the A residue of the branch-point YNYURAY sequence reacts with the phosphate group of the G residue at the 5’ss, cleaving the exon-intron bond at the intronic 5’-end and forming a lariat structure (36,37). The exonic 3’-end has then a free 3’-hydroxyl group (37). The final splicing reaction binds the phosphate group at the intronic 3’-end and the free end of the detached exon together, releasing the intron in a lariat structure (f) (36,37).

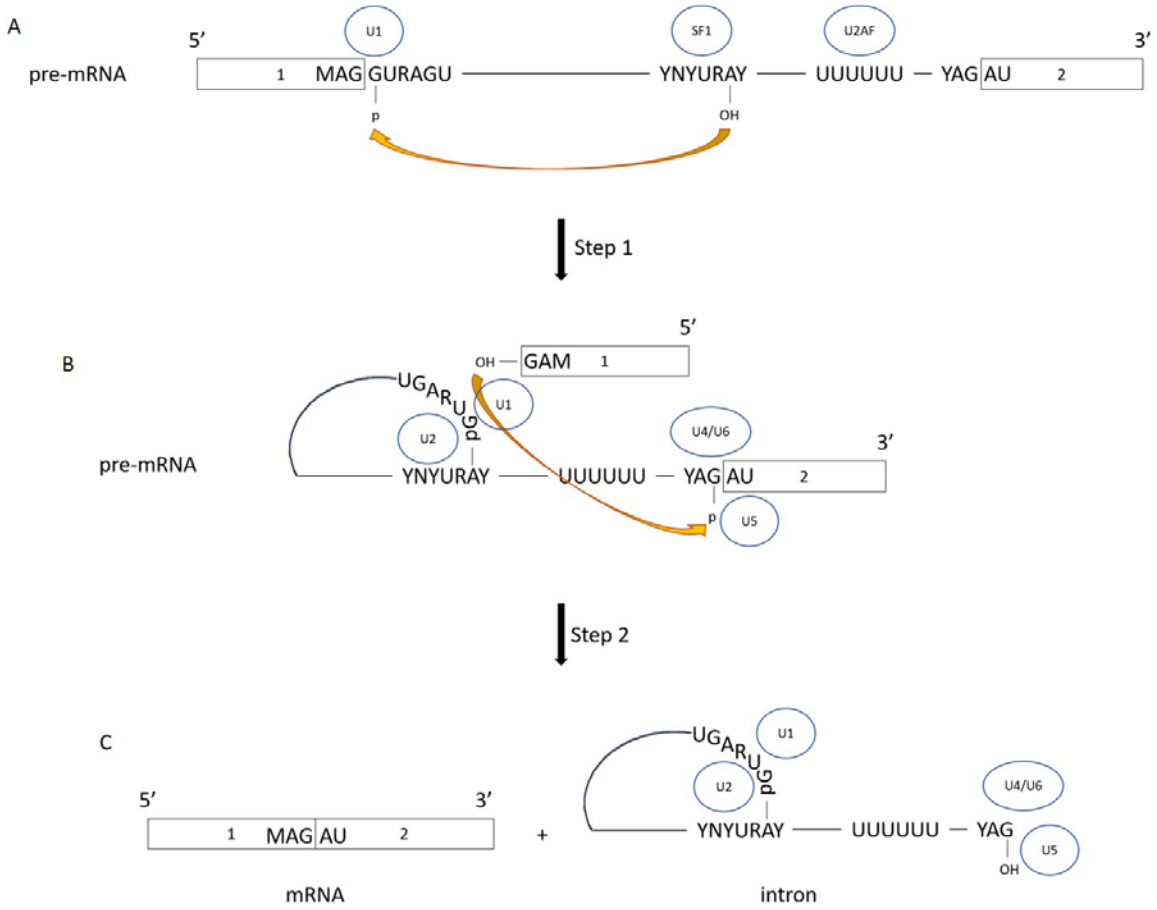

Figure 2 – Schematics of splicing reaction.
(A) The hydroxyl group of the branch-point adenine residue reacts with the phosphate group of the 5'ss guanine, the intronic 5'end is cleaved and a lariat structure is formed **(B)**. For the second step, snRNPs U4-U6 bind to the intron/exon 2 junction and the free hydroxyl group in exon 1 reacts with the phosphate group of the intronic 3'ss guanine. The exons are joined together and the intron is released in the lariat form within the spliceosome complex **(C)**.

1.2.1 Cis-acting regulatory sequences and trans-acting factors

Splice-site selection and the choice as to whether splicing is activated or inhibited is influenced by the non-spliceosomal RNA-binding proteins that interact with intronic and exonic cis-acting elements (38). ESEs were traditionally associated with interactions with members of the SR-rich protein family while ESSs may recruit hnRNPs (Figure 1) (15,29). In contrast to exons, intronic splicing regulatory sequences and their binding properties have not been studied as extensively. However, identical elements can, depending on the genomic context, act either as enhancers or silencers. For example, the effect of CA-repeats on splice site recognition depends on their proximity to the splice sites; these are bound by hnRNP L, which may promote or inhibit splicing (39). The brain- and muscle-specific splicing factors Fox1/Fox2 bind to the ISEs UGCAUG hexanucleotides. Pairs of YCAY motifs interact with Nova family factors, and as for CA-repeats, these can function as either ESSs or ISSs (15,29,39,40). A third class of RNA-binding proteins (RBPs),

termed tissue-specific RBPs, are also thought to bind to both types of cis-acting elements and act as either activators or repressors (38).

SR-rich proteins (41) and hnRNPs (42) are the most abundant and best-characterized splicing factors. SR proteins like SRSF1 (ASF/SF2) and SRSF2 (SC35) regulate splice site selection but also have roles in mRNA export from the nucleous, localization, translation and non-mediated decay (NMD) (43). SR-rich proteins bind to ESEs through their N-terminal RNA-recognition motifs (RRMs), recruiting and interacting directly with spliceosomal machinery components via their C-terminal SR-rich domains (41,43,44). It is still unclear whether SR proteins regulate splicing in an independent manner with relation to other family members or in cooperativity with each other (43).

1.2.1.1 hnRNP family

The hnRNP family comprises a group of 20 abundant, major proteins named hnRNPs A-U, and other less abundant, minor hnRNPs (45,46). hnRNPs have varied functions that depend on their cellular localization, assisting in transcription, splicing regulation, 5'capping, polyadenylation, mRNA cellular transport, translation and degradation processes (46,47). Although, most hnRNPs are located in the nucleus, post-translational modifications (methylation, phosphorylation, ubiquitination or sumoylation) or recruitment by other hnRNPs members lead to their translocation to the cytosol (45–47). The different functions of hnRNPs are due to a multiplicity of interactions with pre-mRNAs and other hnRNPs, giving rise to alternative splicing isoforms as a result of a diversified combination of exons in mature transcripts (47).

hnRNPs have mainly been associated with splicing inhibitory mechanisms since they typically bind to splicing silencer elements (15,29,48). Although hnRNP-mediated repression of spliceosomal assembly has been associated with different phenomena such as multimerization along exons, blockage of snRNP recruitment or looping out of exons, their underlying mechanism of action is not yet fully understood (44,47).

hnRNPs structural properties arise from arrangements of a number of domains with different functions (47). There are four types of unique RBPs as hnRNPs building-blocks: the RRM, the quasi-RRM (q-RRM), the glycine-rich domain (repeats of Arg-Gly-Gly tripeptides that constitute RGG boxes) and the KH domain (46,47). Similar RNA-binding properties and functions among hnRNPs result from the presence of the same RBP, which facilitates classification into sub-families (46–48).

RRMs are responsible for the interaction of hnRNPs with single-stranded nucleic acids of variable lengths (46), while the RGG box establishes interaction with other hnRNPS, and the KH domain

specifically binds to RNA (45,47). qRRMs lack two degenerate RNP consensus sequences present in RRMs, therefore recognizing and binding to RNA in a different manner, enclosing RNA G-tracts (46).

The hnRNP F/H family, including hnRNP F, H1 (H), H2 (H') and H3 (2H9), lack the conservative degenerate RNA-binding sequence present in most hnRNPs; therefore, their RBDs are described as qRRMs (46,47,49,50). Each protein contains three qRRMS; qRRM3 is structurally similar to canonical RRM but qRRM1 and qRRM2 adopt a different fold with a more exposed RNA-binding surface (46,49).

hnRNP F and H specifically bind poly(G) tracts (51–53) and are highly similar in sequence and structure (46). Although both proteins have been found to be involved in the regulation of alternative splicing, the mechanisms that drive hnRNPs F/H interaction with pre-mRNAs and what the role of this interaction is in splicing regulation of genes remain unknown (46,54–57).

1.2.2 *Alternative RNA processing*

The complexity of gene expression is increased by alternative transcriptional initiation (Figure 3A) (58) and/or AS (Figure 3B) and/or polyadenylation events (Figure 4) (59–61), resulting in the formation of multiple mRNA isoforms from the same gene by joining the exons in different combinations (43,62). Alternative transcription initiation is generally associated with usage of alternative promoters, rendering mRNAs with different starting exons (Figure 3A). AS may involve mutually exclusive exons, alternative 5'ss, alternative 3'ss, cassette exon skipping, intron retention (IR) (Figure 3B) (62–64). More complex splicing events may occur by combining two or more of these events (12). Maturation of mRNA 3'ends occurs by RNA cleavage followed by the synthesis of a poly(a) tail. Most genes contain more than one polyadenylation site, leading to the formation of mRNAs with distinct 3'UTRs (60,61). As illustrated in Figure 4, four different types of alternative polyadenylation (APA) events may occur: tandem 3'UTR APA, alternative terminal exon APA, Intronic APA and internal exon APA (61).

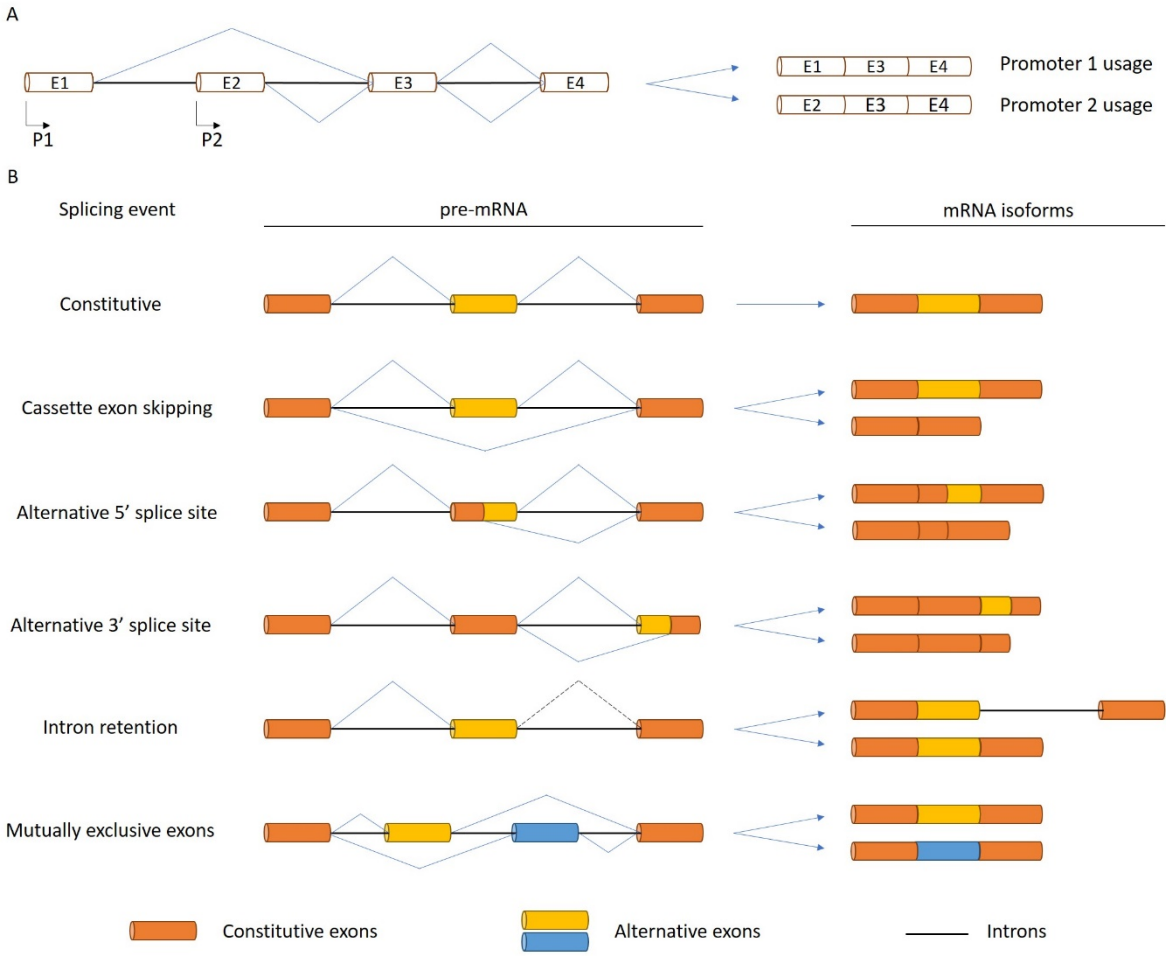

Figure 3 – Schematics of gene expression regulatory alternative events.
(A) Alternative promoters for the same gene create mRNA diversity. Usage of promoter 1 (P1) leads to the constitutive inclusion of exons 1 (E1), 3 (E3) and 4 (E4) in the mature transcript, while the use of promoter 2 (P2) originates a final transcript including exons 2 (E2), 3 and 4. Exons are shown as numbered white boxes, introns as thick black lines. Promoters are denoted by black arrows. Splicing patterns are indicated by blue lines. **(B)** Several different mRNA isoforms may arise from alternative splicing events occurring within one gene. Beyond constitutive splicing, from which a single mRNA transcript is created, a specific exon may be partially or fully excluded from the mature transcript, via one out of four events: cassette exon skipping, alternative 5'ss, alternative 3'ss or mutually exclusive exons. Retention of introns leads to transcripts with extended segments, either in untranslated regions (UTR) or in the coding region.

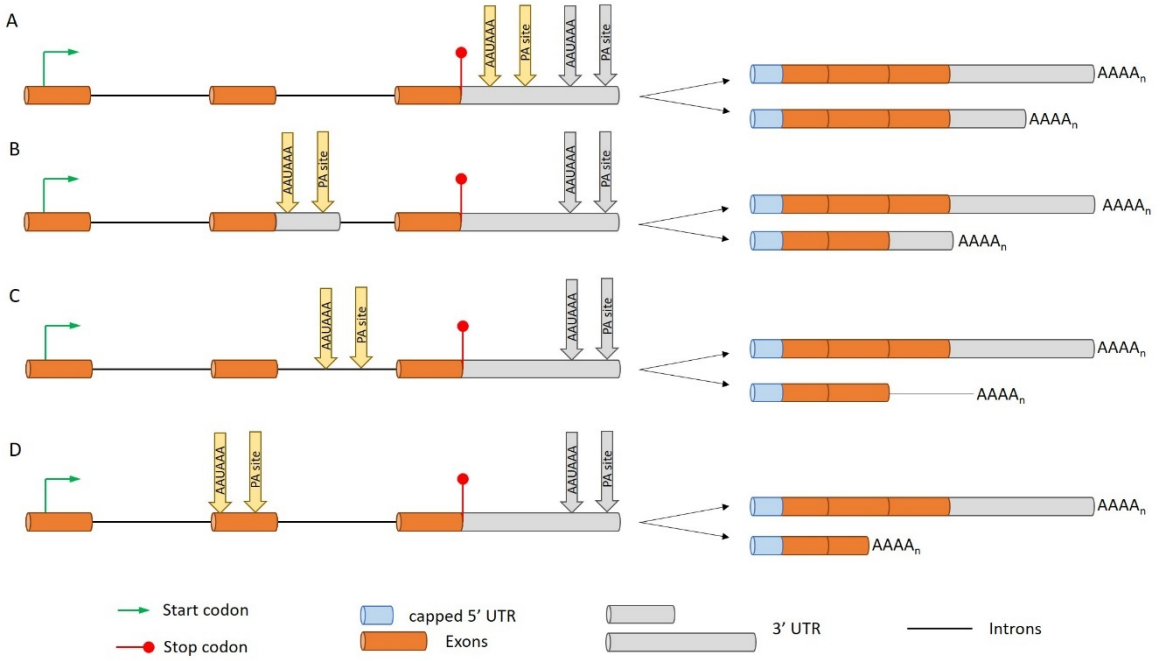

Figure 4 – Schematics of alternative polyadenylation events that modulate gene expression. Most human genes contain more than one polyadenylation signal, which lead to four different types of alternative polyadenylation (APA) events. Tandem 3'UTR APA (A) and alternative terminal exon APA (B) are the most frequent events and involve cleavage at 3'UTRs. In tandem 3'UTR APAs occur in the same terminal exon, originating mRNA isoforms with different 3'UTR lengths without altering the coding region. Alternative terminal exon APAs results from a combination of the use of an alternative polyadenylation site and alternative splicing, giving rise to transcripts with different terminal exons. Intronic APA (C) and internal exon APA (D) are less frequent, leading to alterations in the coding region and originating truncated proteins. Cleavage at a cryptic intronic polyadenylation signal extends an internal exon that becomes the terminal one. Cleavage and polyadenylation at an internal exon occurs within the coding region.

AS is also a gene-regulatory mechanism, highly tissue and developmental specific (20), mostly leading to the inclusion or exclusion of exons and introns that can control mRNA levels (13,62,65).

In humans, >95% of multi-exonic genes undergo alternative splicing which potentially allows genes to encode different proteins or isoforms of proteins possessing different structures and functions (13,65–67). Hence, AS is a gene expression control mechanism that generates large protein diversity in higher eukaryotic cells (67).

Pre-mRNA splicing is regulated at more than one level; recent studies demonstrate that transcription elongation rate, RNA editing and chromatin structure affect splice site recognition, along with previously described RBP recognition of cis-acting elements (68). Thus, transcription, splicing and polyadenylation are coupled processes that influence one another.

1.2.3 Co-transcriptional splicing

Separate analysis of different gene expression processes as static and independent steps may facilitate their study, however, most of these dynamic processes are orchestrated (69,70).

Splicing frequently starts soon after transcription initiation; analysis of nascent RNA transcripts showed degradation of the first intron while the second intron is still being transcribed (64). In addition, immunofluorescence and chromatin immunoprecipitation assays show co-localization of both splicing and transcriptional machineries (68,71).

The co-transcriptional nature of splicing involves a fine-tuned set of interlinked processes leading to the production of functional mRNAs, via coordinated interaction of many proteins with DNA, RNA and other proteins.

Any of these processes is the target of components from any of the other processes. Therefore, formation of primary transcripts and release from the transcription machinery as pre-mRNAs, around which spliceosome assembles to remove introns, might not exist separated mechanisms. On the contrary, the co-transcriptional nature of splicing implies intron removal as soon as relevant splice sites and splicing regulatory sequences are synthetized, especially in very long genes. The strength of these newly transcribed splice sites, along with their positioning and proximity to stronger or weaker splice sites, determines their efficient recognition and lead to different alternative splicing events (Figure 3B) (72).

Currently, the model used to describe gene expression regulation states that coordination of chromatin organization, histone modifications, direct association of RNA pol II CTD with splicing factors, and RNA pol II elongation rate, is required for an accurate and efficient processing of RNA transcripts. Therefore, chromatin, transcription and splicing are organized in such a way that ensure temporal and spatial control of splicing (72).

Independently of whether splicing occurs co- or post-transcriptionally, splicing initiation relies on the evaluation of which units are to be removed and which are joined together, along with the identification of genuine splice sites amongst several pseudo sites (72,73). As previously mentioned, the relative strength of genuine splice sites plays an important role on their selection. However, many weak splice sites, located at suboptimal contexts, are efficiently identified, while other strong splice sites are ignored by the splicing machinery (73). The selection of genuine splice sites occurs concomitantly with the definition of exons and introns and the distinction between the two. There are two mechanisms through which the splicing units are recognized: intron definition and exon definition (73). Both mechanisms may take place in, virtually, any gene. Distinction between one or the other is based on both intron and exon sizes (73,74). Intron definition mechanism is

characterized by selection and binding of splicing factors to splice sites within intronic sequences, as depicted in Figure 1 in section 1.2. On the other hand, intron definition tends to take place when exons are long and introns short, while exon definition and splicing machinery assembly occurs if exons are small and introns long (73,74). The exon definition mechanism is characterized by the search and pairing of splice sites located across the exons. Selection of pairs of closely spaced splice sites leads to recruitment and binding of splicing factors to the downstream 5'ss and the upstream 3'ss define the flanked exon. Following definition, interactions between splicing factors in individual exons promote juxtaposition of neighbouring exons and introns are removed (74).

Although these two processes imply different coordinated interactions between splicing factors and RNA cis-acting elements, the underlying spliceosome assembly mechanism is the same and both exon and intron definition may occur in the same transcript (73).

Trans-acting factors recruitment, whether in exon or intron definition mechanism, occurs while the transcript is in contact with DNA, via RNA pol II C-terminal domain (CTD) (72). CTD is highly conserved through evolution, its length and structural diversity increasing with organisms' complexity. Mammalian CTD is composed of 52 repeats, of which 21 consist of a conserved peptide with the sequence Tyr^{1}-Ser^{2}-Pro^{3}-Thr^{4}-Ser^{5}-Pro^{6}-Ser^{7}, and the remaining being more degenerate (75). Such a repetitive sequence confers CTD with a highly flexible structure, enabling it the potential to bind other splicing factors with diverse conformations (76).

Post-translational modifications, specifically phosphorylation at defined amino acid residues, also regulate CTD activity (75–77). Residues Ser^{2} and Ser^{5} are the main targets of phosphorylation, coordinating multiple events during RNA synthesis (75,76,78). Therefore, through changes in the phosphorylation pattern, as RNA pol II translocates along the gene, CTD promotes the recruitment of histone modifiers, chromatin remodelling complexes and splicing factors (76,78). Links of CTD activity with many regulatory processes during transcription has been showed through the identification of CTD-bound proteins with different functions. SR-like proteins, Prp40, cleavage/polyadenylation factors and the capping enzyme complex, involved in RNA processing, interact with phosphorylated CTD (78). The histone acetyltransferase PCAF and the histone methyltransferase Set2 also interact with the phosphorylated form of CTD, facilitating RNA pol II mobility through chromatin and transcription elongation, respectively (78). CTD may also play a role in DNA damage responsiveness since it has been shown to interact with Hrr25, a protein kinase involved in this process (78).

In summary, CTD of RNA Pol II acts as a bridge, recruiting and promoting the binding of transcription and elongation factors, interacting and activating the 5' capping enzyme factors, establishing links

with histone modifications and chromatin remodelling, and being required for the localization of splicing factors to transcription sites (64,68,76,78).

Histone modifications directly play important roles in RNA processing as well. A histone acetyltransferase has been shown to regulate the association of U2 snRNP components to the nascent transcript (79,80). Histone modifications direct nucleosome positioning and chromatin remodelling through binding to SR proteins (79,81,82). SR proteins may directly affect transcription, since some members of this family have been found to interact with intronless genes. However, the presence of introns, in the vast majority of human genes, further promote transcription via recruitment of transcription initiation factors and enhancement of the pre-initiation complex by functional 5'ss (79,80,83–85).

All the above processes are, thus, interconnected and strongly influence one another. Disruption of either mechanism may lead to impaired expression of one or several genes, simultaneously.

1.2.4 Introns in splicing

Introns have always been considered has having only two possible fates: removal from pre-mRNA followed by degradation or retention in processed RNA transcripts. Recently, introns have been classified as exitrons (86), retained introns (87) and detained introns (70), according to their involvement in RNA transcripts fate and whether their splicing is co- or post-transcriptional (70,88).

IR is an alternative splicing regulatory event characterized by the presence of one or more introns in polyadenylated mRNA (89,90). It can alter different gene expression steps, including transcription, polyadenylation, mRNA export to the cytoplasm, translational efficiency and mRNA decay (91–93).

A detailed study of retained introns (90) showed that IR is widespread in mammals. IR is characterized by a set of features that allow the distinction of retained from constitutive introns: the former show reduced length, high G/C content, weaker splice sites, relative location in the primary transcript, elevated G/C content in flanking exonic sequences and ratios of intron and upstream exon lengths to downstream exon length.

Intron-retaining transcripts may potentially be removed by nuclear retention and exosome degradation or by NMD. NMD is the cellular process through which mRNAs with premature termination codons (PTCs) are degraded during the termination step of the first round of translation, therefore preventing further translation into aberrant proteins (92–98). Most transcripts with retained introns are, in fact, not exported from the nucleus and usually lead to the introduction of

PTCs (90) or upstream open reading frames (uORFs) (99,100). PTCs in retained introns often give rise to C-terminal truncated proteins that potentially have dominant negative properties, if PTCs are not recognized by the NMD system (90,101), while the presence of uORFs usually correlate with decreased protein expression. AUG-starting uORFs are often translated, which makes it difficult to reinitiate translation at downstream canonical start codons, reducing the efficiency of translation initiation of the main ORF, and often trigger mRNA decay (102,103).

Recently, a new set of transcripts containing slowly spliced introns has been described (70). Detained introns (DIs) in polyadenylated RNAs are spliced post-transcriptionally, in agreement with an earlier proposal that, within the same gene, 5'-end introns are generally co-transcriptionally spliced while 3'-end introns are post-transcriptionally spliced (104,105). An extensive analysis of transcripts containing DIs demonstrated that these introns are often found in the flanking regions of alternatively spliced exons (70) and most DIs contain PTCs. Regardless of the presence of PTCs, DI-containing transcripts are often held in a nuclear-detained pool until changes in the cellular environment promote post-transcriptional splicing (70).

Nevertheless, not all intron-containing transcripts are degraded or retained in the nucleus, some have been identified in close proximity with polysomes, indicating their transportation to the cytoplasm (70,88).

Some retained introns show a G/C content and codon usage similar to coding exons and display the capacity of encoding protein domains (91,106). For example, the retained intron positioned between nucleotides 723 and 1207 in the *Homo sapiens* EF1a-like protein mRNA encodes the Elongation factor Tu domain; the intron located between nucleotides 995 and 1176 in the *H. sapiens* JM2 protein mRNA partially encodes a Fork Head domain (87).

Finally, a subset of retained introns, named exitrons (exon-like introns), have been found within protein-coding exons and allow the preservation of the transcript's protein-coding potential. Their properties comprise a high G/C content, absence of PTCs, prevalence of synonymous substitutions and highly conserved sequences (88).

Exitron splicing may strongly affect protein structure and function since they are mostly found in intrinsically disordered regions and in coding regions associated with post-translational modifications, such as phosphorylation, ubiquitylation, sumoylation, S-nitrosylation and lysine acetylation (86,88).

Considering their described properties, exitrons have features in common with both introns and exons. They show relatively weak splice sites and high G/C content, which leads to inefficient splicing, just like in introns. However, Marquez and colleagues (86) have shown that exitron

processing responds differently to distinct cellular environments, which distinguish them from retained introns. Transcripts containing exitrons are exported to the cytoplasm and translated, while transcripts with retained introns are usually kept in the nucleus and translation is prevented. PTCs are generally a consequence of a retained intron, but are absent in transcripts containing exitrons with a length divisible by three. Finally, a number of transcripts with retained introns were reclassified as exitrons; 670 retained introns in 577 genes are now termed exitrons. These, together with other previously classified exitrons, account for a total of 923 exitron events in 747 human genes (86,88).

Hence, exitron splicing may be defined as another form of alternative splicing that, under different cellular stress conditions, might significantly alter protein diversity.

Regardless of the classification of introns, their role in the fate of mRNAs demonstrated that introns play important roles in gene expression and nuclear mRNA export regulation, as well as in the synthesis of protein isoforms by alternative splicing (96).

1.2.5 *The importance of RNA secondary structure in splicing*

Like DNA and proteins, RNAs adopt highly versatile structures (**Figure 5**) and different conformations that govern their function in the cell. This does not apply just to structured RNAs such as tRNA or snRNA, but also to pre-mRNAs, where structural constraints can markedly influence RNA processing, by both promoting or inhibiting it.

Pre-mRNAs are capable of adopting complex secondary and tertiary structures, considering the large number of base-pairing possibilities (12,107). The same nucleotide sequence can form many diverse structures (Figure 5), which can bring together or separate, as well as expose or hide, splicing regulatory elements and modulate alternative splicing (27,107) (Figure 5).

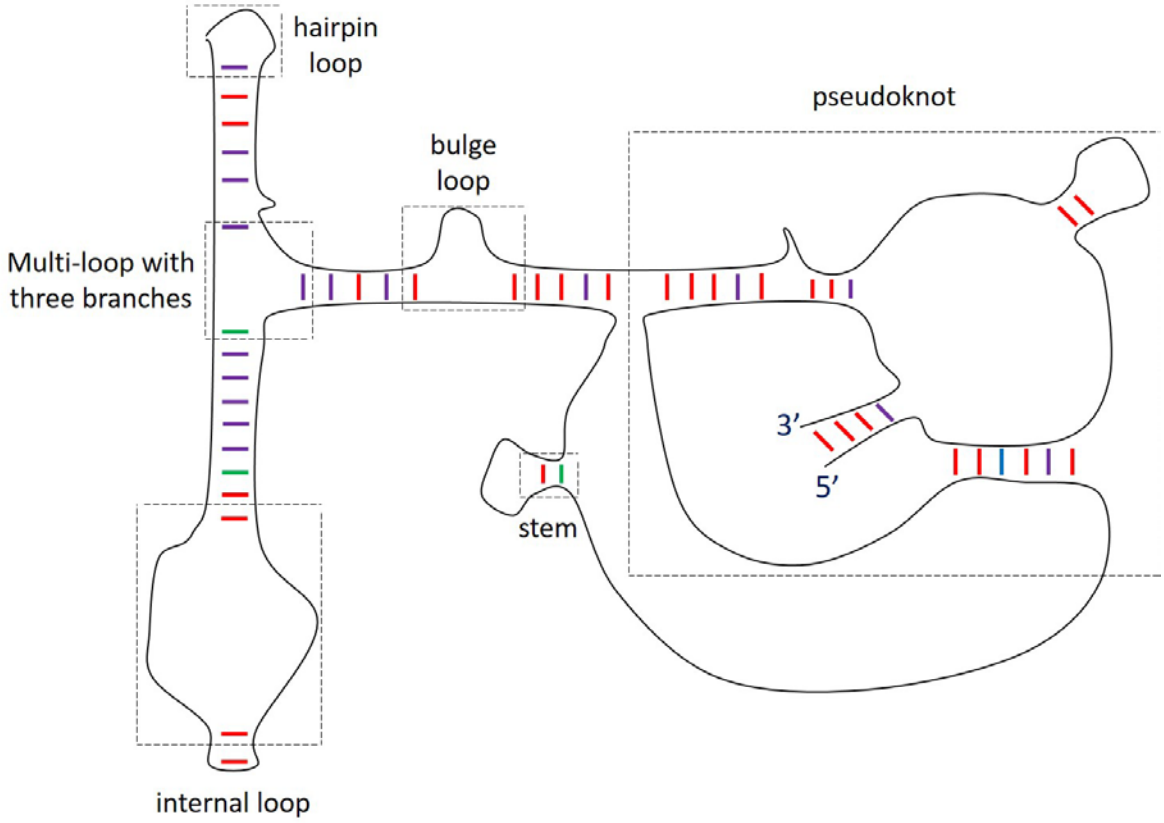

Figure 5 – Schematics of the secondary estructures adopted by RNase P RNA strand of *Methanococcus marapaludis*.
A single strand of RNA can adopt different secondary structures, such as pseudoknots, stems, bulges, apical or internal loops (highlighted by dashed boxes). Thick coloured lines indicate base pairs; G-C in red, A-U in purple, G-U in green and U-U in blue (modified from RNA STRAND v2.0 – The RNA secondary STRucture and statistical Analysis Database (108)).

Changes in RNA structure may impair accurate recognition of essential elements in RNA processing (27). Of high importance for efficient splicing are the sequences that comprise 5'ss and 3'ss, the branch-point and the Py-tract. Several native base-paired structures that sequester these motifs have been identified (27). Since U1 and U2 snRNPs bind to single-stranded sequences (109,110), folding of these regions leads to binding failure and splicing inhibition. The inverse situation may have the opposite effect; folding can bring essential sequences together, allowing splicing factors to bind and promote transcript's processing. Stem-loops can bring into closer proximity the 3'ss with the 5'ss and the branch-point or mask cryptic splice sites (27,111).

Canonical Watson-Crick A-T and G-C pairings are not the only possible interactions between bases. In fact, a large set of different base-base interactions have been described to stabilize both secondary and tertiary structures, including A-C, G-U, A-A, A-G, U-U, U-C interactions (112–114).

The impact of structural changes on splicing modulation remains poorly understood since studies have mainly been performed to the analysis of short-range interactions in short sequences (115).

From these, however, evidence showing that pre-mRNA secondary structure plays an important role in regulation of AS is clear (116–118).

The high flexibility of RNAs has led researchers to postulate that most pre-mRNAs exhibit only local structures (118,119) and that their folding is strongly influenced by their context (length and sequence of flanking segments) (118,120). Several reports show that pre-mRNA folding is transient and structural stability time-windows *in vivo* are small (118,120).

Pre-mRNA folding occurs mainly co-transcriptionally, hence most *in vivo* pre-mRNA structures are expected to be local (115). This is attributed to binding of splicing factors to the nascent RNA, which limits molecular spatial freedom and sequence length available for conformational changes to 50nt downstream of the transcribing polymerase. Therefore, short-range base-pair interactions are preferred and long-range ones are disfavoured (121). In particular, simple local hairpin conformations have been shown to be the most prevalent ones (121). Thus, most studies have been applied to uncover the role of local secondary structures on AS events (115).

A very relevant study (122) showed that computational predictions of splice-sites are more robust and accurate when pre-mRNA secondary structure data is combined with conventional prediction algorithms for sequence-based splice-sites (122,123). In agreement with this, some studies showed that alternative splice sites are generally flanked by structures with higher stability than the ones surrounding constitutive and skipped splice-sites (123–125).

A few examples of alternative splicing events modulated by RNA secondary structure have been well described. In example, sequestration of ESE and ESS elements in RNA structures reduces their splicing regulatory activities (115).

Using computational analysis to determine propensity of splicing enhancer/silencer motifs for folding, Michael et al. concluded that these elements are preferentially located in single-stranded arrangements (118). Confirmation of their predictions was verified in transfected cells by stronger activities of both elements when located in hairpin loops against activities in hairpin stems, leading to stronger exon inclusion or skipping, respectively (118).

Wei Liu et al. showed the same tendency with a 7nt hairpin structure containing an ESE motif of a SMN1 minigene model (121), which activity proved dependent on its sequence and location within the hairpin structure. AG-rich ESE in the loop region were fully active, while UCG-rich ESE is prone to non-canonical interactions, significantly decreasing enhancer activity (121). Furthermore, ESE activity is very strong when these motif is located downstream of the hairpin, regardless of their sequence, and is maximized when right adjacent to the hairpin 3’ end (121).

Woodson SA and Cech TR showed that the Tetrahymena group I intron can adopt two alternative secondary structures, one of which being a stable conserved hairpin that inhibits the use of the 5'ss (117,126).

Long-range interactions have also been shown to modulate splicing. Introns within an exon cluster of the Drosophila Dscam gene contain specific base-pairing sequences that seem to be required for inclusion of exon 6 and which strength contributes to the frequency of exon 6 inclusion. These base-pairing sequences have the potential to span several thousand nucleotides (115,127,128). Other structures within Dscam gene modulate exon 4 inclusion or influence mutually exclusive exon selection in exon 17 cluster (115,129,130). Mutations within 202 long-range structures in Drosophila introns led to changes in the alternative splicing patterns of respective mutated genes (115,131).

Secondary and tertiary structures do not determine, per se, whether an exposed splicing-regulatory sequence is used or not; dynamic interactions with splicing regulatory factors or base pairing with other RNAs followed by RNA:protein interaction is required (117).

Regulation of the human cardiac troponin T exon 5 splicing depends on the binding of the protein MBNL1 at the 3' end of the upstream intron, stabilizing a local hairpin and blocking U2AF65 association to pre-mRNA (115,132).

Recruitment of SR proteins by both ESE and ESS elements present in the EDA exon of the fibronectin gene are highly dependent on the structural context comprising these elements (111,115,133). RNA rearrangements leading to exposure of an ESE motif in a single-stranded loop followed by SF2/ASF splicing factor binding enhance EDA splicing (111,121,133).

A deletion in EDA exon of SMN2 gene causes a structural rearrangement of a ESE from a single-stranded to a stem conformation that sequesters the 3'ss and leads to the skipping of exon 7 (111,118,134).

Binding of splicing factors such as B52, SRp55, NOVA-1 and hnRNP A1, is highly dependent on the presence of certain RNA secondary structures and nucleotide sequences (116,135–138).

RNA global structure is also affected by RNA:protein interactions. Association of U2AF65 to the 3'ss drives pre-mRNA to undergo structural rearrangements forming a more compact structure that brings together the 3'ss and the branch-site (116,139).

A growing number of genes reported to present a non-canonical secondary structure called G-quadruplex, which is able to function as a cis-acting element that modulates splicing is another

indicator of the important role of RNA secondary structure on alternative splicing events regulation (140–142).

The potential role of these structures on splicing regulation has been shown through their interaction with a number of trans-acting factors (140,143–149). Huilin Huang et al. demonstrated that the cis-acting element termed I-8, located in the intron downstream from the CD44 variable exon 8 (140,150), folds into this non-canonical secondary structure, G-quadruplex, promoting alternative splicing and production of the epithelial-specific CD44v isoform through the binding of the trans-acting factor hnRNP F to this secondary structure (140).

These data correlate with previous statements that formation of certain RNA secondary structures mask some splicing regulatory motifs while exposing others, modulating RNA processing, either by promoting or inhibiting (27,107).

1.2.5.1 G-quadruplex

A high-ordered structure characterized by non-canonical G-G pairing is commonly found in gene regulatory regions. This conformation is referred to as G-quadruplex (G4) and occurs in both DNA and RNA (151–153). G4s are usually found within sequences containing several repeats of two or more consecutive guanines, also referred to as G-tracts (Figure 6A).

Guanines in G-tracts are able to serve as both donor and acceptor and form two stable hydrogen bonds with one another, forming a square co-planar array of guanines, named G-tetrad or G-quartet (Figure 6B). These cyclic Hoogsteen hydrogen bonds involve N1-O6 and N2-N7 pairings, in a total of eight hydrogen bonds per tetrad, from single-stranded nucleic acids connected by loops with diverse lengths (154–157) (Figure 6B). Four G-quartets further assemble into G4s (50,154,158),

G4s require a minimum of two contiguous G residues with typical gaps between G-strecthes of one to seven nucleotides which comprise the loops formed in intramolecular G4 assemblies (157).

Intramolecular G4s are generally more complex than intermolecular ones, showing a variety of topologies, loop conformations and capping structures (156). The same sequences may acquire different topologies and this diversity is dependent on several factors, such as the number of separate DNA/RNA strands involved in G4 formation, the pattern of strand orientation, oligonucleotide sequence and length, length and nucleotide composition of loops, and type of alkali metal ions present (153,156,157) (Figure 6C). G4s high polymorphism reflects a variety of different conformations, generally grouped accordingly to their relative strand orientation (154,156,159,160).

Structural and topological variety is further enhanced by the presence of other secondary structures within the G4 (160,161), such as homo-tetrads (A-, U-, T- or C-), mixed-tetrads (G:C:G:C, G:T:G:T or A:T:A:T) (152), bulges (162) and/or vacancies (163).

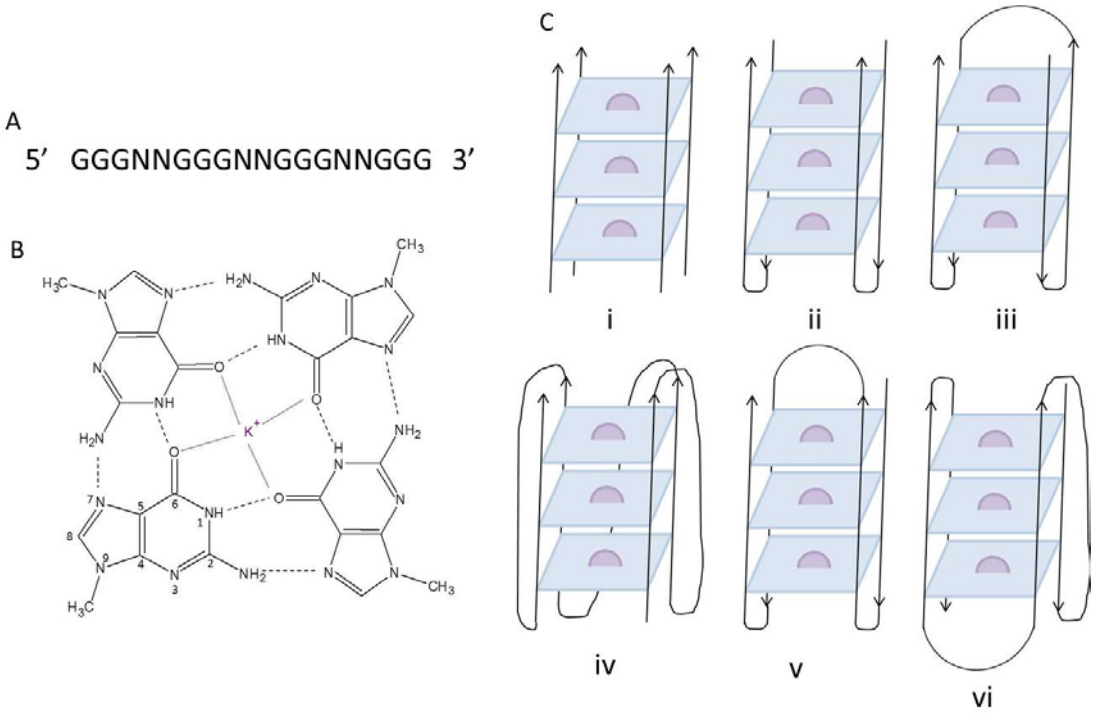

Figure 6 - Illustration of a G-tract folding into G4.
(A) A generic G-tract sequence that can form G4 structures. The letter N denotes any base. **(B)** Arrangement of guanine hydrogen bonds in a G-quartet coordinated with potassium ions (K^+). Structure obtained with ACD/ChemSketch Freeware [1]. **(C)** Examples of intermolecular and intramolecular G4 conformations, composed of three G-quartets. Intermolecular G4s result from the interaction between two or more separate DNA/RNA strands (i, ii); intramolecular G4s are formed by a single strand (iii, iv, v, vi). Purple semi-circles denote coordinated cations.
[1] ACD/ChemSketch Freeware, version 15.01, Advanced Chemistry Development, Inc., Toronto, ON, Canada, www.acdlabs.com, 2015.

Although G4s may be tetra-, bi- or unimolecular, topological classification is mainly based on strand orientation: parallel G4s contain strands oriented in the same direction with respect to one another, while strands of anti-parallel G4s are opposite oriented to the two adjacent strands. Hybrid parallel and anti-parallel strand orientations have also been observed (157,164,165).

Positively charged cations are essential for formation and stabilization of both DNA and RNA G4s, in particular, potassium (K+) and sodium (Na+) (166). Depending on the physiological conditions, different metal ions can induce considerable conformational changes (153,156,167). Independent studies have shown that G4 topology may be determined by the coordinated cation. Each cation has its own ionic radius, which determines ion-specific affinity and capacity for G4 stabilization and transitions between different secondary structures (166). Potassium shows a stronger stabilization

capacity when compared to other monovalent cations: $K^+ > Rb^+ > Na^+ > Li^+ = Cs^+$. Lithium was usually considered as a destabilizing cation; however, it may also play a neutral role (157). G4s may also coordinate with divalent cations which were shown to stabilize these non-canonical structures in the order of $Sr^{2+} > Ba^{2+} > Ca^{2+} > Mg^{2+}$ (157).

RNA structural diversity is much larger than its DNA counterpart, which can be partially explained by the absence of a complementary strand competing for hybridization (157). RNA G4 assemblies are more thermodynamically stable and show more compact structures with respect to DNA G4s. G4-forming RNAs are structurally more homogeneous and the parallel conformation has been found to be formed in the vast majority of studied sequences (157). Finally, it has been reported that G4 antiparallel orientation is strongly disfavoured in RNAs, although it may be possible in a very small set of sequences, such as the one found in the Spinach aptamer (168).

The role of G4s in gene expression *in vitro* has already been demonstrated by their presence in specific regions such as splice sites, polyadenylation signals, 5'untranslated regions (5'UTRs) and 3'UTRs, telomeres, gene promoters and rRNA (158). For example, formation of an intramolecular G4 in the 5'UTR of the human *NRAS* proto-oncogene mRNA is responsible for inhibition of its translation (169). An intramolecular G4 in the 5'UTR of *TERF2* mRNA prevents translation into the telomeric specific protein TERF2 (170). G4s present in 3'UTR regions of *LRP5* and *FXR1* mRNAs led to an increased protein expression (171). Decorsière and colleagues demonstrated that the interaction between hnRNP F/H proteins with a G4 promoted *TP53* pre-mRNA 3'-end processing, and enhanced protein expression and p53-mediated apoptosis (53). Formation of these structures within intron 3 of the same gene, *TP53*, correlated with a higher efficiency of intron 2 splicing (142). As a last example, a G-rich sequence modulates selection of an alternative 5'ss of BACE1 exon 3 by assembling into G4 and recruiting hnRNP H, activating production of the 501 isoform (172).

1.2.5.2 G4 detection tools and methodologies

G4s have diverse molecular structures (Figure 6). Understanding their chemical and biochemical properties elucidates the role of G4 structures in gene expression regulation and provides insights into development of G4 targeting ligands (173). Insights on biological applications of G4 structures are obtained by tools used to identify G-tracts in sequences, predict G4 formation, and design molecular and chemical methodologies for G4 detection *in vitro* and *in vivo* (173).

Any sequence containing four runs of at least three guanines separated by short stretches of any other bases can potentially fold into intramolecular G4s, therefore, the propensity to form G4

structures can be predicted by analysing the primary sequence in which these G-runs are contained (173).

Several computational tools have been developed to predict the formation of both intra- and intermolecular G4s directly by screening the primary sequence of both DNA and RNA (173–175). The QGRS Mapper, G4P Calculator, nBMST, Pqsfinder and QGRS-H predictor are some examples.

QGRS Mapper (176) predictions are based on the presence of quadruplex forming G-rich sequences in nucleotide sequences, through the identification of four sets of guanines with equal number of guanines, separated by arbitrary nucleotide sequences. However, this tool is very limited since it does not consider sequence and loop length and the number of tetrads, as well as the uniformity of lengths between G-runs (176,177).

G4P Calculator algorithm (178) scans nucleotides sequences using windows of fixed length, computing percentages of the number of G- and C-runs, total number of windows, number of windows containing G- or C-runs and the sum of the two percentages. Therefore, G-quadruplex propensity scoring is independent from sequence length (177,178).

nBMST algorithm (179) is designed to identify non-B motifs in nucleotide sequences, through the recognition of four or more individual G-runs of at least three guanines with 1-7 nucleotides between runs (177,179).

Pqsfinder (180) uses an algorithm that first identifies sequences of four consecutive G-runs. The putative g-quadruplexes are identified on the basis of their start location, length (width), score, number of G-tetrads, and loops lengths. This tool has the advantage of allowing the identification of G4-forming sequences even if the analysed sequence partially mismatch the generic pattern $G_{\geq 3}N_{1\text{-}7}G_{\geq 3}N_{1\text{-}7}G_{\geq 3}N_{1\text{-}7}G_{\geq 3}$ (177,180–183).

QGRS-H predictor (176) analyses the composition and distribution of putative quadruplex G-rich sequences in homologous RNAs, allowing the identification of evolutionary conserved motifs expected to fold into these structures, which also helps the validation of computational predictions by other tools (176,184).

QGRS Mapper was selected for G4 prediction of INS intron-derived oligonucleotides used in this study, since it has been the most widely used tool for the prediction of these non-canonical structures.

The consensus sequence, $G_{\geq 3}N_{1\text{-}7}G_{\geq 3}N_{1\text{-}7}G_{\geq 3}N_{1\text{-}7}G_{\geq 3}$, for putative G4 segments (177) is increasingly recognized to be inefficient for accurate prediction of G4-forming sequences, since it has been shown that large loops or non-guanine bulges have been found to also stabilize G4 structures (173).

Most algorithms allow the user to define loop length, but they do not count with non-guanine bases interrupting three-guanine runs or the fact that G4s are also stably assembled by sequences containing only two-guanine runs, particularly in RNA (173). Therefore, it is important for users to refine the parameters considered by the algorithm, decreasing both false positive and negatives.

Computational predictions for putative G4-forming sequences should, thus, be confirmed using *in vitro* and/or *in vivo* methodologies that allow the detection and characterization of G4 structures in predicted sequences. Many biophysical and biochemical methodologies have been developed and applied in combination for *in vitro* detection and characterization of G4 structures (173).

Each methodology is elucidative on a specific biophysical or biochemical property. Fluorescent dyes have been used as *in vitro* light-up structural probes for the detection of G4s due to their fluorescence enhancement in the presence of these structures (173). Fluorescent probes such as the benzothiazole Thioflavin T (ThT) (185–190), N-methyl mesoporphyrin IX (NMM) (190–193), triphenylmethane dyes (TPM) (190,194,195), thiazole orange (TO) (190,196) and triphenylamine (TPA) (190,197) provide a sensitive and selective methodology for the detection and distinction of G4 topologies among other secondary structures (173).

ThT is an efficient light-up probe that shows strong fluorescence enhancements and a red shift, in its absorption spectrum, in the presence of G4 structures, when compared to its fluoroscopic properties in water (190). High selectivity of ThT for G4 structures has been demonstrated, several times, via observation of large increments of its fluorescence emission around 490 nm, in contrast to very low emissions in the presence of double- or single-stranded DNA sequences (190), for which ThT was selected as the dye for G4 detection in the present project.

Similarly, TPM dyes, such as malachite green (MG) (190,194) and crystal violet (CV) (190,193,195) have proved as good sensors for detection of G4 formation. MG displays red shifts in both absorption and fluorescence spectra in the presence of G4s. Fluorescence intensities of both dyes are consistently largely increased for G4-forming sequences, when compared to fluorescence intensities in the presence of double- or single-stranded DNAs. Two TPA-based dyes, cyanovinyl-pyridinium triphenylamine (CPT) (190) derivatives 1 and 2, were designed for the same purpose and display the same spectroscopic properties as ThT and TMP dyes (190).

G4s also bind and are stabilized by porphyrin and phthalocyanine derivatives. N-methyl mesoporphyrin IX is the most well-studied derivative. Although, specific for these noncanonical structures, NMM displays low-to-modest fluorescence enhancements in the presence of G4s. Phthalocyanine derivatives show not only high specificity but also high affinity for G4s (190,198).

However, G4 detection and binding properties for these two dyes had been less explored than ThT at the moment this project design; hence the selection of ThT.

The presence of G4 structures can also be addressed via analysis of the thermal difference spectra (TDS) of nucleic acid sequences (199). This technique provides distinct spectroscopic signatures for each nucleic acid structure by determination of their thermodynamic stability at different wavelengths. Determination of each nucleic acid structure is based on changes in ultraviolet absorbance upon heat, reflecting conformational transitions caused by the disruption of base-pairing interactions (199,200). The global shape of each spectrum, rather than specific wavelength absorbance changes, should be considered to ascertain on each structure, due to ambiguity of transitions observed at the same wavelength for more than one structure, i.e. both G4, Z-DNA, i-motif, Hoogsteen duplex and pyrimidine triplex display an inverted transition at 295 nm (200).

Thermostability of G4s can also be determined by observing UV or CD spectra or gain/loss of signal in fluorescence resonance energy transfer (FRET) assays (200–202). Using these techniques, the denaturation process is monitored, relying on distinctive differences in spectroscopic properties between the folded and unfolded states, which allows determination of G4 melting (denaturation) temperature, specific for each structure (200,203). Characteristic UV- and CD-melting curves for G4 stability determination are measured at 295 nm and 264 nm, respectively (174,203). For detection of G4 structures by FRET, oligonucleotides are labelled with two fluorophores acting as energy donor and acceptor at different positions (203,204). To characterize thermal stability, fluorescence emission from the acceptor fluorophore is measured as a function of temperature. Commonly, labels are positioned as such to display fluorescence upon folded G4 structures and the signal decreases with temperature as the structures unfold (203–206).

The topology of G4 structures can be addressed by measuring the CD signal of each conformation. Parallel and antiparallel conformations show positive and negative peaks at specific wavelengths. Parallel G4s have a negative signal at 240 nm and a positive one at 262 nm, while antiparallel conformations show negative and positive signals at 262 and 295 nm, respectively (173). To corroborate G-quadruplex formation, the structures spectra should also be performed in the presence of different stabilizing ions, such as potassium, or destabilizing, like lithium (173).

Three-dimensional structures and interactions with ligands are obtained using NMR and X-ray crystallography. These techniques provide high-resolution information, at atomic level, on structures and data on kinetics and molecular interactions (207–209).

The majority of three-dimensional G4 structures, coupled with ligands, has been determined by X-ray crystallography. Comparing to NMR, X-ray crystallography has the advantage of providing

unambiguous ligand biding sites without prior prediction or knowledge of their location in the structure, through electron density maps. As for protein crystallography, G4 crystals diffract high-intensity X-rays to which they are exposed to and the intensity of the diffracted signal is measured. Data collected allow not only the determination of the intensity of diffracted X-rays but also recording the position of the crystal in relation to each diffraction signal measurement (210).

G4 structures originate NMR spectra with unique features. Chemical shifts of imino ($R_2C=NR$) protons from G-tetrads are observed within the range of 10-12 ppm, while the ones in Watson-Crick base pairing exhibit chemical shifts within 13-14 ppm. The compact structure of G4s protects imino protons from solvent exchange. Therefore, twelve sharp guanine imino protons consistent with a three-layered G4 exchange very slowly with the solvent and are detectable long after dissolving the structure in D_2O solution. The NMR spectrum of a single G-rich sequence elucidates on the presence of multiple conformations, by displaying a number of imino protons that exceeds the number of guanines involved in the structure. Therefore, performing point sequence modifications that favour one conformation over others allows accurate determination of all possible conformations of a single sequence.

Different NMR techniques are also very useful for the determination of G4 stoichiometry (207).

These biophysical techniques (TDS, NMR, CD, UV and fluorescence) are widely used on the characterization of G4 structures in vitro. However, they are expensive and limited to the analysis of short oligonucleotides or isolated molecules and, therefore, do not account for the effect flanking sequences may have on G4 folding (173,211,212).

The use of biochemical methods contributes to suppress these limitations and have been applied to ascertain whether G4 structures assemble in long sequences, mimicking *in vivo* contexts. Precise starting location of G4s, at nucleotide resolution, can be addressed using many different assays.

Formation of G4 structures in both DNA and RNA sequences can act as blocking elements, halting either DNA polymerase or reverse transcriptase polymerization (173). Polymerase stop assay and reverse transcriptase stalling (RTS) are confirmed by the presence of low molecular weight segments observed by agarose or acrylamide electrophoresis (213–216). G4s are protected from cleavage by piperidine, since N7 is protected from methylation caused by dimethyl sulfate (DMS). The result is a pattern of cleavage-protected segments that include the G4 regions and allow determination of guanines involved in G4s (173,213,217).

G4s in mRNAs have been reported in several studies in which the presence of these structures was determined by in-line probing, characterized by the slow structure-dependent spontaneous cleavage of RNA by alkaline hydrolysis or RNase T1 digestion (218,219). Results show

electrophoretic bands corresponding to short lengths, indicative of cleavage in segments that does not contain paired bases (218–220).

Chemical probing of RNAs with DMS and selective 2'hydroxyl acylation analysed by primer extension (SHAPE) reagents are currently used in combination with other techniques like RTS to demonstrate *in vitro* formation of G4s (173,218,221).

Assembly of these structures may be corroborated, independently of the followed methodology, by comparing data obtained from WT sequences and 7-deazaguanine-subsituted RNAs (N7s of guanines are modified, impeding Hoogsteen pairing and prohibiting G4 folding) (222). Based on this principle, the FOLDeR (footprinting of long 7-deazaguanine-subsituted RNAs) method was designed to compare the footprinting of G4-forming RNAs with RNAs that are not able to fold into G4s (165,173,223,224).

Demonstrating formation of G4 structures in cells is of high importance for their structural characterization. Combination of some of the techniques above mentioned with functional assays may elucidate G4 roles *in vivo*.

A range of structure-dependent antibodies have been developed for accurate and specific detection of G4s in eukaryotic cells via immunofluorescence. Although sensitivity has proved quite low for most of them, antibodies BG4, Hf2 and 1H6 have proved as suitable for whole-cell immunofluorescence; however, it is not clear yet whether high density of G4s is required (173).

Finally, G4 detection and localization in genomes can be addressed by antibody-mediated pulldown or polymerase stalling followed by new generation sequencing (NGS) (173). Hf2 and BG4 antibodies are being successfully used in chromatin immunoprecipitation (ChIP) of G4s, showing their presence in noncoding regulatory regions of highly transcribed genes (225,226). 1H6 antibody has been shown good reactivity in ELISA and microscale thermophoresis assays for intermolecular G4 with a (T4G4)2 sequence motif (227). Polymerase stalling followed by NGS provides a detection method for location of G4-forming sequences that impede polymerization reaction and lead to increased mutation rate in sequenced data at the G4 region (173,228–230).

1.2.6 Alternative splicing and human disease

Although tightly regulated, changes in cellular environment or pathological conditions may alter the splicing pattern of a gene. These alterations often lead to the production of aberrant mRNA transcripts, which are directly associated with disease development (24,231,232).

Changes in the AS profile of a gene can dramatically affect its product's phenotypes (233). Nonsense or missense mutations and exonic deletions or insertions alter splicing and/or AS patterns by either creating or disrupting exonic splicing enhancers or silencers, generating or eliminating splice sites, strengthening cryptic splice sites or even promoting changes in RNA Pol II function (231). Mutations that disrupt trans-acting factors may have even stronger effects since they can result in global splicing defects (232).

A large number of mutations that alter splicing have been shown to cause genetic diseases. Several studies (234–236) have been dedicated to understanding the fundamental processes and defects involved in disease, and have uncovered a high number of disease-associated alleles that impaired AS, including cassette exon inclusion or alternative splice site usage (Table 1). A brief description of the genetic mutations and their role in splicing or splicing regulatory factors activity is presented.

Table 1 – Examples of genetic diseases caused by mutations or variants that alter splicing processes (233,237)**.**

Disease	Gene/mechanism	Splicing effect
Spinal muscular atrophy	SMN1	Altered RNP metabolism
Limb girdle muscular dystrophy type 1B	5'ss mutation on LMNA	Intron 9 retention (NMD)
Limb girdle muscular dystrophy type 1G	Mutations in HNRPDL	HNRPDL target mis-splicing
Familial partial lipodystrophy type 2	5'ss mutation on LMNA	Intron 8 retention (NMD)
Hutchinson-Gilford progeria syndrome	Alternative 5'ss activation on LMNA	Deletion of 150 nt in exon 11
Dilated cardiomyopathy	Alternative 3'ss activation on LMNA	9 nt extension of exon 4
	RBM20	TTN mis-splicing
Familial dysautonomia	Decreased U1 recruitment to IKBKAP	Exon 20 skipping
Duchenne muscular dystrophy	Exons 45-55 deletions/skipping on DMD	Frameshift
Becker muscular dystrophy	ESS creation in DMD	Partial exon 31 skipping
Early-onset Parkinson disease	Mutation of U1 binding site on PINK1's 5'ss	Cryptic site site activation and exon 7 skipping

Frontotemporal dementia and parkinsonism linked to chromosome 17 (FTDP-17)	ESS mutation on MAPT	Increased exon 10 inclusion
Retinitis pigmentosa	Missense mutation leads to abnormal PRPF6 localization	Decreased U4/U6 interaction
	Mutation in SNRNP200	Inefficient ss recognition

Disease	**Gene/mechanism**	**Splicing effect**
Myelodysplastic syndromes	Alteration of U2AF1 3'ss preference	Increased alternative 3'ss usage
Microcephalic osteodysplastic primordial dwarfism type 1	5' and 3' mutations in RNU4ATAC	Inefficient minor spliceosome activity
Amyotrophic lateral sclerosis	Mutations in TARDP alter protein-protein interactions	TDP-43 target mis-splicing
	Mutations in FUS decrease interaction with U1 and increase SMN binding	FUS target mis-splicing
Autosomal dominant leukodystrophy	Increased RAVER2 expression due to LMNB1 duplication	PTBP1 target mis-splicing
Different types of cancer	Mutation at a splice site in APC intron 4	Exon 4 skipping
	Mutation at a splice site in APC intron 7	Cryptic ss creation
	Nonsense mutation in BRCA1 exon 18	ASF/SF2 ESE disruption causing exon 18 skipping
	Intronic point mutation in BRCA1	Cryptic 3'ss creation
	Intronic point mutation in intron 5 of oestrogen receptor	Cryptic 5'ss creation in intron 5
	Double point mutation in NF1 exon 7	ASF/SF2 and SC35 ESE binding sites disruption
	Intron mutation in NF2	Consensus branch-site and cryptic splice site creation
	Mutations in codon 659 of MLH1	Exon 17 skipping

Spinal muscular atrophy (SMA) is an example of a disease caused by mutations that alter the splicing profile of a gene. This is a neuromuscular disorder that is developed in individuals possessing a mutation or deletion in the survival motor neuron 1 (SMN1) gene (238). Loss of SMN1 gene is not caused by splicing defects, although it is a splicing event that determines disease severity (238,239). SMN2 possesses a C to T transition in exon 7 that leads to skipping of this exon. Exon 7-lacking transcripts originate truncated, not fully functional and easily degraded proteins. Low levels (5-10%) of the full-length SMN protein are still produced from SMN2 but fail to compensate for the loss of of SMN1 (238–240).

The LMNA gene codifies for a group of slightly different proteins named lamins that are involved in mechanical stability of the inner nuclear membrane and play important roles in several processes, such as nuclear positioning, chromatin structure, DNA replication, DNA damage response, amongst others (241). LMNA gene is very susceptible to mutations or defective post-translational processing, leading to the development of conditions generically termed laminopathies (241), such as Limb girdle muscular dystrophy types 1B and 1G, Hutchinson-Gilford progeria syndrome and Dilated cardiomyopathy.

Limb girdle muscular dystrophy type 1B is a slowly progressive form of a genetic myogenic disorder caused by a transversion (substitution of purine for a pyrimidine or *vice versa*) in the consensus splice donor site of intron 9 of LMNA gene, which leads to abnormal splicing corresponding to retention of intron 9 (242,243). The intron-retained transcript contains a premature stop codon and can be translated into a truncated protein lacking half of its globular tail domain. This domain is responsible for protein interaction with chromatin and proteins of the inner nuclear membrane, therefore, its malfunction and degradation by NMD is associated with disease development (242,243).

Limb girdle muscular dystrophy type 1G is caused by two independent mutation in exon 6 of the HNRPDL gene, which increases nuclear/cytoplasmic localization variability, altering its targets splicing patterns (244).

Hutchinson-Gilford progeria syndrome is a laminopathy caused by a C-to-T substitution in codon 608 of LMNA gene, which activates a cryptic splice site in exon 11 that leads to an in-frame deletion of a 50-amino acid-coding sequence containing a posttranslational cleavage site. The result protein is not posttranslationally cleaved and induces nuclear membrane abnormalities (241).

Dilated cardiomyopathy (DCM) is the most common form of heart muscle disease, corresponding to dilated and poorly functioning left or both ventricles (245). DCM development is associated with genetic defects of structural elements of cardiomyocytes (245). One of the most common genes in

familial DCM is LMNA (246,247). Recently, DCM has been associated with mutations in a ribonucleic acid binding protein. RNA binding motif protein 20 (RBM20) encodes for a protein containing one RRM followed by one RS domain involved in splicing regulation (246,247).

DCM has been associated with a set of heterozygous missense mutations with the RS domain coding region. The mutations lead to a deletion of exons 2-14 of RBM20 and, consequently, to a loss of protein function (248,249)s. As a splicing factor of the sarcomeric protein titin (TTN), disruption of RBM20 function naturally impairs the normal splicing of TTN pre-mRNA. TTN is part of the sarcomere, the contractile unit of muscles (247,250,251). Therefore, an abnormally spliced TTN originates a truncated protein that decreases thick filament length and muscle force, leading to dilated cardiomyopathy phenotypes.

Familial dysautonomia (FD) is a fatal hereditary autosomal recessive disease caused by a homozygous T-to-C point mutation in the 5' splice site region of intron 20 of IKBKAP/ELP1 gene (252,253). The mutation impairs U1 snRNP binding, leading to exon 20 skipping and introducing a frameshift in the final transcript. The exon-skipped transcript is translated into a truncated protein (252,253).

Duchenne (DMD) and Becker (BMD) muscular dystrophy are two related disorders caused by mutations in the dystrophin protein encoding gene (254,255). Dystrophin plays an important role, acting as a structural linker between the cytoskeletal F-actin and β-dystroglycan (255).

DMD is characterised by the complete absence of dystrophin or the presence of non-functional protein. In contrast, BMD individuals are able to produce dystrophin, but the protein is only partially functional (254). Most mutations occur within exons 48-53 and dystrophin presence or absence is dependent on maintenance of the reading frame in the mutated gene (254,255). In-frame mutations are associated with the development of BMD, since translation is not prohibited, while out-of-frame mutations abrogate protein synthesis leading to DMD (254,255). Examples of DMD gene mutations leading to DMD are: exon 51 deletion, exon 50 duplication, nonsense mutation in exon 51, insertion/deletion of one or two nucleotides causing a frameshift, missense mutation in exon 51, and inclusion of a frameshifting pseudo-exon (intronic segment) in the final transcript (254,255). In BMD, mutations are: deletion of exons 50 and 51, exon 49 duplication, nonsense mutation that alters splicing signal, missense mutation in exon 51, and in-frame insertion of a pseudo-exon (254,255).

In the absence of dystrophin, the muscle membrane is damaged, increasing serum levels of creatine kinase and promoting calcium influx to the muscle fiber. Calcium-dependent proteases are activated and the organism enters in a cycle of fiber necrosis, degeneration and regeneration,

leading to fibrosis and fat replacement of muscles, with concomitant loss of muscle contractile function (254).

Parkinson's disease (PD) is a debilitating neurological disorder strongly associated with genetic mutations that lead to alternative splicing of several genes (256). Mutations in PARK2 and PINK1 genes are the two most common causes of autosomal recessive early-onset Parkinson disease. About 50% of the causes for development of this type of parkinsonism is related with variations on differential expression of PARK2 alternative spliced transcripts. Loss-of-function mutations in PINK1 gene, the second most common early-onset parkinsonism cause, involve nonsense and missense mutations, insertions and deletions, and single/multiple exon multiplications (256). PINK1 exon 7 splicing regulation has showed an important role for the development of this form of the disease. Namely, a 23-bp deletion that disrupts its splice acceptor site, whole exon deletion or mutation of a U1-dependent 5'ss, leads to the production of several aberrant transcripts (256). PINK1 proteins are responsible for the recognition of dysfunctional mitochondria, recruiting Parkin (encoded by PARK2 gene) to specifically ubiquitinate and target mitochondria for mitophagy. Therefore, abnormal PINK1 proteins do not respond adequately to damaged mitochondria, which are directly related to PD pathogenesis (256).

Frontotemporal dementia with parkinsonism chromosome 17 (FTDP-17) is an extremely rare syndrome associated with 38 unique mutations (257). The majority of FTDP-17-causing mutations are located within the MAPT gene that encodes for the tau protein (257). The MAPT gene produces six tau isoforms through alternative splicing in the adult brain. All six isoforms are present in the nervous system and are responsible for assembling and stabilization of microtubules and their role in maintaining cell shape and assisting in cell division and molecular transport within cells (258–260). Alterations to tau binding to microtubules are caused by mutations affecting alternative splicing of exon 10. These mutations are either missense, silent or deletions in the coding region or are located within the splice-donor site of the intron downstream to exon 10 (260).

Most of known mutations within or close to exon 10 of MAPT gene increase exon 10 inclusion in mature transcripts, unbalancing the isoforms ratio (260,261). The microtubule-binding region of tau is composed of three or four amino acid repeats, the difference being accounted for exon 10 exclusion or inclusion, respectively, in mature transcripts (260,261). Splicing of exon 10 increases levels of the three or four-repeats isoforms, which have been directly associated with FTDP-17 development (260,261).

Retinitis pigmentosa is a genetic degenerative disease associated with mutations in more than 50 genes (262). Among these, mutations within the PRPF genes are of great importance since these code for proteins composing the spliceosome (263). A missense mutation in codon 729, located in

exon 16 of PRPF6, alters the codified amino acid, which is involved in protein:protein interactions (262). The missense mutation in PRPF6 exon 6 affects PRPF6 protein role in spliceosome assembly, by impairing U4/U6 snRNP interaction and, consequently, decreasing pre-mRNA splicing efficiency (262). A missense mutation in exon 25 of SNRNP200 gene lead to slow ATP-dependent unwinding of U4/U6 snRNP, necessary for the catalytic activation of the spliceosome (264).

Myelodysplastic syndrome is a disorder caused by the expansion of hematopoietic stem cells that have acquired sequential somatic mutations (265). In general, the mutations occurring in these cells are located within 3' ss-binding spliceosome components. In particular, mutations in U2AF1 gene alter 3' ss preference of this splicing factor, increasing alternative 3' ss usage and promoting exon skipping (265).

Splicing of about 800 human introns is catalysed by the minor (U12-dependent) spliceosome, which requires splicing factors distinct from the major (U2-dependent) spliceosome (266). The RNU4ATAC gene encodes one of the splicing factors involved in minor spliceosome catalysis (266–268). Among nine distinct mutations in this gene that are directly related to disease development, 6 are located within the 5' stem-loop domain, which interacts with and recruits other splicing factors. Therefore, when assembly of the minor spliceosome is compromised, splicing efficiency is reduced, leading to the development of microcephalic osteodysplastic primordial dwarfism type 1 (MOPD I) (266).

Individuals that develop amyotrophic lateral sclerosis (ALS) possess a common phenotype, the deposition of the TAR-DNA binding protein (TDP)-43, which is a protein that mediates protein:protein interactions involved in splicing and mRNA stabilization (269,270). TDP-43 is also able to autoregulate its levels via TDP-43 RNA stabilization. TDP-43-linked ALS is related to 38 nonsynonymous mutations in TARDP gene that lead to protein aggregation and cytoplasmic accumulation of insoluble deposits, C-terminal fragmentation and nuclear clearing in a subset of motor neurons (269,270). Other ALS-linked mutations occur in RBP fused in sarcoma (FUS) gene, leading to its mislocalization in the cytoplasm and aggregation (271). Both proteins are involved in splicing and mRNA stabilization, therefore, TDP-43 and FUS targets show abnormally spliced transcripts (269–271).

As a final example of abnormal splicing-related diseases, autosomal dominant leukodystrophy (ADLD) develops from increased expression of lamin B1 (LMB1) mRNA and protein, due to the duplication of LMB1 gene (272). LMB1 overexpression alters the expression of genes involved in the immune system response and of RAVER2 and AFF3 genes, which modulate alternative splicing (272). Specifically, RAVER2 mRNA expression is enhanced by LMB1 overexpression. Raver-2 interacts with PTB, also involved in splicing regulation. Therefore, PTB targets have shown abnormal splicing patterns in ADLD individuals (272).

Altered splicing events are common in several types of cancer. Processes such as apoptosis, angiogenesis and metastasis are associated with a large number of genes affected by splice site mutations leading to abnormal AS (273–276). Table 1 shows some examples of mutations in genes generally related to many types of cancer and their effect on splicing events.

Such high number of gene mutations leading to altered AS events and development of dramatically impairing diseases shows the importance of understanding underlying mechanisms that may allow the development of new diagnostic or treatment approaches.

1.2.6.1 IR in 5'UTRs and human disease

AS events account for genome variability, determining protein sequence and function, intracellular localization of expressed genes and post-translational modifications (56,57,62,277). AS is responsible for the regulation of gene expression, controlling transcript abundance and translation levels through coupling of splicing and NMD (277). Therefore, affecting more than 95% of human multi-exonic genes, AS is one of the processes in the origin of broad cellular modulation and maintenance (11,66–68,277,278).

Of the three main types of AS, IR is the least understood (278). Recent studies (87,90,91) have shown that it is more prevalent than originally thought. IR relevance for cellular processes had been often neglected due to difficulties in obtaining reliable measurements of intron-retained transcripts. These difficulties arise from the fact that retained introns (RIs) tend to introduce fate-determining elements that can either be functional or promote transcript elimination (278). An example of a functional element in retained introns is the constitutive transport element present in the Mason-Pfizer monkey virus and in alternatively spliced intron 10 of the Tap gene. The Tap mRNA is present in polyribosomes and encodes for a small protein involved in nuclear RNA export in both human and monkeys (279).

A characteristic feature of RIs is the presence of premature termination codons (PTCs) (277,278). Computational analysis of the occurrence of PTCs in this type of introns revealed that "on average, 95% of the RIs have a PTC in more than one frame and 90% of the RIs have a PTC in all three frames" (277). PTCs located more than 50 nucleotides upstream of the last exon splice junction are detected by the splicing machinery components, which remain assembled in the transcript during nuclear export and until translation, triggering NMD events (101,277).

NMD eliminates these transcripts preventing the expression of C-terminal truncated proteins that could have nefarious effects to the cell and lead to disease development (101,277,278,280).

Studies focused on determination of IR-NMD coupled events prevalence indicate that IR occurs more often than previously considered (88,91,92,277,278). Although described abundances range from 15-67% (277,278), data point towards an important role for IR in the regulation of alternatively spliced transcripts in mammals (278,280,281).

IR-NMD events, thus, represent a selective regulatory mechanism for gene expression patterns, driving cellular differentiation or homeostasis (101,280,281).

Some studies corroborate IR-NMD role on gene expression. Justin J.L. Wong et al. (95) demonstrated that granulocyte differentiation is regulated via coordination of unique patterns of alternative IR in different stages of cellular development. These IR patterns are associated with both Lmnb1 and Upf1, modulating nuclear shape, granulocyte size and peripheral cellular numbers (95).

Differentiated neurons show low levels of the polypyrimidine tract-binding protein (PTBP1), while it is expressed at high levels in both nonneuronal and neural stem cells (282,283). PTBP1 expression is negatively autoregulated via alternative exon skipping within its own pre-mRNA that leads to the introduction of a PTC, recognized by NMD machinery (282,284). PTBP1 also represses its own expression and of the nervous system-specific gene Gabbr1 and Dig4 (285–289).

IR events are used in mammal cells to finely control the levels and production timings of mature transcripts. An example is the regulation of O-linked b-N-acetylglucosamine (O-GlcNAc) transferase (OGT) expression and O-GlcNAc homeostasis. O-GlcNAc increased levels induces retention of the forth intron, leading to higher levels of intron-retained isoforms (290).

There is an apparent non-random distribution of retained introns within RNA transcripts, with a high frequency in 5’ and 3’ UTRs (87). Retention of introns within 5’ UTRs may lead to the introduction of uORFs (99) which have been shown to highly correlate with decreased translation efficiency and, consequently, with reduced protein expression (102). Gene mutations that disrupt/create uORFs or alter peptides encoded by uORFs have been associated with a growing number of disorders (Table 2) (102).

Table 2 - Examples of genetic diseases resulting from mutations or variants that create or eliminate uORFs.

Gene	Disease	References
uORFs created by polymorphisms/mutations, leading decreased translation efficiency		
FXII	Predisposition for thromboembolism	(291,292)
HBB	β-Thalassemia	
PRKAR1A	Carney complex type 1	
IRF6	Van der Woude syndrome	(293)
SRY	Gonadal dysgenesis	
SPINK1	Hereditary pancreatitis	
CDKN2A	Susceptibility to malignant melanome	(294,295)
LDLR	Familial hypercholesterolemia	(296)
CFTR	Disseminated bronchiectasias	(297)
KCNJ11	Congenital hyperinsulinism	(298)
PEX7	Rhizomelic chondrodysplasia punctata	(299)
POMC	Propiomelanocortin deficiency	(300)
GCH1	Levodopa-responsive dystonia	(301)
HAMP	Juvenile Hemochromatosis	(302)
uORFs disrupted by polymorphisms/mutations, increasing translational efficiency		
HR	Marie Unna hereditary hypotrichosis	(303)
TPO	Thrombocythemia	(304,305)
uORF-encoded peptide modified by polymorphisms/mutations, increasing protein levels		
DRD3	Schizophrenia predisposition	(306)
WDR46	Aspirin-exacerbated respiratory disease	(307)
TGFβ3	Arrhythmogenic right ventricular cardiomyopathy	(308)
HT3A	Bipolar affective disorder and major depression	(102)

Gene	Disease	References
Other alterations, which increases expressed protein levels		
C/EBPα (mice deficient of the C/EBPb uORF initiation codon)	Acute myeloid leukaemia Breast cancer	(309)
MDM2 (switch between promoters P1 and P2)	Cancer susceptibility	(310)
BACE1 (uORFs repress translation)	Alzheimer's disease	(311)

Originally, NMD was considered as just a control mechanism that would be activated for degradation of potentially toxic transcripts containing nonsense codons introduced by errors in replication, transcription or splicing (312). However, NMD has gain relevance as a cellular regulatory pathway by targeting naturally occurring transcripts (312,313). Any transcript containing PTCs less than 50 nucleotides upstream of the last exon-exon junction, or downstream to it, is not targeted to NMD (313). Therefore, naturally occurring transcripts, such as uORF-containing mRNAs, AS products, by-products of gene recombination, and transcripts from transposons and retroviruses, may only be targeted to NMD if a PTC is introduced >50 nucleotides upstream of the exon-exon junction (312–314).

Computational analysis showed that uORFs are generally present in oncogenes and transcripts encoding proteins involved in differentiation, cell cycle and stress response (102).

uORFs may inhibit translation by promoting ribosome pausing and blocking additional ribosomes or impeding translation re-initiation at a downstream start codon, leading to dramatically decreased efficiency of the main ORF (102). PTPRJ, AdoMetDC and the β2-adrenergic receptor are examples of gene transcripts containing uORFs that block translation re-initiation.

uORFs may also trigger NMD events, which occur due to the recognition of the uORF termination codon as a PTC, since this PTC is generally distant from the last exon-exon junction and the 3'UTR signals (102). IFRD1, CFTR and SMG5 are examples of transcripts whose uORFs trigger NMD.

Five hundred and nine genes display uORFs that are either created or deleted by polymorphisms. Among these, 143 have a single uORFs while the rest contain multiple ones. Protein levels were uORF dependent and decreased 30-60% (102).

A SNP located 4 nucleotides upstream of the human clotting factor XII (FXII) main ORF leads to disruption of the Kozak context and introduces a short uORF (2 codons), reducing translation levels and inducing thromboembolic conditions (102).

SNP located 6 nucleotides upstream of the *INS* main ORF induces intron 1 retention, which contains an uORF coding for a 3aa peptide, curtailing protein expression and increasing susceptibility to T1DM (100,315).

In both cases, the uORF does not affect mRNA levels but alter protein levels and can induce disease development (100,102).

Mutations that create uORFs in HBB, PRKAR1A, IRF6, SRY and SPINK1 genes showed to decrease protein levels by 30%, which leads to the development of β-Thalassemia, Carney complex type 1, Van der Woude syndrome, Gonadal dysgenesis and Hereditary pancreatitis, respectively (102,316).

Considering the role of uORFs on translation efficiency, polymorphisms or mutations that create, disrupt or modify uORFs may naturally affect protein expression and significantly impact individuals with respect to disease susceptibility (102).

Translation initiation in mammals occurs by identification of the optimal sequence GCCRCC**AUG**G (Kozak context), where the identity of the underlined nucleotides in the -3 and +4 positions, relative to the "A" of **AUG**, is the most important. However, translation initiation may occur at non-AUG codons, if a good Kozak context and a strong secondary structure ≈15 nt downstream of the initiation site are present (317,318).

Some studies have demonstrated the presence of non-AUG uORFs and their regulatory role under physiological conditions. Expression of ornithine decarboxylase is regulated by these non-canonical start codons in many eukaryotic organisms (317,319). Studying the profile of ribosomal density, Ingolia NT et al. (320) found the presence of translating ribosomes on more than 200 non-AUG uORFS in yeast, which were upregulated under amino acid starvation conditions. Ivanov IP et al. (321) showed that stringency of start codon selection correlates with eIF1 intracellular levels variations (317). Performing a systematic analysis of codon substitution in several 5'UTRs of human mRNAs, Ivaylo P. Ivanov et al. (317), found that translation may be initiated at non-AUG start codons leading to the synthesis of alternative N-terminal extended isoforms.

Joanna D. Stewart et al. (318) analysed translation initiation efficiency in the presence of ATP binding/hydrolysis-impaired ABC50, a protein involved in Met-tRNA$^{Met}_{i}$-eIF2 interaction stabilization. Cells expressing ABC50 mutants show a higher capacity of initiating protein expression from a non-AUG start codon that cells transfected with a vector encoding wild-type ABC50 (318),

displaying a decreased discrimination of the start-site selection, independently of whether the adjacent sequence was a correct Kozak consensus or not. Hence, abnormal ABC50 proteins lead to a relaxation of start-site selection stringency, allowing the use of non-AUG codons.

The high prevalence of mutation-induced defects that alter RNA processing and translation efficiency has led to the development of corrective strategies *in vitro* and *in vivo* (232,322). In the past twenty years, several studies have shown the potential of antisense oligonucleotide (AO)-based therapies for the treatment of genetic diseases, such as human β-thalassemias, cystic fibrosis and Duchenne muscular dystrophy (232,322).

1.3 The potential of antisense oligonucleotide therapies for genetic diseases

These therapies are based on oligonucleotide ability to modulate gene expression via interaction with specific genes or gene transcripts (323).

The first tested oligonucleotides were constituted by simple phosphodiester backbones (324,325). However, these had low permeability and solubility and were very susceptible to intracellular degradation by both endo and exonucleases, which leads to the accumulation of dNMPs that exert cytotoxic and antiproliferative effects (324). Therefore, high doses of phosphodiester oligonucleotides were required to obtain efficient therapeutic results that proved highly costly (325).

Since then, a set of chemical modifications have been developed to overcome phosphodiester AOs limitations, allowing cell growth, and decreasing toxicity, improving stability, potency and bioavailability while maintaining specificity (323,324,326). Hence, chemical modifications generate a range of AO analogues with different pharmacological properties, diversifying the mechanisms of action (323,325,327).

The use of AOs is commonly intended to correct mRNA processing errors caused by mutations in genes leading to complete or partial exon loss or retention of intronic sequences (323). Furthermore, this approach has been improved by using bifunctional oligonucleotides that contain the antisense targeting domain and an effector domain that exerts a silencing or enhancing effect on a targeted exon (232,322).

AOs are short synthetic (13-25 bases) fragments of deoxy- or riboxinucleic acids used as therapeutic agents or tools to study gene expression and function (324). AOs act by selective and specific

hybridization with the mRNA sequence of the target gene, via Watson-Crick interactions (324,326), inducing impairment of mRNA processing or strand cleavage. Consequently, gene expression is blocked by prevention of mRNA translation (324,326). Specificity and selectivity of AOs are based on the presence of unique sequences in the total pool of mRNA targets in cells, since sequences with more than 13 (RNA) and 17 (DNA) nucleotides are expected to occur only once in the human genome (326).

Depending on the oligo backbone, chemical modification nucleotide sequence, one can define the mechanism of action through which the oligo modulates gene expression (323).

Based on the chemical modification, AOs are broadly classified into three generations. First generation AOs are obtained by alteration of the phosphate backbone, while the sugar is modified in second generation AOs, and third generation AOs contain unnatural bases (326).

First generation AOs are obtained by substitution of one of the nonbridging phosphate oxygens with a sulfur group (phosphorothioates), a methyl group (methylphosphonates) or amines (phosphoramidates), which confer stability and resistance to nuclease activity and increase plasma life-times (324,326). First generation AOs are generally negatively charged, increasing cell delivery, compared to phosphodiester backbone AOs, and induce RNase H activity (324,326)).

The most widely studied and used first generation AOs are the phosphorothioates. However, inserted sulfur groups introduce quirality, and only the S enantiomer is resistant to nucleases (324).

First generation AOs are helix destabilizing which decreases the melting temperature of the oligo/RNA hybrid (324) and produce non-specific *in vivo* side-effects. By interacting with proteins, these oligonucleotides activate the complement system and stimulate immune responses (326).

Second generation AOs are produced by introducing alkyl groups at the 2’ position of the ribose, improving binding affinity and hybridization stability, increasing nuclease resistance, tissue uptake and half-lives, and decreasing toxicity (326). These oligonucleotides form high melting heteroduplexes with the target mRNA but their antisense effect is RNase H-independent, whose recruitment is considered as very important for AOs activity (324,326). Combining the properties of both first- and second-generation AO principles led to the development of oligonucleotides containing a phosphorothioate backbone, inducer of RNase H activity, and nuclease resistant arms such as 2’-O-Methyl (2’-OME) and 2’-O-Methoxyethyl (2’-MOE). Resulting oligonucleotides induce RNase H activity to target specific mRNA degradation, while their own degradation by nucleases is prevented (326).

Third generation AOs show further improved nuclease stability and target affinity, accomplished by modifications in the furanose ring, combined with modified riboses or phosphate linkages. The most common are the locked nucleic acid (LNA), the peptide nucleic acid (PNA) and the morpholino phosphoroamidates (MF). Increased nuclease and peptidase resistance confer high stability in biological fluids. PNAs recognize double-stranded DNA, which allow their use as direct gene expression modulators or mutation inducers by strand invasion (324,326). Third generation AOs are uncharged. Therefore, they do not bind to serum proteins, which reduces non-specific interactions but impairs solubility. Cellular uptake and impairment of body clearance also occurs (326).

AOs are used for the modulation of protein expression by interfering with one of the processing steps of the target mRNA or inducing transcripts degradation (326).

Phosphodiester and phosphorothioate oligonucleotides act by inducing mRNA degradation via RNase H activity activation. RNase H is a ubiquitous ribonuclease that specifically hydrolyses phosphodiester bonds of RNA strands in DNA:RNA hybrids (326,328). By targeting RNA transcripts for degradation AOs prevent translation of encoded proteins (323). AOs remain intact and get recycled by binding to other mRNA copies, which increases their effect and allow the use of micro or nano molar amounts (326).

Most of other AOs are not recognized by RNase H and, therefore, act by targeting different mRNA synthesis or processing steps, through mechanisms denominated “occupancy-only mediated mechanisms” or “occupancy activated destabilization” (326,329).

Occupancy-only mediated mechanisms are based on the hybridization of AOs with specific sequences responsible for the interaction of the target RNA with proteins, other nucleic acids or regulatory factors. These AOs can, thus, be used for inhibiting steps involved in translation or splicing processes or altering RNA metabolism (329). Among these, splice-switching AOs bind to splicing-intervening sequences redirecting pre-mRNA processing (323). Correction of aberrant splicing events or prevention of splicing reactions, by direct hybridization to splicing cis-acting elements or steric block of splicing trans-acting factors binding, lead to restoration of normal protein synthesis and function or protein synthesis inhibition (326). AOs may also recognize and bind to translation initiation codons, blocking protein translation (326).

Occupancy activated destabilization mechanisms are based on the effects that binding of AOs to RNA have in 5’ capping or 3’ polyadenylation steps of RNA processing (326). Impeding any of these steps results in mRNA destabilization and degradation (326).

Several studies describe antisense therapies as promising approaches for the treatment of many genetic diseases (330–333). There are ongoing studies using antisense oligonucleotides that act via one out of the above mentioned mechanisms (330,333–335).

Two LNA oligonucleotides were designed to target a cryptic splice site in GALT mRNA that induces a frameshift in the canonical open reading frame (ORF) and introduces a premature start codon (PTC), altering the length of two alternatively spliced transcripts. The LNA oligonucleotides block the access of the spliceosome machinery to the cryptic splice site, promoting the usage of the canonical splice site, and restoring the correct splicing, and synthesis and function of the wild-type GALT protein by antisense therapy (336).
For both DMD and SMA, the mutations in DMD and SMN genes, respectively, lead to decreased expression levels of the encoded proteins (237).

Two AOs, a 2'O-methylphosphorothioate (2'OMePS) and a phosphorodiamidate morpholino oligomer (PMO), have progressed to clinical trials for the treatment of Duchenne muscular dystrophy (DMD). The AOs target an ESE in exon 51 of DMD mRNA leading to exon 51 skipping and restoring use of the canonical ORF. The result is the synthesis of partially functional DMD proteins (237).

For the treatment of Spinal muscular atrophy (SMA), the 2'-O-methoxyethyl (MOE) AO acts by blocking an ISS in intron 7 of the survival motor neuron 1 (SMN1) gene, promoting splicing of exon 7 and increasing SMN levels in patients with severe SMA (237).

The above-mentioned AOs have proved as efficient inducers of the correct splicing, inhibiting mRNA degradation and promoting their translation into functional proteins (237).

Myotubular myopathy is a muscular disease that results from overexpression of dynamin 2 (DNM2) as a consequence of mutations in the phosphoinositides phosphatase myotubularin (MTM1) gene. AOs targeting DNM2 transcripts promote RNase H-dependent RNA degradation, efficiently reducing DNM2 protein levels and preventing the development of myotubular myopathy in MTM1 knockout mice (337).

Three 2'-O-methyl phosphodiester (PO-Me) oligonucleotides were designed with the purpose of directly increasing synthesis of therapeutic proteins *in vivo*. These oligonucleotides are complementary to the uAUG start codon of the human RNASEH1 mRNA, which is located within a functional reading frame upstream of the canonical one. Hybridization of PO-Me oligonucleotides to RNASEH1 mRNA efficiently and specifically increase protein translation (338).

Although many studies on the potential use of AOs for the treatment of genetic diseases are being conducted, only four AOs have provided clear clinical benefits and were approved by the Food and

Drug Administration (FDA) (327). The first approved AO is a phosphorothioate oligodeoxynucleotide, designed for the treatment of cytomegalovirus (CMV) retinitis (327,339).

Patients with homozygous familial hypercholesterolemia (HoFH) can now control their circulating levels of low-density lipoprotein cholesterol (LDL-C) with a phosphorothioate 2'-methoxyethoxy (MOE) gapmer. This AO targets the coding region of apoB-100 mRNA, inducing RNase H1-dependent mRNA clevage (327). apoB-100 is responsible for lipid transport, including cholesterol, to cells. Therefore, by reducing apoB-100 levels via antisense therapy, circulating LDL levels are reduced and hypercholesterolemia is prevented (340,341).

Another FDA-approved AO is a phosphomorpholidate oligonucleotide, designed to target the exon 51 splice-donor region of the dystrophin protein, leading to skipping of this exon and allowing the production of a truncated but partially functional dystrophin protein (327).

The most promising FDA-approved AO is a phosphorothioate 2'-O-methoxyethoxy oligonucleotide, which targets and sterically blocks an internal splice site in intron 7 of SMN1 and SMN2 transcripts, inducing intron inclusion on the final transcript and protein translation (237,327).

1.4 Diabetes: classification, pathophysiology and mechanism

Diabetes mellitus is a multifactorial and genetically heterogeneous disease associated with a number of hereditary and environmental factors (342). Diabetes pathogenesis is characterized by defects in insulin secretion and/or action on target issues, associated with abnormalities in carbohydrate, fat and protein metabolisms (343).

Diabetes is etiologically categorized into four classes: I- Type 1 diabetes, II- Type 2 diabetes, III- Other specific types and IV- Gestational diabetes mellitus.

The vast majority of diabetes-diagnosed individuals are within either type 1 or type 2 categories (343,344). However, the diagnosis and assignment to a diabetes category is difficult since many individuals presenting characteristics of a certain type may evolve into fitting to a different category, depending on the circumstances at the time of diagnosis and progression of the condition (343). Therefore, understanding hyperglycaemia pathogenesis is more important for an effective treatment than type classification (343).

After diagnosis, some individuals do not require insulin; a combination of weight reduction, exercise and/or oral glucose-lowering agents is enough for an adequate glycaemic control. Individuals with some residual insulin secretion may require exogenous insulin to control glycaemic levels but can survive without it. The most severe stage/condition involves the autoimmune destruction of the pancreatic β-cells followed by no residual insulin secretion; these individuals require exogenous insulin for survival (343,345,346).

Impaired insulin secretion and defects in its action are often concomitant in the same patient, leading to chronic hyperglycaemia, which is associated with long-term damage, dysfunction and failure of several organs, mainly eyes, kidneys, nerves, heart and blood vessels (344,346).

1.4.1 Type 1 Diabetes

Five to ten percent of diabetic patients have T1DM, which is characterized by an autoimmune destruction of pancreatic β-cells, the presence of autoantibodies and diminished insulin production. The heterogeneous inflammatory reaction against pancreatic islets leading to T1DM requires three conditions: initiation of the immune response against β-cell antigens, strong development of inflammatory mechanisms, and ineffective regulatory control of the autoimmune reaction which becomes chronic and destroys preproinsulin-producing cells (347). Thus, T1DM is clinically characterized by high levels of blood glucose (hyperglycaemia), a high dependency on exogenous

insulin, susceptibility to ketosis (346,348), and is usually manifested by an abrupt onset of symptoms such as polyuria (excessive production of urine), polydipsia (excessive thirst), polyphagia (excessive hunger), severe weight loss, fatigue, restlessness and body pain (347,349).

β-cell destruction leads to release of one or more biomarkers to bloodstream. The classic biomarkers are autoantibodies against islet cells (ICA), insulin (IAA), glutamic acid decarboxylase (GAD/GAD65) and tyrosine phosphatases IA-2 and IA-2, enzyme carboxypeptidase-H, GM-gangliosides, sex determining region-Y b-ox protein (SOX13) and zinc transporter 8 protein (ZnT8A) (350,351); these biomarkers are present in 85-90% of individuals with fasting hyperglycaemia (343,350) and the combination of both genetic and environmental factors determines whether IAA, GAD or both is the first biomarker to appear. Appearance of more biomarkers, their identity and occurrence timeline influence disease progression (352).

The aetiology of diabetes is still unclear. T1DM susceptibility is conferred by a combination of environmental and genetic factors. The environmental factors that may trigger/prevent the disease in genetically predisposed individuals include: the development of infections that lead to β-cell destruction or upregulate MHC class I system and proinflammatory cytokines such as IFN-α; no contact with parasites as a result of more sanitized environments leading to a more reactive immune system; changes in the gut flora or the exposure to certain bacteria conferring a protective environment (347).

Albeit being a disease influenced by environmental factors (353), T1DM individuals show strong genetic predisposition, and many specific susceptibility genes have been identified (348), such as the HNF (hepatocyte nuclear factors) family gene, GCK (glucokinase), LARS (Leucyl-tRNA synthetase), point mutations in mitochondrial DNA and in genes coding for proteases responsible for insulin maturation (346). The strongest evidence for genetic predisposition in T1DM is its association with the Human Leukocyte Antigen (HLA) system of the Major Histocompatibility Complex (MHC) class II, which can be either predisposing or protective for the development of the disease, followed by susceptibility caused by a polymorphism in the promoter region of the preproInsulin gene (104,107). Polymorphisms in PTPN22 and IL2RA loci have also been associated with T1DM (354,355).

HLA association with T1DM is determined by the balance between alleles conferring susceptibility or protection/resistance (350). In addition, more than 50% of the 41 genes known to be associated with T1DM, in 2013, are expressed in human islets and upregulated by proinflammatory stimuli, which stablishes a link to HLA allelic predisposition (347).

Genome-wide association studies (GWAS) revealed several HLA loci linked to T1DM susceptibility: HLA-A, HLA-B, HLA-DPβ1, HLA-DRβ1, HLA-DQα1 and HLA-DQβ1. Diabetogenic and protective molecules encoded in these loci differ in structure, determining antigen peptide selectivity, binding affinity and stability of presented HLA molecule. A complex pattern of DR-DQ combinations is what determines HLA allelic association with T1DM (347).

It has been suggested that HLA-DQ and HLA-DR polymorphisms affect T1DM susceptibility through alterations in the nature of the peptides presented to T-cells. DR3 or DR4 alleles are commonly found in the general population, as a single copy. T1DM-susceptible individuals have two allelic combinations such as DR3/DR3, DR4/DR4 or the high risk DR3/DR4 (350).

Increased risk for T1DM is conferred by HLA alleles, namely, class I molecules (encoded by A*02:01, A*24 and B39) and class II molecules (encoded by DRB1*04 (DR4)-DQA1*03:01-DQB1*03:02 and DRB1*03:01 (DR3)-DQA1*05:01-DQB102:01 haplotypes) (356). The DRB1*15:01-DQA1*01:02-DQB1*06:02 haplotype, encoding the HLA-DQ6 heterodimer confers protection for T1DM development due to suppression of multiple autoantibodies expression in such a way that individuals carrying HLA-DR3 or -DR4 risk alleles on the other chromosome are less likely to develop the disease. Even in the presence of autoantibodies, individuals carrying the protective DRB1*15:01-DQA1*01:02-DQB1*06:02 haplotype are less susceptible than individuals that do not have this variant; expression of IA-2A, ZnT8A, or multiple autoantibodies, indicating advanced islet autoimmunity and more rapid disease progression, is rare. Positivity for IAA autoantibody is not frequent either (356).

The highest T1DM risk genotype is HLA-DR3-DQ2, HLA-DR4-DQ8 combined with homozygosity for the type 1 insulin variable number tandem repeat (VNTR) (357). CD4+ cells, responsible for the recognition of MHC class II, (358), recognize epitopes from the proinsulin C-peptide, supporting the role of CD4+ proinsulin-specific T cells in the pathogenesis of human T1DM (359); CD8+ T cells, that recognize MHC class I molecules (358), can infiltrate islets and recognize epitopes from insulin, islet-glucose-6-phosphatase catalytic subunit-related protein (IGRP), insulinoma antigen 2 (IA-2), glutamic acid decarboxylase-65 (GAD-65) and pre-pro islet amyloid protein (ppIAP) (357).

Despite the scientific progress in the association of several genes with the development of diabetes, there is much remaining unclear regarding the mechanisms involving disease onset, such as the nature of the initial event that triggers the autoimmune response leading to T1DM.

Many people carrying susceptible allelic variants in the HLA locus and presenting islet-specific T cells in the blood do not develop T1DM. These islet-specific T-cells, probably escaping thymic selection, produce anti-inflammatory rather than proinflammatory cytokines. Therefore, in order

to develop the disease, regulation of inflammatory responses must be compromised (347). T1DM individuals have fewer and/or less effective Treg cells, which are responsible for the control of immune response and peripheral immunological tolerance (347).

1.4.2 Preproinsulin gene (*INS*)

Human insulin is encoded by a single gene. In some species, such as rodents, insulin is encoded by two functional copies (360,361). In humans, insulin gene (*INS*) is located on the short arm of chromosome 11 (362,363) and is flanked by an Alu element downstream the 3' end and a polymorphic region upstream the 5' end (364).

The preproinsulin gene is composed of three exons and two non-coding intervening sequences (IVS) or introns (360,361). The canonical translation start is located in exon 2, with intron 1 sited within the 5' UTR and with intron 2 interrupting the C-peptide coding sequence (360). *INS* exon-intron structure is highly conserved in evolution, including the promoter region (TATAAAG), the 5'UTR and the polyadenylation signal sequence (AATAAA) (360,361).

Introns are, generally, much less conserved than exons; for example, the length of *INS* intron 1 varies among species, ranging from 119 base-pair (bp), in rat and guinea pig, to 3500 bp, in chicken (12). Intron 1 is weakly recognized by the splicing machinery in multiple species, leading to IR in a significant fraction of polyadenylated transcripts (365–367). The GC content of the human insulin gene is 64.8%, which is much higher than the average GC content of human DNA, 38% (364,368).

It has been suggested that *INS* intron 2 may be spliced either co-transcriptionally or in a stepwise manner, with the 5' region cleavage occurring in the first step in the nucleus, forming a partially spliced mRNA that is exported to the cytoplasm (369). *INS* intron 1 contains a highly conserved cryptic 5'ss leading to the retention of the first 26 bp of intron 1 in human and primates such as monkeys (370), indicative of alternative processing for *INS* intron 1. It is not known, however, whether *INS* splicing is mainly co- or post-transcriptional, or both. It also remains elusive how these mechanisms are defined, which process is selected, and what roles RNA-protein interactions and RNA structure play.

1.4.2.1 INS intron 1 in T1DM

Insulin-Dependent Diabetes Mellitus locus 2 (IDDM2), the second strongest genetic susceptibility locus associated with T1DM predisposition, is characterized by a set of variants inherited from

mother and father in tight linkage disequilibrium with each other (371). These variants include a repeat polymorphism upstream of *INS* (372) and a single nucleotide polymorphism (SNP) (373) located at position -6 relative to the 3'ss of intron 1 (IVS1-6A/T) (374). The adenine (A) allele at IVS1-6 (rs689) disrupts the Py-tract and impairs recognition of the 3'ss of intron 1, leading to higher retention levels as compared to the thymine allele (100).

Transcripts containing intron 1 have their 5' UTRs extended by 179 nt (372,373), introducing an 3-aa peptide uORF (Figure 7), which decreases preproinsulin translation (100). Figure 37 in appendix B shows a list of potential noncanonical uORFs in the 5'UTR of *INS*.

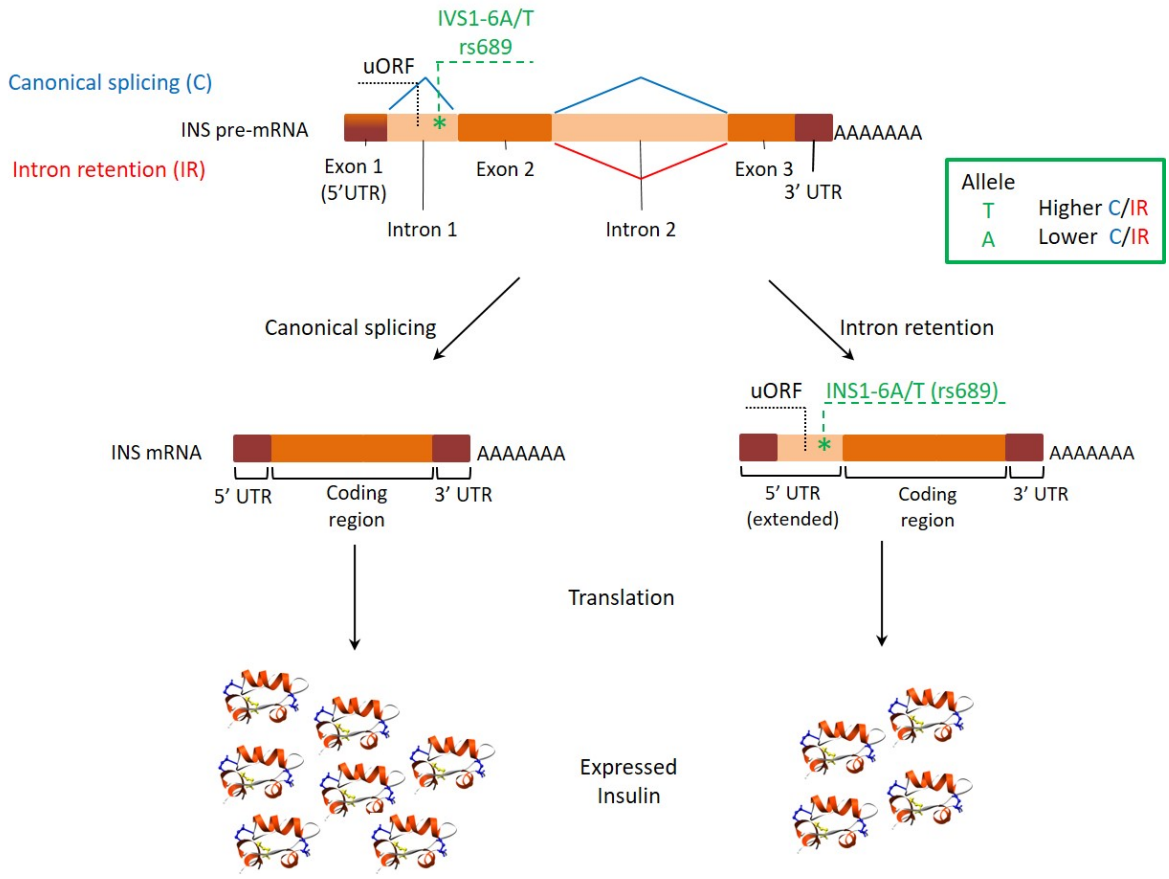

Figure 7 - Allele-dependent INS expression.
Individuals predisposed to T1DM possess an A allele at rs689, a SNP located six nucleotides upstream of the 3'ss of intron 1 (IVS1-6A/T) (green star). The A allele reduces the strength of the Py-tract and impairs canonical splicing (blue lines), by introducing intron 1 in the mRNA (red line), leading to transcripts with a longer 5'UTR and extra uORF (black botted line), curtailing preproinsulin expression (shown by the number of insulin molecules). Tertiary structure of human insulin was visualized in UCSF Chimera (PBD ID: 2HIU); disulphide bonds between A and B chains are in blue; intra-A chain disulphide bond in yellow.

The rs689 SNP link to T1DM pre-disposition was shown by transient transfection of a set minigenes comprising all three exons and two introns of INS gene and containing 6 common INS SNPs showed that INS pre-mRNA processing may potentially originate 6 alternatively spliced isoforms. Minigenes with the IVS1-6A→T mutation produced a significantly lower proportion of isoforms lacking exon 2 and isoforms retaining intron 1. Except for the 4-nt insertion IVS-69+ SNP, which activates a cryptic 5'ss and extends the 3' end of the noncoding exon 1, the remaining SNPs had minor effects on reporter pre-mRNAs splicing (100). Determination of relative amounts of isoforms 2, 4, and 6, resulting from the correct splicing of the 3'ss of intron 2 revealed that the A allele of the rs689 variant leads to intron retention in 12% ± 3 of INS minigene transcripts, 12x higher than IR observed for the T allele (100). Additionally, T->A mutations 6 nt upstream of the 3'ss in INS minigene reporters consistently lead to higher retention levels and reduced proinsulin expression, as compared to levels from the thymine (T) allele. Splicing efficiency is restored upon A->T mutation (100).

These findings led to the hypothesis that IDDM2-dependent T1DM predisposition is related to inadequate presentation of proinsulin peptides, leading to survival of proinsulin-responsive T cells in A allele carriers, as compared to T allele carriers that would have induced T cell apoptosis in the thymus (100,375).

Several intronic properties may contribute to IR in *INS*: high G/C content (66 guanines and 57 cytidines of 179 nt, 68.72%), short length (179 nt) (364), and an evolutionary deletion of a G-run containing a splicing enhancer and a G>A substitution at first position of exon 2 (E2+1 G>A), which weakens the 3'ss of intron 1 (100). Altogether, these features may account for inefficient removal of intron 1 from the *INS* pre-mRNA, particularly in carriers of the adenine allele at rs689 (100).

It has been shown recently that it is possible to modulate intron 1 splicing of the A allele transcripts via antisense oligonucleotide targeting. A RNA 16-mer oligonucleotide complementary to *INS* intron 1 positions 59-74, which are flanked by G-rich regions reduces IR (Figure 8), potentially increasing preproinsulin levels (315). IR was also shown to be influenced by deletion of some intronic segments. A series of 14 overlapping deletions, where 1-4 and 7-14 included at least one guanine of the seven G-runs in *INS* intron 1 and 5/6 comprise the antisense target, revealed that removal of any of the G-runs either led to a significant increase in IR, or did not change it. In accordance with the antisense targeting, deletions 5 and 6, that encompass the target region, improved splicing efficiency (Figure 8) (100).

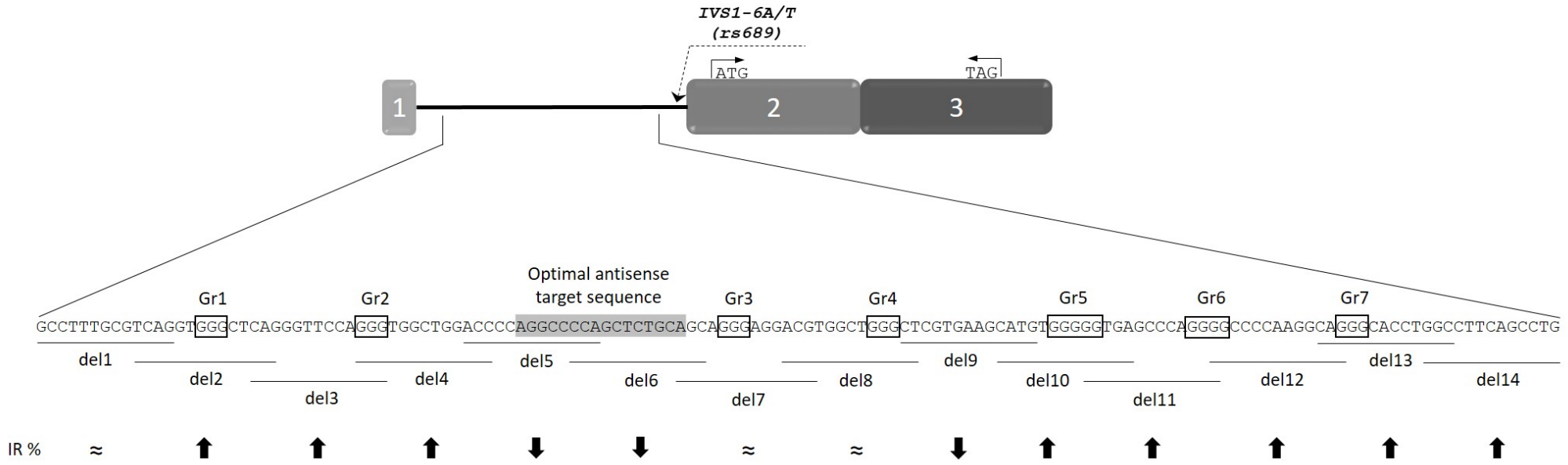

Figure 8 - Haplotype-dependent intron retention is modulated by G-rich motifs.
Schematics of G-rich elements surrounding the antisense target sequence (highlighted in gray) that showed to modulate *INS* intron 1 splicing (100). Gr2, Gr3 and Gr4 were shown to be involved in G4 formation and CD and NMR studies indicated that Gr3/4 form a parallel G4 in vitro (315). Exons are shown as boxes (numbered), intron as line. Start and stop codons are denoted by arrowheads. The location of rs689 is denoted by a dashed arrowhead. G-runs (boxed) and intron 1 deletions 1-14 (horizontal lines) that were previously tested for their importance in intron 1 splicing are indicated. Mutations in any G-runs decreased splicing efficiency (100). *INS* intron retention levels for each deletion construct, in comparison to WT, are at the bottom.

Although the association between the A allele at rs689 and T1DM has been established (374), the underlying pathogenic mechanisms linking the presence of this genotype to disease development are yet to be discovered. Particularly, the role of G-runs, and their potential folding into G4 structures in *INS* pre-mRNA processing remains unclear and further studies to uncover the importance of G4s in T1DM development and their role in IDDM2-mediated susceptibility are essential.

1.5 Hypothesis

INS pre-mRNA efficient splicing is mediated by the folding of highly conserved G-rich sequences into G4 structures, leading to increased protein translation. Intron 1 retention may also be modulated through the binding of hnRNP F and H1 to the G4-forming segments.

1.6 Aims and Objectives

1) To evaluate ThT as an adequate fluorescence light-up probe for G4 detection
    a. To determine ThT capacity to probe G4 formation in sequences known as such
    b. To establish an adequate time-window for the analysis of G4-ThT complexes
    c. To characterize the discriminatory capacity of ThT in the presence of a series of oligos known to fold into G4
    d. To address ThT fluorescence dependence on oligo concentration, molecular saturation and appropriate oligo:ratio

2) To evaluate G4 formation propensity of *INS* intron 1-derived oligos to form G4.
    a. To screen a set of overlapping DNA oligonucleotides derived from INS intron 1 antisense target region
    b. To evaluate the influence of the antisense target sequence on G4 formation by extending intron 1 derived oligos Int1 and Int7
    c. To evaluate the probing capacity of ThT for the analysis of RNA G4 in comparison to their DNA counterparts.
    d. To determine the influence of mono and divalent cations on DNA and RNA G4 propensity

e. To evaluate the influence of pH in G4 formation.
f. To monitor G4 formation during transcription in real-time.
g. To analyse the presence of different secondary structures in RNA oligos and *in vitro* transcripts on a native acrylamide gel

3) To identify proteins that specifically bind to the *INS* intron 1 segment comprising the antisense target region.

4) To evaluate and compare translation efficiencies in human and primate INS 5'UTRs
   a. To clone Human and other 5 primates' *INS* 5' UTRs into a mammalian-expressing bicistronic vector
   b. To transiently transfect HeLa cells with 5' UTR constructs
   c. To use dual-luciferase reporter system for the analysis of translation efficiency of the different *INS* 5' UTR constructs
   d. To analyse the splicing pattern of the different *INS* 5' UTR constructs

Chapter 2: General Material and Methods

2.1 Materials and reagents

Table 3 – General Reagent

Reagent	Supplier, Cat no:
0.1M DTT	Life Technologies, Y00147
1kb DNA Ladder	Promega, G5711
1M HEPES solution	Sigma, H3537
1M $MgCl_2$	Sigma, M1028
1M $MgSO_4$	Sigma, M3409
2-β-Mercaptoethanol	Fisher, BPE176100
7-deaza-GTP	TriLink Biotechnologies, N-1044
40% Acrylamide: Bis-Acrylamide 37.5:1	Fisher Scientific, BP14101
50 bp DNA Ladder	Peqlab, 25-2000
100bp DNA ladder	Promega, G2101
Acetic Acid, Glacial	Fisher Scientific, 64-19-7
Agar, granulated	Fisher Scientific, BP1423500
Agarose	Sigma, A9539
Ammonium Persulphate	Sigma, A-3678
Boric Acid	Fisher Scientific, BP1681
Brilliant Blue G	Sigma, B-0770
Bromophenol blue	BDH, 44305
Cacodylic acid	Sigma, C0125
Carbenicillin	Gibco, 10177-012
Chloroform	Ambion, AM9722 Fisher Scientific, BP1145
DMSO	Thermo Scientific, F-515
DTT	Invitrogen, D1532
EDTA	Fisher Scientific, BP118500

Reagent	Supplier, Cat no:
GelRed™	Biotium, 41003
Glycerol	Fisher Scientific, BP229-1
Glycine	Fisher Scientific, BP3811
HeLa nuclear extract	Santa Cruz Biotechnology, sc-2120
Nitrocellulose membrane	GE Healthcare Life Sciences, RPN203D
IPTG	Thermo Scientific, R0392
Isopropanol	Fisher Scientific, 67-63-0
Kanamycin	Affymetrix, 17924
LB Broth	Fisher Scientific, BP1426500
Lithium Chloride	Sigma, L9650
Lithium Hydroxide	Sigma, 402974
Lysozyme	Sigma, 62971
Methanol	Fisher Scientific, 67-56-1
PBS	Sigma, P4417-100TAB
Phenol:Chloroform	Ambion, AM9722
Ponceau S	Sigma, P3504
Protein-Marker V	Peqlab, 27-2210
Potassium chloride	Fisher, BPE366
Sodium chloride	Fisher Scientific, BP3581
Sodium dodecyl sulphate	Sigma, L3771
Sodium phosphate dibasic	Calbiochem, 567547
TEMED	Sigma, T-8133
Thioflavin T	Sigma, T3516
Tri Reagent	Ambion, AM9738

Reagent	Supplier, Cat no:
Tris Base	Fisher Scientific, BP1521
Tween 20	Bio-rad, 161-0781
Tween 20	H5152
Urea	Fisher Scientific, U16-50
Western Blotting Filter Paper	Thermo, 84784

Table 4 – Reagents for RNA

Reagent	Supplier	Cat no:
0.5M EDTA	Promega	V4231
1M Tris pH 8.0	Ambion	AM9856
3M KCl	Fluka	60135
3M Sodium Acetate	Ambion	AM9740
5M NaCl	Ambion	AM9759
5M NH4OAc	Ambion	AM9070G
10x TBE	Ambion	AM9863
30% Acrylamide: Bis-Acrylamide 37.5:1	Severn Biotech Ltd.	20-2300-10
50 $MgCl_2$	Thermo	F5410Mg
Adipic acid dihydrazide–Agarose	Sigma	A0802
Chloroform	Sigma	C2432
DNae&RNase free-Water	Life Technologies - Gibco	10977-035
Glycreol	Sigma	49767
GlycoBlue™	Ambion	AM9515
Heparin	Sigma	H3393
Isopropanol	Fisher	10588630
Ni-NTA agarose	Qiagen	30210
RNase A	Thermo Scientific	EN0531
RNasin® Ribonuclease Inhibitors	Promega	N2515
Sodium (meta) periodate	Sigma	S1878
UltraPure™ DNase/RNase-Free Distilled Water	Thermo Scientific	10977035
UltraPure™ TBE Buffer, 10X	Invitrogen	15581-044

Table 5 – Primers for cloning

Probe	Forward 5’ -> 3’ Sequence	Reverse5’ -> 3’ Sequence	Supplier
hnRNP F	attggatccGAAattTTGtatTTCcaaGGAgagctcATGATGCTGGGCCCTGAGG	attaagcttCTAGTCATAGCCACCCATG	Eurofins Scientific
F RRM 1	atagagctcagtGTGGTCAAGCTCCGTG	attaagcttTCAGAACACCTCAATGTACCGG	
F RRM 2	atagagctcagtAACAGTGCCGACAGCG	attaagcttTCAGTATGACCTAACTTCCTCC	
F RRM 3	atagagctcAGTGAGTTCACAGTGCAGA	attaagcttTCACACCTGGCTGCTATACGCC	
hnRNP H1	atagagctcATGATGTTGGGCACGGAAG	atactcgagtcaTGCAATGTTTGATTGAA	
H RRM 1	atagagctcagtTTCGTGGTGAAGGTCC	atactcgagtcaGTTGTTTGACTTGAATACT	
H RRM 2	atagagctcagtGGCTTTGTACGGCTTA	atactcgagtcaTCTACTGCTCTTAAAGATT	
H RRM 3	atagagctcCAGAGCACAACAGGACACT	atactcgagtcaCATTTGGCTACCATAAGCA	
***Homo sapiens* 5’UTR**	GGGAGACCCAAGCTGGCT	AGTCGAGGCTGATCAGCGG	
***Pongo pygmeus* 5’UTR** ***Macaca Fuscata* 5’UTR**	agtaagcttCAGCCCTCCGGGACAGGCT	actcCATGGCAGAAGGACAGTGATccgggagacaggc	
***Colobus angolensis* 5’UTR** ***Semnopithecus entellus* 5’UTR**	agtaagcttCAACCCTCCGGGACAGGC	actcCATGGCGGAAGGACAGTGACccgggagacaggc	

Table 6 – Primers for PCR amplification of DNA templates for *in vitro* transcription

Primers	5' -> 3' Sequence	Supplier
T7-sc35	attaatacgactcactataGGATTCCAGGGTGGCT	Eurofins Scientific
R-sc35	TGCAGCAGGGAGGACG	
R2SC	AGGGAGGACGTGGCTGGGC	

Table 7 – Plasmid systems

Vectors	Source
pGEM®-T easy vector system	Promega, A1360
pET28a	Novagen | Millipore, 69864
pGLpest.SEQ	Kindly given by Mark Coldwell
pICtest2	

Table 8 – Enzymes and Buffers

Enzyme	Supplier	Cat no:
GoTaq® G2 Flexi DNA Polymerase	Promega	M7805
Pfu DNA Polymerase	Promega	M7741
HindIII	Promega	R6045
BamHI	Promega	R6025
XhoI	Promega	R6165
NcoI-HF	New England Biolabs	R3193S
SacI	New England Biolabs	R0156S
KpnI	New England Biolabs	R0142S
Shrimp Alkaline Phosphatase (rSAP)	New England Biolabs	M0371S
T4 DNA Ligase	Promega	M1801
RQ1 RNase-free DNase	Promega	M6101
M-MLV Reverse transcriptase	Promega	M1701

Table 9 – Competent cells

Cells	Supplier	Cat no:
JM109 Competent Cells	Promega	L2001
BL21(DE3) Competent *E. coli*	New England Biolabs	C2527I
Rosetta™ 2 (DE3)	Millipore	71397-3

Table 10 – Primers for sequencing

Primers	5' -> 3' Sequence	Supplier
PICf	GCCTCGGCCTCTGAGCTATTCCAG	Eurofins Scientific
Lucr	GTATCTCTTCATAGCCTTATGCAG	
T7	TAATACGACTCACTATAGGG	GATC Biotech AG

Table 11 - Antibodies

Antigen	Source	Cat no:	Secondary antibody
His-tag with HRP	Abcam	Ab1187	Rabbit polyclonal
hnRNP F	Kindly given by Professor Douglas Black		Rabbit polyclonal
hnRNP H1	Kindly given by Professor Douglas Black		Rabbit polyclonal
Rb pAb to 6x His-tag	Abcam	Ab1187-100	N/A
Anti-tb IgG (H+L)	Thermo	31458	N/A

Table 12 – Commercial Laboratory Kits

Kit name	Supplier	Cat no:
BSA standard set	Bio-Rad	500-0207
GeneJET Gel Extraction Kit	Thermo scientific	K0503
GeneJET Plasmid Miniprep Kit	Thermo scientific	K0503
Wizard® *Plus* SV Minipreps DNA Purification Systems	Promega	A1460
Pierce™ BCA Protein Assay Kit	Thermo Scientific	23225
Pierce™ ECL Western Blotting Substrate	Thermo scientific	32209
ProteoSilver™ Silver Stain Kit	Sigma	PROTSIL1-1KT
MEGAshortscript™ T7 Transcription Kit	Life Technologies	AM1354
RT-Ampliscribe™ T7-Flash	Epicentre	ASF3257

Table 13 – DNA oligonucleotides tested for G4 detection with ThT

Oligo	5’ -> 3’ Sequence	Supplier
WT	TGGGCTCAGGGTTCCAGGGTGGCTGGACCCCAGGCCCCAGCTCTGCAGCAGGGAGGACGTGGCTGGGC	Eurofins Scientific
Int1	TGGGCTCAGGGTTCCAGGGTGGCTGG	
Int2	AGGGTTCCAGGGTGGCTGGACCCCA	
Int3	AGGGTGGCTGGACCCCAGGCCCCAGC	
Int4	TGGACCCCAGGCCCCAGCTCTGCA	
Int5	AGGCCCCAGCTCTGCAGCAGGGAGGA	
Int6	AGCTCTGCAGCAGGGAGGACGTGGC	
Int7	AGGGAGGACGTGGCTGGGC	
CD3	CCAGGGTGGCTGGACCCCAGGC	
CD4	CCAGGGTGGCTGGACTTCAGGC	
c-myc	TGAGGGTGGGTAGGGTGGGTAA	
Plas24	GGGTTCAGGGTTCAGGGTTCAGGG	
21DNA	CTAGGGCTAGGGCTAGGGCTAGGG	
DCAF6	GCAAACTTAAAACTGGTTCA	
CLASP1	TACATCCCATACGGCTCATA	
GA8	AAGGAAAGGAAAAGGAAAAGGAAA	
GT8	TTGGTTTGGTTTTGGTTTTGGTTT	
GA12	GAGAGAGAGAGAGAGAGAGAGAGA	
GT12	GTGTGTGTGTGTGTGTGTGTGTGT	
G-tr1	ATCGGGTCGTACGTCATGGGTAC	
G-tr2	ACTGATCGTACGTGGGGTACGTAC	
G-tr3	GGGTACTGACATTAACCGGGAAC	
Int1+2	TGGGCTCAGGGTTCCAGGGTGGCTGGAC	
Int1+4	TGGGCTCAGGGTTCCAGGGTGGCTGGACCC	
Int1+6	TGGGCTCAGGGTTCCAGGGTGGCTGGACCCCA	
Int1+8	TGGGCTCAGGGTTCCAGGGTGGCTGGACCCCAGG	
Int1+10	TGGGCTCAGGGTTCCAGGGTGGCTGGACCCCAGGCC	
In1+12	TGGGCTCAGGGTTCCAGGGTGGCTGGACCCCAGGCCCC	
Int1+14	TGGGCTCAGGGTTCCAGGGTGGCTGGACCCCAGGCCCCAG	
Int1+16	TGGGCTCAGGGTTCCAGGGTGGCTGGACCCCAGGCCCCAGCT	

Oligo	5’ -> 3’ Sequence	Supplier
Int1+18	TGGGCTCAGGGTTCCAGGGTGGCTGGACCCCAGGCCCCAGCTCT	Eurofins Scientific
Int7+2	GCAGGGAGGACGTGGCTGGGC	
Int7+4	CAGCAGGGAGGACGTGGCTGGGC	
Int7+6	TGCAGCAGGGAGGACGTGGCTGGGC	
Int7+8	TCTGCAGCAGGGAGGACGTGGCTGGGC	
Int7+10	GCTCTGCAGCAGGGAGGACGTGGCTGGGC	
Int7+12	CAGCTCTGCAGCAGGGAGGACGTGGCTGGGC	
Int7+14	CCCAGCTCTGCAGCAGGGAGGACGTGGCTGGGC	
Int7+16	GCCCCAGCTCTGCAGCAGGGAGGACGTGGCTGGGC	
Int7+18	AGGCCCCAGCTCTGCAGCAGGGAGGACGTGGCTGGGC	
Int7+20	CCAGGCCCCAGCTCTGCAGCAGGGAGGACGTGGCTGGGC	

Table 14 - Plasticware

Plastic ware	Supplier	Cat no:
15 & 50 ml CELLSTAR® centrifuge tubes	VWR	82050-278/82050-346
0.2 ml Strip tubes	Thermo Scientific	AB0266P
1.5 ml Microcentrifuge tubes	StarLab	E1415-1500
10 µl Graduated Pipette tip	StarLab	S1111-3000
10 ml sterile serological pipettes	Greiner Bio-One	607180
10/20 µl Graduated Filter Pipette tips	StarLab	S1120-3810
1000 µl Graduated Filter Pipette Tips	StarLab	S1122-1830
1000 µl Pipette tips	Fisher Scientific	10787524
200 µl Graduated Filter Pipette Tips	StarLab	S1120-8810
200 µl Pipette tips	Thermo Scientific	50101182
25 ml sterile serological pipettes	Greiner Bio-One	760180
5 ml sterile serological pipettes	Greiner Bio-One	606180
Black 96-well plates	Thermo Scientific	7605
Clear 96-well plates	Thermo Scientific	3855
Petri dishes	Thermo Scientific	4021
T175 Flasks	Therno Scientific	159920

Table 15 - Apparatus

Apparatus	Serial number	Supplier
6050 Bench Colorimeter	2311	Jenway, © Bibby Scientific Limited
pHenomenal pH 1000L	N/A	Fisherbrand
Balance PS-60	N/A	Fisherbrand
Water bath Jencons PLS GD100	GK0231026	Grant Instruments
Universal Hood II	76S/04472	Bio-Rad
Multi Bio RS-24 rotor	N/A	Peqlab brand
Bench top centrifuge, PerfectSpin 24	D801924	Peqlab brand
Bench top centrifuge, refrigerated, PerfectSpin 24R	N/A	Peqlab brand
Chemi Genius 2 Bio Imaging System	N/A	Syngene
FLx800 Microplate Fluorescence Reader	181041	BioTek®
Varioskan Flash	N/A	Thermo Electron Corporation
Incubator Shaker Innova 4200	N/A	New Brunswick Scientific Co., INC
Mini-PROTEAN® Tetra Handcast System	N/A	Bio-Rad
Electrophoresis constant power supply ECPS 3000/150	N/A	Amersham/Pharmacia
Electrophpresis power supply EPS 3501	N/A	Amersham/Pharmacia
Criterion™ blotter	N/A	Bio-Rad
PowerPac™ HC	043BR40171	Bio-Rad
MPW-65R centrifuge	10065R019909	MPW Med. Instruments
Nanodrop Spectrophotometer ND 1000	N/A	Labtech International, Ltd
Shaking incubator, Thriller®	N/A	Peqlab brand
Soniprep 150 desintegrator	A060299	MSE Ltd
Sorval Legend RT easy set centrifuge; rotor: Sorvall Heraeaus autoclavable 121°C Eq 40308317	40320795 #3057	Thermo Scientific
Thermal cycler peqSTAR 96X Universal Gradient	N/A	Peqlab brand
Chromato-Vue transilluminator TM-20	95-0179-05	Ultra-Violet Products (UVP), Ltd.

Table 16 - Software

Software	Supplier	Version/Year
ND-1000	Thermo Scientific	V3.7.1/2007-2008
Fluorescence FLx800 Kineticalc	BioTek®	V3.4

SkanIt software	Thermo Fisher Scientific	V2.4.3.3.7/2004-2007
QuantityOne	Bio-Rad	V4.6.3
GeneSnap	Synaptics Ltd.	V6.00.26/1993-2003
GraphPad Prism	GraphPad Software, Inc	V7.00
Clustal Omega	©EMBL-EBI	2017
UniProtKb	UniProt Consortium	2002-2017
QGRS Mapper	Ramapo College Bioinformatics	2006
RNAstructure	University of Rochester Medical Center – Mathews Lab	V5.8.1/2016

2.2 Methods

2.2.1 Prediction of G4 forming G-rich sequences in *INS* intron

In order to investigate the role of quadruplex forming G-rich sequences (QGRS) in regulated RNA processing, a suite of computational tools has previously been created to map putative G4 elements within mammalian genes (376). The suite contains algorithms that search for occurrences of G4 motifs and analyses their distribution patterns in genes.

To assess the G4 formation capacity of G-rich *INS* intron 1, a portion of this sequence was submitted to the QGRS mapper software for its analysis on the composition and distribution of putative QGRS (376). These predictions were also performed for a series of overlapping oligonucleotides derived from the target region (listed in Table 17-Table **19** in appendix B). DNA and RNA derived oligonucleotides were analysed (Table 13).

QGRS mapper predictions rely on intramolecular interactions and only account for G-run composition and distribution in tested sequence (376). Therefore, it cannot be assumed that a sequence containing G-runs that QGRS mapper does not predict to form G4, does not establish intermolecular interactions and is not involved in G4 formation.

Folding of less stable intermediate states that may co-exist in equilibrium with QGRS mapper predicted structures and with other non-canonical secondary structures are not accounted for in this program. To address the possibility of a single sequence to adopt different conformations, RNAstructure webserver(377) was used to predict the formation of canonical secondary structures in the same sequences analysed by QGRS mapper (Table 17Table **19**).

2.2.2 Screening for G4 formation by the thioflavin T (ThT) fluorescence assay

ThT fluorescence assay has been recently described as a sensitive and highly specific fluorescence probe for detecting, preferentially, parallel G4 structures, both in G-rich DNA and RNA sequences (188). For this purpose, *INS* intron 1-derived oligonucleotides and control oligos were prepared in water or buffer. Water-treated oligonucleotides were prepared at the desired concentrations in a total volume of 50 µl and heated at 90°C for 5 minutes, followed by cooling to room temperature for 1h at a rate of 1°C/min on a peqSTAR 96 Universal Gradient thermocycler (PeqLab). Oligos prepared in buffer (with or without cation supplementation) were heated at 90°C for 5 min, cooled to room temperature for 3h and then incubated ON at 4°C. DNA and RNA derived oligos were treated using the same procedures.

ThT was added (concentrations are indicated for each experiment) to all oligos and fluorescence read on a FLx800 Microplate Fluorescence Reader (Bio-tek Instruments, Inc). Assay conditions were as follows: excitation at 400 nm; emission at 508 nm; assay sensitivity at 90. Each reading was the result of the average of 10 measurements for each sample on the FLx800 Microplate Fluorescence Reader. G4-forming oligos c-myc, plas24 and 21DNA (derived from a promoter sequence, a fragment of a plasmodium telomere and a human telomere variant, respectively) were used as positive controls (188). ThT spectra were obtained on a Varioskan Flash spectral scanning multimode reader (Thermo Electron Corporation). Assay conditions were: excitation at 420 nm; emission scan from 430 to 750 at 2 by 2 wavelength steps. For data analysis, the mean fluorescence of ThT alone was subtracted from all tested oligos fluorescence.

2.2.3 Real-time monitoring of G-quadruplex formation during transcription *in vitro*

2.2.3.1 Polymerase chain reaction (PCR) amplification of transcription templates

INS intron 1 minigene sequences (315) were used as a template for PCR amplification using the forward and reverse primers (5' -> 3') attaatacgactcactataGGGCTCAGGGTTCCAGG | GCCCAGCCACGTCCTCCCT, respectively (Table 6). The forward primer includes a T7 promoter tag to allow transcription. PCR conditions, using Pfu DNA Polymerase (M774A) (Promega), were as follows: 95°C/5 min | 23 x (95°C/ 30 sec | 60.9°C/ 45 sec | 72°C/ 45 sec) | 72°C/ 2 min. PCR products were analysed on an 1.5% agarose gel at 80V, stained with GelRed and visualized using the Chemi Genius 2 Bio Imaging System with the GeneSnap Software (Synaptics, Ltd). PCR product sizes and amount

were compared against 3 µl of PeqGold DNA ladder-mix 100-10,000 bp (Peqlab). To facilitate amplification of a GC-rich content of the templates, DMSO was added to a final concentration of 5% (v/v). PCR products were extracted and purified from the gel using the GeneJET Gel Extraction Kit (K0692) (Thermo).

2.2.3.2 Real-time transcription

RNA transcripts were obtained by *in vitro* transcription of the T7-tagged PCR products using RT – Ampliscribe™ T7-Flash™ Kit (Epicentre, UK) following the manufacturer's instructions. To prove G4 formation in nascent RNA transcripts, GTP was replaced by 7-deaza-GTP, which inhibits guanine Hoogsteen interactions, in the reaction mixtures. ThT was added immediately before starting the transcription reaction by the addition of the polymerase. G-quadruplex formation during transcription was obtained on a Varioskan Flash (Thermo Electron Corporation) and assay conditions were as follows: excitation: 420 nm; emission: 481 nm; fluorescence measurements were collected every 30 sec. After 3h of reaction RNase-Free DNase I was added to stop the reaction and fluorescence collected for another 15 min. RNA transcripts were recovered by phenol:chloroform extraction followed by alcohol precipitation. After resuspension in RNase-free water, RNA transcripts were loaded onto a native 6% acrylamide gel for the analysis of structural conformation diversity in native conditions. Nucleic acids bands were visualized by staining the gel for 30 min with 1x GelRed.

2.2.4 Identification of proteins that bind the antisense target regions for the INS intron 1 retention

2.2.4.1 Polymerase chain reaction (PCR) amplification of transcription template

INS intron 1 minigene sequences (315) were used as a template for PCR amplification using the forward and reverse primers (5' -> 3') attaatacgactcactataGGGCTCAGGGTTCCAGG | TGCAGCAGGGAGGACG. The forward primer includes a T7 promoter tag to allow transcription. PCR conditions, using GoTaq® DNA Polymerase (M300) (Promega), were as follows: 95°C/5 min | 20 x (95°C/ 30 sec | 55°C or 60°C/ 45 sec | 72°C/ 1 sec) | 72°C/ 2 min. PCR products were analysed on an 1.5% agarose gel at 80V, stained with GelRed and visualized using the Chemi Genius 2 Bio Imaging System with the GeneSnap Software (Synaptics, Ltd). PCR product sizes and amount were compared against 3 µl of PeqGold DNA ladder-mix 100-10,000 bp (Peqlab). To facilitate amplification of a GC-rich content of the templates, DMSO was added to a final concentration of 5%

(v/v). PCR products were extracted and purified from the gel using the QIAquick Gel Extraction Kit 250 (Qiagen).

2.2.4.2 INS intron 1 minigene transcription

RNA transcripts were obtained by *in vitro* transcription of the T7-tagged PCR products using MEGAshortscript™ T7 Transcription Kit (Lifetechnologies, USA) following the manufacturer's intrsuctions. RNA transcripts were recovered by phenol:chloroform extraction followed by alcohol precipitation. Transcripts were resuspended in RNase-free water and stored at -80 °C until use.

2.2.4.3 Pull-down assay

Five hundred pmol of *in vitro* transcribed RNA were treated with 5mM sodium *m*-periodate and bound to adipic acid dihydrazide agarose beads (Sigma, USA). Beads with bound RNAs were washed three times in 2 ml of 2 M NaCl and three times in buffer D (20 mM HEPES–KOH, pH 7, 6.5% v/v glycerol, 100 m M KCl, 0.2 mM EDTA, 0.5 mM dithiothreitol) followed by incubation with HeLa nuclear extracts in buffer D supplemented with heparin at a final concentration of 0.5 mg/ml. Unbound proteins were washed five times with buffer D. Bound proteins were separated on 10% SDS-PAGE, stained by Coomassie blue and/or blotted on to nitrocellulose membranes. Gels stained with Coomassie blue were also silver stained using the ProteoSilver™ Silver Stain Kit (Sigma, USA) according to the manufacturer's recommendations. Antibodies for Western Blot were purchased from Sigma (hnRNP E1/E2, product number R4155; U2AF65, product number U4758; and SFRS2, product number S2320), Abcam (DHX36, product number ab70269) and Millipore (SC35, clone 1SC-4F11). Antiserum against hnRNP F and hnRNP H was a generous gift of Prof. Douglas Black, UCLA. Protein identification was confirmed by MS/MS analysis of excised gel fragments, at The Centre of Excellence in Mass Spectrometry at the University of York.

2.2.5 Cloning, expression and purification of recombinant hnRNPs F and H1 and RRMs

2.2.5.1 Cloning

DNA sequences encoding RRM domains of human hnRNP F (UniProtKb entry: P52597) and human hnRNP H1 (UniProtKb entry**:** P31943) were cloned as His-tagged fusion proteins with a TEV protease cleavage site (amino acid sequence for TEV cleavage: ENLYFQG) into *BamHI/Hind III* or *BamHI/XhoI*,

respectively, sites of pET28a (primers list in Table 5). Competent JM109 (Promega) cells were transformed with cloned plasmids by heat-shock transformation. Briefly, 50 µl of competent cells were thawed on ice, mixed with 5 µl of ligation reaction and placed on ice for 15 minutes. Cells were heat-shocked by incubation in a 42°C water bath, followed by 2 minutes on ice. One ml of LB broth medium was added to each transformation and cells grew for 1h 30 min at 37 °C, followed by plating on LB agar with 100 µg/ml kanamycin. Confirmation of clone identities was performed by enzymatic restriction of the plasmids. Clones were sequenced by Source BioScience (Nottingham, United Kingdom) (Table 10).

2.2.5.2 Expression and purification of recombinant proteins

BL21 (DE3) bacterial cells (New England Biolabs, Inc.) were transformed with plasmids containing hnRNP RRM sequences (Figure 35 in appendix B). Cells were grown at 37°C to OD_{600}≈0.4. Protein expression was induced with 1mM isopropyl-b-D-thiogalactopyranoside (IPTG). Cells were harvested 2h after induction by centrifugation at 4000 rpm for 20 min. Cell pellets were resuspended in a lysis buffer (50 mM Tris-Base pH 7.4, 300 mM NaCl, 1 mM DTT) and lysed by 10x 10s sonication, followed by centrifugation at 4000 rpm for 45 min at room temperature (RT). One ml of Ni-NTA agarose beads (Qiagen) were incubated with 4 ml of each lysate and stirred for 1h at room temperature. Unbound proteins were washed four times with 1 ml of washing buffer 1 (50 mM Tris-Base pH 7.4, 300 mM NaCl, 20 mM imidazole), followed by six times 1 ml of washing buffer 2 (50 mM Tris-Base pH 7.4, 300 mM NaCl, 50 mM imidazole), twice with 1 ml of washing buffer 3 (50 mM Tris-Base pH 7.4, 300 mM NaCl, 75 mM imidazole) and twice with 1 ml of washing buffer 4 (50 mM Tris-Base pH 7.4, 300 mM NaCl, 100 mM imidazole). Protein elution was performed four times times with 1 ml of elution buffer (50 mM Tris-Base pH 7.4, 300 mM NaCl, 250 mM imidazole). Aliquots of eluted proteins were visualized on 15% SDS-PAGE and stained with Coomassie or blotted on to nitrocellulose membranes. Antibodies against the penta-His-tag were purchased from Invitrogen™ (product number P-21315).

Full-length hnRNP F and H constructs (Figure 35 in appendix A) were transformed into Rosetta™ 2 competent cells (71397-3) (Millipore) and purified as described for RRMs.

2.2.6 Cloning and transfection of 5'UTR regions of Human and primates *INS* gene

2.2.6.1 Cloning

5' UTR DNA sequences from *Homo sapiens* (Genbank accession number AY138590), *Pongo pygmeus* (AY137503), *Macaca fuscata (*GU901176), *Colobus angolensis* (GU901183),

Semnopithecus entellus (GU901185), *Aotus azarae* (GU901198) preproinsulin genes were cloned into Hind III/NcoI sites of the monocistronic pGLpest.SEQ plasmid (primers in Table 5). The pGLpest.SEQ plasmid was kindly given by Mark Coldwell (Centre for Biological Science, University of Southampton, United Kingdom). Competent JM109 cells (Promega) were transformed with plasmid constructs as described above. Insert sizes were confirmed by enzymatic restriction of the plasmid DNA. Constructs were then subcloned into KpnI sites of the bicistronic pICtest2 (pIC) plasmid (pIC) (also given by Mark Coldwell). Cloning efficiency and insert sizes were confirmed after transformation into DH5α competent cells and enzymatic restriction of the plasmid DNA. All constructs were sequenced at Source BioScience (Nottingham, United Kingdom) (primers in Table 10 and clone sequences in Figure 36 in appendix A).

2.2.6.2 Culturing of HeLa cells

HeLa cells were kindly given by Mark Coldwell (Centre for Biological Science, University of Southampton, United Kingdom). For passaging, the medium was aspirated, cells washed with 500 µl of 1x PBS and incubated at 37°C and 5% CO_2 with 2.5 ml of TrypLE Express reagent (Gibco) per well until cells detached (10-15 min). Seven and half ml of DMEM containing 10% FBS were added to cells and 2.5 ml out of the 10 ml of dissociated cells were transferred into a new T175 flask. Passaging was performed every two to three days. For transfection with Human and primates' 5' UTR constructs, cells were routinely cultured and passaged until they reached at least their fifth passage.

2.2.6.3 Transfection of HeLa with *INS* 5'UTR constructs

For luciferase assays, 5 000 HeLa cells were seeded in 200 µl of DMEM medium per well of a 96-well-plate. Sixty thousand HeLa cells were seeded in 2 ml of DMEM medium per well of 12-well-plates and transfected for total RNA extraction. Twenty-four hours after seeding, cells were transfected with 50 ng (96-well-plate) or 600 ng (12-well-plate) of plasmid DNA, previously mixed with GeneJuice transfection reagent (according to manufacturer's protocol). Medium was removed and replaced by fresh DMEM with 10% FBS 4h after transfection.

2.2.6.4 Dual-Luciferase Reporter Assay

The dual-luciferase reporter assay (E1910) (Promega) was used to compared mRNA processing and translation efficiency of Human and other five primates *INS* 5' UTRs. Two individual reporter enzymes, the firefly and Renilla luciferases, are simultaneous and independently expressed and

their activity measured, where thetranslated firefly reporter is dependent on experimental conditions and the Renilla reporter provides an internal control serving as the baseline response. Normalization of both activities minimizes experimental variability caused by differences in cell viability or transfection efficiency. Forty-eight hours post-transfection, medium was aspirated and HeLa cells were washed with 100 µl of 1x PBS. Following the addition of 20 µl of 1x Passive Lysis Buffer (PLB) to each well, cells were incubated at RT for 15 min with gentle shaking. Five µl of each cell lysate were transferred to a white 96-well-plate and chemiluminescence of each luciferase was measured separately on a GloMax®-Multi+ Microplate Multimode Reader with Instinct® software. The reader automatically injects 25 µl of Luciferase Assay Reagent II, previously prepared according to manufacturer's protocol, and measures the firefly luciferase signal, which is immediately followed by addition of 25 µl of Stop & Glo Reagent to quench firefly luciferase activity and measure the Renilla luciferase signal. The procedure is then repeated for all the wells with HeLa lysates.

Data were transferred into an Excel spread sheet, calculating the ratio of firefly luciferase: Renilla luciferase (fluc:rluc) activities. Each construct was compared to the activity from the transfection with the empty pIC vector.

2.2.6.5 Total RNA extraction

RNA was isolated from HeLa cells 24 hours after transfection in 12-well-plates using the TRIzol isolation method, adapted from Invitrogen.

Medium was removed, cells washed with 1 ml of 1x PBS, 500 µl of TRIzol applied directly to the cells and incubated for 5 min atRT after homogenization by up-and-down pipetting. One-hundred and thirty µl of chloroform was added to cell lysate, briefly vortexed and incubated for 15 min at RT. The sample was centrifuged at 12000 rpm for 15 min at 4°C to allow phase separation. The upper aqueous-phase was transferred into a new 1.5 ml macrocentrifuge tube and 330 µl of isopropanol added. After briefly vortexed, samples were incubated at RT for 15 min and centrifuged at 13000 rpm for 15 min at 4°C. Supernatant was discarded and the pellet was washed with 1 ml of chilled 80% ethanol for 10 min and centrifuged at 12000 rpm at 4°C. Ethanol was removed, the pellet dried at RT for approximately 5 min and dissolved in 30 µl of RNase-free water. RNA concentration was spectrophotometrically measured using NanoDrop (Thermo Scientific) at 260 nm and 280 nm. A ratio of ≈2 for each sample was accepted as "pure" RNA, free of contaminants such as phenol. RNA samples were stored at -80°C until use.

2.2.6.6 Reverse transcription using oligo-dT primer

Isolated RNA was treated with RQ1 DNase enzyme to digest any potential contaminating in the sample. Approximately 800 ng of total RNA, in a total volume of 17 µl, were mixed with 3 µl of the master mix (2 µl of RQ1 DNase 10X Reaction Buffer, 0.4 µl of RQ1 RNase-free DNase (M6101, Promega) and 0.6 µl of RNase-free water) and incubated at 37 °C for 30 min. Reaction was stopped by the addition of 1 µl of DNase stop solution followed by incubation at 65 °C for 10 min. DNase-treated RNA was stored at -80 °C until use.

Four-hundred nanograms of DNase-treated RNA and 1 µl of 15-mer oligo-dT primer (Eurofins) were mixed in a total volume of 5 µl, incubated at 70 °C for 5 min and chilled on ice until 4 µl of Moloney Murine Leukemia Virus (M-MLV) Reverse Transcriptase (T) 5X Reaction Buffer, 5 µl dNTPs, 0.5 µl of RNasin and 1 µl of M-MLV RT were added. Transcription reaction was then incubated at 42 °C for 1h, followed by 5 min at 90 °C. cDNA was stored at -20 °C.

2.2.6.7 cDNA PCR amplification for splicing pattern analysis

The reverse transcribed cDNA was used for the analysis of spliced products from *INS* 5' UTR constructs. PCR amplification was then performed using a peqSTAR 96 Universal Gradient PCR equipment (PeqLab) using the forward and reverse primers (5' -> 3') GCCTCGGCCTCTGAGCTATTCCAG | GTATCTCTTCATAGCCTTATGCAG (Table 10). PCR conditions, using Pfu polymerase were: 95 °C/3 min | 32x (95 °C/ 30 sec | 52 °C/ 1 min | 72 °C/ 1 min) 72 °C/ 2 min. Amplification products were analysed on an 2% agarose gel at 80V, stained with GelRed and visualized using the Chemi Genius 2 Bio Imaging System with the GeneSnap Software (Synaptics, Ltd). PCR product sizes and amount were compared against 3 µl of PeqGold DNA ladder-mix 100-10,000 bp (Peqlab). To facilitate amplification of a GC-rich content of the templates, DMSO was added to a final concentration of 5% (v/v).

2.2.7 Statistical analysis

Using GraphPad Prism, version 7.00 for Windows (GraphPad Software, La Jolia, California, USA, www-graphpad.com), statistical tests were performed to determine significance of data. A Shapiro-Wilk normality test was performed to all data to test whether data followed a Gaussian distribution.

Depending on the result of normality test and the aim of the assay, different tests were performed. Regarding data following a Gaussian distribution, statistical significance of ThT fluorescence time-course in the presence of G4 complexes was examined by comparing the fluorescence intensities

at different incubation times with fluorescence obtained immediately after ThT addition. For that, multiple comparison unpaired t-tests using the Šídák-Bonferroni method were performed (378).

For the saturation of G4 complexes with ThT, data were analysed using a multiple comparative analysis using two-way ANOVA with Tukey's correction. Tukey's method is used for the comparison of every mean with every other mean in tested population. The method computes confidence intervals for every comparison (379).

A Fisher's Least Significant Difference (LSD) test (380) was chosen for the comparison of fluorescence intensities from Int1 derived oligos. Statistical significance of the influence of solvents and pH on G4 propensity was evaluated using the unpaired t-test with Welch's correction, by performing two-by-two comparisons. This test is used to test the hypothesis that two populations have equal means. It is more reliable than Student's t-test when two samples have unequal variances. Assumption of normality is maintained. Welch's t-test tests the null hypothesis that the two population means are equal or the alternative hypothesis that one of the population means is greater than or equal to the other. Welch's t-test is more robust than Student's t-test. It also remains robust for skewed distributions and smaller samples (381).

The Welch's corrected unpaired t-test was performed for the analysis of solvent and pH influence on G4 propensity in RNA oligos.

For significance of luciferase assay data sets, Dunnett's or Tukey's multiple comparison tests or Welch's corrected unpaired t-tests were performed. The Dunnett´s test is similar to Tukey's, but is used for the comparison of every mean with a control mean.

With respect to data sets that did not pass the Shapiro-Wilk normality test were analysed using the nonparametric Friedman test. This test compares the mean fluorescence of each oligo with the mean of every other oligo and via random sampling of every mean evaluates the probability of the differences between means being null. Small p-values (< 0.05) indicate that at least one mean differs from the rest (382).

All tests were chosen based on the type of analysis intended, which is influenced by normality of data (parametric or nonparametric) and size of the sample (t-test for 2 samples, and ANOVA variations for multiple comparisons – Fisher, Friedman, Dunnett or Tukey). The alpha value was set to 0.05 for all the data and were considered significant different when $*p \leq 0.05$, $**p \leq 0.01$ and $***p \leq 0.001$.

Chapter 3: Thioflavin T (ThT) as a fluorescent light-up probe for monitoring of G4 formation

3.1 Introduction

The structure adopted by RNA transcripts can constrain or promote recognition of cis-acting elements or binding of trans-acting factors, thus influencing splicing (27). *INS* intron 1 is rich in G-tracts, which can potentially fold into non-canonical G4 structures *in vivo*, but their contribution to splicing efficiency of this intron is not understood.

To characterize G4 formation in INS intron 1-derived sequences *in vitro*, the fluorescent dye Thioflavin T (ThT) was used as a specific probe for both DNA and RNA G-rich sequences surrounding the antisense target for reduced intron retention (315).

ThT is a fluorescent dye widely used in amyloid fibre formation studies (383–387). In 2013 Mohanty and collaborators induced and evaluated G4 folding of the 22AG ($(TTAGGG)_4$) (388) human telomeric DNA using this fluorogenic dye as a fluorescent light-up probe in the visible spectrum region (389). Since then, ThT has been successfully used as a specific fluorescent G4 ligand capable of distinguishing this non-canonical structure from canonical single- and double-stranded (ss- and ds-) DNA structures (155,187,188,389–391). The dye displays a strong fluorescence enhancement in the presence of both parallel and anti-parallel DNA G4 conformations, depending on the analysed sequence and folding buffers (191,392). ThT is also an efficient and selective fluorescence sensor for all-parallel RNA G4s (189).

G4s were first described in telomeres, located at the ends of eukaryotic chromosomes, and many oncogene promoters (393,394). Therefore, three well-characterized G4-forming oligonucleotides were used to stablish ThT efficiency for the detection of G4 formation: telomere-derived oligonucleotide 21DNA; c-myc, a 24 nt oligo derived from the G-rich promoter region of the human proto-oncogene c-myc; Plas24, a representative oligo from the G-rich sequence of the *Plasmodium* telomere with the same length as c-myc (188). All three oligos were previously shown to form G4 and bind ThT, as shown by fluorescence enhancement (188,190). In addition, the oligo Int7, derived from the parallel G4-forming fragment just to 3'-end of the antisense target for reducing *INS* intron 1 retention, was used to define experimental conditions.

3.2 Results

3.2.1 Optimization of experimental conditions

3.2.1.1 ThT as a fluorescence light-up probe for G4

To ascertain whether ThT displays a fluorescence enhancement in the presence of G4-forming sequences, c-myc oligo was denatured and slowly cooled down to room temperature (RT) to promote secondary structure formation. ThT relative fluorescence (RFU) in the presence of control oligos was compared with the fluorescence of the dye alone (Figure 9). RFU is referred as fluorescence or fluorescence intensity throughout the text.

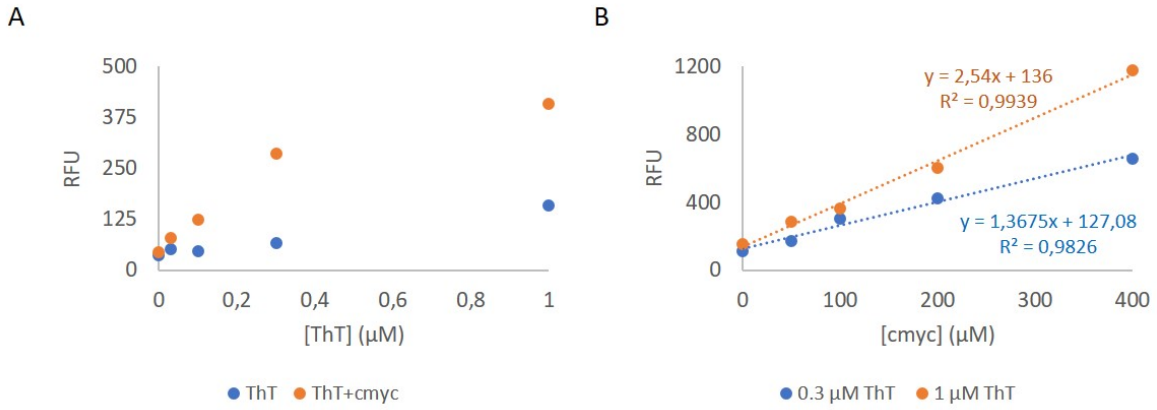

Figure 9 – Fluorescence intensity of ThT variation with increasing dye or oligo concentrations. **(A)** Fluorescence enhancement of serial dilutions of ThT in the presence of a constant amount of oligo c-myc. **(B)** Correlation between fluorescence response of 1µM ThT and serial dilutions of c-myc. For both assays, fluorescence emission of Thioflavin T was measured at 508 nm.

Data in Figure 9A showed that for each ThT concentration, fluorescence intensity of ThT in the presence of the c-myc oligo was, on average, 2.5 times higher than fluorescence of ThT alone.

Fluorescence at two different ThT concentrations for a series of oligo dilutions indicates a linear and positive correlation between the amount of oligo in the analysed range (Figure 9A).

ThT showed a hyperbolic profile when different concentrations of the dye are used to detect G4 formation at a constant amount of same oligo (Figure 9B), likely reflecting a dye saturation.

3.2.1.2 Time-course of ThT fluorescence

The stability of G4 structures and of G4-ThT complexes is important to establish the assay conditions and a time-window when fluorescence of the complexes can be analysed.

Oligos were treated as before and ThT fluorescence was measured immediately after complex formation (0h) and 1h, 2h, 24h and 1 week later (Figure 10). All oligos were prepared in duplicate.

Figure 10 shows, as expected, significant fluorescence enhancements for oligos known to form G4 (c-myc, Plas24and 21 DNA), when compared to ThT alone or either single-stranded and hairpin structures in dT22, DCAF6 and CLASP1. This confirms previous findings (187,188,190) that ThT is a sensitive and specific probe for G4 detection.

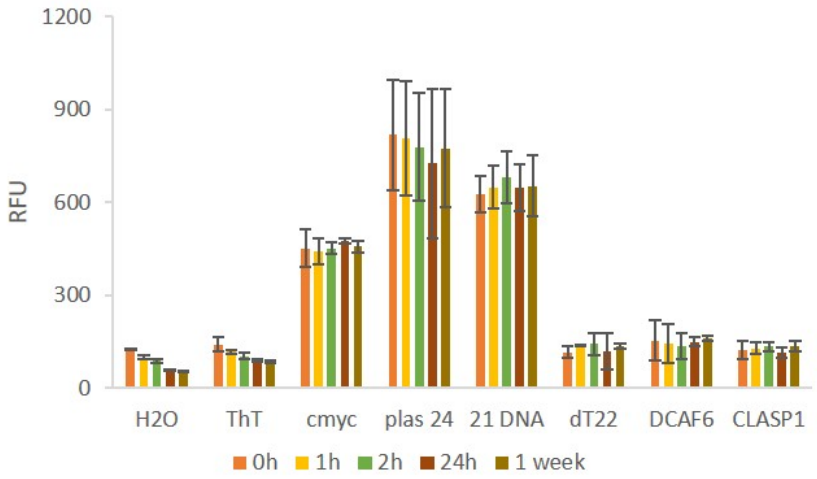

Figure 10 – Time-course of ThT fluorescence of G4-ThT complexes.
Fluorescence of complexes composed of G4-forming c-myc, Plas24 and 21 DNA oligos is compared with the one from oligos that do not fold into this non-canonical secondary structure (dT22, DCAF6 and CLASP1). Fluorescence of 1 µM ThT alone and water is also shown as control.

Statistical testing normality of data using Shapiro-Wilk normality test indicated that the population is normally distributed, as shown by p-values ≥ 0.05 (the null-hypothesis is that the population is normally distributed; the hypothesis is rejected when p-value < alpha (0.05)). Therefore, a gaussian distribution was assumed to perform corrected multiple comparison unpaired t-tests using the Šídák-Bonferroni method.

Comparative analysis showed that there is no significant decrease in fluorescence intensities of oligo-ThT complexes, regardless of the tested oligo, for a week storage at 4 °C (Table 20 in Appendix B). Hence, G4 propensity can be determined by measuring fluorescence of ThT bound to oligos for up to one week after addition of ThT, without loss of information. Comparison of G4-forming

sequences at each time-point revealed that fluorescence intensity was not statistically different between oligonucleotides. Therefore, no conclusions can be assumed regarding discriminatory capacity of ThT, which will be further investigated below.

3.2.1.3 ThT fluorescent signal dependence on oligo concentration

For the optimization of any qualitative and semi-quantitative assay where a probe like ThT is used, it is essential to establish a linear correlation between the amount of sample to be tested and probe signal to be measured. This avoids loss of signal due to a poor sample-probe ratio, saturation of the probe signal or quenching (187).

To confirm that ThT fluorescence intensity is directly proportional to oligo concentration and, therefore, the amount of G4 formed, several dilutions of 2 oligos predicted by QGRS Mapper to fold into this structure (Table 17 in appendix B) were analysed. ThT was added to final concentrations of 10 and 50 µM (Figure 11A-D) or to 1,2 and 5 µM (Figure 11E-H).

Comparison of ThT spectra in the presence of G4-forming oligos Int7 and Plas24 with the spectrum of ThT alone shows fluorescence enhancement in both oligos for most of the concentrations tested (Figure 11A-D). As expected, fluorescence increases as oligo concentration increases, independent of the chosen ThT concentration range.

ThT spectra did not change in the presence of different oligos, displaying two peaks, at 481 and 495 nm. The former corresponds to the maximum fluorescence emission of ThT alone and it is close to the wavelength to which ThT displays fluorescence when bound to amyloid fibrils (482-485 nm (383,387,395). The second peak, 495 nm, does not appear in the unbound ThT spectrum, suggesting that this signal may be specific for the recognition of parallel G4.

Concomitant with fluorescent spectral changes, scatter plots (Figure 11E-G) show linear fluorescence enhancements at 495 nm upon titration of Int7, c-myc and Plas24 oligos, indicating a direct and positive correlation between fluorescence and oligo concentration, in tested conditions. Positive correlations between ThT fluorescence and oligo concentration were supported by highly significant Pearson correlation coefficients. Strong correlations are shown by R coefficients close to 1 (Figure 11H).

Collectively, these data reveal that ThT is capable of detecting G4 formation *in vitro* for any G-rich oligo in tested conditions and that higher fluorescence reflects a stronger propensity to form G4. Therefore, ThT can be used for the detection of G4 formation in vitro in *INS* intron 1.

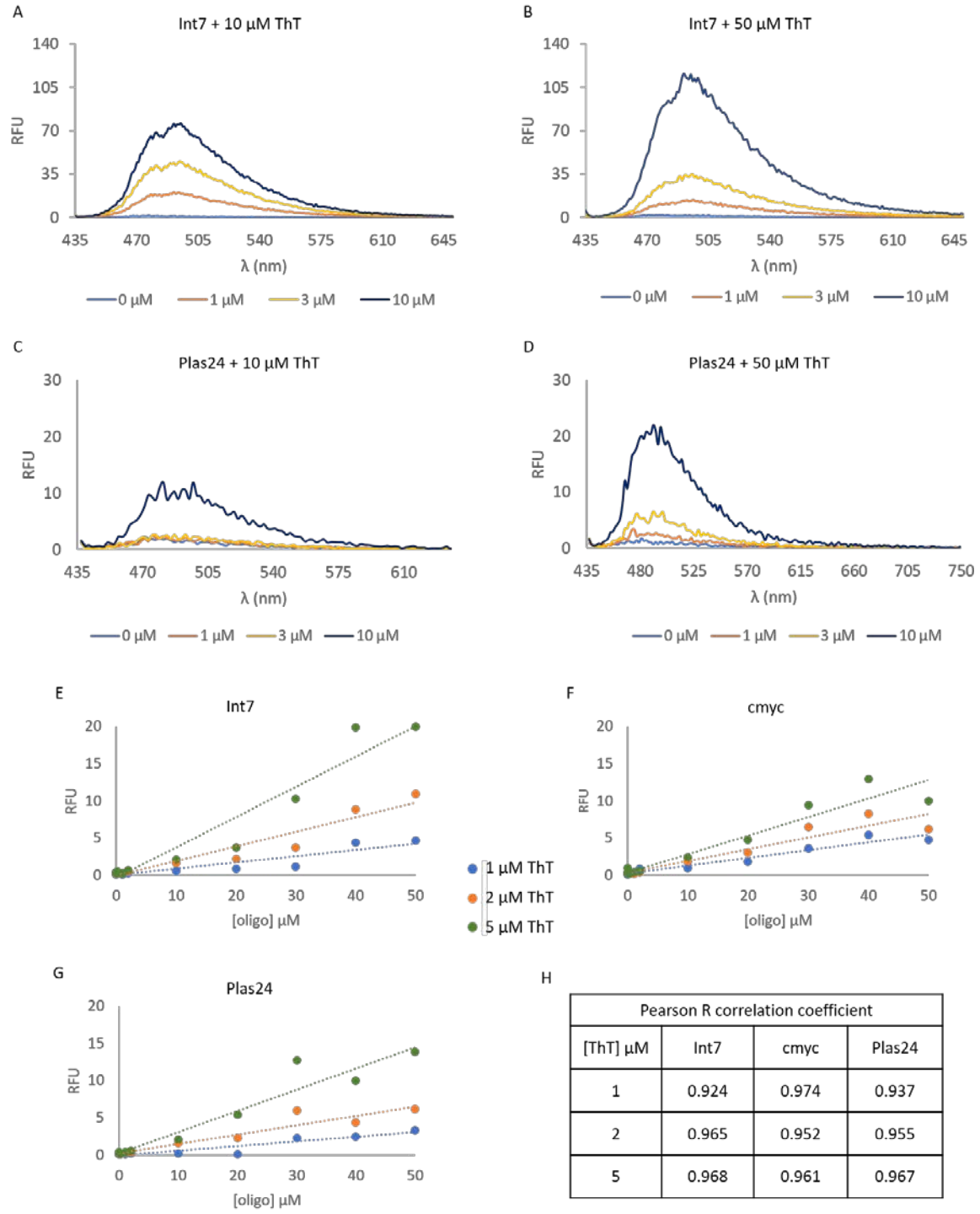

H

Pearson R correlation coefficient			
[ThT] µM	Int7	cmyc	Plas24
1	0.924	0.974	0.937
2	0.965	0.952	0.955
5	0.968	0.961	0.967

Figure 11 - ThT fluorescence intensity increases linearly with increasing oligo concentrations. Fluorescence spectra at 10 (**A** and **C**) and 50 (**B** and **D**) µM of ThT alone or in the presence of increasing concentrations of Int7 (A and B) or Plas24 (C and D). Spectra were compared with scattered plots **(E-G**) showing the correlation between 1 (blue), 2 (orange) and 5 (green) µM of ThT fluorescence intensity and increasing oligo concentrations of Int7 (E), c-myc (F) and Plas24 (G). **(H)** Pearson R correlation coefficients for ThT concentrations in the presence of increasing concentrations of tested oligos.

3.2.1.4 Molecular saturation

To choose the appropriate ThT concentration in further studies and determine maximum ThT-bound fraction, saturation profiles of several oligos by ThT were characterized. Nine oligos (Figure 12), predicted by QGRS Mapper to form G4 (Table 17 in appendix B), and one single-stranded oligo (dT22) as a control, at 2 and 20 μM, were heated and slowly cooled to promote formation of a G4 population as homogeneous as possible. Fluorescence intensities of several concentrations of ThT (10-500 μM) bound to G4 conformations at either 2 or 20 μM were then compared with the signal of unbound ThT (Figure 12).

Saturation profiles revealed a hyperbolic curve, with fluorescence intensity increasing with probe concentrations up to 100-150 μM and gradual loss of the signal until it was slightly above or equal to the background (ThT alone) (Figure 12). This decrease is most likely due to fluorescence quenching, already observed for ThT in other studies (187).

A multiple comparative analysis using two-way ANOVA with Tukey's correction (Table 21 in appendix B) indicated that fluorescence intensity enhancements are significantly higher at 20 μM oligo than at 2 μM for ThT concentrations within the range 50-300 μM (Figure 12). ThT concentrations outside of this range were, therefore, not considered in further studies to avoid unsaturated oligo readings and/or fluorescence quenching.

Comparing fluorescence signals from the ten oligos in Figure 12, enhancements produced by ThT concentrations higher than 50 μM and up to 100 μM are, then, more adequate for the determination of G4 propensity and for oligo discrimination.

Although the saturation profiles were very similar (Figure 12), p-values < 0.05 indicate that different oligo:ThT ratios display different fluorescence intensities, at tested ThT concentrations.

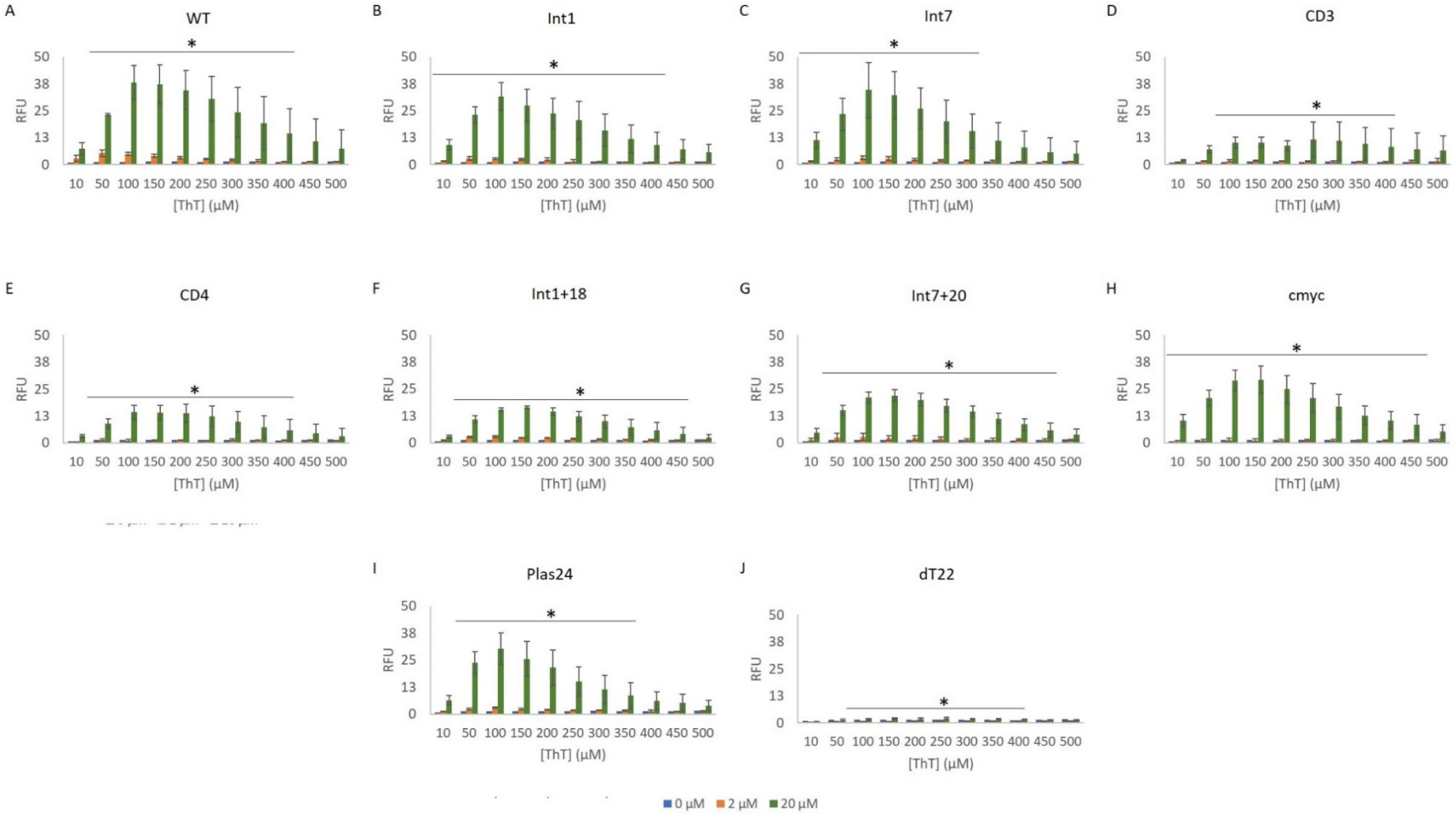

Figure 12 – Saturation of G4 structures of various oligos by Thioflavin T.

Determination of G4 saturation curves by titrating 10 different nucleotides at 2 µM (orange bars) and 20 µM (green bars) with increasing concentrations of ThT (10-500 µM). Fluorescence intensities of G4-ThT complexes, at 495 nm, of WT, Int1, Int7, CD3, CD4, Int1+18, Int7+20, cmyc, Plas24 and dT22 (**A** to **J**, respectively) are compared with fluorescence intensities of ThT alone (blue bars). Error bars denote the standard deviation from three independent fluorescence assays. Asterisks denote p-values < 0.05.

ThT fluorescence from 2- and 4-fold the oligo concentration was then measured to evaluate discrimination power of ThT concentration. Three oligos, Int7, Plas24 and dT22, at 1, 2, 5, 10 and 20 µM, were prepared as above to promote G4 formation.

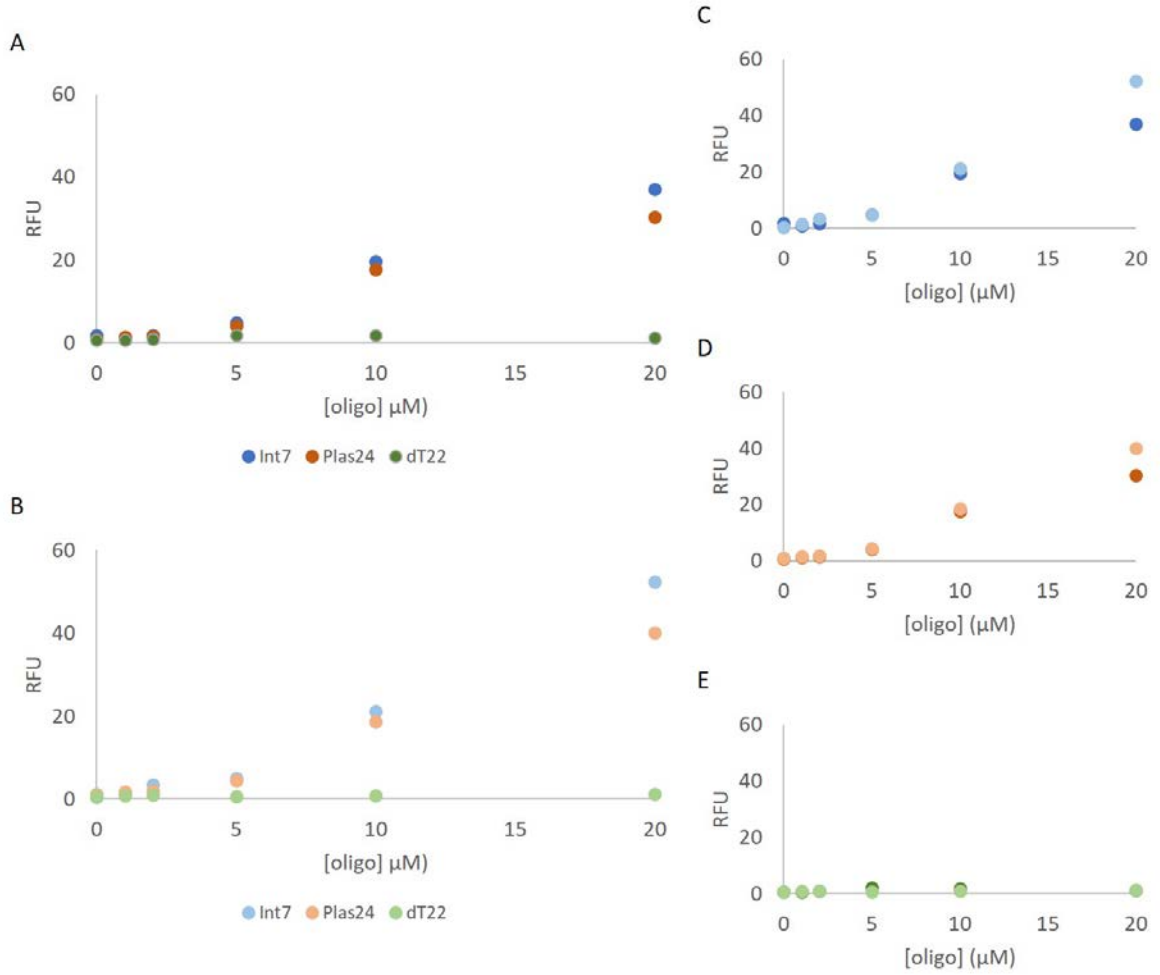

Figure 13 – Comparison of fluorescence intensities of two oligo:ThT ratios.
Fluorescence intensity, at 495 nm, of ThT at twice **(A)** or four-times **(B)** the oligo concentration. Comparison of both ratios for each oligo is also shown. **(C)** Fluorescence intensities of Int7 in the presence of ThT in twice (blue) and four times (light blue) the oligo concentration. **(D)** Fluorescence intensities of Plas24 in the presence of ThT in twice (orange) and four times (light orange) the oligo concentration. **(E)** Fluorescence intensities of dT22 in the presence of ThT in twice (green) and four times (light green) the oligo concentration.

Figure 13 showed that differences in fluorescence were greater when ThT concentration is four times higher than oligo concentration (Figure 13C-E). On the other hand, oligo discrimination at 20 µM is stronger than at 10 µM or lower, where fluorescence intensities are undifferentiated (Figure 13A-B). ThT concentration of 80 µM and 20 µM of oligo, should give more accurate and reproducible results, thus, these conditions were used in further assays.

3.2.1.5 Conclusions:

As in previous studies (167,188–190,389,392), ThT showed significant fluorescent enhancement in the presence of oligos known to fold into G4 (c-myc, Plas24, 21 DNA). Complexes formed by G4 oligos and ThT are very stable, if kept at 4 °C, and their fluorescence signal did not change significantly within a week of their formation.

ThT bound to G4 in a concentration-dependent manner and its fluorescence signal was directly proportional to the amount of oligonucleotide.

For all tested oligos and oligo concentrations, ThT concentrations between 50-100 µM can be used without any significant loss of fluorescence intensity. When ThT concentrations were higher than 150 µM ThT may quench itself and fluorescence intensity progressively decreased until background, ThT alone, levels.

A 1:4 (oligo:ThT) ratio, with oligos at 20 µM, was shown to be adequate for further studies aimed at discriminating G4 propensity of a series of *INS* intron 1-derived oligos.

3.2.2 G4 formation in *INS* intron 1 DNA-derived oligos

The data presented in section 3.2.1 corroborated previous findings (188,189,389) that ThT is an efficient fluorescence dye for the structural probing of G4 formation and displayed a strong and positive linear correlation with nucleic acid concentration.

Having selected experimental conditions (including oligo and dye concentrations incubation time, and temperature) in which DNA oligos fold and/or associate to form G4, ThT was then used to evaluate the ability of a set of overlapping oligonucleotides derived from the G-rich segment of intron 1 to fold into G4 (Table 13). This region surrounds the antisense target for reducing intron 1 retention (315) and may have a therapeutic potential in future. The selection of overlapping sequences was based on oligo length, inclusion or exclusion of segments involved in intron retention (such as the target sequence for antisense oligonucleotides that promote splicing), and G4 predictions. This selection included oligo Int7, which has been previously shown by far-UV CD and NMR to fold into parallel G4 (315), and showed increased fluorescence in preliminary studies (section 3.2.1 - Figure 12 and Figure **13**).

3.2.2.1 *INS* intron 1 and target sequence-derived oligos screening for G4 formation

Preliminary studies with this set of oligos under suboptimal conditions (Figure 32 in appendix A) had indicated that G-runs both upstream and downstream of the antisense target were prone to G4 formation, as shown by 2-4.5-fold enhancements in comparison to DCAF6 fluorescence. In general, ThT fluorescence enhancement correlated positively with QGRS mapper scores (Table 17 in appendix B). However, there were a few inconsistencies such as the low fluorescence intensity in oligos predicted by QGRS mapper as potential G4 forming sequences (376) (Int2 and 3, GT8 and GA8 in Figure 32 in appendix A), and *INS* intron 1-derived oligos Int5 and 6 showed high fluorescence intensity, with relation to the negative controls, although they are not expected to form G4.

These inconsistencies could be due to high variability in five independent assays and, also, low oligo concentrations (1 µM) that could contribute to poor oligo discrimination, as shown in Figure 13A and B.

Following optimization of discriminatory conditions, in section 3.2.1, oligos were prepared at a concentration of 20 µM and G4 propensity was evaluated with 80 µM ThT.

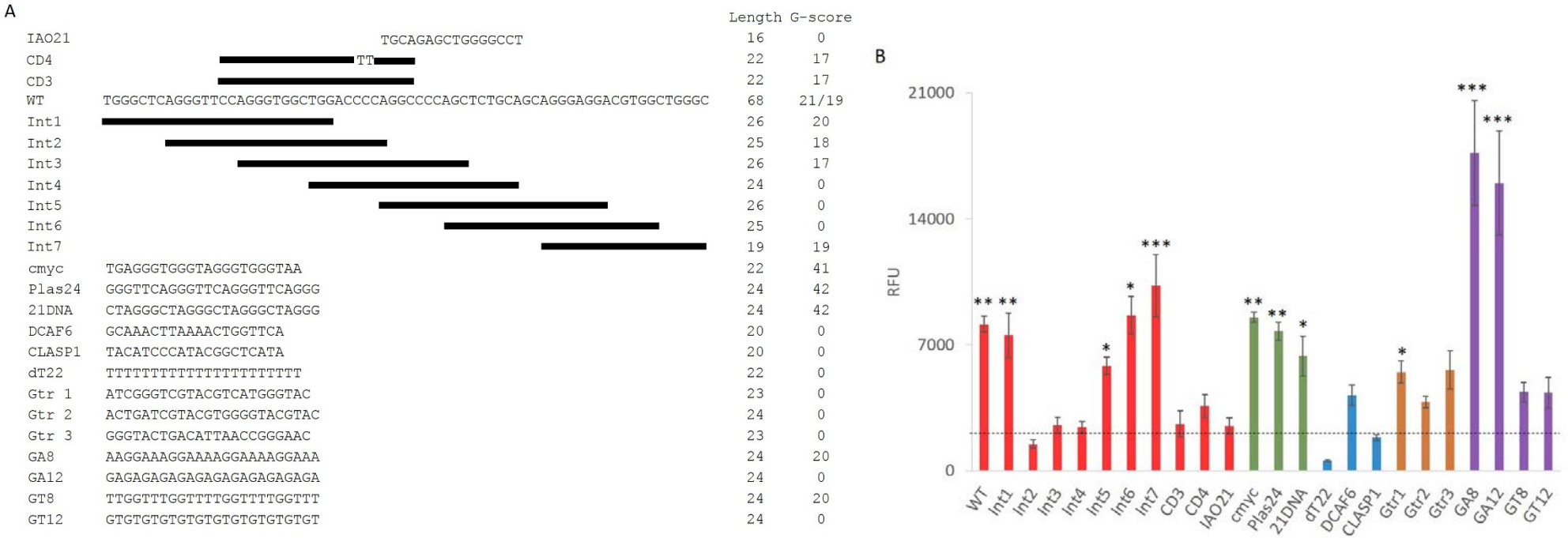

Figure 14 - ThT screening for G4 formation *in vitro* in *INS* intron 1.
(A) Schematics of tested oligonucleotides derived from INS intron 1. Sequences, length and corresponding G-scores of positive and negative controls (coloured in panel (B) are also shown. IAO21 represents the antisense olinucleotide that reduced *INS* intron 1 retention (315). **(B)** Mean fluorescence intensity of 80 µM ThT at 508 nm in the presence of the indicated oligonucleotides. Positive controls are in green, negative controls in blue. Controls for ThT binding to G-tract are in orange and ThT binding according to the number of Gs in purple. Tested oligos are in red. Error bars denote standard deviation from three independent fluorescence assays. Asterisks denote p-values ≤ 0.05 (*), ≤ 0.01 (**) or ≤ 0.001 (***). Oligos were prepared in water, at pH 7.2, and mean fluorescence of ThT alone was removed from all samples. Dashed horizontal line indicates the threshold for G4 formation, based on CLASP1 fluorescence intensity.

The data in Figure 14 showed a weak correlation of QGRS mapper scores and fluorescence intensity of ThT, suggesting that folding predictions should not be based solely on the presence or absence of G-runs. Although they are essential for G4 formation (393,396,397), other factors have an important role, including G-poor loop sequences (398–403).

Hence, folding propensity was examined by comparing of oligo signal enhancement to the background signal. The CLASP1 (negative control) signal (dashed horizontal line in Figure 14B) was taken as the threshold for G4 formation, i.e., any oligo showing higher fluorescence than CLASP1 was considered to be prone for G4 folding. Higher signals correspond to higher propensities/stabilities.

Assuming the fluorescence intensity of CLASP1 as the background, G-runs both upstream and downstream of the antisense IR target were prone to G4 formation (Figure 14B). Oligonucleotides Int 2 and 3, and CD3 and 4 showed a lower signal intensity, when compared to the WT and Int 1 and 7 or with either oligo derived from telomeres (Plas24 and 21 DNA) or oncogene promoter (c-myc) (Figure 14B). Int4 and the antisense oligo IAO21 displayed low fluorescence intensity similar to the background (Figure 14B), in agreement with zero QGRS mapper scores (Figure 14A). Int5 and 6 exhibited signal enhancements nearly as strong as the enhancements observed for WT and Int1 and 7, contradicting their G4 formation prediction (Table 17 in appendix B).

DCAF6, derived from the sequence of the DCAF6 human gene, was selected as a negative control due to the absence of G-runs and potential quadruplex formation. Yet, this oligo appeared to show a higher than background fluorescence signal (p-value = 0.1842), when compared to CLASP1 (Figure 14B).

Five 24 nt and two 23 nt oligos were used as controls for unspecific ThT binding. Three G-rich oligos containing different number of G-tracts (Gtr1-3) were used as negative controls for G4 formation, two oligos with 12 guanines (GA12 and GT12) that should not form intramolecular G4 and two oligos predicted to form G4 containing 4 G-runs each (GA8 and GT8). Fluorescence intensities of these seven oligos do not point towards unspecific ThT binding but they do not exclude it either (Figure 14B).

Four oligos (Int5 and 6, Gtr1 and 3), that should not form G4, contain at least two G-runs and show enhanced fluorescence in comparison to CLASP1, whilst DCAF6 and Gtr2 contain only one G-run, displaying slightly lower intensities (Figure 14). In fact, for these six oligos, fluorescence intensity increases as the number of G-runs increase, which could reflect the propensity to form intermolecular interactions. The same was not observed for the remaining tested oligos, indicating

that unspecific ThT binding to G-runs can be excluded. Therefore, Int5 and 6, Gtr1-3, and DCAF6 oligos potentially fold into intermolecular G4.

For a multiple comparison of data in Figure 14, the nonparametric Friedman test was performed since data were not normally distributed. The Friedman test (Table 22 in appendix B) showed that all positive controls and *INS* intron 1 derived oligos WT, Int1, 5, 6 and 7 were statistically significantly different ($p < 0.05$) from negative controls dT22 and CLASP1 (defines the background signal). WT, Int 1, 5, 6 and 7 means were not statistically significantly different ($p \geq 0.05$) from positive controls (c-myc, Plas24 and 21 DNA) or from GA8 and GA12. GA8 and GA12 were also statistically significantly different from negative controls. The remaining oligos were not significantly different from negative controls. Full Friedman test table results are shown in appendix B. These results proved that a region surrounding the antisense target for of *INS* intron 1 retention form G4 structures *in vitro* that are specifically identified by ThT.

Oligo CD3 was derived from a fragment of INS intron 1 that undergoes conformational hairpin/G4 transitions in equilibrium (315). A CC->UU mutation, disrupting the segment of four cytosines, induces a shift in structural equilibrium towards the G4 conformation (315), which is in agreement with a higher RFU of CD4 in comparison to CD3 (Figure 14B). Both signals from CD3 and CD4 are quite low, suggesting that these structures might be unstable.

The strong fluorescence signal shown by GA8 and GA12 (Figure 14B) may arise from the stabilization of alternative non-canonical conformations that specifically bind ThT, leading to a strong fluorescent enhancement. Low signal intensities in sequences containing stretches of thymines (GT8 and GT12 in Figure 14B) would form structures that do not bind ThT.

Int1, 6 and 7 oligos indicate that, of the G-runs surrounding the antisense target, those that are more distant, are more prone to form G4, as shown by their increased fluorescence in comparison to the other tested *INS* intron 1 derived oligos (Figure 14). This opens the questions as to whether the sequence of the antisense target could reduce G4 propensity of its flanking segments and if the antisense oligonucleotides could interfere with putative G4 formation *in vivo* or their interactions with ligands.

3.2.2.2 G4 formation in Int1 and Int7 derived oligos

To explore the putative influence of the antisense target on G4 propensity of flanking G-runs, a set of oligonucleotides extending Int1 and Int7 sequences by 2 nt were examined (Int1+ and Int7+ in Figure 15).

Analysis of oligos Int1+ and Int7+ for potentially-G4 forming elements by QGRS mapper indicated that G4 formation propensity should not significantly change by extension of Int1 and Int7 sequences (Figure 15A) (Table 17 in appendix B).

Figure 15 demonstrated that all extended oligos were still prone to G4 formation; nevertheless, a global decrease in fluorescence as the length increases was observed (see p-values for comparison analysis in Table 23 and Table 24 in appendix B. This is in agreement with previous results (Figure 14), where *INS* intron 1 Int2-4 oligos used for G4 formation screening showed very low fluorescence. Changes in fluorescence intensities as Int1 and 7 fragment sequences are extended contradicts what was expected by QGRS mapper scores, as observed in Figure 14.

Data from Int1+ passed both D'Agostino & Pearson and Shapiro-Wilk tests, hence a Gaussian distribution was assumed for the analysis of the differences between oligo means using ANOVA. No correction for multiple comparison was performed. Uncorrected Fisher's LSD results' summary is shown in Table 23 in appendix B. Int7+ data did not pass D'Agostino & Pearson and Shapiro-Wilk tests. Therefore, to determine whether the differences in the means are significant or not, a non-parametric Friedman test was performed, which is shown in Table 24 in appendix B.

Comparative analysis showed that nucleotides closer or within the antisense target region promote significant changes in G4 propensity, which is more pronounced for Int7+ oligos (Figure 15B). Inclusion of the AC dinucleotide in Int1 sequence was strongly disruptive for the formation of parallel G4, although, extending Int1 by 2, 4 or 6 nt re-establishes G4 formation propensity. Fluorescence intensity of Int1 is even surpassed if the eight-nucleotide ACCCCAGG (Figure 15A) sequence is included (Table 23 in appendix B). The signal decreases again when oligo is extended by including the antisense target fragment (Figure 15B)

Comparative analysis demonstrated that extending Int7 sequence by 2 nt did not produce a significant change in fluorescence intensity (Figure 15B), reflecting no change on G4 propensity. However, there seems to be a tendency for a stronger propensity of the 21 nt oligo (Int7+2) in comparison to the 19 nt (Int7), which may be due to assay's high variability. ThT fluorescence decreased once the 6-mer TCTGACGC is included in the extended Int7 sequence (Figure 15A), disrupting the parallel G4. Propensity for G4 formation is re-established, as in Int1+, by adding the CAGC segment and disrupted again when the GCCCCAGC fragment is included.

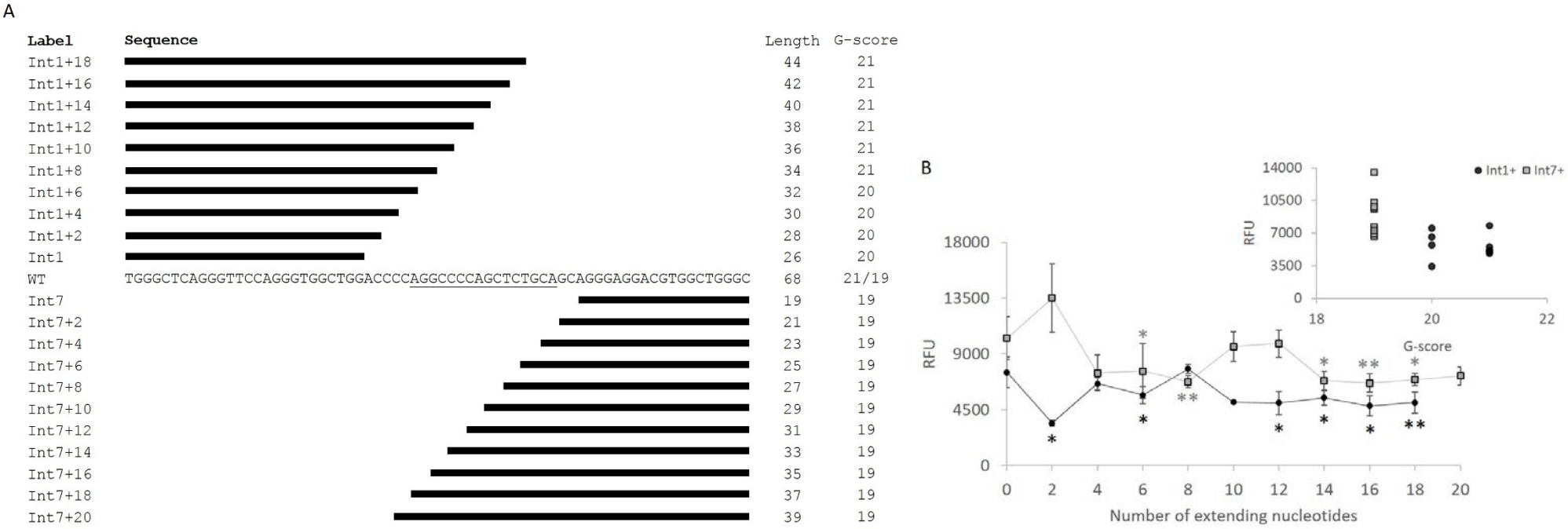

Figure 15 - Variation of ThT fluorescence in the presence of INS intron 1- derived Int1 and Int7 extended oligos (denoted as Int1+ and Int7+ in (B)).
(A) Schematics of tested oligos extending Int1 or Int7 sequences (black horizontal bars) into the antisense target sequence (underlined) Their predicted G-scores are to the right. **(B)** Mean fluorescence intensity, at 508 nm, of 80 µM ThT in the presence of extended oligos in (A). Error bars denote the standard deviation from three independent fluorescence assays. Asterisks denote p-values ≤ 0.05 (*) or ≤ 0.01 (**). The inset shows fluorescence dependence on G-score.

The inset in Figure 15B revealed that G4 propensity based on oligo length has no correlation with the G-score. Contradicting QGRS mapper prediction (Table 13A), the antisense target sequence, which reduces intron retention, reduced G4 propensity of both upstream and downstream G-runs, leading to significantly lower fluorescence intensities in longer oligos (Figure 15B). Therefore, by adding different nucleotide combinations in different lengths, the preferential G4 conformation will necessary be competing with other conformations, whether canonical or non-canonical.

Such an influence of the nucleotide sequence on different molecular structures in equilibrium is well established for nucleic acids (316,404,405). This raises the question whether the relative proportion of one nucleotide in sequences with constant lengths may dictate the transition between two or more conformations. To address this, the variation of ThT fluorescence intensity versus the number and percentage of each nucleotide within tested oligos was evaluated by determination of correspondent Pearson correlation coefficients of Int1+ and Int7+ oligos (Figure 16).

Pearson correlation coefficients (Figure 16B) indicated a global negative correlation between fluorescence intensity and either the total number or percentage of nucleotides in Int1+ and Int7+ sequences (Figure 16A), in agreement with the decreased fluorescence intensities as oligo length increases. The anti-sense target sequence is rich in cytosines that can pair with guanines to form a stable hairpin, hindering G4 formation and leading to the observed fluorescence loss (Figure 15B).

The exception was the positive correlation between the percentage of guanines (which is dependent on length) and ThT fluorescence, i.e., the total number of guanines is not enough per se to account for G4 propensity (Figure 16B and C). Not only guanines must be distributed in groups of 2 or more consecutive nucleotides (G-runs), as their relative amount has a strong impact on folding. Thereafter, along with the loop size and sequence, a minimum number of guanines in relation to oligo length seems to determine whether G4 is formed and stable.

A weak positive correlation between the relative amount of thymines in Int1+ oligos and fluorescence intensity was also observed (Figure 16B and C), which may arise from the fact that loops with T produce more stable complexes than loops with C and A, respectively (403). Further studies should be performed to corroborate this hypothesis.

Taken together, the data shows that the antisense target sequence for *INS* intron 1 retention has a negative effect on G4 propensity of both upstream and downstream G-runs and corroborate previous findings (400,403,406) that G4 formation is influenced by nt sequence surrounding G-runs.

A

	Int1+										WT	Int7+										
	0	2	4	6	8	10	12	14	16	18		0	2	4	6	8	10	12	14	16	18	20
#G	13	13	13	13	15	15	15	16	16	16	29	11	12	12	13	13	14	14	14	15	16	16
%G	50.0	46.4	43.3	40.6	44.1	41.7	39.5	40.0	38.1	36.4	42.6	57.9	57.1	52.2	52.0	48.1	48.3	45.2	42.2	42.9	43.2	41.0
#A	2	3	3	4	4	4	4	5	5	5	9.0	3	3	4	4	4	4	5	5	5	6	6
%A	7.7	10.7	10.0	12.5	11.8	11.1	10.5	12.5	11.9	11.4	13.2	15.8	14.3	17.4	16.0	14.8	13.8	16.1	15.2	14.3	16.2	15.4
#C	5	6	8	9	9	11	13	13	14	15	20	3	4	5	5	6	7	8	10	11	11	13
%C	19.2	21.4	26.7	28.1	26.5	30.6	34.2	32.5	33.3	34.1	29.4	15.8	19.0	21.7	20.0	22.2	24.1	25.8	30.3	31.4	29.7	33.3
#T	6	6	6	6	6	6	6	6	7	8	10	2	2	2	3	4	4	4	4	4	4	4
%T	23.1	21.4	20.0	18.8	17.6	16.7	15.8	15.0	16.7	18.2	14.7	10.5	9.5	8.7	12.0	14.8	13.8	12.9	12.1	11.4	10.8	10.3

B

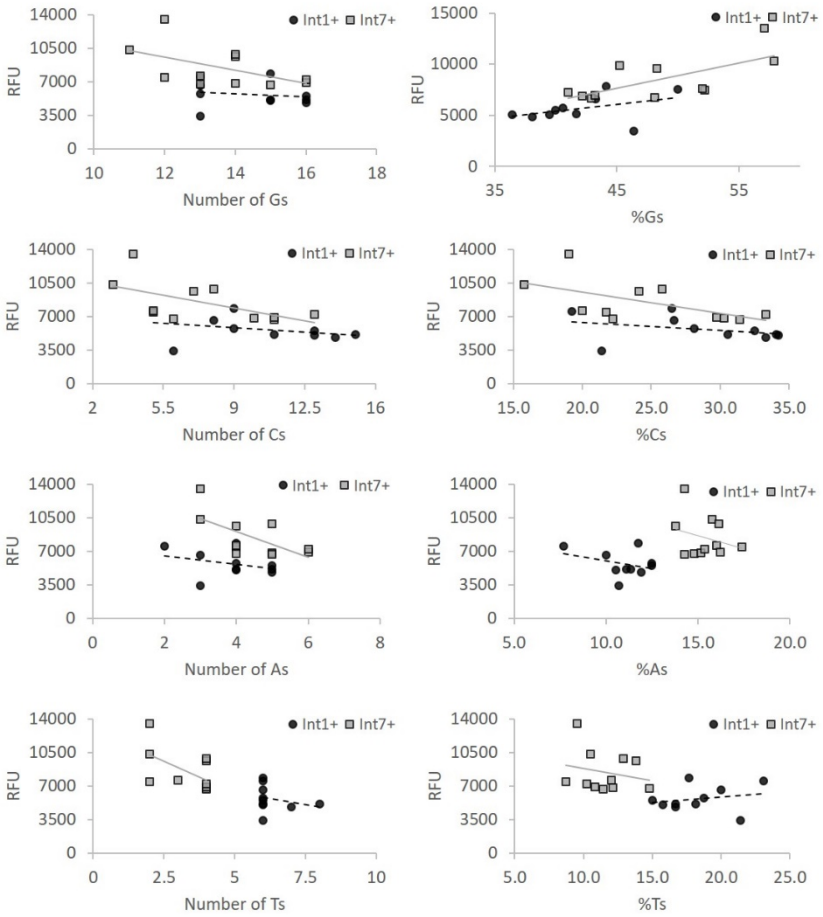

C

Pearson R correlation coefficient							
Int1+				Int7+			
%G	#G	%A	#A	%G	#G	%A	#A
0.401	-0.18	-0.34	-0.34	0.682	-0.53	-0.27	-0.64
%C	#C	%T	#T	%C	#C	%T	#T
-0.32	-0.33	0.218	-0.25	-0.59	-0.58	-0.22	-0.56

Figure 16 – G4 formation dependence upon nucleotide's number and percentage in Int1+ and Int7+ sequences.

(A) Total number and percentage of each nucleotide in the indicated oligos. Except for GT8, all oligos were not predicted as prone to form quadruplex by QGRS Mapper, as shown by the G-score on the right. **(B)** Correlation between the number / percentage of each nucleotide and ThT fluorescence intensity in Int1 and Int7 derived oligos. **(C)** Pearson correlation coefficients between each nucleotide *versus* fluorescence for Int1+ and Int7+ sequences.

3.2.2.3 G4 formation in the presence of monovalent cations and influence of pH on G4 formation

Following data showing G4 formation in INS intron 1 in vitro, the next objective was to address whether G4 propensity was maintained when solvent conditions changed, to approximate tested conditions to cellular environment.

Most of the studies on the role of mono- and divalent cations on G4 formation and stability show that several DNA sequences adopt the same or similar conformation in the presence of different cations (407,408); however, some oligonucleotides show slight conformational changes in the presence of different ions (409). In addition, cation binding to G4 complexes is not only dependent on the sequence itself (due to interactions between available oligos and the relevant cation) but on the cationic radius as well (410). At the same time, it has been demonstrated for different G-rich sequences that different cations induced and/or stabilize distinct G4 conformations (411–413). Some studies have also shown an influence of pH and solvent on G4 formation, structure and stability (413,414). This reveals the importance of characterizing G4 propensity in the presence of different cations, solvents and pH.

For this purpose, Int1 and Int7 were first selected to address whether G4 propensity, evaluated using ThT binding and fluorescence, changes when these oligos are incubated in buffer (lithium cacodylate - Licac) in comparison to G4 propensity in water. Two more conditions were tested: Licac supplemented with potassium chloride (KCl) or lithium chloride (LiCl). The pH of all solvents was adjusted to either 7.2 or 5.8 and both conditions were tested as well (Figure 17).

Two factors dictated the selection of these two oligos: both oligos represent the G-runs flanking the antisense target reducing *INS* intron 1 retention, form G4 structures *in vitro* (Figure 14B and Figure **15**B); and G4 propensity in both oligos was not influenced by the target sequence. In contrast, the two oligos have different properties: Int7 should not be able to fold into any type of secondary structure, other than G4 (as shown by secondary predictions in Table 17 in appendix B); Int1, on the other hand, is able to fold into G4 or form two independent hairpins (Table 17 in appendix B). The second hairpin of Int1, closer to the antisense target, contains a portion of the CD3 oligo, which was previously shown to be in equilibrium with G4 (315). The CD4 oligo is a derivation of CD3 by two C->U mutations that shifts the equilibrium towards G4formation. Hence, CD3 and CD4 were also included in G4 formation assays in buffer, with or without supplementation with monovalent cations. Plas24 and dT22 were the positive and negative controls, respectively.

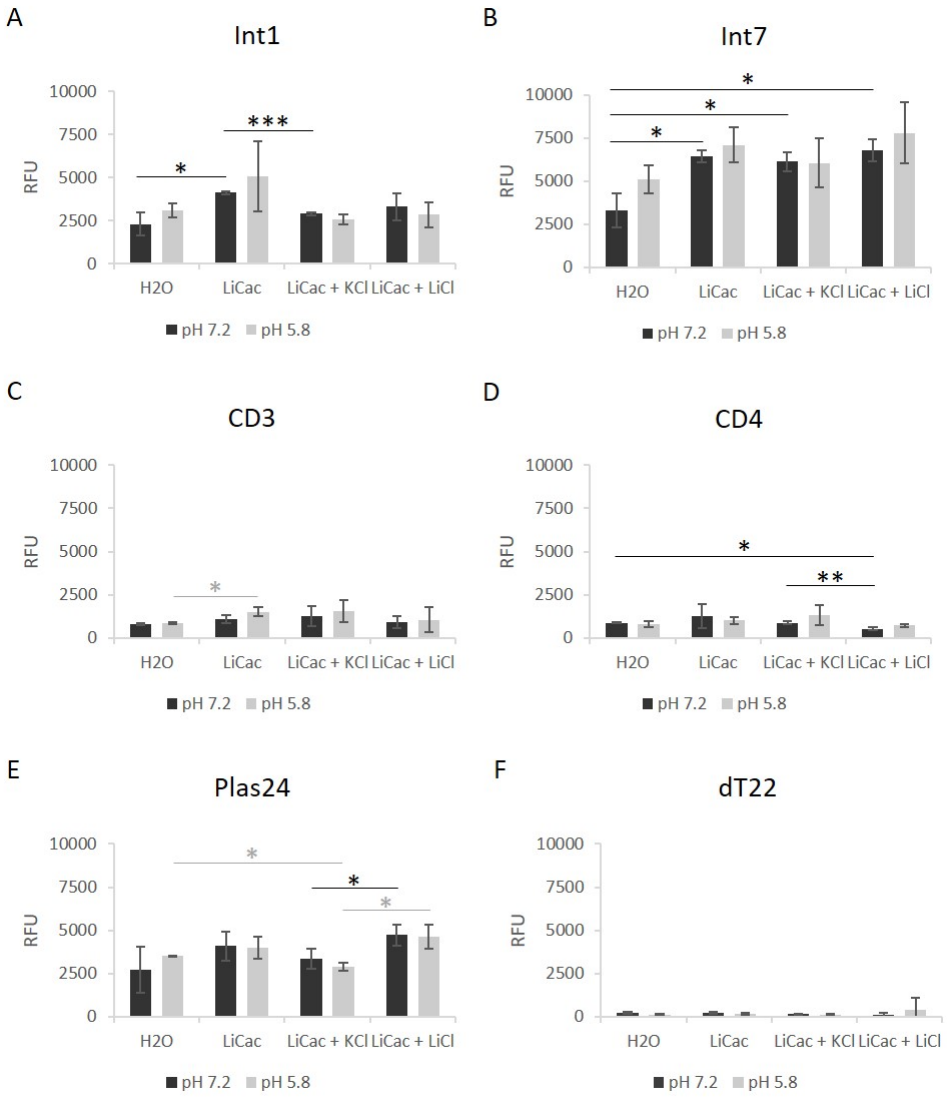

Figure 17 – ThT fluorescence intensity in the presence of DNA G4s formed in water or lithium cacodylate buffer (Licac), at neutral or acidic pH conditions.
Mean fluorescence intensity of DNA oligos in water or 50 mM Licac and in buffers supplemented with 5 mM KCl or 95 mM LiCL in the presence of Int1 **(A)**, Int7 **(B)**, CD3 **(C)**, CD4 **(D)**, a positive control (Plas24 - **E**) and a negative (dT22 - **F**) control. pH Samples were prepared in duplicate and pH was adjusted to 7.2 (black bars) or 5.8 (gray bars). Error bars denote standard deviations of three independent fluorescence assays. Asterisks denote p-values ≤ 0.05 (*), ≤ 0.01 (**) or ≤ 0.001 (***).

A comparative analysis using One-way ANOVA with the Greenhouse-Geisser correction/Tukey's multiple comparisons test show that there are no significant changes in fluorescence intensity of ThT in the presence of tested oligos (Table 25 and Table **26**), i.e., G4 structures formed in water are the same that are formed in buffer with or without salt supplementation, at either tested pH condition, for all tested oligos, as shown in Figure 17.

Data showed that global G4 propensity of *INS* intron 1 DNA derived oligos is not dependent on tested conditions, which indicates that guanine-guanine interactions leading to non-canonical

secondary structures in vitro are very stable *in vitro* and able to resist to changes in solvent conditions and pH (Figure 17).

This contradicts results from a comparative analysis, which indicated that Int7 is more prone to form G4 in Licac (alone or supplemented) than it is in water at pH 7.2, as shown by significantly lower fluorescence intensity in water (Figure 17B). Plas24 (Figure 17E), on its turn, displays high fluorescence in buffer supplemented with lithium chloride in comparison to buffer supplemented with potassium chloride, at both pH 7.2 and 5.8.

Thus, data in Figure 17 point towards the *in vitro* formation of very stable DNA G4 structures that are not easily disrupted by changes in experimental conditions. However, there is the potential for sequence-dependent minor structural alterations, since each oligo responds differently to solvent changes; as mentioned above, significant loos of fluorescence intensity may be observed once potassium is added to one oligo (Int1) (Figure 17A) while no changes were observed for other (Int7) (Figure 17B). Both Int1 and 7 did not show changes in fluorescence in the presence of either K or Li, while Plas24 displayed a significant increase in Li, when compared to K (Figure 17E).

3.2.2.4 Conclusions

Using ThT as a fluorescent probe for G4 formation of short synthetic DNA, it was shown that G-runs flanking the antisense target for *INS* intron 1 retention are prone to form G4 complexes. The propensity to form G4 *in vitro* was influenced by flanking nucleotides and those that extend into the sequence for promotion of intron 1 splicing, possibly accounting for an equilibrium of structural transitions between canonical secondary structures and G4.

G4 complexes of DNA oligos derived from INS intron 1 showed high resistance to changes in experimental conditions, indicating that these structures are very stable *in vitro*. G4 stability may correlate with altered mechanisms such as histone modification (415).

3.2.3 G4 formation in *INS* intron 1 RNA-derived oligos

In a comparative study of DNA and RNA G4 complexes (159) well-characterized sequences that fold into intramolecular G4 with different thermodynamic stabilities were analysed. The authors demonstrated that folding of G-rich sequences such as the human telomeric repeat, the *Oxytricha* telomeric repeat and the TBA aptamer is dependent on the solvent conditions and whether cations are present, along with cation-dependent conformational transitions (159). The same study also showed that RNA G4 assemblies are generally more stable than their DNA counterparts (398,416). Stability proved to be highly dependent on the sequence and loop size, as shown for other tested sequences (402,406). RNA G4s are more stable if their loops are shorter, while longer loops stabilize DNA G4 (159). Joachimi A, et al. (159) theorised that loop size-stability correlation may be due to a preference of RNAs to fold intro parallel topologies.

3.2.3.1 ThT fluorescence signal of INS-derived DNA and RNA counterparts

DNA G4s have been extensively studied and their structural conformations and properties are well defined and characterized (161,162,406,417,418). Structural features such as the type of interactions established (intra- or intermolecular), strand orientation, coordination of mono- and divalent cations, loop length and sequence, and association with other molecules, and their effect on G4 formation and stability have been described (157,400,419,420).

As in DNA, RNAs containing G-tracts can fold into G4 under physiological conditions, with stabilization factors and folding pathways similar to those observed for DNA G4s [372]. Although the absence of a complementary strand to hybridize with the RNA should increase chances for G4 assembly, the availability of C-tracts capable of hybridization with the G-tracts may interfere with the formation of four-stranded RNA structures [95].

To evaluate the capacity of RNA G-rich sequences to assemble into G4 structures, and compare ThT signal to DNA counterparts, their ThT fluorescence was evaluated at the same concentrations and in the same conditions. ThT fluorescence was consistently higher in the presence of short synthetic RNAs than their DNA counterparts (Figure 18), at the same concentration.

This could be explained by cooperative folding processes at high oligo concentrations, leading to more homogeneous populations (Figure 18C), which would reflect increased ThT binding. The same way, oligos at low concentrations (Figure 18A) may originate highly heterogenous populations leading to lower ThT fluorescence intensities due to ThT incapacity of binding to these structures. This would also apply to RNA G4 conformations, which have been determined to be generally more

homogeneous (all-parallel topology) (165,189). Thus, ThT fluorescence in the presence of RNA oligonucleotides would only be dependent on oligo concentration.

Data in Figure 18 corroborate previous findings, as shown by significant fluorescence intensities of ThT in the presence of RNA G4 with respect to DNA G4 (Table 27 in appendix B).

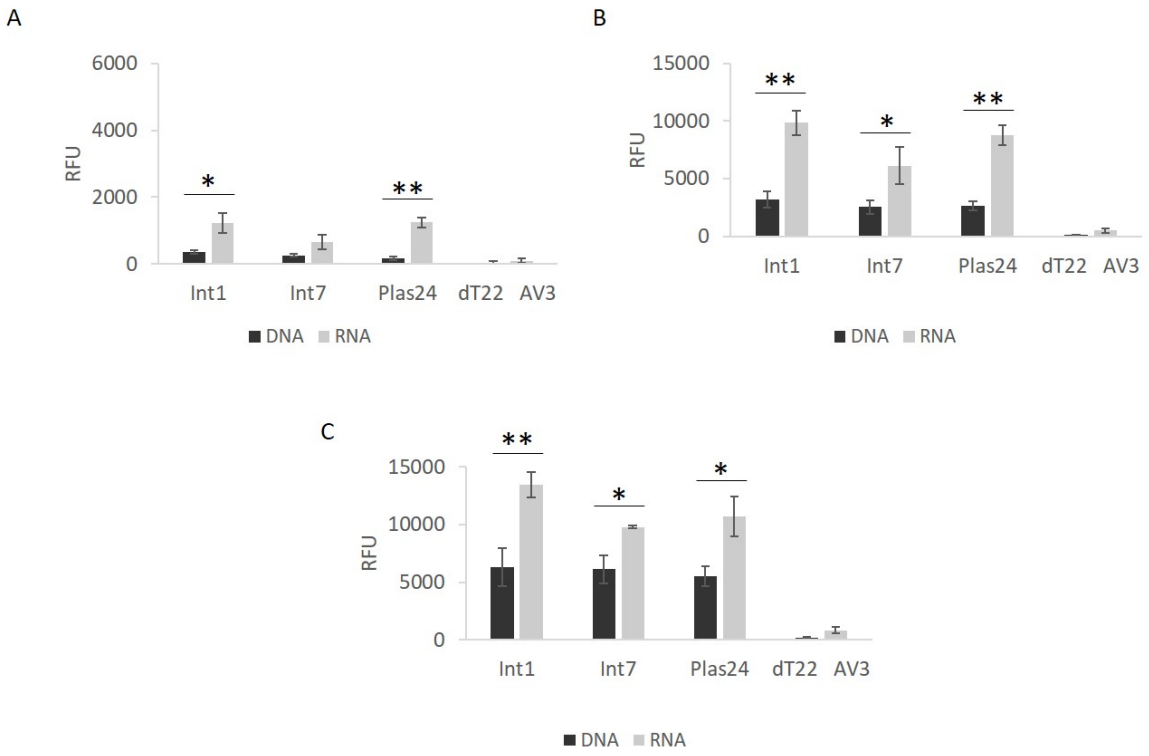

Figure 18 – ThT fluorescence intensity enhancement for DNA and RNA G4s.
Oligos were analysed at 2 **(A)**, 10 **(B)** and 20 **(C)** µM. DNA oligo dT22 and RNA oligo AV3 are shown as the negative controls for both DNA and RNA sequences. Error bars denote the standard deviation from three independent fluorescence assays. Asterisks denote p-values ≤ 0.05 (*) or ≤ 0.01 (**) (p-values for the Tukey's multiple comparison of the means of three oligo concentrations for each oligo is shown in Table 27 in appendix B).

Previous findings have shown that ThT preferentially binds parallel G4 (155,191) The topology variety of DNA G4s cannot be selectively and specifically discriminated by ThT since not all conformations bind this dye, hence the low fluorescence intensities. The all-parallel conformations of RNA G4s, in the other hand, allow a better discrimination of RNA G4 forming oligonucleotides, as shown by the inversion of signal intensities of Int1 and Int7 DNA sequences (Figure 15 and Figure **17**) to RNA sequences (Figure 18). This is in agreement with the mixture of hairpin/mixed G4 folding of Int1, which would produce lower fluorescence, in comparison to its RNA counterpart folding into all-parallel G4 and displaying higher signal. Differences between DNA and RNA Int7 would then reflect higher affinity of ThT to RNA structures than to DNA.

3.2.3.2 G4 formation screening in INS intron 1 RNA-derived oligos

Having established the preferential binding of ThT to RNA oligos due to their high propensity to form homogeneous populations of stable G4s, in comparison to DNA counterparts, the analysis of G4 formation using RNA oligos derived from INS intron 1 target region will provide further insights into non-canonical conformations folding relevance for intron retention.

For this purpose, a set of synthetic oligoribonucleotides was tested for propensity to fold into G4s using ThT. As for DNA oligos in Figure 14, RNA oligonucleotides were derived from the intronic G-rich segment surrounding the antisense target for enhancing splicing (315) (Figure 19A).

The selection of RNA sequences was based on: (1) previous data obtained by CD/NMR for *INS* intronic segments within the target sequence, (2) alteration of predicted structures upon mutation of nucleotides within and upstream of the antisense target segment and (3) the role of these mutations on IR (315). This selection included oligos Int1 and 7 as references for G4 formation, showed by fluorescence enhancement of DNA sequences using ThT (Figure 14). Int7 also corresponds to CD1 segment previously shown by far-UV CD and NMR to fold into parallel G4 (315). In Figure 19A, CD2 is a 20-mer derived from a region upstream of the antisense target showed by NMR the formation of stable hairpin structures (315). CD3 encompasses the 3'end of CD2 and the 5'end of the intron retention target (CD5), predicted to establish an equilibrium between two hairpins and G4 (315). The non-canonical conformation was stabilized by a CC -> UU mutation (oligo CD4) that demonstrated to reduce intron retention (315). Mut3, Mut5 and Mut6 were designed to explore how the G4/hairpin equilibrium affects intron splicing. Intron retention levels of their transcripts showed that elimination of the G4 increased intron retention (315), showing that INS intron splicing may be controlled by conformational transitions between canonical and non-canonical structures.

Figure 19B shows that the three intronic segments analysed here have different propensities to fold into G4 structures. In agreement with previous findings (315) and differential ThT fluorescence enhancement in the presence of overlapping DNA oligos derived *from* INS intron 1, G-rich sequences upstream and downstream of the antisense target are prone to parallel G4 formation. Int1/CD2 and Int7, display fluorescence enhancements significantly different from negative controls Av3 and double-stranded (ds) RNA oligo (Figure 19B). Int1 and 7 intensities do not differ, which indicates that these regions are equally prone to fold into non-canonical conformations. CD2 intensity, however, is significantly lower than both Int1 and 7. This may be explained by previous data (315) showing that CD2 segment preferentially acquires hairpin conformations in equilibrium. Hence, fluorescence enhancement in the presence of CD2 demonstrates that it can form parallel G4 structures, given adequate conditions (Figure 19B).

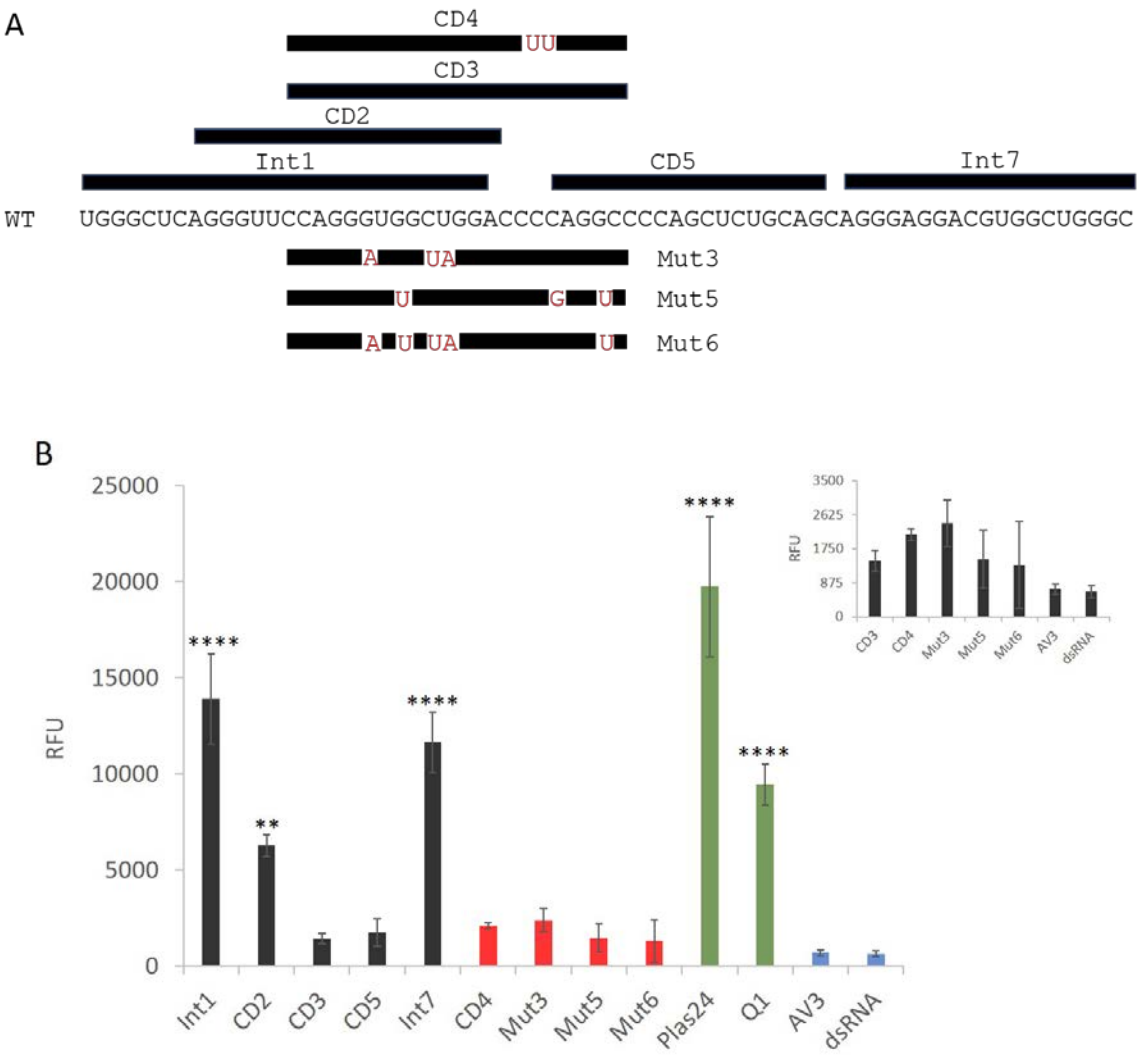

Figure 19 - Screening for G4 formation *in vitro* in *INS* intron 1.
(A) Schematics of tested RNA oligoribonucleotides derived from INS intron 1. Location of oligoribonucleotides is represented by horizontal black bars below and above the primary transcript (WT). Mutations (in red) that altered G4/hairpin equilibrium shown by NMR (CD4) and increased/reduced intron retention (Mut3, Mut5 and Mut6) (315). **(B)** Mean fluorescence intensity of 80 µM ThT at 508 nm in the presence of the indicated oligoribonucleotides. INS intron 1 derived oligos are in black, mutant oligos in red, positive controls in green and negative controls in blue. Error bars denote standard deviation from three independent fluorescence assays. Asterisks denote p-values ≤ 0.01 (**) or ≤ 0.0001 (****) determined using ANOVA, and indicate samples showing fluorescence intensities significantly higher than intensities of negative controls. Oligos were prepared in water, at pH 7.2, and mean fluorescence of ThT alone was removed from all samples. The inset shows fluorescence intensity of CD3 and its mutated versions at a different scale.

Differences found between Int1 and CD2 propensities may point towards an important role for the Gr1 (Figure 8) located upstream of the CD2 segment. As expected, CD5 oligo (Figure 19B) displays a very low fluorescence enhancement that is not significantly different from negative controls. CD3 signal is also very low, as shown for DNA derived oligos in Figure 14, in agreement to hairpin/G4 equilibria shown by NMR (315). This equilibrium seems to be shifted towards G4 by a CC -> UU mutation (315), as displayed by a slight fluorescence enhancement in the presence of CD4, when compared to CD3 signal (Figure 19B), although this is not statistically significant.

Fluorescence signals obtained for Mut3, Mut5 and Mu6 are not statistically different between each other (inset in Figure 19B). However, there seems to be a tendency for differential propensity for G4 formation. Mutations in Mut3 were designed to eliminate both hairpins present in CD3, maintaining G4; Mut5 retains folding for hairpin but quadruplex is abolished, while all three are prevented in Mut6 (315). Signal variations obtained for CD3 mutants (inset in Figure 19B) correspond structure predictions and correlate with IR data (315), which may indicate that hairpin/G4 equilibrium in this segment plays an important role in *INS* splicing. However, fluorescence enhancement of these RNA oligos is significantly lower in relation to signals of Int1, CD2 and Int7 (Figure 19B). Therefore, further insight regarding the influence of these mutations in G4 propensity will be discussed in chapter 3.2.3.5.

3.2.3.3 RNA G4 formation in the presence of monovalent cations and influence of pH

RNA oligos Int1 and 7 and CD3, were selected for G4 studies evaluating the influence of ions and pH (Figure 20). The two oligos target G-rich regions whose deletions led to an increase in IR. Oligos were treated as described before (Figure 17).

Fluorescence intensity of RNA oligos derived from *INS* intron 1 in water was generally higher from that in Licac supplemented with either KCl or LiCl, at both pH 7.2 and 5.8 (Figure 20). The exception was CD3, whose signal was more intense in Licac supplemented with potassium chloride than in water (Figure 20C). Fluorescence in water was not significantly different from fluorescence in Licac, except, once again, for CD3 (Table 28 and Table **29** in appendix B). This could be explained by a more homogeneous population of parallel G4 that is more stable in Licac than in water.

Decrease in signal intensity, in the light of previous observations that RNA G-tracts form all-parallel G4 complexes (159), might be due to conformational transitions/disruption of G4 induced by tested cations, which vary with the type of cation.

In the tested conditions, which were previously described (188,413) for the formation of both parallel and anti-parallel in several oligonucleotides, lithium chloride has a stronger disruptive effect upon parallel G4 than potassium in Int1 (Figure 20A) and CD3 (Figure 20C). The effect was opposite for Int7 (Figure 20B) and Plas24 (Figure 20D) oligonucleotides, although the treatment with the later oligo did not reach statistical significance (Table 28 and Table **29** in appendix B). Potassium seems to induce, and probably stabilize, the parallel conformation in CD3 (315), as shown by fluorescence enhancement in relation to water (Figure 20C).

In summary, significant changes in RFU upon addition of Li or K, or both ions, were observed. Changes in fluorescence intensity in different solvents points towards the presence of different conformations in water and in buffers. Propensity to form G4 tended to decrease in the presence of potassium or lithium. Reducing pH to acidic conditions did not indicate significant changes in structural conformations of any of tested oligos (Table 30 in appendix B).

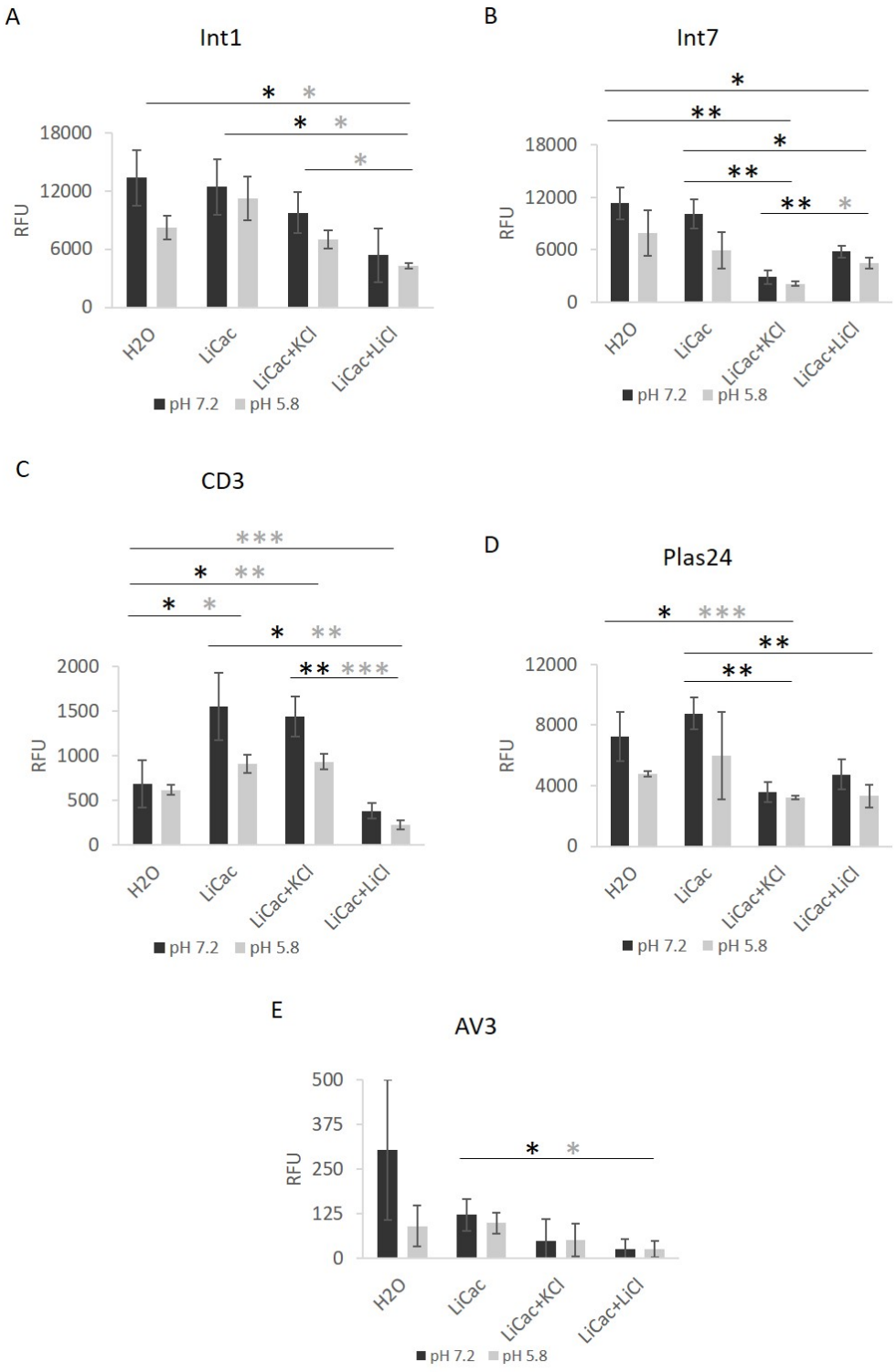

Figure 20 - ThT fluorescence intensity in the presence of RNA G4s formed in water or Licac, at neutral or acidic pH conditions.

Mean fluorescence intensity representative of RNA G4 folding propensity in water or 50 mM Licac and in buffers supplemented with 5 mM KCl or 95 mM LiCL in the presence of Int1 **(A)**, Int7 **(B)**, CD3 **(C)**, a positive control Plas24 **(D)** and a negative control AV3 **(E)**. Samples were prepared in duplicate and pH was adjusted to 7.2 (black bars) or 5.8 (gray bars). Error bars denote standard deviations of three independent fluorescence assays. Asterisks denote p-values ≤ 0.05 (*), ≤ 0.01 (**) or ≤ 0.001 (***).

3.2.3.4 G4 formation in the presence of mono- and divalent cations

Data in Figure 20 raised the question whether significant changes in RFU are concentration dependent and if they also reflect changes in major divalent ions. The same RNA oligonucleotides were incubated in Licac supplemented with increasing concentrations of potassium (Figure 21) or magnesium (Figure 22). A full summary of statistical comparative analysis that corroborate results in Figures 21-**23** is presented in Table 31-Table **33** in Appendix B.

Fluorescence intensity decreased as the concentration of both potassium and magnesium increased, for each tested oligo. Magnesium showed a stronger effect than potassium: much higher concentrations of potassium are required to disrupt equimolar amounts of the parallel G4 conformation (for $0 \leq KCl < 100$ mM, p-value > 0.05; for $0 \leq MgCl_2 < 1$ mM, p-value < 0.05) (Figures 21 and 22).

A significant decrease in signal intensity was observed for magnesium concentrations of 0.3 mM (Int1), 1 mM (Int7, CD3 and Plas24) (Figure 22), whilst a 10-100 fold in potassium concentrations was needed to get the same response: 30 mM (Int1), 1 mM (Int7 and Plas24) and 100 mM (CD3) (Figure 21). These results indicate that concentrations below 10 mM potassium or 0.3 mM magnesium are favourable for parallel G4 assembly *in vitro*. Higher ionic concentrations should then promote anti-parallel or mixed populations or prevent parallel G4 formation altogether.

If RNA G-rich sequences can only adopt all-parallel G4, as previously stated (159,212), these results suggest that *INS* intron 1 RNA derived oligos may not establish G-G interactions at *in vitro* conditions that mimic physiological ones (100-150 mM of potassium and 0.3-1 mM of magnesium).

Would, then, there be any possibility of G4 formation in the presence of both ions? Is potassium or magnesium affinity strong enough to reverse the effect of the other ion?

To address this, two concentrations (one low, allowing parallel G4 formation, and the highest concentration within physiological range, preventing folding) were selected for each cation and propensity for structural assembly was analysed in the presence of their combinations (Figure 23).

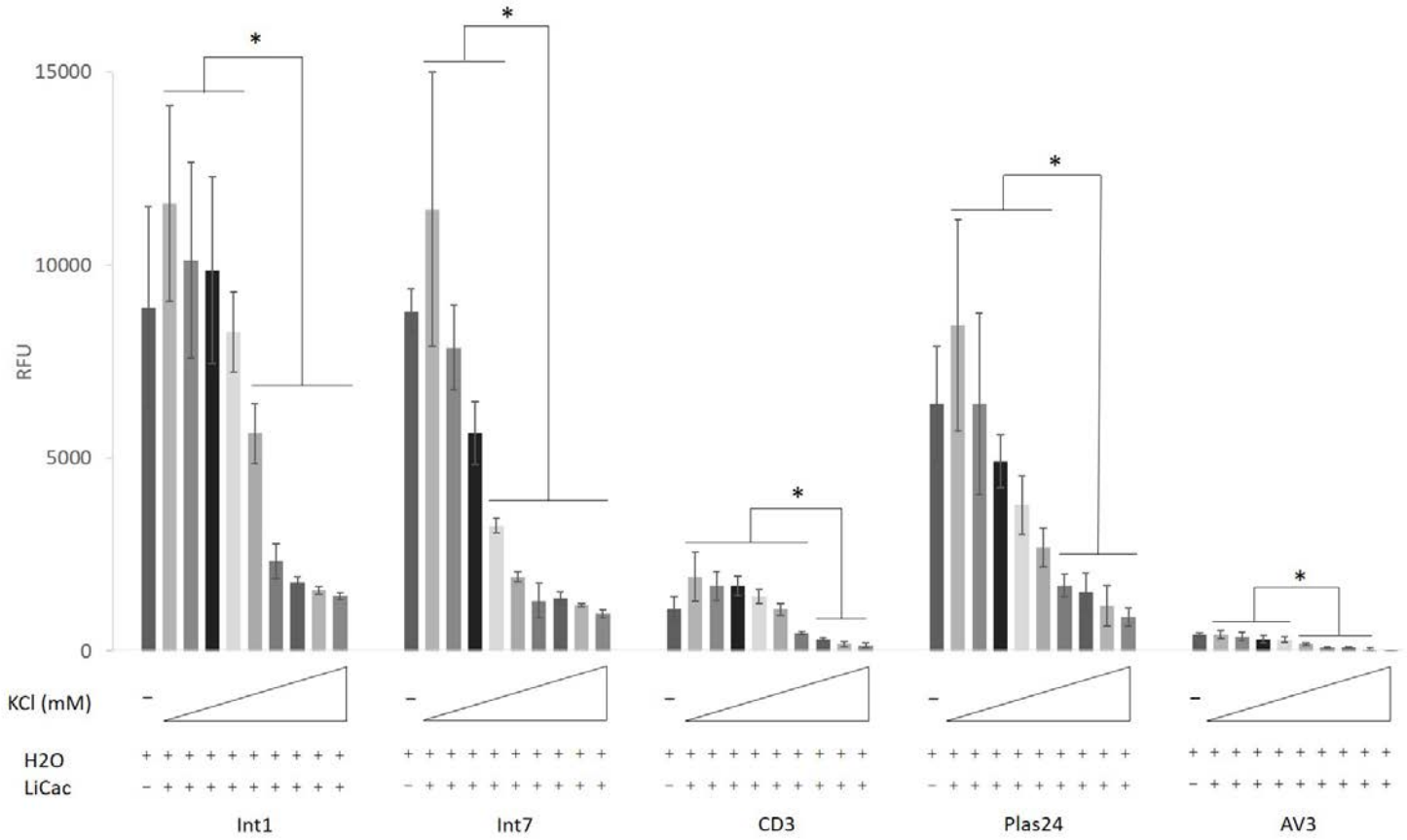

Figure 21 – Influence of KCl concentration on ThT fluorescence probing for RNA G4s.

Mean fluorescence intensity of *INS* intron 1-ThT complexes in the presence of increasing concentrations of KCl (0, 1, 3, 10, 30, 100, 150, 300 and 500 mM). Plas24 and AV3 are the positive and negative, respectively, G4 controls. The first columns show mean fluorescence intensity for G4 in water. Error bars denote the standard deviation from three independent fluorescence assays. Asterisks denote p-values ≤ 0.05 of Welch's-corrected unpaired t-tests comparing fluorescence intensities in the presence of consecutive cationic concentrations.

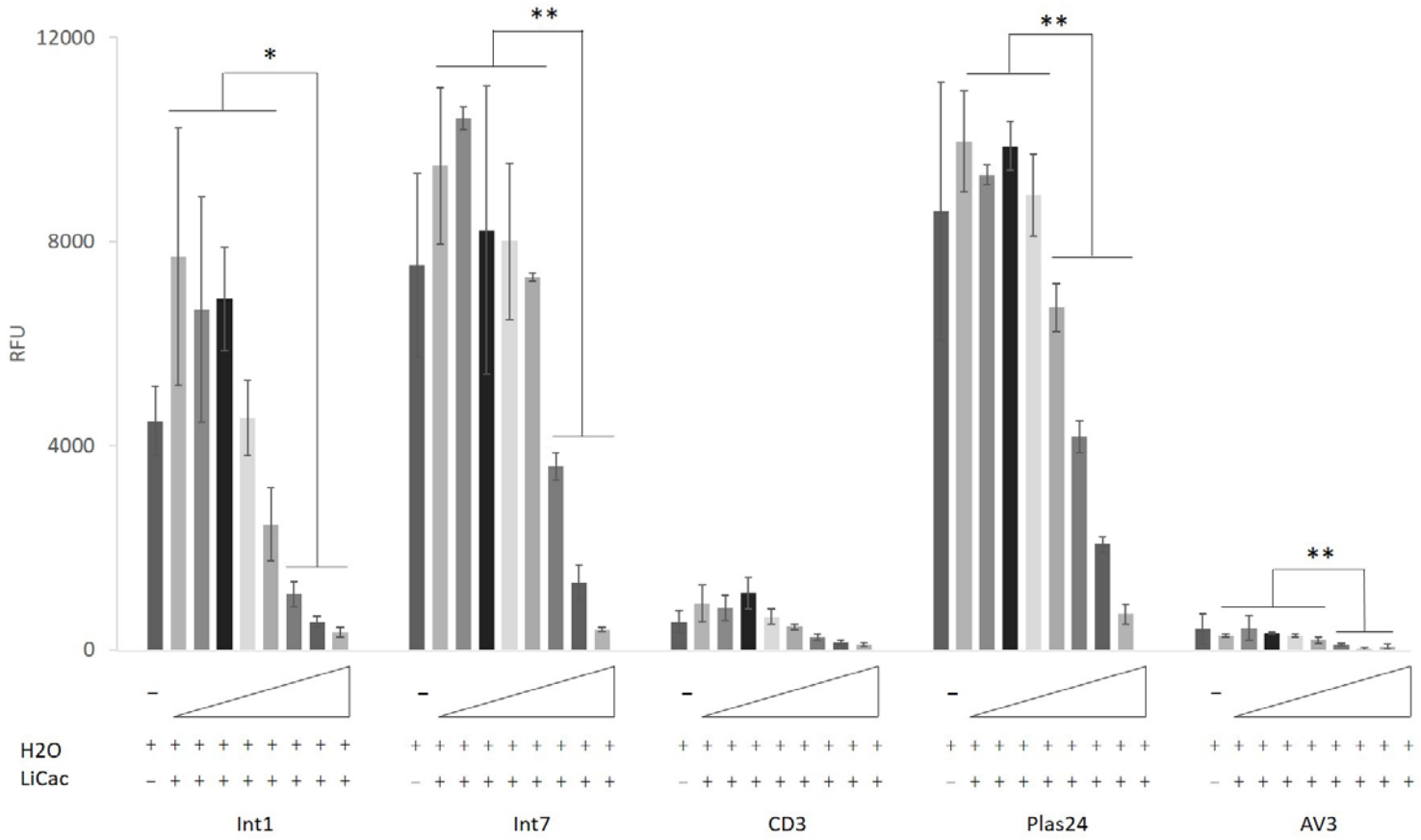

Figure 22 – Influence of $MgCl_2$ concentration on ThT fluorescence probing for RNA G4s.

Mean fluorescence intensity of INS intron 1 RNA derived oligos-ThT complexes in the presence of increasing concentrations of $MgCl_2$ (0, 0.01, 0.03, 0.1, 0.3, 1, 3 and 10 mM). Plas24 and AV3 are the positive and negative, respectively, G4 controls. Mean fluorescence intensity for G-quadruplex in water only is shown for comparison. Error bars denote the standard deviation from three independent fluorescence assays. Asterisks denote p-values ≤ 0.05 (*) or ≤ 0.01 (**) of Welch's-corrected unpaired t-tests comparing fluorescence intensities in the presence of consecutive cationic concentrations.

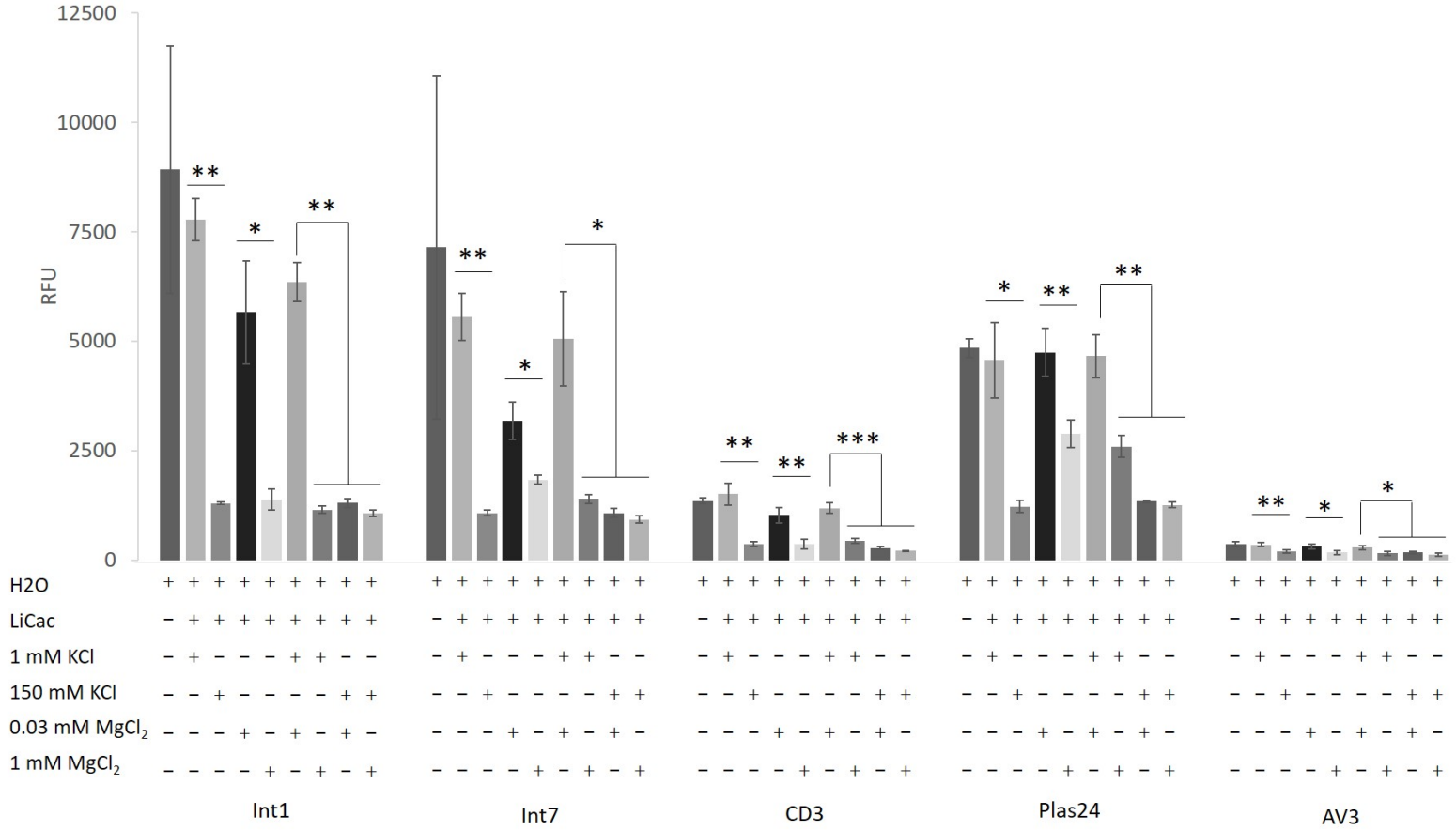

Figure 23 - Influence of combined KCl and $MgCl_2$ concentrations on ThT fluorescence probing for RNA G4s.

Mean fluorescence intensity of *INS* intron 1 RNA derived oligos-ThT complexes in the presence of combinations of KCl (1 and 150 mM) and $MgCl_2$ (0.03 and 1 mM). Plas24 and AV3 are the positive and negative controls for G4 formation. Mean fluorescence intensities for G4 in water and buffer only are shown for comparison. Error bars denote standard deviation from three independent fluorescence assays. Asterisks denote p-values ≤ 0.05 (*), ≤ 0.01 (**) or ≤ 0.001 (***) of Welch's-corrected unpaired t-tests comparing fluorescence intensities in the presence of low vs. high cationic concentrations or combinations of low and/or high ionic concentrations.

RNA oligonucleotides derived from *INS* intron 1 were prone to parallel G4 formation in the presence of low concentrations of either mono- or divalent cation (1 mM or 0.03 mM, respectively) (Figure 23), as previously shown (Figures 21 and **22**). G4 formation at low ionic strength was corroborated by significantly high fluorescence of derived oligos Int1 and 7, CD3 and positive control Plas24, in comparison to negative control AV3 (Table 33 in appendix B). A significant signal loss in the presence of physiologically relevant concentrations for both cations was also observed (150 mM or 1 mM) (Figure 23).

Intron 1 derived oligos in Figure 23 showed, however, lower propensity for G4 formation in the presence of lower magnesium concentrations than potassium. Addition of 1 mM of potassium to 0.03 mM of magnesium led to signal enhancement, producing a response similar to the one obtained for 1 mM potassium alone. Therefore, magnesium at 0.03 mM was not sufficient to induce G4 in the presence of 1 mM potassium. This might indicate replacement of magnesium ions within the structure for potassium (421) or simultaneous coordination of both cations, which have also been observed before (422). When at least one of the cations (K^+ or Mg^{2+}) was tested in physiological conditions there was a significant loss of signal intensity of all three intron 1 derived oligos, independently of the concentration of the second oligo (Mg^{2+} or K^+, respectively).

In summary, data showed that *INS* intron 1 RNA-derived oligos were not prone for G4 formation at both K^+ and Mg^{2+} physiological concentrations. Results also indicated that potassium has a stronger stabilizing effect on G4 formation than magnesium, for which lower concentrations are sufficient to promote equimolar conformational changes, in comparison to potassium.

3.2.3.5 Real-time G4 formation during *in vitro* transcription

Transcripts start adopting secondary structure as soon after transcription is initiated and RNA sequences are long enough to fold, in a process referred to as co-transcriptional folding (423). Nascent RNA transcripts adopt different canonical or non-canonical structure, such as stem, bulge, hairpin, loops, pseudoknot and G4, which can rearrange and interact with each other giving rise to a more complex tertiary structure (424). Adoption of these structures in pre-mRNA is modulated by the properties of RNA Pol II, such as the speed of elongation, site-specific pausing and co-transcriptional interactions with the nascent RNA and proteins (423). Therefore, nucleotides in the 5' region of the nascent RNA transcripts can establish transient canonical or non-canonical interactions, producing interchangeable structures that can unfold and refold during transcription (423).

Recently, Tamaki Endoh and co-workers (425) described a technique allowing monitoring of RNA G4s' co-transcriptional folding using fluorescent probes such as ThT. Applying the same technique, fluorescence signals of ThT were monitored throughout *in vitro* transcription of *INS* intron 1 templates (Figure 24).

DNA templates were selected from minigene constructs used in our previous IR study (315), where elimination of putative G4 forming G-runs, along with removal of cytosine runs, led to increased intron 1 retention. In the same study, removal of one hairpin segment upstream of the antisense target for *INS* intron 1 retention, along with the elimination of at least one C4 run within the same region improved intron 1 splicing (315).

DNA minigenes del5, Mut3, Mut5 and Mut 6 showed different IR levels, in comparison to WT (315). del5 was constructed by deleting a 13 nt segment containing two C4-runs from the WT intron 1 sequence, keeping putative G4 G-runs, which significantly decreased IR. To create Mut 3, two hairpin elements upstream of the C4-runs were eliminated and G4 integrity was kept, leading to a significant decrease in intron 1 retention. For Mut 5, both C4-runs were eliminated with C -> G mutations, along with the G-run in the position -7, relative to the first C4-run, which promoted a 4-fold enhancement in intron retention. In Mut 6 both G-run at -7 position and hairpin elements were altered, remaining the C4-runs unaltered, resulting in IR enhancement (Figure 24A) (315).

A

Oligo	Sequence[1]	G-score	IR (%)[1]
WT	GGGCUCAGGGUUCCAGGGUGGCUGGACCCCAGGCCCCAGCUCUGCAGCAGGGAGGACGUGGCUGGGC	21/19; 21	4
del5	GGGCUCAGGGUUCCAGGGUGGCUGG----------GCUCUGCAGCAGGGAGGACGUGGCUGGGC	41/19; 18	1
Mut 3	GGGCUCAGGGUUCCAGGAUGGUAGGACCCCAGGCCCCAGCUCUGCAGCAGGGAGGACGUGGCUGGGC	21/19; 21	2
Mut 5	GGGCUCAGGGUUCCAGGGUUGCUGGACCCGAGUCGCCAGCUCUGCAGCAGGGAGGACGUGGCUGGGC	20/19; 0	16
Mut 6	GGGCUCAGGGUUCCAGGAUUGUAGGACCCCAGUCCCCAGCUCUGCAGCAGGGAGGACGUGGCUGGGC	20/19; 0	8

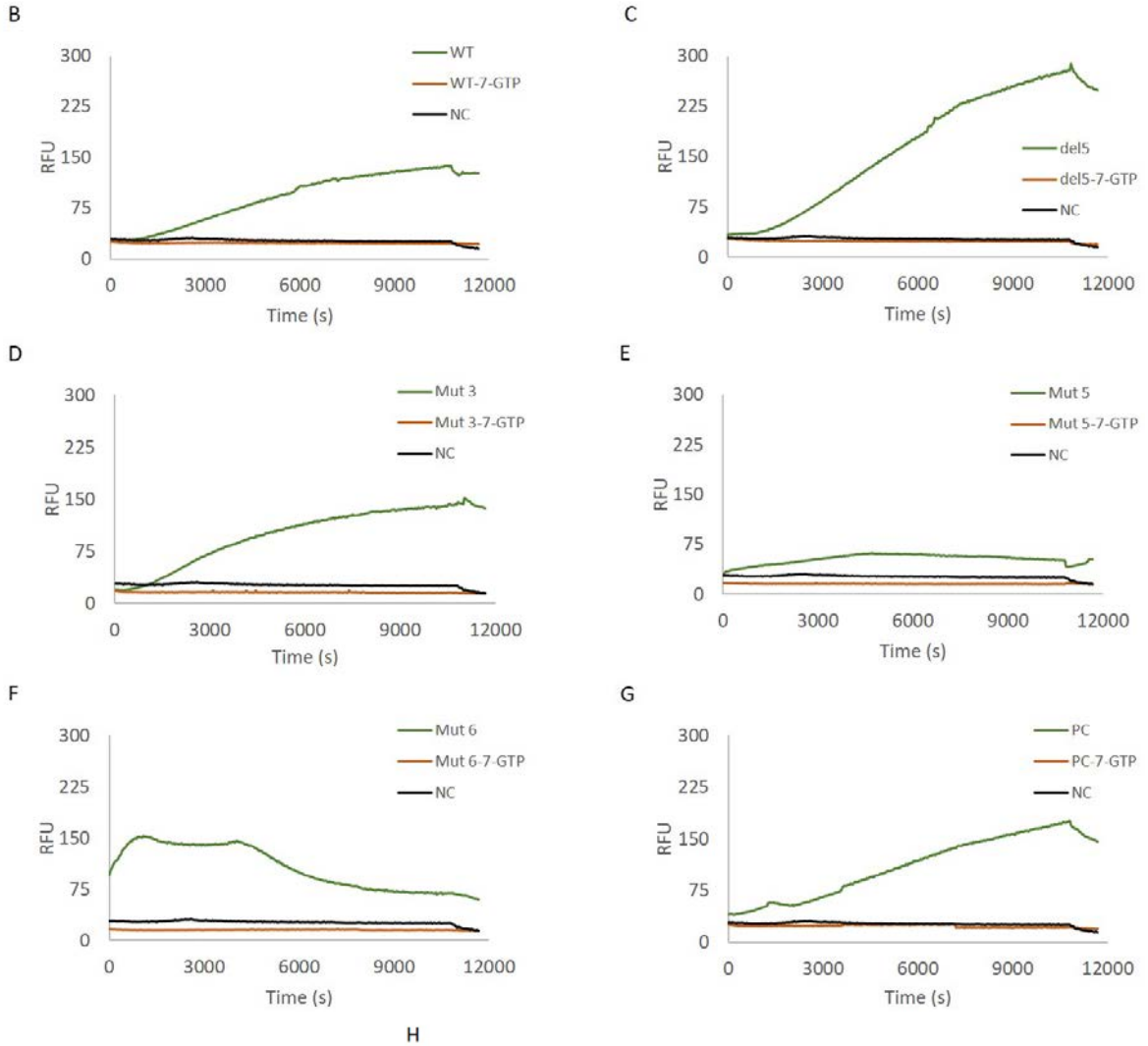

H

Pearson R correlation coefficient			
	3000s	6000s	9000s
IR %	-0.105	-0.838	-0.782

Figure 24 – Real-time monitoring of G4 formation during transcription using ThT.
(A) Sequences of RNA transcripts for intron retention modulation via G- and C4-runs elimination [1](315). Mutated nucleotides and deleted segment that alter folding propensity and intron retention levels are in yellow; antisense target sequence for increased intron splicing is in green. Mutations were designed to alter predicted G4s, stem loops and cytosines runs in underlined segments. G-scores of each transcript and altered segment. IRs are on the right. **(B-G)** Fluorescence intensity of ThT measured during transcription (10 800s) and for 900s after DNase addition to stop transcription of minigene sequences in (A). Their G4 formation was confirmed by comparing fluorescence intensities of native sequences (green lines) to transcripts where guanine was replaced by 7-GTP (orange lines) and to no template control (black lines). Sequence of the control (PC) for the transcription reaction, containing three putative G4 structures (predicted by QGRS mapper) is in Figure 33 in appendix A. **(H)** Pearson R correlation coefficients between three time-points and IR %.

The fluorescence signal of ThT was then measured during transcription of WT, del5, Mut 3, Mut 5 and Mut 6 constructs (Figure 24B), and a 1,380-bp runoff control transcript with three putative G4 forming segments (Figure 33 in appendix A).

To ensure that signal obtained during *in vitro* transcription was only due to binding of ThT to G4 structures, native structure of nascent transcripts was compared with co-transcriptional folding of 7-deazaguanine (7-GTP)-substituted RNA transcripts. 7-GTP is a guanosine ribonucleotide in which the N7 was substituted for a C, abolishing the possibility of Hoogsteen base pairing, while still permitting canonical base pairing. Therefore, by replacing all guanines by 7-GTP in the transcription reaction, G4 formation is prevented and ThT should not display significant fluorescence enhancements, although structures like stem-loops or hairpins are still adopted (222,224).

Although a single experiment was carried out with no measures of variability, a significant enhancement of ThT fluorescence during the three hours of transcription reaction for transcripts with GTP, compared to negative controls (without template – black lines in Figure 24B-G - and without reverse transcriptase – used during the assay but not shown) and the same transcripts in the presence of 7-GTP (Figure 24B) was observed.

ThT detection of non-canonical folding in tested transcripts correlates positively with G- and C-runs mutations/deletions for intron splicing modulation and negatively with IR levels (Figure 24H), i.e., nucleotide sequence alterations that decrease G4 propensity in the order del5 > mut 3 > WT > mut 6 > mut 5, shown to increase intron retention levels in reverse order (Figure 24A), bind ThT and produce signals as high as propensity increases. Hence, *INS* intron 1 segment transcribed *in vitro* are prone to G4 formation.

3.2.3.6 Visualization of intron 1 transcripts / oligos on polyacrylamide gels

The variety of canonical and non-canonical base pairings leading to the formation of stable secondary structures of a single sequence results in different conformations that may exist in equilibrium, some less stable than others. Most RNA oligonucleotides and transcripts analysed for G4 formation propensity were predicted by RNAstructure to form only one secondary structure with lowest free energy (Table 18 and Table **19**, respectively). This does not exclude, however, folding into less stable intermediate states that may co-exist in equilibrium with predicted structures and with non-canonical secondary structures such as G4.

Native polyacrylamide gels can separate structurally different conformations, i.e., two or more conformations of the same primary sequence, producing molecules of the same molecular weight, but with distinct mobility (426).

Synthetic RNA oligonucleotides and T7 transcripts were loaded onto a native polyacrylamide gel to visualize each putative sub-population (Figure 25).

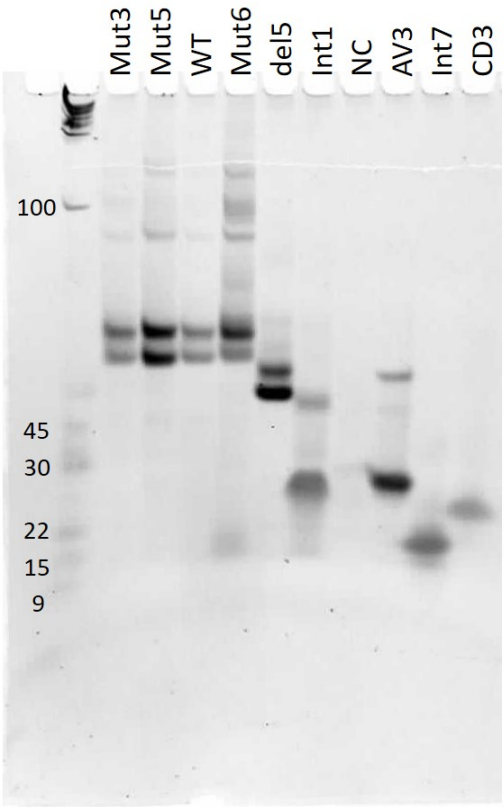

Figure 25 – Visualization of different native conformations in INS intron 1 RNA transcripts and RNA derived oligos.
Purified transcripts used for the real-time analysis of G4 formation during *in vitro* transcription and *INS*-derived RNA oligonucleotides (315) were loaded together with controls onto a native 6% polyacrylamide gel, stained with Gelred and visualized on a UV transilluminator. Transcripts and oligos were prepared in RNase-free water, which was loaded as a negative control (NC).

Longer RNA transcripts have a higher number of possible canonical Watson-Crick and non-canonical intramolecular interactions, with more possibilities for tertiary conformation interactions. This is consistent with five *INS* intron 1 transcripts, which showed two major bands that are likely to correspond to distinct conformations. Further slow migrating bands suggest the existence of heterogeneous populations, with the two conformations dominating RNA space (Figure 25).

Mut 3 and Mut 6 transcripts showed a higher proportion of the high molecular weight species in comparison to WT, whereas del5 displayed a lower proportion (Figure 25). These bands may represent different conformants with distinct free energies and secondary structures, as predicted

(Table 19). An increased fraction of high-mobility fraction of del5 could be related to a sharp decline of IR compared to the WT sequence, and/or, with a rapid accumulation of ThT fluorescents, indicative of G4 formation in vitro (Figure 25). In contrast, Mut 5 and Mut 6 variants led to an increase in IR (315). It is tempting to speculate that the two lower bands could reflect an equilibrium between two different conformations that regulate the efficiency of intron removal.

A subset of *INS* intron 1 RNA derived oligos showed two bands (exemplified by Int1 in Figure 25). This oligo showed the equilibrium between a hairpin structure and G4 *in vitro*, while Int7 mainly folded into parallel G4 (Table 18 in appendix B), as determined by CD (315). On the other hand, oligo CD3 displayed only one band, reflecting the presence of only one conformation (Figure 25), which most likely corresponds to the hairpin conformation showed by NMR (315), in agreement with low ThT fluorescence intensities observed in Figure 21Figure **23**.

In order to get a better understanding of structural conformants population of tested ribonucleotides, further analysis should be performed. Visualization of both *INS* transcripts and synthetic oligoribonucleotides (Figure 25) on a gel under denaturing conditions would provide additional insights towards the number of molecular species present, along with a more accurate estimation of their molecular weight. This would enable discrimination between different conformations adopted by the same RNA sequence that would show different migrating patterns under native conditions but run together in denaturing conditions, due to the lack of secondary/tertiary structures.

A denaturing gel would also allow to eliminate the presence of transcripts longer/shorter than expected. Staining the gel with G4 specific dyes, such as ThT, would permit determination on-site of whether G4 structures were formed and maintained on the gel, improving discrimination of molecular species population. Comparison of RNA migrating pattern under native and denaturing conditions would abolish any doubts arising from the fact that major bands in Figure 25 largely run at their size, suggesting that there may not be extensive intramolecular G4s under these conditions.

3.2.3.7 Conclusions

ThT fluorescence intensity was much higher in the presence of *INS* RNA oligos than in the presence of correspondent DNA sequences. This increase was concentration independent.

INS intron 1 RNA derived oligonucleotides showed more propensity for G4 formation in vitro in water than in tested buffers, except for oligo CD3 that showed the opposite. Reducing pH to acidic condition did not induce significant conformational changes in tested RNAs. However, RNA G4s

were shown to be highly susceptible to variations in cationic concentration. Conformational changes were induced by increasing concentrations of both potassium and/or magnesium, as shown by a decrease in fluorescence intensities in these conditions. It was also observed that higher concentrations of potassium than magnesium are required to produce similar conformational transitions.

The follow-up of ThT fluorescence during *in vitro* transcription indicated that G4 structures can be adopted while RNAs are synthesized, with putative differences between intron 1-derived transcription templates, potentially contributing to their distinct splicing outcome.

INS intron 1 RNA-derived oligo Int1 showed two bands that correlate with the equilibrium between hairpin and G4 structures and Int7 displayed a major high-mobility band that could reflect the high G4 propensity. The single band obtained for CD3 shows a single conformation, most likely hairpin, in agreement with the low ThT fluorescence displayed by this oligonucleotide.

Chapter 4: Identification of *INS* intron1-binding proteins

4.1 Identification and characterization of proteins binding to *INS* intron 1 antisense target region

Splicing is a complex process that can occur both co- or post-transcriptionally (105) and requires binding of many proteins to RNA to accurately remove introns from pre-mRNA. These auxiliary proteins interact with different *cis*-regulatory RNA elements and modulate splicing by either enhancing or inhibiting it (427).

4.1.1 Pull-down using *INS* intron 1 transcripts containing the antisense target and flanking G-runs

To gain insight into interactions between trans-acting factors and this intronic region (intron 1 nucleotides 36–61 and 78–93) (315) (Figure 26A) pull-down assay was carried out as a screening method for the identification of unknown molecular interactions (Figure 26B) (428). In this assay, HeLa nuclear extracts were incubated with RNA transcripts containing the antisense target region and after washing unbound HeLa proteins, RNA transcripts were loaded onto a gel and specific RNA-binding proteins were identified.

The majority of the splicing factors known to date have molecular weights comprised between 35 and 70 kDa. Pull-down assays were performed using a wild-type (WT) transcript of a portion of INS intron1 containing the antisense target for intron retention reduction and a second transcript from which the two C4-runs were deleted. Pull-down assays showed that either in the presence or absence of the antisense oligo IAO21 that promotes intron removal, the molecular weight of proteins that specifically bind to this intronic segment fall within the 35-70 kDa range, as shown by different band intensities marked with the pink rectangle in Figure 26B. The majority of the splicing factors known to date have molecular weights comprised between the referred range.

hnRNP F and H splicing factors have previously been shown to have an important role in INS pre-mRNA splicing. hnRNP F/H-depleted cells showed increased levels of intron retention when compared to non-depleted or overexpressing cells (100). Due to the highly G-rich nature of INS intron1 tested transcripts, the presence of these two proteins in the RNA pull-down assays was analysed by western blotting using hnRNP F/H specific antibodies. Specific antibodies against hnRNP E and the serine/arginine-rich splicing factor 2 (sc35) were also used to evaluate their binding to this intronic region. hnRNP E binds preferentially to poly(rC) regions (429) and sc35 interacts with purine-rich sequences (430,431).

Data showed that hnRNP F and hnRNP H1 specifically bound *INS* intron 1 transcripts, (Figure 26B and C). MS/MS analysis of excised gel fragments (pink box in Figure 26B) showed four proteins to specifically bind to either WT or del5 transcripts, as compared to beads and AV3 controls: hnRNP F, hnRNP H1 and H2, and SRSF6 (Table 34Table **36** in appendix B), corroborating western blot data.

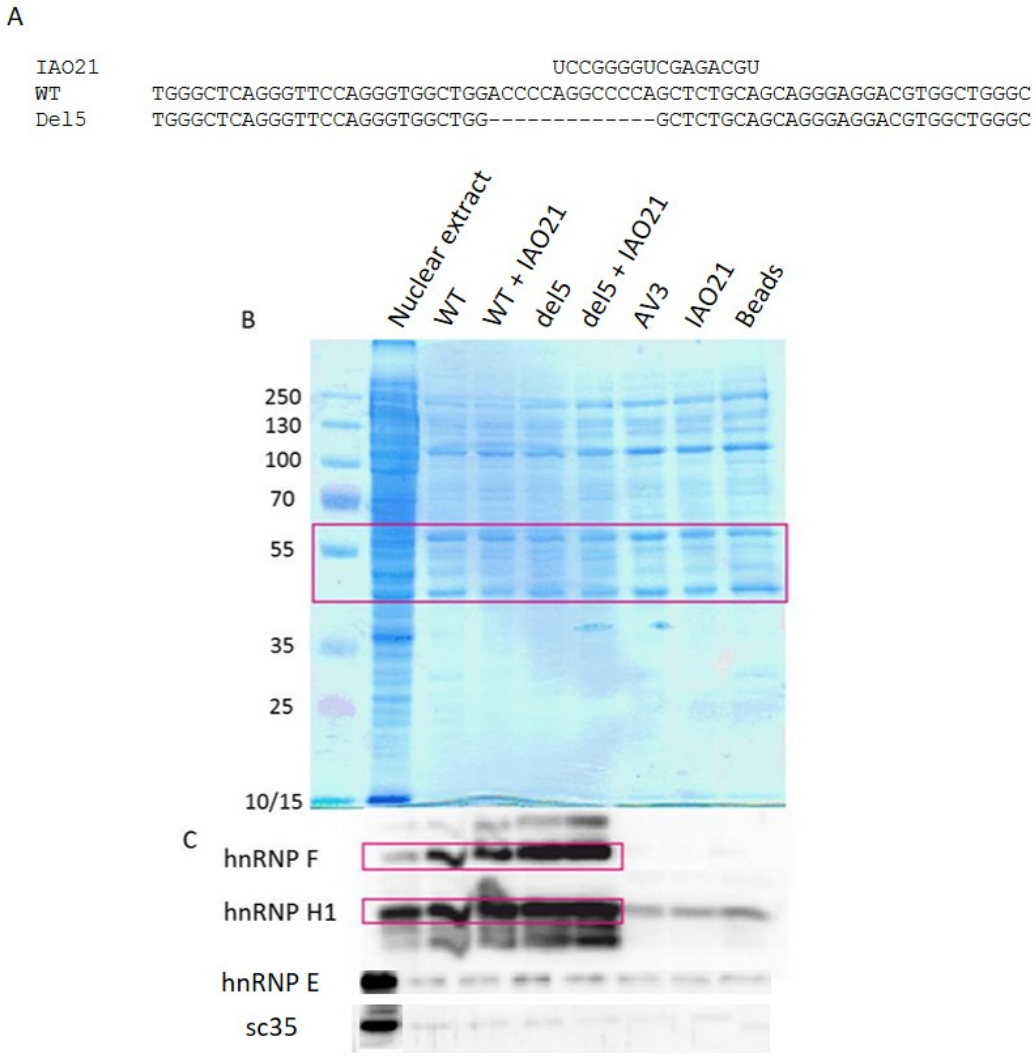

Figure 26 - Identification of proteins that interact with INS intron 1.
(A) Sequences of WT transcript containing the antisense target region, del 5 and IAO21.Construct del 5 (315) lacks a large portion of this target region. **(B)** SDS-PAGE analysis of the pull-down assay. Pink box indicates the gel section analysed by mass spectrometry; **(C)** Western Blot analysis of the pull-down assay with antibodies against common splicing factors, indicated to the left. Pink boxes highlight hnRNP F and H1 proteins, identified by correspondent antibodies.

hnRNP E and sc35 were not detected by western blotting neither MS/MS analysis. SRSF6 was not tested by western blot since this splicing factor has been mainly associated with alternative splicing of exons of MAPT/Tau and TNC pre-mRNAs (432–434). MS/MS data are shown in Tables 34-36 in appendix B.

hnRNP F and hnRNP H1 belong to the most abundant RNA-binding protein families (44). Although their binding specificities have been studied (17,49,53,55,56,435), exact structural correlates of their target regions are still poorly understood. These interactions may be exploited in the future in inviduals predisposed to T1DM.

To identify domains that specifically bind to *INS* intron 1, each RNA recognition motif (RRM) domain (Figure 34 in appendix A) from both hnRNP F and hnRNP H1 was separately cloned into the bacterial expression vector pET28a, which was followed by expression in BL21 and Rosetta bacterial strains, respectively, and product purification (Figure 27). Purified proteins will be further used in RNA-protein binding assays using ThT fluorescence changes in the presence of pre-formed G4s incubated with proteins to evaluate interactions.

4.1.2 Cloning, expression and purification of full-length hnNRP F/H1 and their individual RRM domains

Constructs carrying sequences that encode full-length hnRNPs F and H1 and individual RRMs were cloned as fusion proteins with an N-terminal His-tag and *Tobacco Etch Virus* endopeptidase (TEV) cleavage site (Figure 27A). TEV cleavage nucleotide sequence was introduced within the construct backbone to allow clean and direct ellution of recombinant proteins bound to the beads by protease cleavage.

A

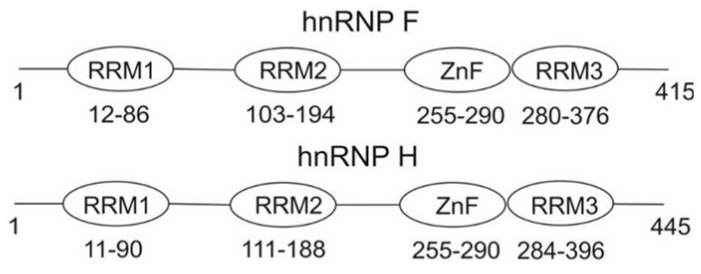

hnRNP F – 50.31 kDa
F RRM1 – 13.1 kDa
F RRM2 – 14.9 kDa
F RRM3 – 15.4 kDa
hnRNP H – 53.89 kDa
H RRM1 – 13.9 kDa
H RRM2 – 13.6 kDa
H RRM3 – 16.9 kDa

B

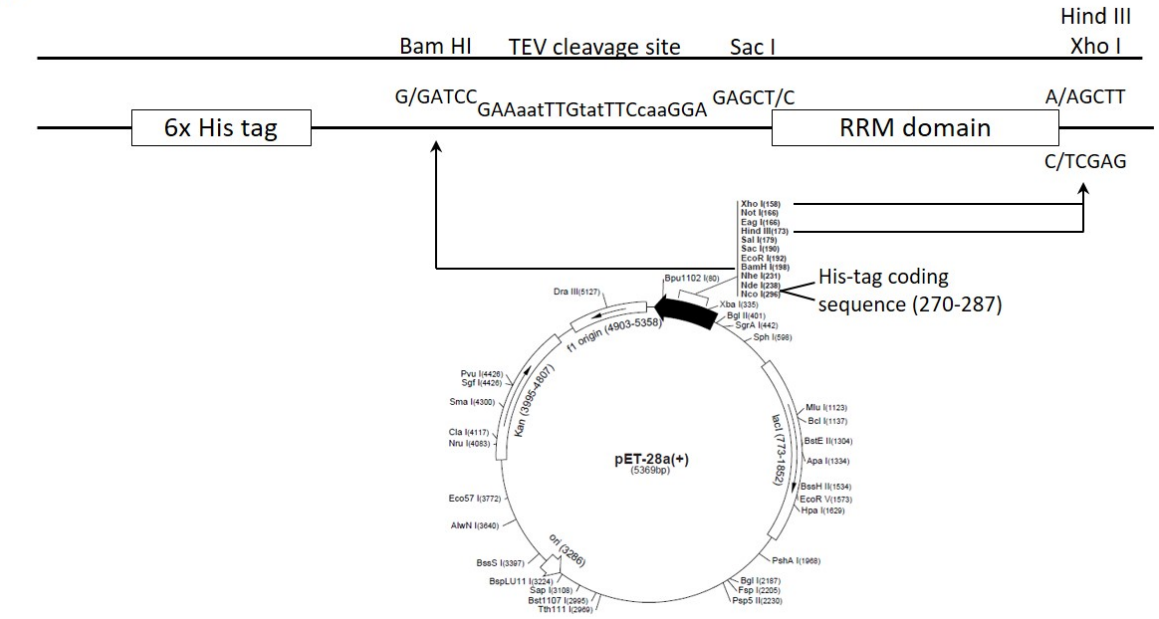

Figure 27 - Cloning of hnRNP RRM constructs.
(A) Schematic representation of hnRNP F and hnRNP H1 domain organization. Each protein is composed of three RRMs and a putative zinc-finger domain (ZnF). Number of aminoacids in each domain is indicated below; total number of aminoacids in each protein and the expected molecular weights of expressed recombinant proteins are to the right. **(B)** Diagram illustration of recombinant His-tagged RRM domains cloning into BamH I/Hind III (hnRNP F RRMs) or BamH I/Xho I (hnRNP H1 RRMs) pET28a cloning sites. The TEV protease cleavage site was introduced between His-tag and each domain to facilitate protein purification.

To confirm the accuracy of the inserts, the pET28a cloned vector was sequenced with vector specific forward and reverse primers (Table 5). Sanger sequencing was carried out by Source BioScience (Nottingham, United Kingdom) and the accuracy was verified. Mutation-free sequences were aligned to nucleotide sequences from Ensembl (hnRNP F: ENSG00000169813; hnRNP H1: ENSG00000169045). Nucleotide sequences are shown in Figure 35 in appendix A.

Recombinant proteins were first expressed in *Escherichia coli* BL21 (DE3). Full-length proteins showed a very low yield in this strain in comparison to RRM domains, hence their constructs were transformed into Rosetta™ 2, a host strain derived from BL21 that contains codons rarely used in *E. coli* facilitating expression of eukaryotic proteins.

Recombinant protein expression was induced with IPTG for 2 hours at 37°C, as shown by separation of whole cell lysates on 15% SDS-PAGE (**Figure 28**). All proteins were found in the soluble fraction, although RRM 1 to a lesser extent than RRM 2 or RRM 3 of both proteins. Nevertheless, a native His-tagged protein purification could be performed for all proteins.

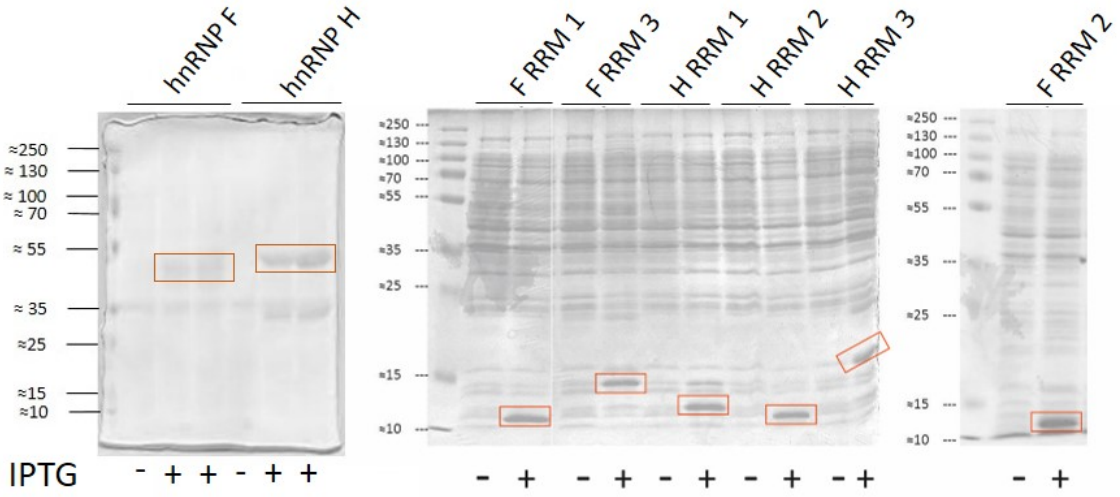

Figure 28 – Expression of recombinant hnRNP F, H1 and RRM constructs.
Expression of hnRNP F and H1 constructs in Rosetta and correspondent RRMs in BL21 (DE3). Whole cellular lysate before (-) and after (+) a two (and/or three)-hour-IPTG-induced expression; hnRNP F and H1 expression was analysed 2 and 3h after induction with IPTG; expression of RRMs was analysed 2h after induction. Protein marker on the left. Bands corresponding to expressed recombinant proteins are indicated by red boxes.

The first attempt was the elution of the recombinant proteins, bound to nickel beads through the His-tag, using a TEV protease, which cleaves the aminoacid sequence Glu-Asn-Leu-Tyr-Phe-Gln-Gly between underlined residues. Therefore, eluted proteins would only have an extra residue that would not alter their native structures. However, eluants recovered after TEV cleavage did not contain RRM domains or full-length proteins. Furthermore, analysis of the beads after elution revealed that recombinant proteins remained bound to these at any tested conditions, most likely due to conformational constraints for TEV access.

Purification of recombinant proteins (Figure 29A) was then performed by washing the nickel beads with increasing amounts of free imidazole, which competes with histidine imidazole ring, in order to remove unspecifically bound proteins to the beads, before recombinant hnRNP elution. Firstly,

three imidazole concentrations were used, 50 (two steps), 100 (three steps) and 250 mM (three steps). Full-length proteins and RRM domains were eluted from beads with 250 mM of free imidazole. However, many unspecifically bound proteins were co-eluted with recombinant hnRNP proteins and domains, showing that more washing steps were required. Therefore, on a second purification round, beads were washed twice, four times and three times with 50, 100 and 150 mM of free imidazole, respectively, before eluting recombinant proteins with 250 mM imidazole. Although purity yields increased, a great amount of recombinant proteins was lost in the third set of washes, which led to the conclusion that not only more washing steps were needed but that a fourth imidazole concentration would have to fit within the 50-100 mM range.

After several different combinations of increasing imidazole concentrations for the washing of bead-bound proteins, the one that produced higher recovery yields of recombinant proteins was as follows (described in methods section) (Figure 29A):

- Four washes with buffer supplemented with 20 mM of imidazole;
- Six times with buffer supplemented with 50 mM imidazole;
- Twice with buffer supplemented with 75 mM of imidazole;
- Twice with buffer supplemented with 100 mM of imidazole;
- Twice with buffer supplemented with 250 mM of elution buffer.

SDS-PAGE analysis showed that all recombinant proteins were successfully isolated with a high level of purity (red squares in Figure 29A). hnRNP F showed higher purity yields in fractions corresponding to wells 12-15, than hNRNP H1 in wells 16-20. Purity levels for each recombinant protein was cofirmed by Western blotting using anti-His tag and/or protein-specific antibodies (Figure 29B).

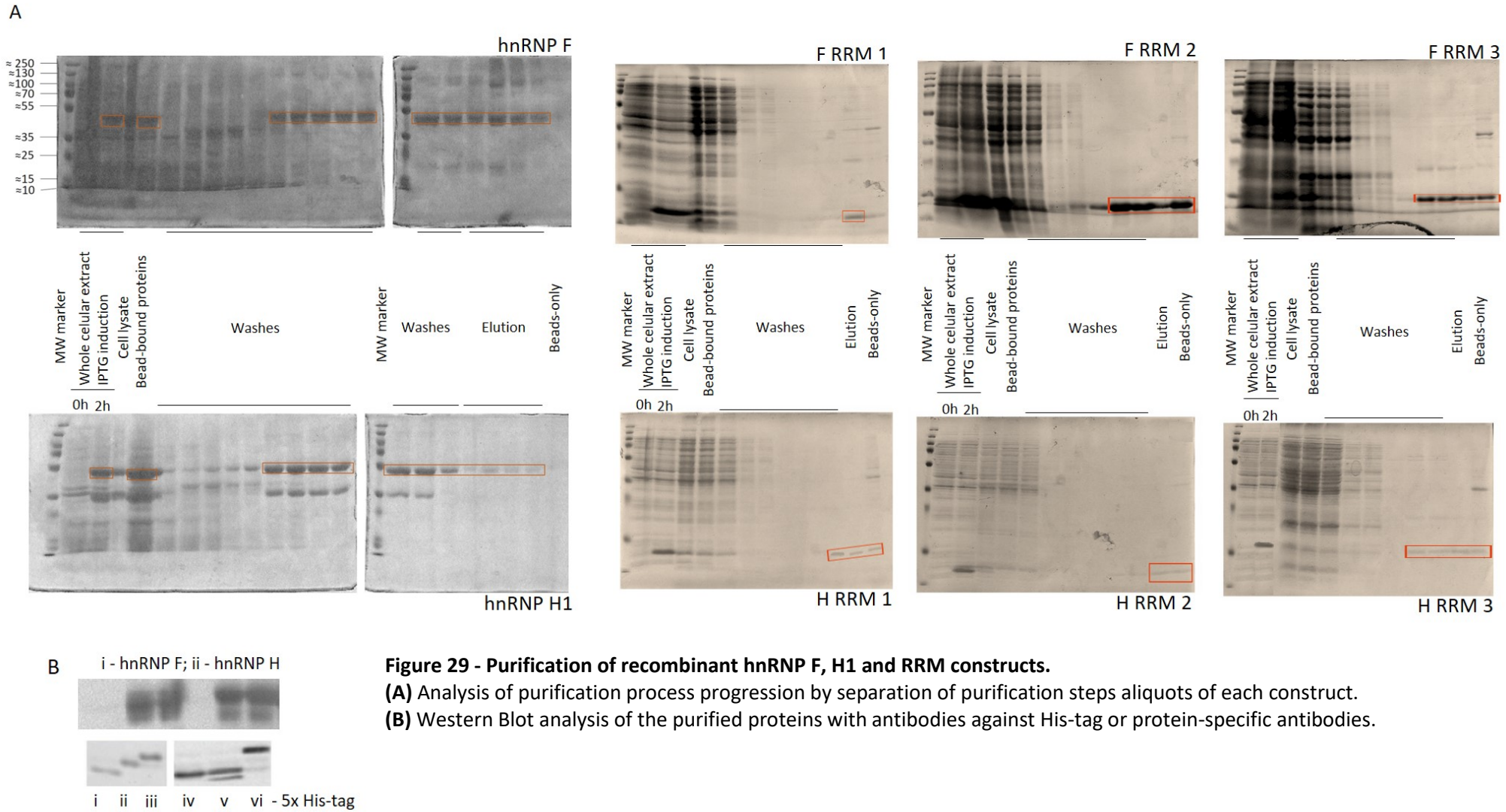

Figure 29 - Purification of recombinant hnRNP F, H1 and RRM constructs.
(A) Analysis of purification process progression by separation of purification steps aliquots of each construct.
(B) Western Blot analysis of the purified proteins with antibodies against His-tag or protein-specific antibodies.

4.1.2.1 Conclusions

hnRNPs F and H are well-characterized trans-acting factors that bind to G-rich intronic sequences; both proteins were identified by pull-down as *INS* intron 1-specific interacting proteins (Figure 26B and C).

All recombinant proteins were successfully isolated with a high level of purity (Figure 29A and B).

Binding of recombinant proteins could be shown through changes in ThT fluorescence intensity, as Dan Zhao and co-workers demonstrated for thrombin aptamer (TBA) (191), which would reflect protein binding to either G4 structures or single-stranded G-tracts.

To further explore interaction between this intronic segment with hnRNPs F and H and elucidate its role in *INS* spicing, techniques like CD and NMR in tested conditions should be used as to address G4 formation in RNA:protein complexes and electrophoretic mobility shift assay (EMSA) to address binding affinities. Characterization of protein binding in vitro should also be analysed using different RNA:protein ratios and in the presence of both hnRNPs and combining RRMs (several proteins, such as spliceosome proteins, require protein:protein interactions to function (436–440); these techniques would also elucidate whether hnRNPs F and H1 require other interactions or are able to bind to RNA via recognition of its sequence *per se*.

Chapter 5: Coupled *INS* 5'UTRs splicing and translation efficiency in higher primates

5.1 Translation efficiency of human and primate *INS* 5'UTRs

Comparative studies between species are very useful for our understanding of how evolutionary DNA sequence divergence influences susceptibility to diseases (441).

The 5'UTR of the *INS* gene (Figure 30B) had previously been sequenced in multiple primate species (100). This study showed that all intron 1 G-triplets were absolutely conserved in Great Apes and Old World Monkeys, which points towards their functional importance. The data also demonstrated a weakening of the 3'ss of intron 1 and associated increase in intron 1 retention in Homininae, which was accompanied by the acquisition of a uORF (Figure 30A) (100). This new uORF codes for a 3-amino acid peptide and diminishes translation, providing efficient means of regulating preproinsulin production in higher primates, possibly in response to their increasing reliance on carbohydrates in their diet, such as grain and honey (100,315).

5.1.1 Cloning

To study the role of additional uORFs in translation, the WT 5'UTRs of five primate species (*Homo sapiens, Pongo pygmeus, Macaca fuscata, Colobus angolensis* and *Semnopithecus entellus)* were cloned into the Firefly Luciferase expression vector. In addition, an a->g mutation, which inactivates the 3' splice site of intron 1 was introduced in some constructs to address the role of intron 1 splicing in translation efficiency (Figure 36 in appendix A).

Cloning involved PCR amplification of intended inserts, their purification, restriction digests and subcloning into vector pICtest2 (pIC) (Figure 30B). Sanger sequencing of resulting plasmids confirmed the presence of desired mutations and absence of PCR-introduced errors and that constructs were in frame with the Firefly Luciferase coding sequence (Figure 36 in appendix A).

5.1.2 Transfection efficiency

Preliminary transient transfections with these constructs, in a monocistronic vector, into HeLa cells confirmed that they were capable of expressing RNA products of predicted sizes and that the mutation prevented correct splicing of intron 1.

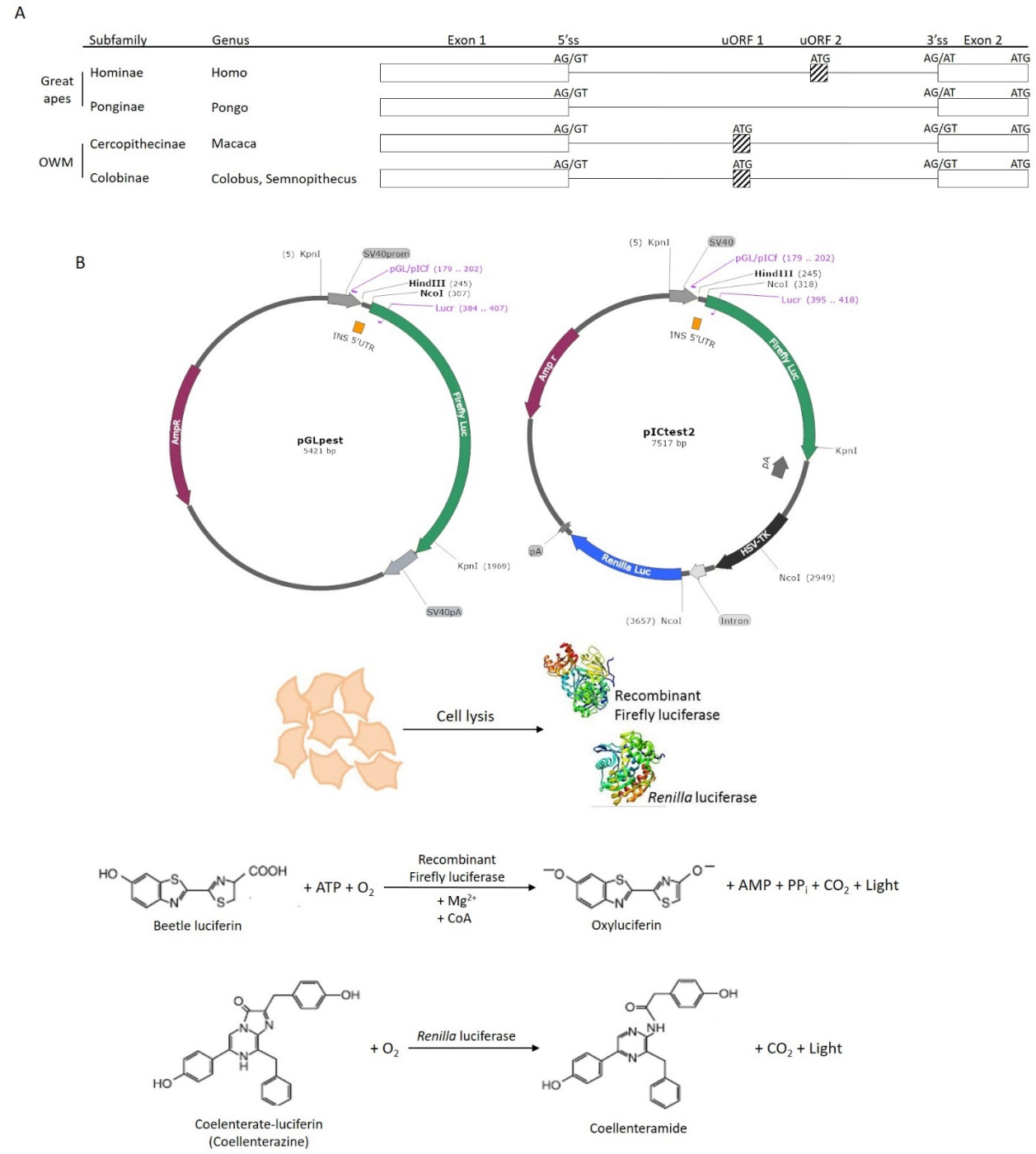

Figure 30 - Luciferase expression system used in the study of the role of additional uORFs in translation efficiency of five primate species.

(A) Schematic representation of uORFs in primates. With the exception of Pongo pygmeus (PP), retention of intron 1 leads to the acquisition of an in frame uORF; Homo sapiens (Hs) uORF, however is located downstream to the one in Old World Monkeys, Macaca fuscata (PM), Colobus angolensis (PC) and Semnopithecus entellus (PS) (adapted from reference (100)). **(B)** Luciferase assay procedure and chemical reactions used for the analysis of intron retention influence upon translation. Lysis of mammalian cells transfected with pGLpest.Seq or pICtest2 releases Firefly luciferase, which translation will be regulated by UTR constructs. Expression of *Renilla* luciferase allows determination of transfection efficiency.

To avoid co-transfection of separate reporter plasmids, a dual-luciferase, pIC, vector was used (442), where the luciferase *Renilla reniformis* (Rluc) acts as an internal control and is constitutively

translated from an AUG in the optimal Kozak consensus GCCACCAUGG (start codon is underlined). *INS* 5'UTRs were inserted in between *Simian virus* 40 (SV40) promoter and luciferase from the firefly (*Photinus pyralis*; Fluc), which allowed study of the translation efficiency of this protein (Figure 30C).

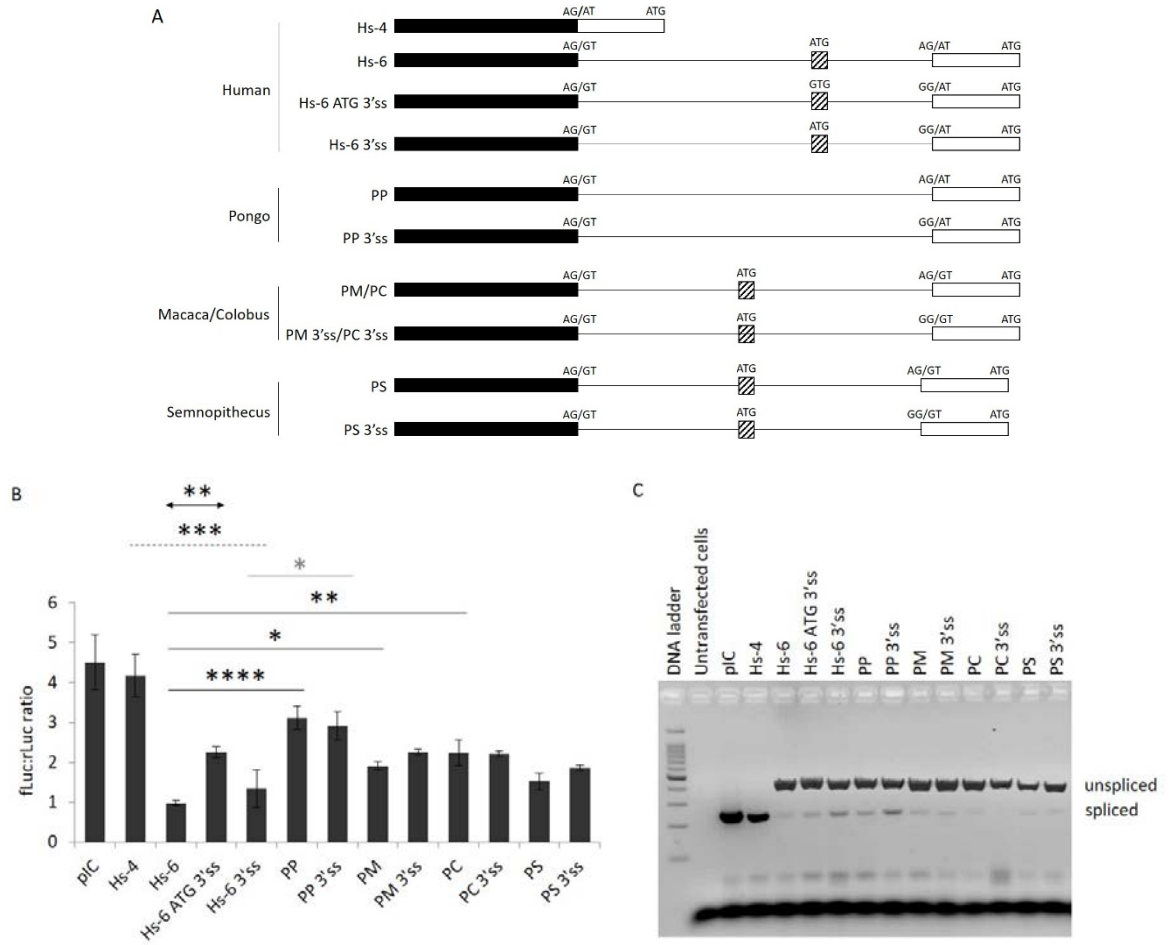

Figure 31 – Transfection efficiencies of human and primates *INS* 5'UTRs.
(A) Schematic representation of human and primates *INS* 5'UTR constructs in pICtest2 bicistronic vector. Exons 1 and 2 are shown as black and white boxes, respectively. Lines denote intron 1. uORFs are shown as dashed boxes. **(B)** Evaluation of WT and mutated 3'ss translation efficiency of *INS* 5'UTR from human, Pongo pygmeus and Old World Monkeys Macaca fuscata, Colobus angolensis and Semnopithecus entellus. Fourty-eight hours after transfection into HeLa cells, the activities of the two luciferases were measured. FLuc values were normalized to those for Rluc. Error bars denote standard deviation from four independent chemiluminescence assays in HeLa cells. Horizontal bars denote comparison of human vs. primate WT constructs (black), human vs. primate mutated 3'ss constructs (gray), intron-containing vs. exon-only human constructs (dashed) and WT vs. mutated uORF/3'ss in Hominidae (arrowed). Asterisks denote p-values ≤ 0.05 (*), ≤ 0.01 (**), ≤ 0.001 (***) or ≤ 0.0001 (****). **(C)** Splicing pattern of primates' *INS* 5'UTR constructs. Spliced- or retained-intron RNA isoforms, are indicated to the right. Amplification was with primers pICf and Lucr (Table 10 in materials and reagents).

The ratio between Firefly luciferase and Renilla luciferase chemiluminescence reflects variability in 5'UTR-dependent luciferase translation.

Insertion of *INS* 5'UTRs in pIC bicistronic vector had an inhibitory effect on luciferase expression in HeLa cells as compared to empty pIC, as shown by a significant decrease in Firefly luciferase chemiluminescence in constructs including *INS* intron 1 (Hs6 to PS 3'ss) (Figure 31A). A slight non-significant decrease of human construct containing only exon 1 and a portion of exon 2 (Hs4) in relation to pIC was observed, but a significantly higher intensity (ratio), when compared to remaining human constructs (Table 37 in appendix B), suggests that removal of intron 1 is essential for high-level translation levels of luciferase in HeLa cells (Figure 31A). Lower signal intensities therefore indicate low levels of intron splicing. *INS* intron 1 has a weak 3'ss (100), thus high levels of unspliced RNA products were expected, as observed in Figure 31B.

The increased intensity of Hs6 ATG 3'ss in comparison to Hs6 (Figure 31B) may be due to the elimination of the uORF in intron 1 that leads to the production of a 3-aa peptide if intron 1 is retained. Hence, in this construct, even if levels of RNA spliced products are not higher than in Hs6, the canonical start codon in exon 2 may still be used and luciferase is normally translated. However, levels of spliced products in Hs6 ATG 3'ss showed to be slightly higher than in Hs6 (Figure 31C), in agreement with previous findings (100) that showed high levels of mRNA proinsulin secretion in reports lacking the short uORF.

Hs6 3'ss construct was designed with the purpose of increasing intron retention levels, in relation to Hs6 construct, by mutation of the A->G mutation in the 3'ss (Figure 36 in appendix A). Expectedly, this would lead to enhanced use of the uORF within intron 1, which would render decreased luciferase expression levels. However, the opposite was observed, and luciferase activity tends to be lower expression for the WT construct (Hs6) (Figure 31B). Luciferase expression levels were corroborated by the apparent presence of high levels of spliced products of the Hs6 3'ss construct than of Hs6 (Figure 31C).

Quantification of reporter mRNA levels in transfected cells would elucidate on the correlation between differences in luciferase expression and splicing levels. In particular, it would be possible to ascertain if lower translation is due to mRNA degradation. This would help addressing the question on whether increased IR, caused by disruption of the 3'ss, could lead to a concentration of mRNA degradation machinery around intron-retained transcripts, leaving room for more translational cycles of normally spliced transcripts. The odd phenomenon that splicing appears to be enhanced when the 3'ss is mutated would, thus, simply reflect levels of transcripts with longer life-times than the Hs6 ones.

Luciferase translations in remaining WT primates showed as significantly higher than human WT in a multiple comparative analysis, which most likely correlates with an evolutionary relaxation of intron 1 3'ss in human *INS* (100).

Comparative analysis using unpaired t tests did not show significant changes in luciferase translation with the elimination of intron 1 3'ss with relation to WT 5'UTRs in either *Pongo pygmeus* (PP) or any of the Old World Monkeys (PM, PC and PS) (Table 37 in appendix B). However, the data indicates a slight tendency for increased translation for PM and PS 5'UTRs (Figure 31A), which might correlate with lower levels of spliced products in mutated 5'UTRs (Figure 31B) and activation of the in frame uORF (Figure 30A). The absence of an uORF in *Pongo pygmeus* (PP) would, thus, be associated with the slight but not significant decrease in luciferase levels in this species. Nevertheless, this does not explain the increased levels of spliced products in PP 3'ss (Figure 31B).

Alternatively, translation levels higher than expected may arise from the use of in frame non-canonical initiation codons.

IR in 5' UTRs often leads to the introduction of upstream start codons (99). The most efficiently used are the ATG start codons, however, translation may also start at alternative start codons, such as ACG, CTG, ATC, ATT, ATA, GTG, TTG, AAG OR AGG (317,443). In a recent study (317), translation initiation from non-canonical ATG codons was demonstrated to occur in 42 human genes, resulting in N-terminal extensions of the encoded proteins. The use of different codons in 5'UTRs may indicate an alternative regulation of translation initiation (317). In the *INS* gene, the increased retention of intron 1 in individuals carrying the A allele at rs689 as compared to T allele leads to a higher fraction of transcripts with the canonical initiation codon, which is out-of-frame and curtails preproinsulin translation (100).

Figure 37 in appendix B shows a distribution of strong and weak non-canonical start codons that are in or out of frame relative to the main *INS* open reading frame. *INS* 5'UTR has 40 potential non-canonical initiation codons, from which 16 are in frame with the main ATG initiation codon. Twelve out of the sixteen in frame codons have a good Kozak context and four are in a poor Kozak context. From the 24 in a different reading frame, 17 are in a good Kozak context and 7 in a poor. Statistical analysis between the frequency of non-ATG initiation codons grouped according to their predicted translation efficiency (443), and correspondent reading frame (relative to the main open reading frame initiated by ATG), indicated that codon distribution was not associated with any particular reading frame (p value = 0.1965) (Figure 37 in appendix A). These results may indicate that usage of alternative start codons in 5'UTRs may depend upon their translation efficiency and surrounding context, playing an important role in regulation of translation. Alterations to the Kozak context and/or elimination of alternative start codons in transcripts with retained introns may elucidate the role of upstream open reading frames in disease.

5.1.3 Conclusions

Translation of firefly luciferase is more efficient in constructs that do not contain human *INS* intron 1 sequence, in comparison to remaining human constructs. This suggests that removal of intron 1 is essential for high-level luciferase translation in HeLa cells. Removal of the uORF in human intron1-retained transcripts (Hs-6 ATG 3'ss) increased luciferase expression levels in relation to WT transcripts (Hs-6), showing the importance of the uORF for regulation of intron-retained transcripts translation. Mutation of intronic 3'ss did not significantly change luciferase expression in any of tested primates, in comparison to WT constructs.

These results highlight the important role of coupled splicing and translation regulation via untranslated regions in *INS* expression and most likely, susceptibility to T1DM.

Chapter 6: General discussion

The adoption of diverse secondary structural motifs is known to contribute to the regulation of RNA processing (108,444–446). Studies in this thesis provide information about the propensity of *INS* intron 1 segments to adopt noncanonical secondary G4 structures *in vitro*, pointing to potential role in *in vivo* regulation of *INS* expression.

The broader aim of this study was to understand the molecular determinants leading to increased *INS* intron 1 retention levels in individuals susceptible to T1DM. These individuals possess an adenine variant in intron 1 that disrupts the Py-tract, which is an essential element for accurate recognition of 3'ss (Figure 1 and Figure **2**) (100). This allele further increases retention of an already weak intron in mature transcripts, extends the 5'UTR and decreases preproinsulin levels, as a result of introducing translation inhibitory motifs (Figure 7) and reducing the stimulating effect of splicing on translation (100,315).

Understanding of the processes involved in RNA processing is still in its early stages. RNA structure is very important for an efficient splicing (108,446); therefore, its characterisation is essential to understand RNA processing.

Our previous study (315) showed that the antisense target for reducing *INS* intron 1 retention is flanked by two G-rich regions predicted to fold into G4. It was shown, using circular dichroism analysis, that the downstream region, represented by oligo Int7 in this study, is capable of forming a parallel G4 (Figure 8) (315).

Using ThT, a specific fluorescent dye for G4 (188), the capacity of a set of intron 1-derived DNA and RNA oligonucleotides to fold into this structure was evaluated (Chapter 3). ThT efficiency for G4 detection was first confirmed via its fluorescent enhancement in the presence of oligos that were previously shown to fold into this structure (Figure 9). This corroborated previous findings (187,189,447) that ThT can be used as a sensor for G4-forming sequences. ThT is a sensitive fluorogenic dye that can reveal formation of stable G4s (Figure 10) in a concentration dependent manner (Figure 11) (187).

G4s are highly polymorphic, adopting all-parallel, all-anti-parallel or mixed conformations, which was reflected by different fluorescence intensities in the presence of either conformation, with all-parallel displaying higher intensities than remaining conformations (187,191,389,392). Experimental conditions such as buffer composition and pH have been shown to determine G4 conformation propensity, even leading to transitions between conformations (448–451) (392). This was confirmed for both *INS* intron 1 DNA- and RNA-derived oligonucleotides (Figure 17 and Figure

20 - Chapter 3). Higher fluorescence signals in the presence of RNA oligos indicated a higher sensitivity to all-parallel conformations (Figure 18), corroborating previous findings (392).

Folding into G4 was shown to be susceptible to ionic strength, as demonstrated by the loss of ThT signal with increasing potassium and magnesium concentrations (Figure 21-Figure **23**), indicating that these structures can be modulated *in vitro* by altering experimental conditions. Furthermore, the tested set of *INS* intron 1 DNA- and RNA-derived oligos displayed distinct signals, proving a differential and discriminatory G4 stabilization and detection capacity (Chapter 3) (188,189).

ThT assays do not guarantee the homogeneity of the population in solution. It is likely that most sequences have assembled into G4 structures, but, these are, presumably, in equilibrium with other secondary structures. In agreement with this, fluorescence correlated weakly with the QGRS mapper predictions (Figure 14). However, ThT was not able to recognize some predicted structures (Int 2 and 3; GT8 and GA8), which may be explained by its specificity to the parallel G4 conformation or incorrect predictions (191).

Quadruplex forming G-rich Sequences (QGRS) mapper scores are only predictive indicators of the occurrence of putative G4s (376) and do not give absolute certainty on G4 propensity of analysed sequences. The software generates information based on composition and distribution of those putative QGRS in single nucleotide sequences. It does not consider the sequences in between the G-runs that constitute loops in G4s and have an important role in the stability of the structure (402,403). On the other hand, the software evaluates the presence of putative G-runs that can establish intramolecular interactions, regardless the possible formation of intermolecular bonds. Hence, no conclusion can be inferred for potential intermolecular G4s.

G-scores may thus be used as G4 formation indicators but folding needs to be further demonstrated by *in vitro* or *in vivo* assays.

ThT fluorescence could respond to structural transitions to other G4 conformations or to canonical secondary structures. Adoption of structures other than parallel G4 would explain signal intensities of tested oligos with a null G-score, such as Int5/6 and GA12 (Figure 14 and Table 17 in appendix B), and confirm data in Figure 25, suggesting the existence of different conformations in equilibrium for the same sequence, in agreement with both RNAstructure and QGRS predictions (Table 17-Figure **22**). Nevertheless, further work would be needed to confirm structural properties of each species and to determine which is the predominant structure in equilibrium.

It has also been demonstrated that RNA containing G-tracts can assemble into G4 conformations *in vivo*, which has been shown for mammalian telomeric transcripts containing 5'-UUAGGG-3' repeats (212). These results suggest that G4 formation in *INS*-derived primary transcripts could have a physiological function. In addition, the detection of G4s under conditions that intend to mimic transcription in cells is very promising for exploiting modulation of these structures in cells and ascertain their role in preproinsulin pre-mRNA processing.

Real-time monitoring of G4s during transcription further corroborate and validate data obtained with synthetic RNA oligos in water, showing that the ThT assay used in this project can be used to address G4 formation for other RNAs and explore their role in splicing-mediated diseasea development.

For example, G4 structures in G-rich segments flanking the antisense target sequence may be important for efficient splicing. This should be addressed in future studies since these noncanonical structures could provide efficient means to correct the minor splicing defects object in T1DM predisposed individuals carrying the A allele at rs689 SNP.

These results validate the ThT assay as a screening method for evaluating G-rich DNA or RNA sequences (Chapter 3) to fold into the non-canonical G4 structures. However, it only shows the capacity to inform about parallel G4 conformations. Hence, to ascertain that the decrease in ThT fluorescence intensities is due to loss of G4 structures, which may or may not be accompanied of folding into canonical structures, structural properties should be corroborated using, whenever possible and appropriate, complementary assays. These might include preparation of the same DNA and RNA oligos or RNA *in vitro* transcripts to be analysed by circular dichroism and/or NMR. These may also include similar fluorescence assays using probes specifically recognizing anti-parallel G4, such as N-Methyl mesoporphyrin IX (NMM).

Pull-down assays (Chapter 4) showed that RNA constructs derived from the region targeted to promote *INS* intron 1 splicing (315) specifically bind hnRNP F and H1 (Figure 26). Both hnRNP F and hnRNP H1 recognize and bind to G-rich regions, which are able to fold into G4 *in vitro* (154). However, it is not clear yet if they bind to canonical structures or to the non-canonical G4s. Further studies are necessary to understand the role of G4 formation in binding of hnRNPs to *INS* intron 1 and promotion of its removal (100).

In summary of chapters 3 and 4, folding of nascent RNAs is transient, limited to 50nt downstream of the transcribing polymerase and subject to changes upon interaction of RNA with splicing factors. However, G4 structures may generally assemble from sequences with 18 nt (Figure 6A), which

indicates that pre-mRNAs may adopt this non-canonical secondary structure during transcription *in vivo*, as shown in the real-time monitoring of G4 formation in Figure 24. It is also tempting to speculate that G4 formation here shown by G-rich segments of *INS* intron 1 indicate that *INS* pre-mRNA folding into G4 may occur *in vivo* and modulate splicing efficiency. Demonstration of G4 assembly *in vivo* is yet difficult, due to rapid equilibrium transitions between secondary structures and binding of trans-acting factors that may mask RNA structures or promote their folding/unfolding. Nevertheless, G4s have already been shown to modulate splicing through its interaction with hnNRP F promoting alternative splicing and production of the epithelial-specific CD44v isoform. Interaction of hnNRPs F and H1 with *INS* intronic segment comprising the antisense target flanked by G4-forming regions (Figure 14 and Figure 19), revealed by pulldown assays also point towards a role of this structure on INS pre-mRNA splicing via its interaction with these proteins. In agreement with this, our previous study showed that overexpression of either protein led to increased splicing efficiency, while protein depleted increased intron retention levels.

Further studies on the characterization of G-runs folding into G4s in *INS* intron 1 and their role in IR should be performed. Using CD and NMR, the presence of G4 structures detected by ThT could be confirmed, and characterization of G4 conformations in these assemblies addressed. Using RNA polymerase pausing assays and transcription assays in the presence of G4 Resolvase1 (452,453), G4 formation could also be explored via evaluation of transcription efficiency, in WT and G4-abolished constructs.

Additionally, using ThT to detect G4 structures in G-rich intronic sequences comprising the antisense target, in the presence of our splicing stimulating oligos (315), would help addressing if these ribonucleotides promote G4 formation. This data would directly correlate G4 formation with splicing promotion/inhibition. Combination with mutated G-rich sequences and/or mutated target region, in the presence of the same antisense oligoribonucleotides, would also provide a better insight into the influence each region has over the folding of the remaining segments.

Studies on the characterization of the interaction of hnRNP F, hnRNP H1 and their RRM domains, in separate, with *INS* intron 1 should also be performed. Using WT and G4-abolished oligonucleotides and RNA transcripts containing the antisense target region for reducing *INS* IR, hnRNPs interaction with these intronic sequences could be explored. For this purpose, G4-specific probe ThT could be used to detect G4 formation/inhibition upon protein binding to oligonucleotides or RNA transcripts. Binding affinities of each purified recombinant hnRNP and RRM domain to transcripts or oligos would be determined by performing EMSA combined with western blotting using protein- and G4-specific antibodies (51,454,455).

G4 pre-folding could be modulated using a range of ionic strength conditions, from low to ionic concentrations above physiological levels.

G-tracts have shown to be essential for splicing regulation of some introns, particularly short introns rich in guanine, (53,142) and their highly conserved location within 5'UTRs may point to a critical role in the evolution of some genes, like preproinsulin gene (100). G4 formation, along with an uORF in *INS* mRNA transcripts with retained introns, has a potential to markedly influence coupled splicing and translation regulation of short G-rich introns.

A secondary purpose of my study was to investigate how these new uORFs, combined with IR, modulate protein translation, using constructs derived from 5'UTRs of different primate species (Figure 31 - Chapter 5). Results showed that luciferase translation levels were higher in constructs lacking intron 1 sequence in comparison to WT and mutated constructs containing *INS* intron 1, regardless of tested primate species (Figure 31). This indicates the importance of intron removal from untranslated regions. The data point towards the importance of human uORF within the 5'UTR as a splicing regulatory motif in *INS* gene expression, as shown by increased luciferase translation, in human constructs lacking both uORF and 3'ss (Figure 31A - Chapter 5).

Further studies are necessary to understand the role of intron retention in *INS* expression in other primates. These studies should exploit the evolutionary conservation of the importance of G4 formation and the interaction of G4/G-tracts with hnRNPs on *INS* intron 1 splicing efficiency. Such investigation should be facilitated by a set of constructs developed in this study combined with constructs containing mutated Gr1, 2 and 7 (Figure 8). The role of the non-canonical structure in splicing and translation can be studied using dual-luciferase-reporter assays. The role of individual domains of hnRNPs F and H can be investigated using their specific RNA targets. Finally, these studies will provide further insights into evolution of regulatory motifs in untranslated regions, which have been subject to distinct selection pressures as compared to coding regions.

In summary, data obtained in this project corroborate previous findings, validating ThT as an external sensitive and specific water-soluble fluorogenic probe for the detection of G4 structures in *INS* intron 1 *in vitro* (Figure 14, Figure **23** and Figure **24**). Demonstration of propensity for G4 formation of *INS* intronic G-runs improve the understanding of the molecular mechanisms driving IR in T1DM susceptible individuals. G-runs are the RNA binding sites for proteins such as hnRNPs F and H1, which specifically bind to *INS* intron 1 (Figure 26) and increase the efficiency of intron 1 elimination from RNA. Further studies on the *in vitro* characterization of intron1 G-runs: hnRNPs interactions and their role in *INS* RNA processing are essential to expand our knowledge about IDDM2-mediated susceptibility. A combined approach of *in vitro* findings with modulation of RNA

processing of *INS* 5'UTR of higher primates (Figure 31), in mammalian cells, elucidate the importance of G4 in *INS* gene evolution, also contributing to future development of potential treatments applied to disease prevention.

Overall, the assay system presented in this project could also be used to screen for small molecule enhancers/inhibitors of G4 folding in order to modulate splicing and develop novel treatments for T1DM.

VII. References

1. Hoopes L. Introduction to the gene expression and regulation topic room. Nat Educ. 2008;1(1):160.

2. Mariño-Ramírez L, et al. Histone structure and nucleosome stability. Expert Rev Proteomics. 2005;2(5):719–29.

3. Annunziato A. DNA Packaging: Nucleosomes and Chromatin. Nat Educ. 2008;1(1):26.

4. Radman-Livaja M, Rando OJ. Nucleosome positioning: How is it established, and why does it matter?. Vol. 339, Developmental Biology. NIH Public Access; 2010. p. 258–66.

5. Kouzarides T. Chromatin Modifications and Their Function. Cell. 2007;128(4):693–705.

6. Nocetti N, Whitehouse I. Nucleosome repositioning underlies dynamic gene expression. Genes Dev. 2016;30(6):660–72.

7. Bai L, Morozov A V. Gene regulation by nucleosome positioning. Vol. 26, Trends in Genetics. 2010. p. 476–83.

8. Struhl K, Segal E. Determinants of nucleosome positioning. Vol. 20, Nature Structural and Molecular Biology. NIH Public Access; 2013. p. 267–73.

9. Kim M-S, et al. A draft map of the human proteome. Nature. 2014;509(7502):575–81.

10. Hattori M. Finishing the euchromatic sequence of the human genome. Nature. 2004;431:931–45.

11. Baker MS, et al. Accelerating the search for the missing proteins in the human proteome. Nat Commun. 2017;8(14271):1–13.

12. McManus CJ, et al. RNA structure and the mechanisms of alternative splicing. Curr Opin Genet Dev. 2011;21(4):373–9.

13. Smith CWJ, Valcárcel J. Alternative pre-mRNA splicing: the logic of combinatorial control. Trends Biochem Sci. 2000;25(8):381–8.

14. Cascino I, et al. Three functional soluble forms of the human apoptosis-inducing Fas molecule are produced by alternative splicing. J Immunol. 1995;154(6):2706–13.

15. Wang Z, Burge CB. Splicing regulation: From a parts list of regulatory elements to an

integrated splicing code. RNA. 2008;14(5):802–13.

16. Von Philipsborn AC, et al. Cellular and behavioral functions of fruitless isoforms in Drosophila courtship. Curr Biol. 2014;24(3):242–51.

17. Matunis MJ, Xing J, Dreyfuss G. The hnRNP F protein: unique primary structure, nucleic acid-binding properties, and subcellular localization. Nucleic Acids Res. 1994;22(6):1059–67.

18. Lodish H, Berk A, Zipursky SL, Matsudaira P, Baltimore D, Darnell J. Processing of Eukaryotic mRNA. In: Molecular Cell Biology 4th edition. 4th ed. New York: W. H. Freeman; 2000

19. Slomovic S, et al. Polyadenylation of ribosomal RNA in human cells. Nucleic Acids Res. 2006;34(10):2966–75.

20. Schellenberg, M., et al. Pre-mRNA splicing: a complex picture in higher definition. Trends Biochem Sci. 2008;33(6):243–6.

21. Phillips T. Small non-coding RNA and gene expression. Nat Educ. 2008;1(1):115.

22. Wilusz JE. Long noncoding RNAs: Re-writing dogmas of RNA processing and stability. Biochim Biophys Acta. 2016 Jan;1859(1):128–38.

23. Palazzo AF, Lee ES. Non-coding RNA: what is functional and what is junk? Front Genet. 2015;6(2):1–11.

24. Nissim-Rafinia M, Kerem B. Splicing regulation as a potential genetic modifier. Trends Genet. 2002;18(3):123–7.

25. Braunschweig U, et al. Dynamic integration of splicing within gene regulatory pathways. Cell. 2013;152(6):1252–69.

26. Baralle D, Baralle M. Splicing in action: assessing disease causing sequence changes. J Med Genet. 2005;42(10):737–48.

27. Warf MB, Berglund JA. Role of RNA structure in regulating pre-mRNA splicing. Trends Biochem Sci. 2010;35(3):169–78.

28. Wang Y, et al. Mechanism of alternative splicing and its regulation. Biomed Reports. 2015;3(2):152–8.

29. Chen M, Manley JL. Mechanisms of alternative splicing regulation: insights from molecular and genomics approaches. Nat Rev Mol Cell Biol. 2010;10(11):741–54.

30. Zhang XH-F, et al. Exon inclusion is dependent on predictable exonic splicing enhancers. Mol Cell Biol. 2005 Aug;25(16):7323–32.

31. Zhang XH-F, Chasin LA. Computational definition of sequence motifs governing constitutive exon splicing. Genes Dev. 2004 Jun 1;18(11):1241–50.

32. Wang Z, et al. Systematic Identification and Analysis of Exonic Splicing Silencers. Cell. 2004 Dec 17;119(6):831–45.

33. Fairbrother WG, et al. Predictive Identification of Exonic Splicing Enhancers in Human Genes. Science (80-). 2002;297(5583):1007–13.

34. Panchapakesan SSS, Ferguson ML, Hayden EJ, Chen X, Hoskins AA, Unrau PJ. Ribonucleoprotein purification and characterization using RNA Mango. RNA. 2017;23(10):1592–9.

35. Wahl MC, et al. The Spliceosome: Design Principles of a Dynamic RNP Machine. Cell. 2009;136(4):701–18.

36. Lin C-L, et al. RNA Structure in Splicing: an Evolutionary Perspective. RNA Biol. 2016;13(9):766–71.

37. Pagani F, Baralle FE. Genomic variants in exons and introns: identifying the splicing spoilers. Nat Rev Genet. 2004;5:389–96.

38. Lee Y, Rio DC, Biology S, Biology C. Mechanisms and Regulation of Alternative Pre-mRNA Splicing. AnnuRevBiochem. 2015;(258):291–323.

39. Hui J, et al. Intronic CA-repeat and CA-rich elements: a new class of regulators of mammalian alternative splicing. EMBO J. 2005;24(11):1988–98.

40. Blencowe BJ. Exonic splicing enhancers: Mechanism of action, diversity and role in human genetic diseases. Trends Biochem Sci. 2000;25(3):106–10.

41. Blencowe BJ. Exonic splicing enhancers: mechanism of action, diversity and role in human genetic diseases [published erratum appears in Trends Biochem Sci 2000 May;25(5):228]. Trends Biochem Sci. 2000;25(3):106–10.

42. Wang, Z. et al. General and specific functions of exonic splicing silencers in splicing control. Mol Cell. 2006;23(1):61–70.

43. Bradley T, et al. SR proteins control a complex network of RNA-processing events. RNA. 2015

Jan;21(1):75–92.

44. Busch A, Hertel KJ. Evolution of SR protein and hnRNP splicing regulatory factors. Wiley Interdiscip Rev RNA. 2012;3(1):1–12.

45. Chaudhury A, et al. Heterogeneous nuclear ribonucleoproteins (hnRNPs) in cellular processes: Focus on hnRNP E1's multifunctional regulatory roles. RNA. 2010;16(8):1449–62.

46. Han SP, et al. Functional diversity of the hnRNPs: past, present and perspectives. Biochem J. 2010;430(3):379–92.

47. Geuens T, Bouhy D, Timmerman V. The hnRNP family: insights into their role in health and disease. Hum Genet. 2016;135(8):851–67.

48. Martinez-Contreras R, Cloutier P, Shkreta L, Fisette J-F, Revil T, Chabot B. hnRNP proteins and splicing control. Adv Exp Med Biol. 2007;623:123–47.

49. Dominguez C, Allain FHT. NMR structure of the three quasi RNA recognition motifs (qRRMs) of human hnRNP F and interaction studies with Bcl-x G-tract RNA: A novel mode of RNA recognition. Nucleic Acids Res. 2006;34(13):3634–45.

50. Dominguez C, et al. Structural basis of G-tract recognition and encaging by hnRNP F quasi-RRMs. Nat Struct Mol Biol. 2010;17(7):853–61.

51. Alkan S a, et al. The hnRNPs F and H2 bind to similar sequences to influence gene expression. Biochem J. 2006;393:361–71.

52. Martinez-Contreras R, et al. Intronic binding sites for hnRNP A/B and hnRNP F/H proteins stimulate pre-mRNA splicing. PLoS Biol. 2006;4(2):172–85.

53. Decorsière A, et al. Essential role for the interaction between hnRNP H/F and a G quadruplex in maintaining p53 pre-mRNA 3'-end processing and function during DNA damage. Genes Dev. 2011;25(3):220–5.

54. Yoshida T, et al. Heterogeneous nuclear RNA-ribonucleoprotein F binds to DNA via an oligo(dG)-motif and is associated with RNA polymerase II. Genes Cells. 1999;4(12):707–19.

55. Chou MY, et al. hnRNP H is a component of a splicing enhancer complex that activates a c-src alternative exon in neuronal cells. Mol Cell Biol. 1999;19(1):69–77.

56. Buratti E, et al. hnRNP H binding at the 5' splice site correlates with the pathological effect of two intronic mutations in the NF-1 and TSH?? genes. Nucleic Acids Res.

2004;32(14):4224–36.

57. Zhang YZ, et al. Evidence that Dim1 associates with proteins involved in pre-mRNA splicing, and delineation of residues essential for Dim1 interactions with hnRNP F and Npw38/PQBP-1. Gene. 2000;257(1):33–43.

58. Ayoubi T. Alternative Promoter Usage. In: eLS. Chichester, UK: John Wiley & Sons, Ltd; 2005

59. Elkon R, Ugalde AP, Agami R. Alternative cleavage and polyadenylation: extent, regulation and function. Nat Rev Genet Vol. 2013;14:496–506.

60. Tian B, Manley JL. Alternative polyadenylation of mRNA precursors. Nat Rev Mol Cell Biol. 2017;18:18–30.

61. B. Akman H, E. Erson-Bensan A. Alternative Polyadenylation and Its Impact on Cellular Processes. MicroRNA. 2014;3(1):2–9.

62. Pal S, et al. Alternative transcription exceeds alternative splicing in generating the transcriptome diversity of cerebellar development. Genome Res. 2011;21(8):1260–72.

63. Sprung CN, et al. Alternative transcript initiation and splicing as a response to DNA damage. PLoS One. 2011;6(10):e25758.

64. Wada Y, et al. A wave of nascent transcription on activated human genes. PNAS. 2009;106(43):18357–61.

65. Blencowe BJ. Alternative Splicing: New Insights from Global Analyses. Cell. 2006;126(1):37–47.

66. Brett D, et al. Alternative splicing and genome complexity. Nat Genet. 2002;30(1):29–30.

67. Zhou X, et al. Transcriptome analysis of alternative splicing events regulated by SRSF10 reveals position-dependent splicing modulation. Nucleic Acids Res. 2014;42(6):4019–30.

68. Shukla S, Oberdoerffer S. Co-transcriptional regulation of alternative pre-mRNA splicing. Biochim Biophys Acta - Gene Regul Mech. 2012;1819(7):673–83.

69. Goldstrohm AC, et al. Co-transcriptional splicing of pre-messenger RNAs: Considerations for the mechanism of alternative splicing. Gene. 2001;277(1–2):31–47.

70. Boutz PL, et al. Detained introns are a novel, widespread class of post-transcriptionally spliced introns. Genes Dev. 2014;29:63–80.

71. Neugebauer KM, Roth MB. Distribution of pre-mRNA splicing factors at sites of RNA polymerase II transcription. Genes Dev. 1997;11(9):1148–59.

72. Naftelberg S, Schor IE, Ast G, Kornblihtt AR. Regulation of Alternative Splicing Through Coupling with Transcription and Chromatin Structure. Annu Rev Biochem. 2015;84:165–98.

73. De Conti L, Baralle M, Buratti E. Exon and intron definition in pre-mRNA splicing. WIREs RNA. 2013;4(1):49–60.

74. Berget SM. Exon recognition in vertebrate splicing. J Biol Chem. 1995;270(6):2411–4.

75. de Almeida SF, Carmo-Fonseca M. The CTD role in cotranscriptional RNA processing and surveillance. Vol. 582, FEBS Letters. 2008. p. 1971–6.

76. Hsin J-P, Manley JL. The RNA polymerase II CTD coordinates transcription and RNA processing. Genes Dev. 2012;26(19):2119–37.

77. Millhouse S, Manley JL. The C-Terminal Domain of RNA Polymerase II Functions as a Phosphorylation-Dependent Splicing Activator in a Heterologous Protein. Mol Cell Biol. 2005;25(2):533–44.

78. Phatnani HP, Greenleaf AL. Phosphorylation and functions of the RNA polymerase II CTD. Vol. 20, Genes and Development. 2006. p. 2922–36.

79. Merkhofer EC, Hu P, Johnson TL. Introduction to cotranscriptional RNA splicing. Vol. 1126, Methods in Molecular Biology. 2014. p. 83–96.

80. Gunderson FQ, Johnson TL. Acetylation by the transcriptional coactivator Gcn5 plays a novel role in co-transcriptional spliceosome assembly. Madhani HD, editor. PLoS Genet. 2009;5(10):e1000682.

81. Hsin J-P, Manley JL. The RNA polymerase II CTD coordinates transcription and RNA processing. Genes Dev. 2012;26(19):2119–37.

82. Tanny JC. Chromatin modification by the RNA Polymerase II elongation complex. Transcription. 2014;5(5):e988093.

83. Huang Y, Steitz JA. Splicing factors SRp20 and 9G8 promote the nucleocytoplasmic export of mRNA. Mol Cell. 2001;7(4):899–905.

84. Pozzoli U, Riva L, Menozzi G, Cagliani R, Comi GP, Bresolin N, et al. Over-representation of exonic splicing enhancers in human intronless genes suggests multiple functions in mRNA

processing. Biochem Biophys Res Commun. 2004;322(2):470–6.

85. Damgaard CK, Kahns S, Lykke-Andersen S, Nielsen AL, Jensen TH, Kjems J. A 5′ Splice Site Enhances the Recruitment of Basal Transcription Initiation Factors In Vivo. Mol Cell. 2008;29(2):271–8.

86. Marquez Y, et al. Unmasking alternative splicing inside protein-coding exons defines exitrons and their role in proteome plasticity. Genome Res. 2015;25:995–1007.

87. Galante PA, et al. Detection and evaluation of intron retention events in the human transcriptome. RNA. 2004;10(5):757–65.

88. Staiger D, Simpson GG. Enter exitrons. Genome Biol. 2015;16:136–8.

89. Mayer K, et al. Three novel types of splicing aberrations in the tuberous sclerosis TSC2 gene caused by mutations apart from splice consensus sequences. Biochim Biophys Acta - Mol Basis Dis. 2000;1502(3):495–507.

90. Braunschweig U, et al. Widespread intron retention in mammals functionally tunes transcriptomes. Genome Res. 2014;24:1774–86.

91. Ner-Gaon H, et al. Intron retention is a major phenomenon in alternative splicing in Arabidopsis. Plant J. 2004;39(6):877–85.

92. Nott A, Meislin SH, Moore MJ. A quantitative analysis of intron effects on mammalian gene expression. RNA. 2003;9(5):607–17.

93. Buckley PT, et al. Cytoplasmic intron retention, function, splicing, and the sentinel RNA hypothesis. Wiley Interdiscip Rev RNA. 2014;5(2):223–30.

94. Lareau LF, et al. The evolving roles of alternative splicing. Curr Opin Struct Biol. 2004;14(3):273–82.

95. Wong JJL, et al. Orchestrated intron retention regulates normal granulocyte differentiation. Cell. 2013;154(3):583–95.

96. Wong JJ-L, et al. Intron retention in mRNA: No longer nonsense. BioEssays. 2016 Jan;38(1):41–9.

97. Popp MW-L, Maquat LE. Organizing Principles of Mammalian Nonsense-Mediated mRNA Decay. Annu Rev Genet. 2013;47(1):139–65.

98. Nomakuchi TT, Rigo F, Aznarez I, Krainer AR. Antisense oligonucleotide–directed inhibition

of nonsense-mediated mRNA decay. Nat Biotechnol. 2016;34(2):164–6.

99. Rípodas C, et al. Annotation , phylogeny and expression analysis of the nuclear factor Y gene families in common bean (Phaseolus vulgaris). Front Plant Sci. 2015;14(5):761–73.

100. Kralovicova J, Vorechovsky I. Allele-specific recognition of the 3' splice site of INS intron 1. Hum Genet. 2010;128(4):383–400.

101. Ge Y, Porse BT. The functional consequences of intron retention: Alternative splicing coupled to NMD as a regulator of gene expression. BioEssays. 2014;36(3):236–43.

102. Barbosa C, Peixeiro I. Gene Expression Regulation by Upstream Open Reading Frames and Human Disease. PLOS Genet. 2013;9(8):e1003529.

103. Xue S, Barna M. Specialized ribosomes: a new frontier in gene regulation and organismal biology. Nat Rev Mol Cell Biol. 2012;13(6):355–69.

104. Neugebauer KM. On the importance of being co-transcriptional. J Cell Sci. 2002;115:3865–71.

105. Kornblihtt AR, et al. Multiple links between transcription and splicing. RNA. 2004;10:1489–98.

106. Sakabe NJ, de Souza SJ. Sequence features responsible for intron retention in human. BMC Genomics. 2007;8:59–72.

107. Russell R. RNA misfolding and the action of chaperones. Front Biosci. 2008;13:1–20.

108. Andronescu M, et al. RNA STRAND: the RNA secondary structure and statistical analysis database. BMC Bioinformatics. 2008 Aug 13;9:340.

109. Tatei K, et al. U1 RNA-protein complex preferentially binds to both 5' and 3' splice junction sequences in RNA or single-stranded DNA. Proc Natl Acad Sci U S A. 1984;81(20):6281–5.

110. Mitrovich QM, Guthrie C. Evolution of small nuclear RNAs in S. cerevisiae, C. albicans, and other hemiascomycetous yeasts. RNA. 2007;13(12):2066–80.

111. Buratti E, et al. RNA folding affects the recruitment of SR proteins by mouse and human polypurinic enhancer elements in the fibronectin EDA exon. Mol Cell Biol. 2004;24(3):1387–400.

112. Nagaswamy U, et al. NCIR: a database of non-canonical interactions in known RNA structures. Nucleic Acids Res. 2002;30:395–7.

113. Words K, Words K. Structural motifs in RNA. Annu Rev Biochem. 1999;68:287–300.

114. Lemieux S, Major F. RNA canonical and non-canonical base pairing types: a recognition method and complete repertoire. Nucleic Acids Res. 2002;30(19):4250–63.

115. McManus CJ, Graveley BR. RNA structure and the mechanisms of alternative splicing. Curr Opin Genet Dev. 2011;21(4):373–9.

116. Buratti E, Baralle FE. Influence of RNA Secondary Structure on the Pre-mRNA Splicing Process MINIREVIEW Influence of RNA Secondary Structure on the Pre-mRNA Splicing Process. Mol Cell Biol. 2004;24(24):10505–14.

117. Klaff P, Riesner D, Steger G. RNA structure and the regulation of gene expression. Plant Mol Biol. 1996;32(1–2):89–106.

118. Hiller M, Zhang Z, Backofen R, Stamm S. Pre-mRNA secondary structures influence exon recognition. PLoS Genet. 2007;3(11):2147–55.

119. Graveley BR, Hertel KJ, Maniatis T. A systematic analysis of the factors that determine the strength of pre-mRNA splicing enhancers. EMBO J. 1998;17(22):6747–56.

120. Schroeder R, Grossberger R, Pichler A, Waldsich C. RNA folding in vivo. Vol. 12, Current Opinion in Structural Biology. 2002. p. 296–300.

121. Liu W, Zhou Y, Hu Z, Sun T, Denise A, Fu XD, et al. Regulation of splicing enhancer activities by RNA secondary structures. FEBS Lett. 2010;584(21):4401–7.

122. Patterson DJ, Yasuhara K, Ruzzo WL. Pre-mRNA secondary structure prediction aids splice site prediction. Pac Symp Biocomput. 2002;234:223–34.

123. Soemedi R, Cygan KJ, Rhine CL, Glidden DT, Taggart AJ, Lin CL, et al. The effects of structure on pre-mRNA processing and stability. Vol. 125, Methods. 2017. p. 36–44.

124. Shepard PJ, Hertel KJ. Conserved RNA secondary structures promote alternative splicing Conserved RNA secondary structures promote alternative splicing. Rna. 2008;14:1463–9.

125. Zhang J, Kuo CCJ, Chen L. GC content around splice sites affects splicing through pre-mRNA secondary structures. BMC Genomics. 2011;12:90.

126. Woodson SA, Cech TR. Alternative Secondary Structures in the 5’ Exon Affect both Forward and Reverse Self-Splicing of the Tetrahymena Intervening Sequence RNA. Biochemistry. 1991;30(8):2042–50.

127. Graveley BR. Mutually exclusive splicing of the insect Dscam Pre-mRNA directed by competing intronic RNA secondary structures. Cell. 2005;123(1):65–73.

128. May GE, Olson S, McManus CJ, Graveley BR. Competing RNA secondary structures are required for mutually exclusive splicing of the Dscam exon 6 cluster. RNA. 2011;17:222–9.

129. Anastassiou D, Liu H, Varadan V. Variable window binding for mutually exclusive alternative splicing. Genome Biol. 2006;7(1):R2.

130. Kreahling JM, Graveley BR. The iStem, a long-range RNA secondary structure element required for efficient exon inclusion in the Drosophila Dscam pre-mRNA. Mol Cell Biol. 2005;25(23):10251–60.

131. Raker VA, Mironov AA, Gelfand MS, Pervouchine DD. Modulation of alternative splicing by long-range RNA structures in Drosophila. Nucleic Acids Res. 2009;37(14):4533–44.

132. Warf MB, Diegel J V., von Hippel PH, Berglund JA. The protein factors MBNL1 and U2AF65 bind alternative RNA structures to regulate splicing. Proc Natl Acad Sci. 2009;106(23):9203–8.

133. Muro a F, Caputi M, Pariyarath R, Pagani F, Buratti E, Baralle FE. Regulation of fibronectin EDA exon alternative splicing: possible role of RNA secondary structure for enhancer display. Mol Cell Biol. 1999;19(4):2657–71.

134. Singh NN, Singh RN, Androphy EJ. Modulating role of RNA structure in alternative splicing of a critical exon in the spinal muscular atrophy genes. Nucleic Acids Res. 2007;35(2):371–89

135. Buckanovich RJ, Darnell RB. The neuronal RNA binding protein Nova-1 recognizes specific RNA targets in vitro and in vivo. Mol Cell Biol. 1997;17(6):3194–201.

136. Damgaard CK, Tange TØ, Kjems J. HnRNP A1 controls HIV-1 mRNA splicing through cooperative binding to intron and exon splicing silencers in the context of a conserved secondary structure. RNA. 2002;8(11):1401–15.

137. Nagel RJ, Lancaster AM, Zahler AM. Specific binding of an exonic splicing enhancer by the pre-mRNA splicing factor SRp55. RNA. 1998;4(1):11–23.

138. Shi H, Hoffman BE, Lis JT. A specific RNA hairpin loop structure binds the RNA recognition motifs of the Drosophila SR protein B52. Mol Cell Biol. 1997;17(5):2649–57.

139. Kent OA, Reayi A, Foong L, Chilibeck KA, MacMillan AM. Structuring of the 3′ Splice Site by U2AF65. J Biol Chem. 2003;278(50):50572–7.

140. Huang H, Zhang J, Harvey SE, Hu X, Cheng C. RNA G-quadruplex secondary structure promotes alternative splicing via the RNA-binding protein hnRNPF. Genes Dev. 2017;31(22):2296–309.

141. Blice-Baum AC, Mihailescu M-R. Biophysical characterization of G-quadruplex forming FMR1 mRNA and of its interactions with different fragile X mental retardation protein isoforms. RNA. 2014;20(1):103–14.

142. Marcel V, et al. G-quadruplex structures in TP53 intron 3: Role in alternative splicing and in production of p53 mRNA isoforms. Carcinogenesis. 2011;32(3):271–8.

143. Garneau D, Revil T, Fisette JF, Chabot B. Heterogeneous nuclear ribonucleoprotein F/H proteins modulate the alternative splicing of the apoptotic mediator Bcl-x. J Biol Chem. 2005;280(24):22641–50.

144. Khateb S, Weisman-Shomer P, Hershco-Shani I, Ludwig AL, Fry M. The tetraplex (CGG)ndestabilizing proteins hnRNP A2 and CBF-A enhance the in vivo translation of fragile X premutation mRNA. Nucleic Acids Res. 2007;35(17):5775–88.

145. Lattmann S, Giri B, Vaughn JP, Akman SA, Nagamine Y. Role of the amino terminal RHAU-specific motif in the recognition and resolution of guanine quadruplex-RNA by the DEAH-box RNA helicase RHAU. Nucleic Acids Res. 2010;38(18):6219–33.

146. Von Hacht A, Seifert O, Menger M, Schütze T, Arora A, Konthur Z, et al. Identification and characterization of RNA guanine-quadruplex binding proteins. Nucleic Acids Res. 2014;42(10):6630–44.

147. Zhang K, Donnelly CJ, Haeusler AR, Grima JC, Machamer JB, Steinwald P, et al. The C9orf72 repeat expansion disrupts nucleocytoplasmic transport. Nature. 2015;525(7567):56–61

148. Liu X, Ishizuka T, Bao HL, Wada K, Takeda Y, Iida K, et al. Structure-Dependent Binding of hnRNPA1 to Telomere RNA. J Am Chem Soc. 2017;139(22):7533–9.

149. Conlon EG, Lu L, Sharma A, Yamazaki T, Tang T, Shneider NA, et al. The C9ORF72 GGGGCC expansion forms RNA G-quadruplex inclusions and sequesters hnRNP H to disrupt splicing in ALS brains. Elife. 2016;5

150. Xu Y, Gao XD, Lee JH, Huang H, Tan H, Ahn J, et al. Cell type-restricted activity of hnRNPM promotes breast cancer metastasis via regulating alternative splicing. Genes Dev. 2014;28(11):1191–203.

151. Bardin C, Leroy JL. The formation pathway of tetramolecular G-quadruplexes. Nucleic Acids Res. 2008;36(2):477–88.

152. Tran PLT, De Cian A, Gros J, Moriyama R, Mergny J-L. Emergence and evolution of meaning. Top Curr Chem. 2012;330:243–73.

153. Neidle S, Parkinson GN. The structure of telomeric DNA. Curr Opin Struct Biol. 2003;13(3):275–83.

154. Simonsson T. G-quadruplex DNA structures - Variations on a theme. Biol Chem. 2001;382(4):621–8.

155. Luo D, Mu Y. All-Atomic Simulations on Human Telomeric G-Quadruplex DNA Binding with Thioflavin T. J Phys Chem B. 2015;119:4955–67.

156. Yang D, Okamoto K. Structural insights into G-quadruplexes: towards new anticancer drugs. Future Med Chem. 2010;2(4):619–46.

157. Bhattacharyya D, et al. Metal Cations in G-Quadruplex Folding and Stability. Front Chem. 2016;4:38.

158. Lorenz R, et al. 2D meets 4G: G-quadruplexes in RNA secondary structure prediction. IEEE/ACM Trans Comput Biol Bioinforma. 2013;10(4):832–44.

159. Joachimi A, et al. A comparison of DNA and RNA quadruplex structures and stabilities. Bioorganic Med Chem. 2009;17(19):6811–5.

160. Varizhuk A, et al. The expanding repertoire of G4 DNA structures. Biochimie. 2017;135:54–62.

161. Malgowska M, et al. Distinctive structural motifs of RNA G-quadruplexes composed of AGG, CGG and UGG trinucleotide repeats. Nucleic Acids Res. 2014;42(15):10196–207.

162. Mukundan VT, Phan AT. Bulges in G-Quadruplexes: Broadening the Definition of G-Quadruplex-Forming Sequences. J Am Chem Soc. 2013 Apr 3;135(13):5017–28.

163. Li X, et al. Guanine-vacancy-bearing G-quadruplexes responsive to guanine derivatives. Proc Natl Acad Sci U S A. 2015 Nov 24;112(47):14581–6.

164. Seow N, Kirk Y, Yung LYL. Detection of G-Quadruplex Formation via Light Scattering of Defined Gold Nanoassemblies Modulated by Molecular Hairpins. Bioconjug Chem. 2016;27(5):1236–43.

165. Weldon C, et al. Do we know whether potential G-quadruplexes actually form in long functional RNA molecules? Biochem Soc Trans. 2016;44(6):1761–8.

166. Hardin CC, et al. Cation-dependent transition between the quadruplex and Watson-Crick hairpin forms of d(CGCG3GCG). Biochemistry. 1992;31(3):833–41.

167. Jin B, et al. Fluorescence light-up probe for parallel G-quadruplexes. Anal Chem. 2014;86(1):943–52.

168. Mendoza O, et al. Orienting Tetramolecular G-Quadruplex Formation: The Quest for the Elusive RNA Antiparallel Quadruplex. Chem - A Eur J. 2015 Apr 27;21(18):6732–9.

169. Kumari S, et al. An RNA G-quadruplex in the 5' UTR of the NRAS proto-oncogene modulates translation. Nat Chem Biol. 2007;3(4):218–21.

170. Gomez D, et al. A G-quadruplex structure within the 5'-UTR of TRF2 mRNA represses translation in human cells. Nucleic Acids Res. 2010;38(20):7187–98.

171. Beaudoin JD, Perreault JP. Exploring mRNA 3'-UTR G-quadruplexes: Evidence of roles in both alternative polyadenylation and mRNA shortening. Nucleic Acids Res. 2013;41(11):5898–911.

172. Fisette JF, et al. A G-Rich element forms a G-quadruplex and regulates BACE1 mRNA alternative splicing. J Neurochem. 2012;121(5):763–73.

173. Kwok CK, Merrick CJ. G-Quadruplexes: Prediction, Characterization, and Biological Application. Vol. 35, Trends in Biotechnology. Elsevier Current Trends; 2017. p. 997–1013

174. Beaudoin J-D, Jodoin R, Perreault J-P. New scoring system to identify RNA G-quadruplex folding. Nucleic Acids Res. 2014;42(2):1209–23.

175. Lorenz R, Bernhart SH, Externbrink F, Qin J, Siederdissen CH zu, Amman F, et al. RNA Folding Algorithms with G-Quadruplexes. In: de Souto MCP, Kann MG, editors. Advances in Bioinformatics and Computational Biology. Berlin, Heidelberg: Springer Berlin Heidelberg; 2012. p. 49–60. (Lecture Notes in Bioinformatics; vol. 7409).

176. Menendez C, Frees S, Bagga PS. QGRS-H Predictor: a web server for predicting homologous quadruplex forming G-rich sequence motifs in nucleotide sequences. Nucleic Acids Res. 2012;40(Web Server issue):W96–103.

177. Tradigo G, Mannella L, Veltri P. Assessment of G-quadruplex Prediction Tools. In: 2014 IEEE 27th International Symposium on Computer-Based Medical Systems. 2014. p. 243–6.

178. Eddy J, Maizels N. Gene function correlates with potential for G4 DNA formation in the human genome. Nucleic Acids Res. 2006;34(14):3887–96.

179. Cer RZ, Bruce KH, Donohue DE, Temiz AN, Bacolla A, Mudunuri US, et al. Introducing the non-B DNA Motif Search Tool (nBMST). Genome Biol. 2011;12(Suppl 1):P34.

180. Hon J, Martínek T, Zendulka J, Lexa M. pqsfinder: an exhaustive and imperfection-tolerant search tool for potential quadruplex-forming sequences in R. Bioinformatics. 2017;33(21):3373–9.

181. Harkness RW, Mittermaier AK. G-quadruplex dynamics. Biochim Biophys Acta - Proteins Proteomics. 2017;1865(11):1544–54.

182. Hänsel-Hertsch R, Di Antonio M, Balasubramanian S. DNA G-quadruplexes in the human genome: Detection, functions and therapeutic potential. Nat Rev Mol Cell Biol. 2017;18(5):279–84.

183. Hon J, Lexa M, Martinek T. pqsfinder: User Guide. pqsfinder: an exhaustive and imperfection-tolerant search tool for potential quadruplex-forming sequences in R. 2017

184. Frees S, Menendez C, Crum M, Bagga PS. QGRS-Conserve: a computational method for discovering evolutionarily conserved G-quadruplex motifs. Hum Genomics. 2014;8(1):8.

185. Chen J, Lin J, Zhang X, Cai S, Wu D, Li C, et al. Label-free fluorescent biosensor based on the target recycling and Thioflavin T-induced quadruplex formation for short DNA species of c-erbB-2 detection. Anal Chim Acta. 2014;817:42–7.

186. Du Y-C, Zhu L-N, Kong D-M. Label-free thioflavin T/G-quadruplex-based real-time strand displacement amplification for biosensing applications. Biosens Bioelectron. 2016;86:811–7.

187. Gabelica V, et al. Multiple and cooperative binding of fluorescence light-up probe thioflavin t with human telomere DNA G-quadruplex. Biochemistry. 2013;52(33):5620–8.

188. De La Faverie AR, Guédin A, Bedrat A, Yatsunyk L a., Mergny JL. Thioflavin T as a fluorescence light-up probe for G4 formation. Nucleic Acids Res. 2014;42(8):1–8.

189. Xu S, et al. Thioflavin T as an efficient fluorescence sensor for selective recognition of RNA G-quadruplexes. Sci Rep. 2016;6(1):24793.

190. Bhasikuttan AC, Mohanty J. Targeting G-quadruplex structures with extrinsic fluorogenic dyes: promising fluorescence sensors. Chem Commun. 2015;51(36):7581–97.

191. Zhao D, et al. Selective recognition of parallel and anti-parallel thrombin-binding aptamer G-quadruplexes by different fluorescent dyes. Nucleic Acids Res. 2014;42(18):11612–21.

192. Li M, Zhao A, Ren J, Qu X. *N* -Methyl Mesoporphyrin IX as an Effective Probe for Monitoring Alzheimer's Disease β-Amyloid Aggregation in Living Cells. ACS Chem Neurosci. 2017;8(6):1299–304.

193. Kreig A, Calvert J, Sanoica J, Cullum E, Tipanna R, Myong S. G-quadruplex formation in double strand DNA probed by NMM and CV fluorescence. Nucleic Acids Res. 2015;43(16):7961–70.

194. Bhasikuttan AC, Mohanty J, Pal H. Interaction of Malachite Green with Guanine-Rich Single-Stranded DNA: Preferential Binding to a G-Quadruplex. Angew Chemie Int Ed. 2007;46(48):9305–7.

195. Kong D-M, Guo J-H, Yang W, Ma Y-E, Shen H-X. Crystal violet–G-quadruplex complexes as fluorescent sensors for homogeneous detection of potassium ion. Biosens Bioelectron. 2009;25:88–93.

196. Lubitz I, Zikich D, Kotlyar A. Specific High-Affinity Binding of Thiazole Orange to Triplex and G-Quadruplex DNA. pubs.acs.org/Biochemistry Biochem. 2010;49:3567–74.

197. Wang M-Q, Zhu W-X, Song Z-Z, Li S, Zhang Y-Z. A triphenylamine-based colorimetric and fluorescent probe with donor-bridge-acceptor structure for detection of G-quadruplex DNA. Bioorg Med Chem Lett. 2015;25:5672–6.

198. Yaku H, Fujimoto T, Murashima T, Miyoshi D, Sugimoto N. Phthalocyanines: a new class of G-quadruplex-ligands with many potential applications. Chem Commun. 2012;48:6203–16.

199. Tran PLT, Mergny J-L, Alberti P. Stability of telomeric G-quadruplexes. Nucleic Acids Res. 2011;39(8):3282–94.

200. Mergny JL, Li J, Lacroix L, Amrane S, Chaires JB. Thermal difference spectra: A specific signature for nucleic acid structures. Nucleic Acids Res. 2005;33(16):e138.

201. Olsen CM, Lee H-T, Marky LA. Unfolding Thermodynamics of Intramolecular G-Quadruplexes: Base Sequence Contributions of the Loops. J Phys Chem. 2009;113(9):2587–95.

202. Chaires JB. Human telomeric G-quadruplex: thermodynamic and kinetic studies of telomeric quadruplex stability. FEBS J. 2010;277(5):1098–106.

203. Lane AN, Chaires JB, Gray RD, Trent JO. Stability and kinetics of G-quadruplex structures. Vol. 36, Nucleic Acids Research. 2008. p. 5482–515.

204. Gray RD, Chaires JB. Analysis of multidimensional G-quadruplex melting curves. Curr Protoc nucleic acid Chem. 2011;Chapter 17:Unit17.4.

205. Lee JY, Yoon J, Kihm HW, Kim DS. Structural Diversity and Extreme Stability of Unimolecular Oxytricha nova Telomeric G-Quadruplex. Biochemistry. 2008;47(11):3389–96.

206. Medeiros-Silva J, Guédin A, Salgado GF, Mergny J-L, Queiroz JA, Cabrita EJ, et al. Phenanthroline-bis-oxazole ligands for binding and stabilization of G-quadruplexes. Biochim Biophys Acta - Gen Subj. 2017;1861(5):1281–92.

207. Adrian M, Heddi B, Phan AT. NMR spectroscopy of G-quadruplexes. Methods. 2012;57:11–24.

208. Gulerez IE, Gehring K. X-ray crystallography and NMR as tools for the study of protein tyrosine phosphatases. Methods. 2014;65:175–83.

209. Xiao C-D, Ishizuka T, Xu Y. Antiparallel RNA G-quadruplex Formed by Human Telomere RNA Containing 8-Bromoguanosine. Sci Rep. 2017;7(1):6695.

210. Campbell N, Collie GW, Neidle S. Crystallography of DNA and RNA G-Quadruplex Nucleic Acids and Their Ligand Complexes. In: Current Protocols in Nucleic Acid Chemistry. Hoboken, NJ, USA: John Wiley & Sons, Inc.; 2012. p. 17.6.1-17.6.22.

211. Ma D-L, et al. Recent Developments in G-Quadruplex Probes. Chem Biol. 2015 Jul;22(7):812–28.

212. Dolinnaya NG, et al. Structure, Properties, and Biological Relevance of the DNA and RNA G Quadruplexes : Overview 50 Years after Their Discovery. Vol. 81, Biochemistry (Moscow). 2016. 1602-1649 p.

213. Sun D, Hurley LH. Biochemical techniques for the characterization of G-quadruplex structures: EMSA, DMS footprinting, and DNA polymerase stop assay. Methods Mol Biol. 2010;608:65–79.

214. Lormand JD, Buncher N, Murphy CT, Kaur P, Lee MY, Burgers P, et al. DNA polymerase δ stalls on telomeric lagging strand templates independently from G-quadruplex formation. Nucleic Acids Res. 2013;41(22):10323–33.

215. Eddy S, Tillman M, Maddukuri L, Ketkar A, Zafar MK, Eoff RL. Human translesion polymerase kappa exhibits enhanced activity and reduced fidelity two nucleotides from G-quadruplex DNA. Biochemistry. 2016;55(37):5218–29.

216. Edwards DN, Machwe A, Wang Z, Orren DK. Intramolecular telomeric G-quadruplexes dramatically inhibit DNA synthesis by replicative and translesion polymerases, revealing their potential to lead to genetic change. PLoS One. 2014;9(1)

217. Sun D, Guo K, Shin Y-J. Evidence of the formation of G-quadruplex structures in the promoter region of the human vascular endothelial growth factor gene. Nucleic Acids Res. 2011;39(4):1256–65.

218. Beaudoin J-D, Jodoin R, Perreault J-P. In-line probing of RNA G-quadruplexes. Methods. 2013;64(1):79–87.

219. Waldsich C. Dissecting RNA folding by nucleotide analog interference mapping (NAIM). Nat Protoc. 2008;3(5):811–23.

220. Gopinath SCB. Mapping of RNA–protein interactions. Anal Chim Acta. 2009;636(2):117–28.

221. Kwok CK, Sahakyan AB, Balasubramanian S. G-Quadruplexes Structural Analysis using SHALiPE to Reveal RNAG-Quadruplex Formationi nHuman Precursor MicroRNA. AngewChem Int Ed. 2016;55:8958–61.

222. Weldon C, et al. Identification of G-quadruplexes in long functional RNAs using 7-deazaguanine RNA. Nat Chem Biol. 2016;13(1):18–20.

223. Weldon C, Dacanay JG, Gokhale V, Boddupally PVL, Behm-Ansmant I, Burley GA, et al. Specific G-quadruplex ligands modulate the alternative splicing of Bcl-X. Nucleic Acids Res. 2018 ;46(2):886–96.

224. Murchie AIH, Lilley DMJ. Retinoblastoma susceptibility genes contain 5’ sequences with a high propensity to form guanine-tetrad structures. Nucleic Acids Res. 1992;20(1):49–53.

225. Lam EYN, Beraldi D, Tannahill D, Balasubramanian S. G-quadruplex structures are stable and detectable in human genomic DNA. Nat Commun. 2013;4:1796.

226. Hänsel-Hertsch R, Beraldi D, Lensing S V, Marsico G, Zyner K, Parry A, et al. G-quadruplex structures mark human regulatory chromatin. Nat Genet. 2016;48(10):1267–72.

227. Kazemier HG, Paeschke K, Lansdorp PM. Guanine quadruplex monoclonal antibody 1H6 cross-reacts with restrained thymidine-rich single stranded DNA. Nucleic Acids Res. 2017 Jun 2;45(10):5913–9.

228. Chambers VS, Marsico G, Boutell JM, Di Antonio M, Smith GP, Balasubramanian S. High-throughput sequencing of DNA G-quadruplex structures in the human genome. Nat

Biotechnol. 2015;33(8):877–81.

229. Fenouil R, Cauchy P, Koch F, Descostes N, Cabeza JZ, Innocenti C, et al. rG4-seq reveals widespread formation of G-quadruplex structures in the human transcriptome. Nat Methods. 2016;13(10):2399–408.

230. Kwok CK, Balasubramanian S. Targeted Detection of G-Quadruplexes in Cellular RNAs. Angew Chemie Int Ed. 2015;54(23):6751–4.

231. Cáceres JF, Kornblihtt AR. Alternative splicing: multiple control mechanisms and involvement in human disease. Trends Genet. 2002;18(4):186–93.

232. Garcia-Blanco M a, et al. Alternative splicing in disease and therapy. Nat Biotechnol. 2004;22(5):535–46.

233. Tazi J, et al. Alternative splicing and disease. Biochim Biophys Acta - Mol Basis Dis. 2009;1792:14–26.

234. Pajares MJ, et al. Alternative splicing: an emerging topic in molecular and clinical oncology. Lancet Oncol. 2007;8(4):349–57.

235. Wang G-S, Cooper T a. Splicing in disease: disruption of the splicing code and the decoding machinery. Nat Rev Genet. 2007;8(10):749–61.

236. Ward AJ, Cooper TA. The Pathobiology of Splicing. J Pathol. 2010;220:152–63.

237. Scotti MM, Swanson MS. RNA mis-splicing in disease. Nat Rev Genet. 2015;17(1):19–32.

238. Ahmad S, Bhatia K, Kannan A, Gangwani L. Molecular Mechanisms of Neurodegeneration in Spinal Muscular Atrophy. J Exp Neurosci. 2016;10:39–49.

239. Zhou J, Zheng X, Shen H. Targeting RNA-splicing for SMA treatment. Vol. 33, Molecules and Cells. 2012. p. 223–8.

240. Lorson CL, Rindt H, Shababi M. Spinal muscular atrophy: Mechanisms and therapeutic strategies. Hum Mol Genet. 2010;19(R1).

241. Gonzalez JM, Pla D, Perez-Sala D, Andres V. A-type lamins and Hutchinson-Gilford progeria syndrome: pathogenesis and therapy. Front Biosci (Schol Ed). 2011;3:1133–46.

242. Muchir A, Bonne G, van der Kooi a J, van Meegen M, Baas F, Bolhuis PA, et al. Identification of mutations in the gene encoding lamins A/C in autosomal dominant limb girdle muscular dystrophy with atrioventricular conduction disturbances (LGMD1B). Hum Mol Genet.

2000;9(9):1453–9.

243. Todorova A, Halliger-Keller B, Walter MC, Dabauvalle M-C, Lochmüller H, Müller CR. A synonymous codon change in the LMNA gene alters mRNA splicing and causes limb girdle muscular dystrophy type 1B. J Med Genet. 2003;40(10):e115.

244. Vieira NM, Naslavsky MS, Licinio L, Kok F, Schlesinger D, Vainzof M, et al. A defect in the RNA-processing protein HNRPDL causes limb-girdle muscular dystrophy 1G (LGMD1G). Hum Mol Genet [. 2014;23(15):4103–10.

245. Sisakian H. Cardiomyopathies: Evolution of pathogenesis concepts and potential for new therapies. World J Cardiol. 2014;6(6):478.

246. Dellefave L, McNally EM. The genetics of dilated cardiomyopathy. Curr Opin Cardiol. 2010;25(3):198–204.

247. Mestroni L, Brun F, Spezzacatene A, Sinagra G, Taylor MR. GENETIC CAUSES OF DILATED CARDIOMYOPATHY. Prog Pediatr Cardiol. 2014;37(1–2):13–8.

248. Wyles SP, Li X, Hrstka SC, Reyes S, Oommen S, Beraldi R, et al. Modeling structural and functional deficiencies of RBM20 familial dilated cardiomyopathy using human induced pluripotent stem cells. Hum Mol Genet. 2016;25(2):254–65.

249. Streckfuss-Bömeke K, Tiburcy M, Fomin A, Luo X, Li W, Fischer C, et al. Severe DCM phenotype of patient harboring RBM20 mutation S635A can be modeled by patient-specific induced pluripotent stem cell-derived cardiomyocytes. J Mol Cell Cardiol. 2017;113:9–21.

250. Tonino P, Kiss B, Strom J, Methawasin M, Smith JE, Kolb J, et al. The giant protein titin regulates the length of the striated muscle thick filament. Nat Commun. 2017;8(1).

251. Guo W, Schafer S, Greaser ML, Radke MH, Liss M, Govindarajan T, et al. RBM20, a gene for hereditary cardiomyopathy, regulates titin splicing. Nat Med. 2012;18(5):766–73.

252. Rubin BY, Anderson SL. IKBKAP/ELP1 gene mutations: Mechanisms of familial dysautonomia and gene-targeting therapies. Vol. 10, Application of Clinical Genetics. Dove Press; 2017. p. 95–103.

253. Lee G, Papapetrou EP, Kim H, Chambers SM, Tomishima MJ, Fasano CA, et al. Modelling pathogenesis and treatment of familial dysautonomia using patient-specific iPSCs. Nature. 2009;461(7262):402–6.

254. Wein N, Alfano L, Flanigan KM. Genetics and Emerging Treatments for Duchenne and Becker

Muscular Dystrophy. Pediatr Clin North Am. 2015;62(3):723–42.

255. Le Rumeur E, Rumeur E Le. Dystrophin and the two related genetic diseases, Duchenne and Becker muscular dystrophies. Bosn J Basic Med Sci. 2015;15(3):14–20.

256. La Cognata V, D'Agata V, Cavalcanti F, Cavallaro S. Splicing: is there an alternative contribution to Parkinson's disease?. Vol. 16, Neurogenetics. Springer; 2015. p. 245–63.

257. Wszolek ZK, Tsuboi Y, Ghetti B, Pickering-Brown S, Baba Y, Cheshire WP. Frontotemporal dementia and parkinsonism linked to chromosome 17 (FTDP-17). Vol. 1, Orphanet Journal of Rare Diseases. BioMed Central; 2006. p. 30.

258. AVILA J. Role of Tau Protein in Both Physiological and Pathological Conditions. Physiol Rev. 2004;84(2):361–84.

259. Rademakers R, Melquist S, Cruts M, Theuns J, Del-Favero J, Poorkaj P, et al. High-density SNP haplotyping suggests altered regulation of tau gene expression in progressive supranuclear palsy. Hum Mol Genet. 2005;14(21):3281–92.

260. Goedert M. Tau gene mutations and their effects. Vol. 20, Movement Disorders. 2005. p. S45–52.

261. Goedert M, Spillantini MG. Tau mutations in frontotemporal dementia FTDP-17 and their relevance for Alzheimer's disease. Vol. 1502, Biochimica et Biophysica Acta - Molecular Basis of Disease. Elsevier; 2000. p. 110–21.

262. Tanackovic G, Ransijn A, Ayuso C, Harper S, Berson EL, Rivolta C. A missense mutation in PRPF6 causes impairment of pre-mRNA splicing and autosomal-dominant retinitis pigmentosa. Am J Hum Genet. 2011;88(5):643–9.

263. Tanackovic G, Ransijn A, Thibault P, Abou Elela S, Klinck R, Berson EL, et al. PRPF mutations are associated with generalized defects in spliceosome formation and pre-mRNA splicing in patients with retinitis pigmentosa. Hum Mol Genet. 2011;20(11):2116–30.

264. Zhao C, Bellur DL, Lu S, Zhao F, Grassi MA, Bowne SJ, et al. Autosomal-Dominant Retinitis Pigmentosa Caused by a Mutation in SNRNP200, a Gene Required for Unwinding of U4/U6 snRNAs. Am J Hum Genet. 2009;85(5):617–27.

265. Sperling AS, Gibson CJ, Ebert BL. The genetics of myelodysplastic syndrome: from clonal haematopoiesis to secondary leukaemia. Nat Rev Cancer. 2017;17(1):5–19.

266. Jafarifar F, Dietrich RC, Hiznay JM, Padgett RA. Biochemical defects in minor spliceosome

function in the developmental disorder MOPD I. RNA. 2014;20(7):1078–89.

267. Krøigård AB, Jackson AP, Bicknell LS, Baple E, Brusgaard K, Hansen LK, et al. Two novel mutations in RNU4ATAC in two siblings with an atypical mild phenotype of microcephalic osteodysplastic primordial dwarfism type 1. Clin Dysmorphol. 2016;25(2):68–72.

268. Nagy R, Wang H, Albrecht B, Wieczorek D, Gillessen-Kaesbach G, Haan E, et al. Microcephalic osteodysplastic primordial dwarfism type I with biallelic mutations in the RNU4ATAC gene. Clin Genet. 2012;82(2):140–6.

269. Scotter EL, Chen HJ, Shaw CE. TDP-43 Proteinopathy and ALS: Insights into Disease Mechanisms and Therapeutic Targets. Vol. 12, Neurotherapeutics. Springer; 2015. p. 352–63.

270. Geser F, Lee VM-Y, Trojanowski JQ. Amyotrophic lateral sclerosis and frontotemporal lobar degeneration: a spectrum of TDP-43 proteinopathies. Neuropathology. 2010 Apr;30(2):103–12.

271. Rademakers R, Stewart H, Dejesus-Hernandez M, Krieger C, Graff-Radford N, Fabros M, et al. Fus gene mutations in familial and sporadic amyotrophic lateral sclerosis. Muscle Nerve. 2010;42(2):170–6.

272. Bartoletti-Stella A, Gasparini L, Giacomini C, Corrado P, Terlizzi R, Giorgio E, et al. Messenger RNA processing is altered in autosomal dominant leukodystrophy. Hum Mol Genet. 2015;24(10):2746–56.

273. Sveen A, Kilpinen S, Ruusulehto A, Lothe RA, Skotheim RI. Aberrant RNA splicing in cancer; Expression changes and driver mutations of splicing factor genes. Vol. 35, Oncogene. 2016. p. 2413–27.

274. Ctor Climente-Gonzá Lez H, Porta-Pardo E, Godzik A, Correspondence EE, Eyras E. The Functional Impact of Alternative Splicing in Cancer. CellReports. 2017;20:2215–26.

275. Lee SCW, Abdel-Wahab O. Therapeutic targeting of splicing in cancer. Vol. 22, Nature Medicine. 2016. p. 976–86.

276. Singh B, Eyras E. The role of alternative splicing in cancer. Vol. 8, Transcription. 2017. p. 91–8.

277. de Lima Morais DA, Harrison PM. Large-scale evidence for conservation of NMD candidature across mammals. PLoS One. 2010;5(7):e11695.

278. Middleton R, Gao D, Thomas A, Singh B, Au A, Wong JJ-L, et al. IRFinder: Assessing the impact of intron retention on mammalian gene expression. Genome Biol. 2017;18(1):51.

279. Li Y, Bor YC, Misawa Y, Xue Y, Rekosh D, Hammarskjöld ML. An intron with a constitutive transport element is retained in a Tap messenger RNA. Nature. 2006;443(7108):234–7.

280. Bergeron D, Pal G, Beaulieu YB, Chabot B, Bachand F. Regulated Intron Retention and Nuclear Pre-mRNA Decay Contribute to PABPN1 Autoregulation. Mol Cell Biol. 2015;35(14):2503–17.

281. Naro C, Sette C. Timely-regulated intron retention as device to fine-tune protein expression. Vol. 16, Cell Cycle. 2017. p. 1321–2.

282. Yap K, Lim ZQ, Khandelia P, Friedman B, Makeyev E V. Coordinated regulation of neuronal mRNA steady-state levels through developmentally controlled intron retention. Genes Dev. 2012 ;26(11):1209–23.

283. Makeyev E V, Zhang J, Carrasco MA, Maniatis T. The MicroRNA miR-124 Promotes Neuronal Differentiation by Triggering Brain-Specific Alternative Pre-mRNA Splicing. Mol Cell. 2007;27(3):435–48.

284. Wollerton MC, Gooding C, Wagner EJ, Garcia-Blanco MA, Smith CW. Autoregulation of Polypyrimidine Tract Binding Protein by Alternative Splicing Leading to Nonsense-Mediated Decay. Mol Cell. 2004;13(1):91–100.

285. Nicholson P, Mühlemann O. Cutting the nonsense: the degradation of PTC-containing mRNAs. Biochem Soc Trans. 2010;38(6):1615–20.

286. Isken O, Maquat LE. The multiple lives of NMD factors: Balancing roles in gene and genome regulation. Vol. 9, Nature Reviews Genetics. NIH Public Access; 2008. p. 699–712.

287. Boutz PL, Stoilov P, Li Q, Lin CH, Chawla G, Ostrow K, et al. A post-transcriptional regulatory switch in polypyrimidine tract-binding proteins reprograms alternative splicing in developing neurons. Genes Dev. 2007;21(13):1636–52.

288. Spellman R, Llorian M, Smith CWJ. Crossregulation and Functional Redundancy between the Splicing Regulator PTB and Its Paralogs nPTB and ROD1. Mol Cell. 2007;27(3):420–34.

289. Zheng S, Gray EE, Chawla G, Porse BT, O'Dell TJ, Black DL. PSD-95 is post-transcriptionally repressed during early neural development by PTBP1 and PTBP2. Nat Neurosci. 2012;15(3):381–8.

290. Park SK, Zhou X, Pendleton KE, Hunter O V., Kohler JJ, O'Donnell KA, et al. A Conserved Splicing Silencer Dynamically Regulates O-GlcNAc Transferase Intron Retention and O-GlcNAc Homeostasis. Cell Rep. 2017;20(5):1088–99.

291. Kanaji T, et al. A common genetic polymorphism (46 C to T substitution) in the 5'-untranslated region of the coagulation factor XII gene is associated with low translation efficiency and decrease in plasma factor XII level. Blood. 1998;91(6):2010–4.

292. Matafonov A, et al. Factor XII inhibition reduces thrombus formation in a primate thrombosis model. Blood. 2014 Mar 13;123(11):1739–46.

293. Calvo SE, et al. Upstream open reading frames cause widespread reduction of protein expression and are polymorphic among humans. Proc Natl Acad Sci U S A. 2009;106(18):7507–12.

294. Liu L, et al. Mutation of the CDKN2A 5' UTR creates an aberrant initiation codon and predisposes to melanoma. Nat Genet. 1999;21(1):128–32.

295. Bisio A, et al. Functional analysis of CDKN2A/p16INK4a 5'-UTR variants predisposing to melanoma. Hum Mol Genet. 2010;19(8):1479–91.

296. Sözen MM, et al. The molecular basis of familial hypercholesterolaemia in Turkish patients. Atherosclerosis. 2005;180:63–71.

297. Lukowski SW, et al. Disrupted post-transcriptional regulation of the cystic fibrosis transmembrane conductance regulator (CFTR) by a 5'UTR mutation is associated with a CFTR-related disease. Hum Mutat. 2011;32(10):E2266–682.

298. Huopio H, et al. Acute insulin response tests for the differential diagnosis of congenital hyperinsulinism. J Clin Endocrinol Metab. 2002;87(10):4502–7.

299. Braverman N, et al. Mutation Analysis of PEX7 in 60 Probands With Rhizomelic Chondrodysplasia Punctata and Functional Correlations of Genotype With Phenotype. Hum Mutat. 2002;20:284–97.

300. Krude H, et al. Severe early-onset obesity , adrenal insufficiency and red hair pigmentation caused by POMC mutations in humans. Nat Genet. 1998;19:155–7.

301. Tassin J, et al. Levodopa-responsive dystonia. GTP cyclohydrolase I or parkin mutations? Brain. 2000;123 (Pt 6:1112–21.

302. Kit DM. Molecular mechanism of hepcidin deficiency in a patient with juvenile

hemochromatosis. Haematol Hematol J. 2007;92:127–8.

303. Wen Y, et al. Loss-of-function mutations of an inhibitory upstream ORF in the human hairless transcript cause Marie Unna hereditary hypotrichosis. Nat Genet. 2009;41(2):228–33.

304. Ghilardi N, Skoda RC. A single-base deletion in the thrombopoietin (TPO) gene causes familial essential thrombocythemia through a mechanism of more efficient translation of TPO mRNA. Blood. 1999;94:1480–2.

305. Guilardi N, et al. Hereditary thrombocythaemia in a Japanese family is caused by a novel point mutation in the thrombopoietin gene. Br J Haematol. 1999;107:310–6.

306. Sivagnanasundaram S, et al. A cluster of single nucleotide polymorphisms in the 5'-leader of the human dopamine D3 receptor gene (DRD3) and its relationship to schizophrenia. Neurosci Lett. 2000;279:13–6.

307. Pasaje CF, et al. WDR46 is a Genetic Risk Factor for Aspirin-Exacerbated Respiratory Disease in a Korean Population. Allergy Asthma Immunol Res. 2012;4(4):199–205.

308. Beffagna G, et al. Regulatory mutations in transforming growth factor-beta3 gene cause arrhythmogenic right ventricular cardiomyopathy type 1. Cardiovasc Res. 2005;65:366–73.

309. Wethmar K, et al. C / EBPb DuORF mice — a genetic model for uORF-mediated translational control in mammals. Genes Dev. 2010;24:15–20.

310. Brown CY, et. Role of two upstream open reading frames in the translational control of oncogene mdm2. Oncogene. 1999;18(41):5631–7.

311. Mihailovich M, et al. Complex translational regulation of BACE1 involves upstream AUGs and stimulatory elements within the 5' untranslated region. Nucleic Acids Res. 2007;35(9):2975–85.

312. Lareau LF, Brooks AN, Soergel DAW, Meng Q, Brenner SE. The coupling of alternative splicing and nonsense-mediated mRNA decay. Adv Exp Med Biol. 2007;623:190–211.

313. Lejeune F, Maquat LE. Mechanistic links between nonsense-mediated mRNA decay and pre-mRNA splicing in mammalian cells. Vol. 17, Current Opinion in Cell Biology. 2005. p. 309–15.

314. Malabat C, Feuerbach F, Ma L, Saveanu C, Jacquier A. Quality control of transcription start site selection by nonsense-mediated-mRNA decay. Elife. 2015;2015(4):1–59.

315. Kralovicova J, et al. Optimal antisense target reducing INS intron 1 retention is adjacent to a

parallel G quadruplex. Nucleic Acids Res. 2014;42(12):8161–73.

316. Hunter CA. Sequence-dependent DNA Structure. J Mol Biol. 1993 Apr;230(3):1025–54.

317. Ivanov IP, et al. Identification of evolutionarily conserved non-AUG-initiated N-terminal extensions in human coding sequences. Nucleic Acids Res. 2011;39(10):4220–34.

318. Stewart JD, Al E. ABC50 mutants modify translation start codon selection. Biochem J. 2015;467:217–29.

319. Ivanov IP, Loughran G, Atkins JF. uORFs with unusual translational start codons autoregulate expression of eukaryotic ornithine decarboxylase homologs. Proc Natl Acad Sci. 2008;105(29):10079–84.

320. Ingolia NT, Ghaemmaghami S, Newman JRS, Weissman JS. Genome-wide analysis in vivo of translation with nucleotide resolution using ribosome profiling. Science. 2009;324(5924):218–23.

321. Ivanov IP, Loughran G, Sachs MS, Atkins JF. Initiation context modulates autoregulation of eukaryotic translation initiation factor 1 (eIF1). Proc Natl Acad Sci. 2010;107(42):18056–60.

322. Havens M, et. Targeting RNA splicing for disease therapy. Wiley Interdiscip Rev RNA. 2012;29(6):997–1003.

323. Martinovich KM, Shaw NC, Kicic A, Schultz A, Fletcher S, Wilton SD, et al. The potential of antisense oligonucleotide therapies for inherited childhood lung diseases. Mol Cell Pediatr. 2018;5(1):3.

324. Dias N, Stein CA. Antisense oligonucleotides: basic concepts and mechanisms. Mol Cancer Ther. 2002;1(5):347–55.

325. Khvorova A, Watts JK. The chemical evolution of oligonucleotide therapies of clinical utility. Nat Biotechnol. 2017;35(3):238–48.

326. Mansoor M, Melendez AJ. Advances in antisense oligonucleotide development for target identification, validation, and as novel therapeutics. Gene Regul Syst Bio. 2008;2:275–95.

327. Stein CA, Castanotto D. FDA-Approved Oligonucleotide Therapies in 2017. Mol Ther. 2017;25(5):1069–75.

328. Donis-Keller H. Site specific enzymatic cleavage of RNA. Nucleic Acids Res. 1979;7(1):179–92.

329. Crooke ST. Progress in Antisense Technology. Annu Rev Med. 2004;55(1):61–95.

330. Havens MA, Hastings ML. Splice-switching antisense oligonucleotides as therapeutic drugs. Nucleic Acids Res. 2016;44(14):6549–63.

331. Geary RS, Crooke R, Bhanot S, Singleton W. Antisense therapies for cardiovascular/metabolic diseases. Drug Discov Today Ther Strateg. 2013;10(3):e165–70.

332. Rigo F, Seth PP, Bennett CF. Antisense oligonucleotide-based therapies for diseases caused by pre-mRNA processing defects. Adv Exp Med Biol. 2014;825:303–52.

333. Lukasz J. Kielpinki, Peter H. Hagedorn, Morten Lindow, Jeppe Vinther. RNase H sequence preferences influence antisense oligonucleotide efficiency. Nucleic Acids Res. 2017;45(22):12932–44.

334. Liang XH, Sun H, Nichols JG, Crooke ST. RNase H1-Dependent Antisense Oligonucleotides Are Robustly Active in Directing RNA Cleavage in Both the Cytoplasm and the Nucleus. Mol Ther. 2017;25(9):2075–92.

335. Liang X-H, Nichols JG, Sun H, Crooke ST. Translation can affect the antisense activity of RNase H1-dependent oligonucleotides targeting mRNAs. Nucleic Acids Res [. 2017;46(10):293–313.

336. Coelho AI, Lourenço S, Trabuco M, Silva MJ, Oliveira A, Gaspar A, et al. Functional correction by antisense therapy of a splicing mutation in the GALT gene. Eur J Hum Genet. 2015;23(4):500–6.

337. Tasfaout H, Buono S, Guo S, Kretz C, Messaddeq N, Booten S, et al. Antisense oligonucleotide-mediated Dnm2 knockdown prevents and reverts myotubular myopathy in mice. Nat Commun. 2017;8:15661.

338. Liang X, Shen W, Sun H, Migawa MT, Vickers TA, Crooke ST. Translation efficiency of mRNAs is increased by antisense oligonucleotides targeting upstream open reading frames. Nat Biotechnol. 2016;34(8):875–80.

339. Henry SP, Miner RC, Drew WL, Fitchett J, York-Defalco C, Rapp LM, et al. Antiviral activity and ocular kinetics of antisense oligonucleotides designed to inhibit CMV replication. Invest Ophthalmol Vis Sci. 2001;42(11):2646–51.

340. Toth PP. Emerging LDL therapies: Mipomersen - Antisense oligonucleotide therapy in the management of hypercholesterolemia. J Clin Lipidol. 2013;7(3 SUPPL.).

341. Parhofer KG. Mipomersen: evidence-based review of its potential in the treatment of

homozygous and severe heterozygous familial hypercholesterolemia. Core Evid. 2012;7:29–38.

342. Davies JL, et al. A genome-wide search for human type 1 diabetes susceptibility genes. Vol. 371, Nature. 1994. p. 130–6.

343. Of D, Mellitus D. Diagnosis and classification of diabetes mellitus. Diabetes Care. 2014;37(SUPPL.1):81–90.

344. Bastaki S. Diabetes mellitus and its treatment. Int J Diabetes Metab. 2005;13(3):111–34.

345. ASSOCIATION AD. Diagnosis and Classification of Diabetes Mellitus. Diabetes Care. 2004;27(Suppl 1):S5–10.

346. Diabetes DOF. Diagnosis and classification of diabetes mellitus. Diabetes Care. 2010;33(SUPPL. 1):S62–9.

347. Wållberg M, Cooke A. Immune mechanisms in type 1 diabetes. Trends Immunol. 2013;34(12):583–91.

348. Pociot F, McDermott MF. Genetics of type 1 diabetes mellitus. Genes Immun. 2002;3:235–49.

349. Ramachandran A. Know the signs and symptoms of diabetes. Indian J Med Res. 2014 Nov;140(5):579–81.

350. Precechtelova J, et al. Type I Diabetes Mellitus: Genetic Factors and Presumptive Enteroviral Etiology or Protection. J Pathog. 2014;2014:1–21.

351. Bonifacio E. Predicting type 1 diabetes using biomarkers. Diabetes Care. 2015;38(6):989–96.

352. Regnell SE, Lernmark Å. Early prediction of autoimmune (type 1) diabetes. Diabetologia. 2017;1–12.

353. Knip M, Simell O. Environmental triggers of type 1 diabetes. Cold Spring Harb Perspect Biol. 2011;3(10):1–15.

354. Cerosaletti K, Buckner JH. Protein tyrosine phosphatases and type 1 diabetes: genetic and functional implications of PTPN2 and PTPN22. Rev Diabet Stud. 2012;9(4):188–200.

355. Tang W, et al. Association of common polymorphisms in the IL2RA gene with type 1 diabetes: Evidence of 32,646 individuals from 10 independent studies. J Cell Mol Med. 2015;19(10):2481–8.

356. Pugliese A, et al. HLA-DRB1∗15:01-DQA1∗01:02-DQB1∗06:02 haplotype protects autoantibody-positive relatives from type 1 diabetes throughout the stages of disease progression. Diabetes. 2016;65(4):1109–19.

357. Coppieters KT, et al. Demonstration of islet-autoreactive CD8 T cells in insulitic lesions from recent onset and long-term type 1 diabetes patients. J Exp Med. 2012;209(1):51–60.

358. Jr JC, et al. The Immune System in Health and Disease. 5th edition. New York: Garland Science. 2001.

359. Pathiraja V, et al. Proinsulin-specific, HLA-DQ8, and HLA-DQ8-transdimer-restricted CD4+ T cells infiltrate islets in type 1 diabetes. Diabetes. 2015;64(1):172–82.

360. Steiner DF, et al. Structure and evolution of the insulin gene. Ann Rev Genet. 1985;19:463–84.

361. Sander M, German MS. The beta cell transcription factors and development of the pancreas. J Mol Med. 1997;75:327–40.

362. Owerbach D, et al. The insulin gene is located on the short arm of chromosome 11 in humans. Diabetes. 1981;30:267–70.

363. Owebach D, et al. The insulin gene is located on chromosome 11 in humans. Nature. 1980;286:82–4.

364. Bell GI, et al. Sequence of the human insulin gene. Nature. 1980;284(5751):26–32.

365. Wang J, et al. Regulation of insulin preRNA splicing by glucose. Proc Natl Acad Sci U S A. 1997;94(9):4360–5.

366. Lu S, Cullen BR. Analysis of the stimulatory effect of splicing on mRNA production and utilization in mammalian cells. RNA. 2003 May;9(5):618–30.

367. Mansilla A, et al. Developmental regulation of a proinsulin messenger RNA generated by intron retention. EMBO Rep. 2005;6(12):1182–7.

368. Arrighi FE, et al. Buoyant densities of DNA of mammals. Biochem Genet. 1970;4(3):367–76.

369. Evans-Molina C, et al. Glucose regulation of insulin gene transcription and pre-mRNA processing in human islets. Diabetes. 2007;56:827–35.

370. Shalev A, et al. A Proinsulin Gene Splice Variant with Increased Translation Efficiency Is Expressed in Human Pancreatic Islets. Endocrinology. 2002 Jul 1;143(7):2541–7.

371. Bennett ST, et al. Susceptibility to human type 1 diabetes at IDDM2 is determined by tandem repeat variation at the insulin gene minisatellite locus. Nat Genet. 1995;9(3):284–92.

372. Marchand L, Polychronakos C. Evaluation of polymorphic splicing in the mechanism of the association of the insulin gene with diabetes. Diabetes. 2007;56(3):709–13.

373. Kralovicova J, et al. Variants in the Human Insulin Gene That Affect Pre-mRNA Splicing Is −23HphI a Functional Single Nucleotide Polymorphism at IDDM2? Diabetes. 2006;55:260–4.

374. Barratt BJ, et al. Remapping the insulin gene/IDDM2 locus in type 1 diabetes. Diabetes. 2004;53:1884–9.

375. Alizadeh BZ, Koeleman BPC. Genetic polymorphisms in susceptibility to Type 1 Diabetes. Clin Chim Acta. 2008;387(1–2):9–17.

376. Kikin O, D'Antonio L, Bagga PS. QGRS Mapper: A web-based server for predicting G-quadruplexes in nucleotide sequences. Nucleic Acids Res. 2006;34(WEB. SERV. ISS.):676–82.

377. Bellaousov S, et al. RNAstructure: Web servers for RNA secondary structure prediction and analysis. Nucleic Acids Res. 2013;41(Web Server issue):471–4.

378. Abdi HH. The Bonferonni and Šidák Corrections for Multiple Comparisons. Encycl Meas Stat. 2007;1:103–7.

379. Haynes W. Tukey's Test. In: Encyclopedia of Systems Biology. New York, NY: Springer New York; 2013. p. 2303–4.

380. McDonald JH. Fisher's exact test of independence. In: Handbook of Biological Statistics. 2nd editio. Baltimore, Maryland: Sparky House Publishing; 2009. p. 70–5.

381. Sawilowsky SS. The Probable Difference Between Two Means When σ_1^2≠σ_2^2. J Mod Appl Stat Methods. 2002;1(2):461–72.

382. MacFarland TW, Yates JM. Friedman Twoway Analysis of Variance (ANOVA) by Ranks. In: Introduction to Nonparametric Statistics for the Biological Sciences Using R. Cham: Springer International Publishing; 2016. p. 213–47.

383. Oliveira LM, et al. Insulin glycation by methylglyoxal results in native-like aggregation and inhibition of fibril formation. BMC Biochem. 2011;12(1):41–53.

384. Matthew Biancalana SK. Molecular Mechanism of Thioflavin-T Binding to Amyloid Fibrils. Biochim Biophys Acta. 2010;1804(7):1405–12.

385. Reinke A, Gestwicki J. Insight into Amyloid Structure Using Chemical Probes. Chem Biol Drug Des. 2011;77(6):399–411.

386. Kuznetsova IM, et al. Analyzing thioflavin t binding to amyloid fibrils by an equilibrium microdialysis-based technique. PLoS One. 2012;7(2):1–8.

387. Tu LH, et al. Mutational analysis of the ability of resveratrol to inhibit amyloid formation by islet amyloid polypeptide: Critical evaluation of the importance of aromatic-inhibitor and histidine-inhibitor interactions. Biochemistry. 2015;54(3):666–76.

388. Saccà B, Lacroix L, Mergny J-L. The effect of chemical modifications on the thermal stability of different G-quadruplex-forming oligonucleotides. Nucleic Acids Res. 2005;33(4):1182–92.

389. Bhasikuttan AC. Thioflavin T as an Efficient Inducer and Selective Fluorescent Sensor for the Human Telomeric G-Quadruplex DNA. J. 2013;135(3670376).

390. Tong LL, et al. Stable label-free fluorescent sensing of biothiols based on ThT direct inducing conformation-specific G-quadruplex. Biosens Bioelectron. 2013;49:420–5.

391. Chen J, et al. Label-free fluorescent biosensor based on the target recycling and Thioflavin T-induced quadruplex formation for short DNA species of c-erbB-2 detection. Anal Chim Acta. 2014;817:42–7.

392. Li Y, et al. Thioflavin T as a fluorescence light-up probe for both parallel and antiparallel G-quadruplexes of 29-mer thrombin binding aptamer. Anal Bioanal Chem. 2016;408(28):8025–36.

393. Henderson E, et al. Telomeric DNA oligonucleotides form novel intramolecular structures containing guanine-guanine base pairs. Cell. 1987;51(6):899–908.

394. Sen D, Gilbert W. Formation of parallel four-stranded complexes by guanine-rich motifs in DNA and its implications for meiosis. Nature. 1988;334(6180):364–6.

395. Noor H, Cao P, Raleigh DP. Morin hydrate inhibits amyloid formation by islet amyloid polypeptide and disaggregates amyloid fibers. Protein Sci. 2012;21(3):373–82.

396. Marathias VM, Bolton PH. Determinants of DNA quadruplex structural type: Sequence and potassium binding. Biochemistry. 1999;38(14):4355–64.

397. Granqvist L, Virta P. Characterization of G-Quadruplex/Hairpin Transitions of RNAs by19F NMR Spectroscopy. Chem - A Eur J. 2016;22(43):15360–72.

398. Zhang AYQ, et al. A sequence-independent analysis of the loop length dependence of intramolecular RNA G-quadruplex stability and topology. Biochemistry. 2011;50(33):7251–8.

399. Bugaut A, Balasubramanian S. A sequence-independent study of the influence of short loop lengths on the stability and topology of intramolecular DNA G-quadraplexes. Biochemistry. 2008;47(2):689–97.

400. Hazel P, et al. Loop-length-dependent folding of G-quadruplexes. J Am Chem Soc. 2004;126(50):16405–15.

401. Xu Y, et al. T-loop formation by human telomeric G-quadruplex. Nucleic Acids Symp Ser. 2007;51(51):243–4.

402. Guédin A, et al. How long is too long? Effects of loop size on G-quadruplex stability. Nucleic Acids Res. 2010;38(21):7858–68.

403. Rachwal PA, et al. Sequence effects of single base loops in intramolecular quadruplex DNA. FEBS Lett. 2007;581(8):1657–60.

404. Yakovchuk P, et al. Base-stacking and base-pairing contributions into thermal stability of the DNA double helix. Nucleic Acids Res. 2006;34(2):564–74.

405. Assenberg R, et al. Sequence-dependent folding of DNA three-way junctions. Nucleic Acids Res. 2002 Dec 1;30(23):5142–50.

406. Guédin A, Alberti P, Mergny JL. Stability of intramolecular quadruplexes: Sequence effects in the central loop. Nucleic Acids Res. 2009;37(16):5559–67.

407. Zhang X-Y, et al. K + and Na + -Induced Self-Assembly of Telomeric Oligonucleotide d(TTAGGG) n. J Biomol Struct Dyn. 2003;20(5):693–701.

408. Šket P, Črnugelj M, Plavec J. D(G 3T 4G 4) forms unusual dimeric G-quadruplex structure with the same general fold in the presence of K +, Na + or NH 4 + ions. Bioorganic Med Chem. 2004;12(22):5735–44.

409. Cheng Q, Benson DR, Rivera M, Kuczera K. Formation and Temperature Stability of G-Quadruplex Structures Formation and Temperature Stability of G-Quadruplex Structures Studied Studied by Electronic and Vibrational Circular Dichroism by Electronic and Vibrational Circular Dichroism Spectroscopy Co. Biopolymers. 2007;83(2):144–52.

410. Williamson JR, Raghuraman MK, Cech TR. Monovalent cation-induced structure of telomeric

DNA: The G-quartet model. Cell. 1989;59(5):871–80.

411. Miyoshi D, et al. Effect of divalent cations on antiparallel G-quartet structure of d(G4T4G4). FEBS Lett. 2001;496(2–3):128–33.

412. Zhang Z, Gaffney BL, Jones RA. c-di-GMP displays A monovalent metal ion-dependent polymorphism. J Am Chem Soc. 2004;126(51):16700–1.

413. Sabharwal NC, et al. N-methylmesoporphyrin IX fluorescence as a reporter of strand orientation in guanine quadruplexes. FEBS J. 2014;281(7):1726–37.

414. Miyoshi D, Matsumura S, Li W, Sugimoto N. Structural Polymorphism of Telomeric DNA Regulated by pH and Divalent Cation. Nucleosides Nucleotides Nucleic Acids [Internet]. 2003;22(2):203–21. Available from: www.dekker.com

415. Schiavone D, et al. Determinants of G quadruplex-induced epigenetic instability in REV1-deficient cells. EMBO J. 2014 Nov 3;33(21):2507–20.

416. Zhang AYQ, Balasubramanian S. The kinetics and folding pathways of intramolecular G-quadruplex nucleic acids. J Am Chem Soc. 2012;134(46):19297–308.

417. Kuo MHJ, Wang ZF, Tseng TY, Li MH, Hsu STD, Lin JJ, et al. Conformational transition of a hairpin structure to G-quadruplex within the WNT1 gene promoter. J Am Chem Soc. 2015;137(1):210–8.

418. Balasubramanian S, Hurley LH. Targeting G-quadruplexes in gene promoters : a novel anticancer. Nat Rev Drug Discov. 2011;10(4):261–75.

419. Marušič M, Plavec J. The Effect of DNA Sequence Directionality on G-Quadruplex Folding. Angew Chemie - Int Ed. 2015;54(40):11716–9.

420. Gomez D, et al. Telomerase downregulation induced by the G-quadruplex ligand 12459 in A549 cells is mediated by hTERT RNA alternative splicing. Nucleic Acids Res. 2004;32(1):371–9.

421. Bugaut A, Murat P, Balasubramanian S. An RNA hairpin to g-quadruplex conformational transition. J Am Chem Soc. 2012;134(49):19953–6.

422. Ageely EA, Kartje ZJ, Rohilla KJ, Barkau CL, Gagnon KT. Quadruplex-Flanking Stem Structures Modulate the Stability and Metal Ion Preferences of RNA Mimics of GFP. ACS Chem Biol. 2016;11(9):2398–406.

423. Pan T, Sosnick T. RNA folding during transcription. Annu Rev Biophys Biomol Struct. 2006;35:161–75.

424. Chheda N, Gupta MK. RNA as a Permutation. arXiv.org [Internet]. 2014;(March). Available from: http://arxiv.org/pdf/1403.5477v1.pdf

425. Endoh T, Rode AB, Takahashi S, Kataoka Y, Kuwahara M, Sugimoto N. Real-Time Monitoring of G-Quadruplex Formation during Transcription. Anal Chem. 2016;88(4):1984–9.

426. Woodson SA, Koculi E. Analysis of RNA Folding by Native Polyacrylamide Gel Electrophoresis. 1st ed. Vol. 469, Biophysical, Chemical, and Functional Probes of RNA Structure, Interactions and Folding: Part B. Elsevier Inc.; 2009. 189-208 p.

427. Matera AG, Wang Z. A day in the life of the spliceosome. Nat Rev Mol Cell Biol. 2014;15(2):108–21.

428. Bendak K, et al. A rapid method for assessing the RNA-binding potential of a protein. Nucleic Acids Res. 2012;40(14):1–11.

429. Walter BL, Parsley TB, Ehrenfeld E, Semler BL. Distinct poly(rC) binding protein KH domain determinants for poliovirus translation initiation and viral RNA replication. J Virol. 2002;76(23):12008–22.

430. Jang S-W, Liu X, Fu H, Rees H, Yepes M, Levey A, et al. Interaction of Akt-phosphorylated SRPK2 with 14-3-3 mediates cell cycle and cell death in neurons. J Biol Chem. 2009;284(36):24512–25.

431. Edmond V, Moysan E, Khochbin S, Matthias P, Brambilla C, Brambilla E, et al. Acetylation and phosphorylation of SRSF2 control cell fate decision in response to cisplatin. EMBO J. 2011;30(3):510–23.

432. Wang J, Gao Q-S, Wang Y, Lafyatis R, Stamm S, Andreadis A. Tau exon 10, whose missplicing causes frontotemporal dementia, is regulated by an intricate interplay of cis elements and trans factors. J Neurochem. 2004;88(5):1078–90.

433. Yin X, Jin N, Gu J, Shi J, Zhou J, Gong C-X, et al. Dual-specificity tyrosine phosphorylation-regulated kinase 1A (Dyrk1A) modulates serine/arginine-rich protein 55 (SRp55)-promoted Tau exon 10 inclusion. J Biol Chem. 2012;287(36):30497–506.

434. Jensen MA, Wilkinson JE, Krainer AR. Splicing factor SRSF6 promotes hyperplasia of sensitized skin. Nat Struct Mol Biol. 2014;21(2):189–97.

435. Samatanga B, Dominguez C, Jelesarov I, Allain FHT. The high kinetic stability of a G-quadruplex limits hnRNP F qRRM3 binding to G-tract RNA. Nucleic Acids Res. 2013;41(4):2505–16.

436. Klass DM, et al. Quantitative proteomic analysis reveals concurrent RNA-protein interactions and identifies new RNA-binding proteins in Saccharomyces cerevisiae. Genome Res. 2013 Jun;23(6):1028–38.

437. Yeh F-L, Tung L, Chang T-H. Detection of Protein–Protein Interaction Within an RNA–Protein Complex Via Unnatural-Amino-Acid-Mediated Photochemical Crosslinking. In: Methods in molecular biology (Clifton, NJ). 2016. p. 175–89.

438. Pires MM, et al. The network organization of protein interactions in the spliceosome is reproduced by the simple rules of food-web models. Sci Rep. 2015;5(March):14865.

439. Chan S-P, et al. The Prp19p-Associated Complex in Spliceosome Activation. Science (80-). 2003 Oct 10;302(5643):279–82.

440. Will CL, Luhrmann R. Spliceosome Structure and Function. Cold Spring Harb Perspect Biol. 2011 Jul 1;3(7):a003707–a003707.

441. Park S, et al. Evolutionary history of human disease genes reveals phenotypic connections and comorbidity among genetic diseases. Sci Rep. 2012;2:757–63.

442. Stewart JD, et al. ABC50 mutants modify translation start codon selection. Biochem J. 2015;467(2):217–29.

443. Peabody DS. Translation initiation at non-AUG triplets in mammalian cells. J Biol Chem. 1989;264(9):5031–5.

444. Jin Y, Yang Y, Zhang P. New insights into RNA secondary structure in the alternative splicing of pre-mRNAs. RNA Biol. 2011;8(3):450–7.

445. Mortimer SA, et al. Insights into RNA structure and function from genome-wide studies. Nat Rev Genet. 2014;15(7):469–79.

446. Ding Y, et al. In vivo genome-wide profiling of RNA secondary structure reveals novel regulatory features. Nature. 2013;505(7485):696–700.

447. Sugimoto S, et al. Thioflavin T as a fluorescence probe for monitoring RNA metabolism at molecular and cellular levels. Nucleic Acids Res. 2015;43(14).

448. Yan Y-Y, et al. G-Quadruplex conformational change driven by pH variation with potential application as a nanoswitch. Biochim Biophys Acta - Gen Subj. 2013 Oct;1830(10):4935–42.

449. Tuntiwechapikul W, et al. The influence of pH on the G-quadruplex binding selectivity of perylene derivatives. Bioorg Med Chem Lett. 2006 Aug;16(15):4120–6.

450. Petrovic AG, Polavarapu PL. Quadruplex structure of polyriboinosinic acid: Dependence on alkali metal ion concentration, pH and temperature. J Phys Chem B. 2008;112(7):2255–60.

451. Galer P, et al. Reversible pH Switch of Two-Quartet G-Quadruplexes Formed by Human Telomere. Angew Chemie Int Ed. 2016 Feb 5;55(6):1993–7.

452. Tippana R, Xiao W, Myong S. G-quadruplex conformation and dynamics are determined by loop length and sequence. Nucleic Acids Res. 2014;42(12):8106–14.

453. Creacy SD, et al. G4 resolvase 1 binds both DNA and RNA tetramolecular quadruplex with high affinity and is the major source of tetramolecular quadruplex G4-DNA and G4-RNA resolving activity in HeLa cell lysates. J Biol Chem. 2008 Dec 12;283(50):34626–34.

454. Henderson A, et al. Detection of G-quadruplex DNA in mammalian cells. Nucleic Acids Res. 2014 Jan 1;42(2):860–9.

455. Liu H, et al. RNA G-quadruplex formation in defined sequence in living cells detected by bimolecular fluorescence complementation. Chem Sci. 2016 Jun 21;7(7):4573–81.

456. Larkin MA, Blackshields G, Brown NP, Chenna R, Mcgettigan PA, McWilliam H, et al. Clustal W and Clustal X version 2.0. Bioinformatics. 2007;23(21):2947–8.

457. Kozak M. Initiation of translation in prokaryotes and eukaryotes. Gene. 1999;234:187–208.

458. Kozak M. Point mutations define a sequence flanking the AUG initiator codon that modulates translation by eukaryotic ribosomes. Cell. 1986;44(2):283–92.

459. Reuter JS, Mathews DH. RNAstructure: software for RNA secondary structure prediction and analysis. BMC Bioinformatics. 2010;11(1):129.

VIII. Appendices

Appendix A Supplementary figures

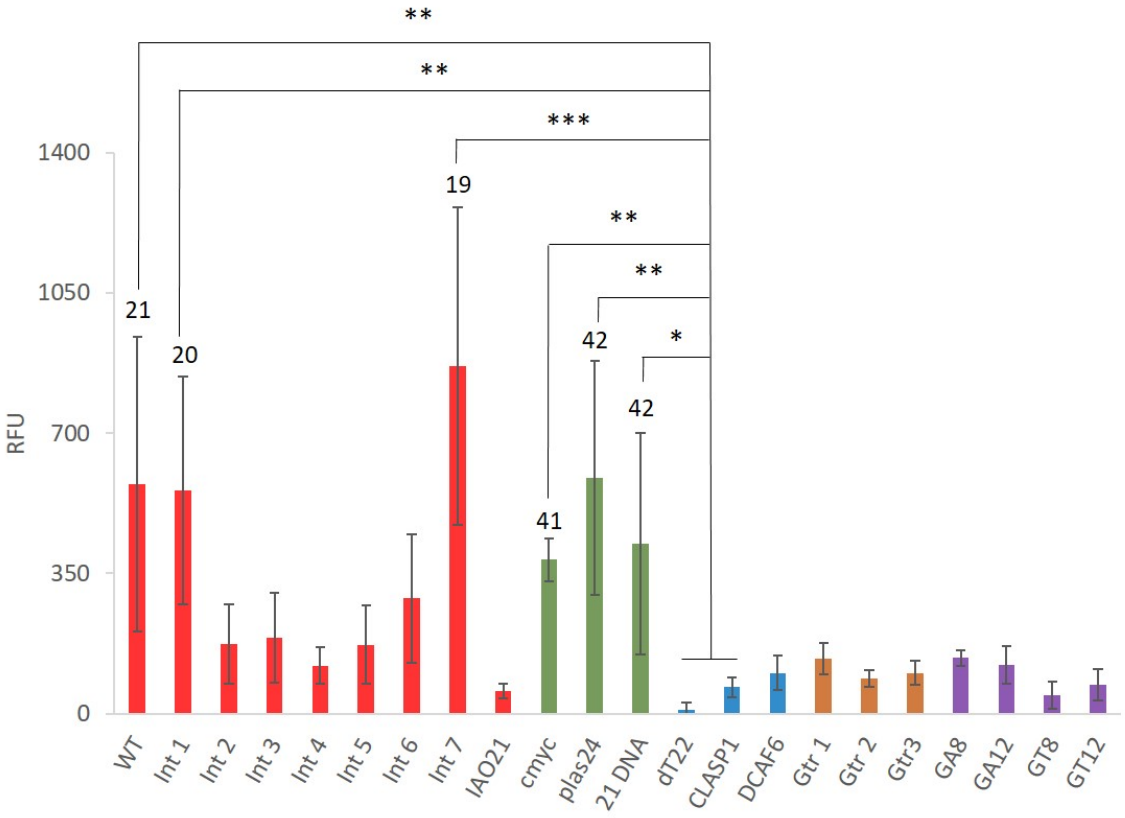

Figure 32 – Preliminary screening of G1 formation propensity using ThT fluorescence.

Mean fluorescence intensity of 2 µM ThT at 508 nm in the presence of indicated oligonucleotides at 1 µM. Positive controls are in green, negative controls in blue. Controls for ThT binding to G-tract are in orange and ThT binding according to the number of Gs in purple. Tested oligos are in red. Fluorescence intensity of the dye was removed from all samples. Error bars denote the standard deviation from five independent fluorescence assays. Asterisks denote p-values ≤ 0.05 (*), ≤ 0.01 (**) or ≤ 0.001 (***).

Figure 33 – Nucleotide sequence of AmpliScribe™ T7-Flash™ Transcription Kit control template. Segments predicted by QGRS mapper to form G-quadruplex structures, with G-scores of 12, 17 and 16, respectively, are highlighted in yellow and nucleotides involved in Hoogsteen interactions are underlined.

```
FRRM1       ----------VVKLRGLPWSCSVEDVQNFLSDCTIHDGAAGVHFIYTREGRQSGEAFVELGSEDDVKMALKKDR
FRRM2       SNSADSANDGFVRLRGLPFGCTKEEIVQFFSGLEIVP--NGITLPVDPEGKITGEAFVQFASQELAEKALGKHK
FRRM3       EFTVQSTTGHCVHMRGLPYKATENDIYNFFSPLNPV----RVHIEIGPDGRVTGEADVEFATHEEAVAAMSKDR
H1RRM1      ---------FVVKVRGLPWSCSADEVQRFFSDCKIQNGAQGIRFIYTREGRPSGEAFVELESEDEVKLALKKDR
H1RRM2      ---------GFVRLRGLPFGCSKEEIVQFFSGLEIVP--NGITLPVDFQGRSTGEAFVQFASQEIAEKALKKHK
H1RRM3      ----QSTTGHCVHMRGLPYRATENDIYNFFSPLNPV----RVHIEIGPDGRVTGEADVEFATHEDAVAAMSKDK
                      *::****: .: ::: .*:*          : :    :*: :*** *:: :.: .  *: *.

FRRM1       ESMGHRYIEVF-----------------------------------
FRRM2       ERIGHRYIEVFKSSQEEVRSY-------------------------
FRRM3       ANMQHRYIELFLNSTTGASNGAYSSQV-------------------
H1RRM1      ETMGHRYVEVFKSNN-------------------------------
H1RRM2      ERIGHRYIEIFKSSR-------------------------------
H1RRM3      ANMQHRYVELFLNSTAGASGGAYEHRYVELFLNSTAGASGGAYGSQM
            :  : ***:*:*
```

Figure 34 – Multiple alignment of amino acid sequences of hnRNP F and H1 RRM constructs. Multiple alignment of sequences was performed at Clustal Omega web service from © EMBL-EBI. Conserved aminoacids (“*”) are highlighted in grey. The “:” (colons) denote aminoacid conservation between groups with strong similar properties. The “.” (periods) indicate aminoacid conservation between groups of weakly similar properties (456).

Appendix A

>hnRNP F

ATGggcagcagccatcatcatcatcacagcagcggcctggtgccgcgcggcagccatatggctagcatgactggtggacagcaaatgggtcgcggatccgaaaatttgtatttccaaggagagctcatgATGCTGGGCC
CTGAGGGAGGTGAAGGCTTTGTGGTCAAGCTCCGTGGCCTGCCCTGGTCCTGCTCTGTTGAGGACGTGCAGAACTTCCTCTCTGACTGCACGATTCATGATGGGGCCGCAGGT
GTCCATTTCATCTACACTAGAGAGGGCAGGCAGAGTGGTGAGGCTTTTGTTGAACTTGGATCAGAAGATGATGTAAAAATGGCCCTGAAAAAAGACAGGGAAAGCATGGGAC
ACCGGTACATTGAGGTGTTCAAGTCCCACAGAACCGAGATGGATTGGGTGTTGAAGCACAGTGGTCCCAACAGTGCCGACAGCGCCAACGATGGCTTCGTGCGGCTTCGAGG
ACTCCCATTTGGATGCACAAAGGAAGAAATTGTTCAGTTCTTCTCAGGGTTGGAAATTGTGCCAAACGGGATCACATTGCCTGTGGACCCCGAAGGCAAGATTACAGGGGAAG
CGTTCGTGCAGTTTGCCTCGCAGGAGTTAGCTGAGAAGGCTCTAGGGAAACACAAGGAGAGGATAGGGCACAGGTACATTGAGGTGTTTAAGAGCAGCCAGGAGGAAGTTA
GGTCATACTCAGATCCCCCTCTGAAGTTCATGTCCGTGCAGCGGCCAGGGCCCTATGACCGGCCCGGGACTGCCAGGAGGTACATTGGCATCGTGAAGCAGGCAGGCCTGGA
AAGGATGAGGCCTGGTGCCTACAGCACAGGCTACGGGGGCTACGAGGAGTACAGTGGCCTCAGTGATGGCTACGGCTTCACCACCGACCTGTTCGGGAGAGACCTCAGCTAC
TGTCTCTCCGGAATGTATGACCACAGATACGGCGACAGTGAGTTCACAGTGCAGAGCACCACAGGCCACTGTGTCCACATGAGGGGCCTGCCGTACAAAGCGACCGAGAACG
ACACTTACAACTTCTTCTCTCCTCTCAACCCTGTGAGAGTCCATATTGAGATTGGCCCAGATGGAAGAGTGACGGGTGAAGCAGATGTTGAGTTTGCTACTCATGAAGAAGCTG
TGGCAGCTATGTCCAAAGACAGGGCCAATATGCAGCACAGATATATAGAACTCTTCTTGAATTCAACAACAGGGGCCAGCAATGGGGCGTATAGCAGCCAGGTGATGCAAGG
CATGGGGGTGTCTGCTGCCCAGGCCACTTACAGTGGCCTGGAGAGCCAGTCAGTGAGTGGCTGTTACGGGGCCGGCTACAGTGGGCAGAACAGCATGGGTGGCTATGACTA
GAAGCTT

>hnRNP H1

ATGggcagcagccatcatcatcatcatcacagcagcggcctggtgccgcgcggcagccatatggctagcatgactggtggacagcaaatgggtcgcggatccga
aaatttgtatttccaaggagagctcatgATGTTGGGCACGGAGGGTGGAGAGGGATTCGTGGTGAAGGTCCGGGGCTTGCCCTGGTCTTGCTCGGCCGATGAAG
TGCAGAGGTTTTTTTCTGACTGCAAAATTCAAAATGGGGCTCAAGGTATTCGTTTCATCTACACCAGAGAAGGCAGACCAAGTGGCGAGGCTTTTGTTGAACTT
GAATCAGAAGATGAAGTCAAATTGGCCCTGAAAAAAGACAGAGAAACTATGGGACACAGATATGTTGAAGTATTCAAGTCAAACAACGTTGAAATGGATTGGGT
GTTGAAGCATACTGGTCCAAATAGTCCTGACACGGCCAATGATGGCTTTGTACGGCTTAGAGGACTTCCCTTTGGATGTAGCAAGGAAGAAATTGTTCAGTTCT
TCTCAGGGTTGGAAATCGTGCCAAATGGGATAACATTGCCGGTGGACTTCCAGGGGAGGAGTACGGGGGAGGCCTTCGTGCAGTTTGCTTCACAGGAAATAGCT
GAAAAGGCTCTAAAGAAACACAAGGAAAGAATAGGGCACAGGTATATTGAAATCTTTAAGAGCAGTAGAGCTGAAGTTAGAACTCATTATGATCCACCACGAAA
GCTTATGGCCATGCAGCGGCCAGGTCCTTATGACAGACCTGGGGCTGGTAGAGGGTATAACAGCATTGGCAGAGGAGCTGGCTTTGAGAGGATGAGGCGTGGTG
CTTATGGTGGAGGCTATGGAGGCTATGATGATTACAATGGCTATAATGATGGCTATGGATTTGGGTCAGATAGATTTGGAAGAGACCTCAATTACTGTTTTTCA
GGAATGTCTGATCACAGATACGGGGATGGTGGCTCTACTTTCCAGAGCACAACAGGACACTGTGTACACATGCGGGGATTACCTTACAGAGCTACTGAGAATGA
CATTTATAATTTTTTTTCACCGCTCAACCCTGTGAGAGTACACATTGAAATTGGTCCTGATGGCAGAGTAACTGGTGAAGCAGATGTCGAGTTCGCAACTCATG
AAGATGCTGTGGCAGCTATGTCAAAAGACAAAGCAAATATGCAACACAGATATGTAGAACTCTTCTTGAATTCTACAGCAGGAGCAAGCGGTGGTGCTTACGAA
CACAGATATGTAGAACTCTTCTTGAATTCTACAGCAGGAGCAAGCGGTGGTGCTTATGGTAGCCAAATGATGGGAGGCATGGGCTTGTCAAACCAGTCCAGCTA
CGGGGGCCCAGCCAGCCAGCAGCTGAGTGGGGGTTACGGAGGCGGCTACGGTGGCCAGAGCAGCATGAGTGGATACGACCAAGTTTTACAGGAAAACTCCAGTG
ATTTTCAATCaaaCATTGCATGACTCGAG

>F RRM 1

ATGggcagcagccatcatcatcatcatcacagcagcggcctggtgccgcgcggcagccatatggctagcatgactggtggacagcaaatgggtcgcggatccgaa
aatttgtatttccaaggagagctcagtGTGGTCAAGCTCCGTGGCCTGCCCTGGTCCTGCTCTGTTGAGGACGTGCAGAACTTCCTCTCTGACTGCACGATTCAT
GATGGGGCCGCAGGTGTCCATTTCATCTACACTAGAGAGGGCAGGCAGAGTGGTGAGGCTTTTGTTGAACTTGGATCAGAAGATGATGTAAAAATGGCCCTGAAA
AAAGACAGGGAAAGCATGGGACACCGGTACATTGAGGTGTTCTGAaagctt

>F RRM 2

ATGggcagcagccatcatcatcatcatcacagcagcggcctggtgcctctcttcatccatatggctagcatgactggtggacagcaaatgggtcgcggatccgaa
aatttgtatttccaaggagagctcAGTAACAGTGCCGACAGCGCCAACGATGGCTTCGTGCGGCTTCGAGGACTCCCATTTGGATGCACAAAGGAAGAAATTGTT
CAGTTCTTCTCAGGGTTGGAAATTGTGCCAAACGGGATCACATTGCCTGTGGACCCCGAAGGCAAGATTACAGGGGAAGCGTTCGTGCAGTTTGCCTCGCAGGAG
TTAGCTGAGAAGGCTCTAGGGAAACACAAGGAGAGGATAGGGCACAGGTACATTGAGGTGTTTAAGAGCAGCCAGGAGGAAGTTAGGTCATACTGAaagctt

>F RRM 3

ATGggcagcagccatcatcatcatcatcacagcagcggcctggtgccgcgcggcagccatatggctagcatgactggtggacagcaaatgggtcgcggatccgaa
aatttgtatttccaaggagagctcagtGAGTTCACAGTGCAGAGCACCACAGGCCACTGTGTCCACATGAGGGGCCTGCCGTACAAAGCGACCGAGAACGACATT
TACAACTTCTTCTCTCCTCTCAACCCTGTGAGAGTCCATATTGAGATTGGCCCAGATGGAAGAGTGACGGGTGAAGCAGATGTTGAGTTTGCTACTCATGAAGAA
GCTGTGGCAGCTATGTCCAAAGACAGGGCCAATATGCAGCACAGATATATAGAACTCTTCTTGAATTCAACAACAGGGGCCAGCAATGGGGCGTATAGCAGCCAG
GTGTGAaagctt

>H RRM 1

ATGggcagcagccatcatcatcatcatcacagcagcggcctggtgccgcgcggcagccatatggctagcatgactggtggacagcaaatgggtcgcggatccgaa
aatttgtatttccaaggagagctcagtTTCGTGGTGAAGGTCCGGGGCTTGCCCTGGTCTTGCTCGGCCGATGAAGTGCAGAGGTTTTTTTCTGACTGCAAAATT
CAAAATGGGGCTCAAGGTATTCGTTTCATCTACACCAGAGAAGGCAGACCAAGTGGCGAGGCTTTTGTTGAACTTGAATCAGAAGATGAAGTCAAATTGGCCCTG
AAAAAAGACAGAGAAACTATGGGACACAGATATGTTGAAGTATTCAAGTCAAACAAGTGACtcgag

>H RRM 2

ATGggcagcagccatcatcatcatcatcacagcagcggcctggtgccgcgcggcagccatatggctagcatgactggtggacagcaaatgggtcgcggatccgaa
aatttgtatttccaaggagagctcagtGGCTTTGTACGGCTTAGAGGACTTCCCTTTGGATGTAGCAAGGAAGAAATTGTTCAGTTCTTCTCAGGGTTGGAAATC
GTGCCAAATGGGATAACATTGCCGGTGGACTTCCAGGGGAGGAGTACGGGGGAGGCCTTCGTGCAGTTTGCTTCACAGGAAATAGCTGAAAAGGCTCTAAAGAAA
CACAAGGAAAGAATAGGGCACAGGTATATTGAAATCTTTAAGAGCAGTAGATGActcgag

>H RRM 3

ATGggcagcagccatcatcatcatcatcacagcagcggcctggtgccgcgcggcagccatatggctagcatgactggtggacagcaaatgggtcgcggatccgaaa
atttgtatttccaaggagagctcatagagctcCAGAGCACAACAGGACACTGTGTACACATGCGGGGATTACCTTACAGAGCTACTGAGAATGACATTTATAATTT
TTTTTCACCGCTCAACCCTGTGAGAGTACACATTGAAATTGGTCCTGATGGCAGAGTAACTGGTGAAGCAGATGTCGAGTTCGCAACTCATGAAGATGCTGTGGCA
GCTATGTCAAAAGACAAAGCAAATATGCAACACAGATATGTAGAACTCTTCTTGAATTCTACAGCAGGAGCAAGCGGTGGTGCTTACGAACACAGATATGTAGAAC
TCTTCTTGAATTCTACAGCAGGAGCAAGCGGTGGTGCTTATGGTAGCCAAATGTGActcgag

Figure 35 - Nucleotide sequences of hnRNPs F and H1 and respective RRM constructs.
RRM sequences are shown in upper case, restriction enzyme sites are highlighted in light grey and start and stop codons in black. TEV cleavage site and plasmid sequence including His-tag are in lower case. Figure 34 in appendix B shows the alignment of hnRNP F and H1 RRMs.

>Hs4
aagcttAGCCCTCCAGGACAGGCTGCATCAGAAGAGGCCATCAAGCAGATCACTGTCCTTCTGccatgg

>Hs-6
aagcttAGCCCTCCAGGACAGGCTGCATCAGAAGAGGCCATCAAGCAGtctgttccaagggcctttgcgtcaggtgggctcagggttccagggtggctggaccccaggccccagctctgcagcagggaggacgtggctgggctcgtgaagcatgtgggggtgagcccaggggccccaaggcagggcacctggcc
ttcagcctgcctcagccctgcctgtcacccagATCACTGTCCTTCTGccatgg

>Hs-6 ATG 3'ss
aagcttAGCCCTCCAGGACAGGCTGCATCAGAAGAGGCCATCAAGCAGtctgttccaagggcctttgcgtcaggtgggctcagggttccagggtggctggaccccaggccccagctctgcagcagggaggacgtggctgggctcgtgaagcgtgtgggggtgagcccaggggccccaaggcagggcacctggcc
ttcagcctgcctcagccctgcctgtcacccggATCACTGTCCTTCTGccatgg

>Hs-6 3'ss
aagcttAGCCCTCCAGGACAGGCTGCATCAGAAGAGGCCATCAAGCAGtctgttccaagggcctttgcgtcaggtgggctcagggttccagggtggctggaccccaggccccagctctgcagcagggaggacgtggctgggctcgtgaagcatgtgggggtgagcccaggggccccaaggcagggcacctggcc
ttcagcctgcctcagccctgcctgtcacccggATCACTGTCCTTCTGccatgg

>PP
aagcttCAGCCCTCCGGGACAGGCTGCATCAGAAGAGGCCATCAAGCAGgtctgttccaagggcctttgcgtcaggtgggctcagggctgccccacttgggggttccagggtggctggaccccggctccagctctgcagctgggaggacgtggctgggctcttgaagcatttgggggtgagcccaggggcccca
gggcagggcacctggccttcagccgacctcagctctgcctgtctcccagATCACTGTCCTTCTGccatgg

>PP 3'ss
aagcttCAGCCCTCCGGGACAGGCTGCATCAGAAGAGGCCATCAAGCAGtctgttccaagggcctttgcgtcaggtgggctcagggctgccccacttgggggttccagggtggctggaccccggctccagctctgcagctgggaggacgtggctgggctcttgaagcatttgggggtgagcccaggggcccca
gggcagggcacctggccttcagccgacctcagctctgcctgtctcccggATCACTGTCCTTCTGccatgg

>PM
aagcttCAACCCTCCGGGACAGGCTGCATCAGAAGAGGCCAGCAAGCAGgtctgttccaagggccttcgcgtcaggtgggctcagggctgccccacttgggggttccagggtggctggaccccaggccccagctctgcaacagggaggacatggctgggctcttgaagcgtttgggggtaagcccaggggcccca
gggcagggcatctggccttcagccggcctcaggcctgcctgtctcccagGTCACTGTCCTTCCGccatgg

>PM 3'ss
aagcttCAACCCTCCGGGACAGGCTGCATCAGAAGAGGCCAGCAAGCAGgtctgttccaagggccttcgcgtcaggtgggctcagggctgccccacttgggggttccagggtggctggaccccaggccccagctctgcaacagggaggacatggctgggctcttgaagcgtttgggggtaagcccaggggcccca
gggcagggcatctggccttcagccggcctcaggcctgcctgtctcccggGTCACTGTCCTTCCGccatgg

>PC
aagcttCAACCCTCCGGGACAGGCTGCATCAGAAGAGGCCAGCAAGCAGgtctgttccgagggccttcgcgtcaggtgggctcagggctgcccgacttgggggttccagggtggctggaccccagactccagctctgcaacagggaggacatggctgggctcttgaagcgtttgggggtgagcccagggaccccaggccagggcacctggccttcag
ccggcctcaggcctgcctgtctcccagGTCACTGTCCTTCCGccatgg

>PC 3'ss
aagcttCAACCCTCCGGGACAGGCTGCATCAGAAGAGGCCAGCAAGCAGgtctgttccgagggccttcgcgtcaggtgggctcagggctgcccgacttgggggttccagggtggctggaccccagactccagctctgcaacagggaggacatggctgggctcttgaagcgtttgggggtgagcccagggaccccaggccagggcacctggccttcag
ccggcctcaggcctgcctgtctcccggGTCACTGTCCTTCCGccatgg

>PS
aagcttCAACCCTCCGGGACAGGCTGCATCAGAAGAGGCCAGCAAGCAGgtctgttccaagggccttcgcgtcaggtgggctcagggctgccccacttggggcagctctgcaacagggagaacatggctgggctcttgaagcgtttgggggtgagcccagggaccccagggcagggcacctggccttcagccagc
ctcaggcctgcctgtctcccagGTCACTGTCCTTCCGccatgg

>PS 3'ss
aagcttCAACCCTCCGGGACAGGCTGCATCAGAAGAGGCCAGCAAGCAGgtctgttccaagggccttcgcgtcaggtgggctcagggctgccccacttggggcagctctgcaacagggagaacatggctgggctcttgaagcgtttgggggtgagcccagggaccccagggcagggcacctggccttcagccagc
ctcaggcctgcctgtctcccggGTCACTGTCCTTCCGccatgg

Figure 36 - Nucleotide sequences of primates INS 5'UTR constructs.
Sequences of the INS 5'UTR of the tested primate species. Nucleotide sequences of primate 5'UTRs from clone sequencing at Source BioScience. Exonic sequences are in upper case, intronic sequences are in lower case. Restriction sites are highlighted in light grey and a -> g mutations that disrupt splicing in yellow.

A

Non-ATG codons in a good Kozak context, in frame with the canonical ATG codon

agccctccaggacAGGCTGcatcagaagAGGccatcaagcAGGtctgttccaAGGgcctttgcgtcaggtgggctc
AGGgttccagggtggCTGgaccccaggccccagctctgcagcAGGgaggacGTGgctgggctcgtgAAGcatGTGg
ggGTGagcccaggggccccaaggcagggcacctggccttcagcctgcctcagccctgcctgtcacccagatcactg
tccttctgcc**ATG**g

Non-ATG codons in a good Kozak context, out of frame with the canonical ATG codon

agccctccaggacaggctgcatcagaagaggccATCAAGcaggtCTGttccAAGggcctttgcgtcAGGtgggctc
agggttccAGGgtggctggaccccaggccccagctCTGcagcagggAGGACGtggCTGggctcgtgaagcATGtgg
gggtgagcccAGGggccccAAGgcAGGgcacCTGgccttcagcCTGcctcagccCTGcctgtcacccagatcactg
tccttctgcc**ATG**g

Non-ATG codons in a weak Kozak context, in frame with the canonical ATG codon

agccctccaggacaggctgcatcagAAGaggccatcaagcaggtctgttccaagggcctttgcgtcaggtgggctc
agggttccagggtggctggacccccAGGccccagctctgcagcagggaggacgtggctgggctcGTGaagcatgtgg
gggtgagcccaggggcccccaAGGcagggcacctggccttcagcctgcctcagccctgcctgtcacccagatcactg
tccttctgcc**ATG**g

Non-ATG codons in a weak Kozak context, out of frame with the canonical ATG codon

agccctccAGGacaggctgcATCagaagaggccatcaagcaggtctgttccaagggcctTTGcgtcaggtgggctc
agggttccagggtggctggaccccaggccccagctctgcagcagggaggacgtggctgggctcgtgagcatgtgg
gggtgagcccaggggccccaaggcagggcacctggccttcagcctgcctcagccctgcCTGtcacccagATCaCTG
tccttCTGccATGg

B

Number of non-canonical codons in 5'UTR

Translation efficiency	Initiation codon	Individually		Grouped	
		In frame	Out of frame	In frame	Out of frame
High	ATG	0	1	6	15
	ACG	0	1		
	CTG	2	9		
	ATC	0	3		
	TTG	0	1		
	GTG	4	0		
Low	AGG	8	6	10	9
	AAG	2	3		

Fisher's exact test	
P value	0.1965
P value summary	Ns
One- or two tailed	Two-tailed
Statistically significant? (alpha<0.05)	No

Figure 37 - Potential non-canonical initiation codons in human *INS* 5'UTR.
(A) Codons are divided according to the surrounding nucleotide context, reading frame and translation efficiency. The preferred context (Kozak sequence) in mammals is GCCRCCAUGG, with the nucleotides in positions -3 and +4 (underlined) relative to the first nucleotide of initiation codon being the most relevant (457,458). For the analysis, it was considered that a codon is in a good Kozak context when one or both nucleotides in positions -3 and +4 are present. For a weak Kozak context, neither of them matches the preferred consensus context. Non-canonical codons (in uppercase) have different translation efficiencies (443): from the most efficient to the least efficient codon: ATG>ACG>CTG>ATC>TTG>GTG>AGG≈AAG (317,443). The main open reading frame initiated by ATG is highlighted in bold. Upstream stop codons are highlighted in black. (B) Distribution of non-canonical codons in *INS* 5'UTR, by their predicted translation efficiency. David Peabody (443) showed that alternative start codons may be used and that they have different relative translation efficiencies. In *INS* 5'UTR, in frame/out of frame distribution (table on the left) of these codons is very similar, shown by the Fisher's exact test (table on the right).

Appendix B Supplementary tables

Table 17 – Secondary structure prediction of INS intron DNA-derived oligonucleotides
The most stable predicted structure, by RNAstructure (377,459) web server, for each tested DNA oligonucleotide, corresponding to the lowest free energy (ΔG), and G-scores of putative G4 forming motifs are shown. For each sequence, motif nucleotides predicted by QGRS mapper (376) are highlighted in blue. Structures are coloured according to probabilities, indicating the likelihood of paired nucleotides being in the correct pair. From the highest probability (p) to the lowest: red (≥ 99%), orange (99% > p ≥ 95%), yellow (95% > p ≥ 90%), dark green (90% > p ≥ 80%), light green (80% > p ≥ 70%), light blue (70% > p ≥ 60%), dark blue (60% > p ≥ 50%) and purple (< 50%). The same is applied to unpaired nucleotides. For some oligonucleotides, no structure (-) was predicted by the web server. [1](377).

Oligo	Sequence	Predicted structure (Fold[1])	ΔG (kcal/mol)	QGRS G-score
WT	TGGGCTCAGGGTTCCAGGGTGGCTGGA CCCCAGGCCCCAGCTCTGCAGCAGGGA GGACGTGGCTGGGC		-13.8	21/19
		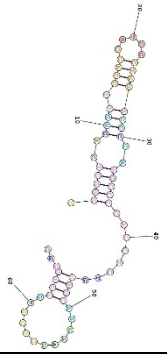	-12.8	
Int1	TGGGCTCAGGGTTCCAGGGTGGCTGG	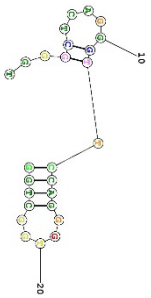	-3.1	20

Appendix B

Oligo	Sequence	Predicted structure (Fold[1])	ΔG (kcal/mol)	QGRS G-score
Int2	AGGGTTCCAGGGTGGCTGGACCCCA	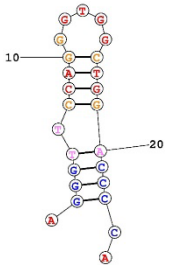	-6.7	18
Int3	AGGGTGGCTGGACCCCAGGCCCCAGC	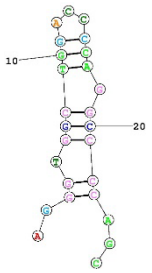	-4.5	17
Int4	TGGACCCCAGGCCCCAGCTCTGCA	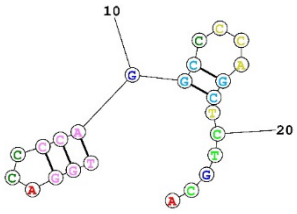	-2.7	0
Int5	AGGCCCCAGCTCTGCAGCAGGGAGGA	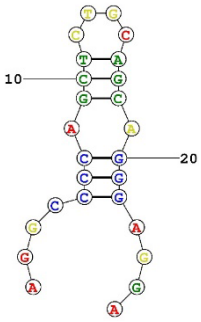	-3.7	0
Int6	AGCTCTGCAGCAGGGAGGACGTGGC	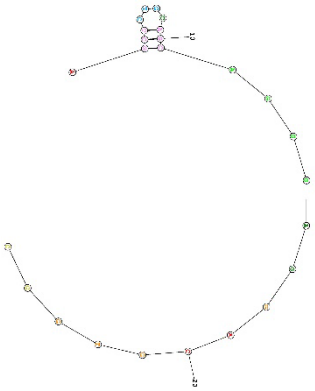	-1.4	0
Int7	AGGGAGGACGTGGCTGGGC	-	-	19

Oligo	Sequence	Predicted structure (Fold[1])	ΔG (kcal/mol)	QGRS G-score
CD3	CCAGGGTGGCTGGACCCCAGGC	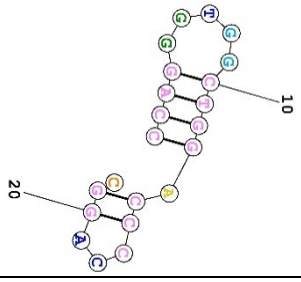	-3.6	17
CD4	CCAGGGTGGCTGGACTTCAGGC	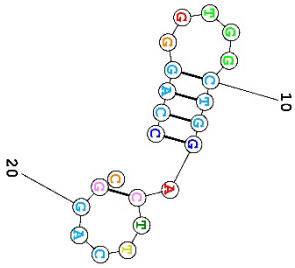	-2.6	17
c-myc	TGAGGGTGGGTAGGGTGGGTAA	-	-	41
Plas24	GGGTTCAGGGTTCAGGGTTCAGGG	-	-	42
21DNA	CTAGGGCTAGGGCTAGGGCTAGGG	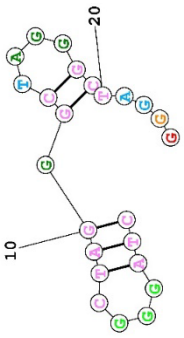	-1.4	42
DCAF6	GCAAACTTAAAACTGGTTCA	-	-	0
CLASP1	TACATCCCATACGGCTCATA	-	-	0
dT22	TTTTTTTTTTTTTTTTTTTTT	-	-	0
Gtr1	ATCGGGTCGTACGTCATGGGTAC	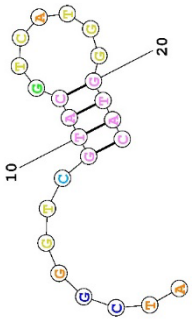	-0.6	0

Appendix B

Oligo	Sequence	Predicted structure (Fold[1])	ΔG (kcal/mol)	QGRS G-score
Gtr2	ACTGATCGTACGTGGGGTACGTAC	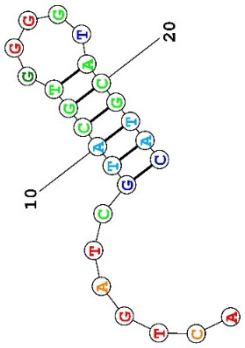	-4.5	0
Gtr3	GGGTACTGACATTAACCGGGAAC	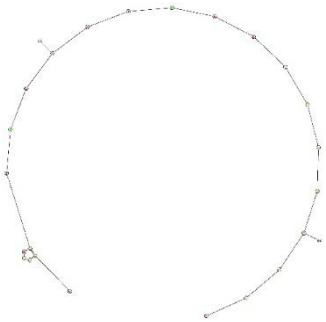	-2.9	0
GA8	AAGGAAAGGAAAAGGAAAAGGAAA	-	-	20
GA12	GAGAGAGAGAGAGAGAGAGAGAGA	-	-	0
GT8	TTGGTTTGGTTTTGGTTTTGGTTT	-	-	20
GT12	GTGTGTGTGTGTGTGTGTGTGTGT	-	-	0

Table 18 - Secondary structure prediction of INS intron 1 RNA-derived oligonucleotides
Fold predictions, by RNAstructure (377,459) web server, for the single most likely structures at equilibrium for each tested RNA oligonucleotide, correspondent lowest free energies (ΔG) and G-scores of putative G-quadruplex forming motifs are shown. Motif nucleotides predicted by QGRS mapper (376) are highlighted in blue. Structures are coloured according to probabilities, indicating the likelihood of paired nucleotides being in the correct pair. From the highest probability (p) to the lowest: red (≥ 99%), orange (99% > p ≥ 95%), yellow (95% > p ≥ 90%), dark green (90% > p ≥ 80%), light green (80% > p ≥ 70%), light blue (70% > p ≥ 60%), dark blue (60% > p ≥ 50%) and purple (< 50%). The same is applied to unpaired nucleotides. [1] (377)

Oligo	Sequence	Predicted structure (Fold[1])	ΔG (kcal/mol)	QGRS G-score
Int1	UGGGCUCAGGGUUCCAGGGUGGC UGG	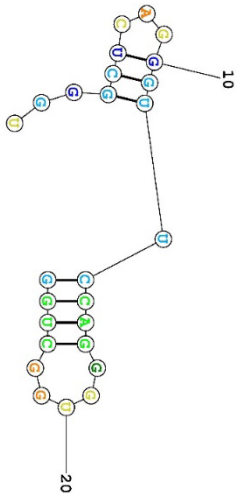	-5.4	20
Int7	AGGGAGGACGUGGCUGGGC	**-**	-	19
CD3	CCAGGGUGGCUGGACCCCAGGC	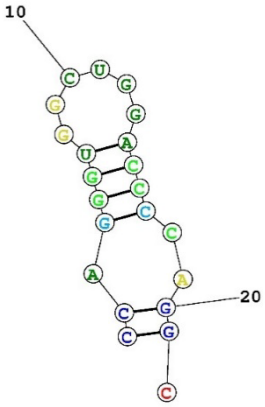	-6.3	17

Appendix B

Oligo	Sequence	Predicted structure (Fold[1])	ΔG (kcal/mol)	QGRS G-score
Plas24	GGGUUCAGGGUUCAGGGUUCAGGG	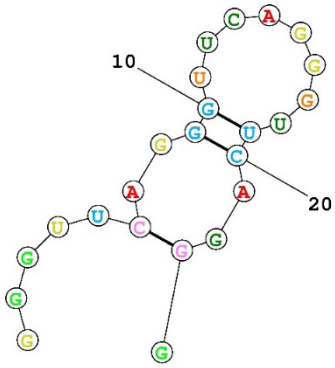	-1.4	42
AV3	CCCUGUCCUUUUUUUUCCACAGCUG	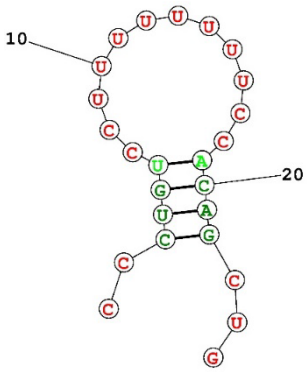	-0.5	0

Table 19 - Secondary structure prediction of INS RNA transcripts

Fold predictions, by RNAstructure (377,459) web server, for the single most likely structures at equilibrium for *INS* intron 1 *in vitro* transcripts, correspondent **l**owest free energies (ΔG) and G-scores of putative G4 forming motifs are shown. Motif nucleotides predicted by QGRS mapper (376) are highlighted in blue. Mutations/deletions are highlighted in yellow. Structures are coloured according to probabilities, indicating the likelihood of paired nucleotides being in the correct pair. From the highest probability (p) to the lowest: red (≥ 99%), orange (99% > p ≥ 95%), yellow (95% > p ≥ 90%), dark green (90% > p ≥ 80%), light green (80% > p ≥ 70%), light blue (70% > p ≥ 60%), dark blue (60% > p ≥ 50%) and purple (< 50%). The same is applied to unpaired nucleotides. [1] (377)

Oligo	Sequence	Predicted structure (Fold[1])	ΔG (kcal/mol)	QGRS G-score
WT	GGGCUCAGGGUUCCAGGGUGGCUGGAC CCCAGGCCCCAGCUCUGCAGCAGGGAGG ACGUGGCUGGGC	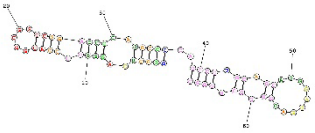	-29.4	21/19
del5	GGGCUCAGGGUUCCAGGGUGGCUGG----- -------- GCUCUGCAGCAGGGAGGACGUGGCUGG GC	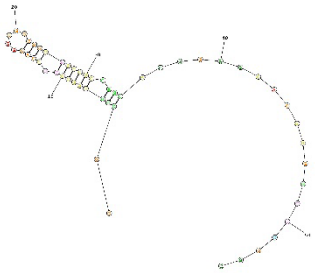	-18.2	41/19
		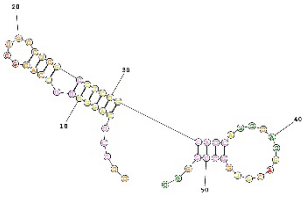	-18.1	
Mut 3	GGGCUCAGGGUUCCAGGAUGGUAGGAC CCCAGGCCCCAGCUCUGCAGCAGGGAGG ACGUGGCUGGGC	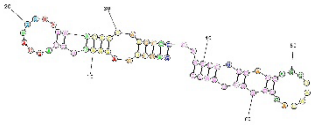	-23.8	21/19
Mut 5	GGGCUCAGGGUUCCAGGGUUGCUGGAC CCGAGUCGCCAGCUCUGCAGCAGGGAGG ACGUGGCUGGGC	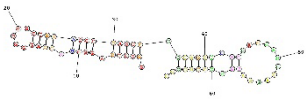	-29.6	20/19
Mut 6	GGGCUCAGGGUUCCAGGAUUGUAGGAC CCCAGUCCCCAGCUCUGCAGCAGGGAGG ACGUGGCUGGGC	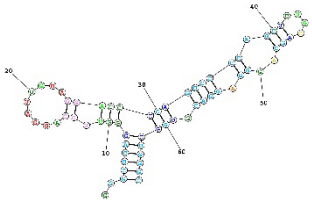	-23.3	20/19
		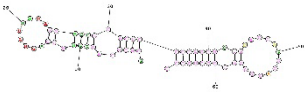	-22.8	

Table 20 – Significance of ThT fluorescence differences in the time-course of G4-ThT complexes.
Summary of the results of Šídák-Bonferroni corrected-multiple unpaired t-tests, performed for the comparison of mean fluorescence intensities of oligo-ThT complexes for one week (relative to Figure 10).

	P value	$\overline{x}_1$	$\overline{x}_2$	$\overline{x}_2 - \overline{x}_1$	SEM	t ratio	df	Adjusted P Value
H2O	0.0171, ns	126	98.5	27.5	3.64	7.555	2	0.1287
ThT	0.2937, ns	141	116	25	17.72	1.411	2	0.9381
c-myc	0.8459, ns	451	439.5	11.5	52.15	0.2205	2	1.0000
Plas24	0.9530, ns	817.5	805.5	12	180.3	0.06654	2	1.0000
21 DNA	0.7659, ns	626.5	648.5	-22	64.59	0.3406	2	1.0000
dT22	0.2458, ns	115	136.5	-21.5	13.24	1.624	2	0.8954
DCAF6	0.8740, ns	153.5	142	11.5	64.02	0.1796	2	1.0000
CLASP1	0.8574, ns	122.5	127.5	-5	24.55	0.2037	2	1.0000

Table 21 – Significance of ThT-DNA G4 saturation curves.
Summary of comparison of fluorescence intensities of titration curves of 10 different nucleotides at 2 and 20 μM with increasing concentrations of ThT, using the Tukey's multiple comparison test (relative to Figure 12).

Oligo	[ThT]	[Oligo]	Tukey's multiple comparison test		
			p-value	$\overline{x}_2 - \overline{x}_1$	95% CI
WT	10	0 vs. 20	0.8419, ns	-2.45	-13 to 8.05
		0 vs. 20	0.2503, ns	-7.04	-17.5 to 3.47
		2 vs. 20	0.5505, ns	-4.59	-15.1 to 5.92
	50	0 vs. 20	0.5675, ns	-4.47	-15 to 6.04
		0 vs. 20	<0.001, ****	-22.4	-32.9 to -11.9
		2 vs. 20	0.0004, ***	-17.9	-28.4 to -7.4
	100	0 vs. 20	0.6293, ns	-4.03	-14.5 to 6.47
		0 vs. 20	<0.0001, ****	-37.2	-47.7 to -26.7
		2 vs. 20	<0.0001, ****	-33.2	-43.7 to -22.6
	150	0 vs. 20	0.7518, ns	-3.16	-13.7 to 7.35
		0 vs. 20	<0.0001, ****	-36.3	-46.8 to -25.8
		2 vs. 20	<0.0001, ****	-33.2	-43.7 to -22.7
	200	0 vs. 20	0.8647, ns	-2.25	-12.8 to 8.25
		0 vs. 20	<0.0001, ****	-33.5	-44 to -23
		2 vs. 20	<0.0001, ****	-31.3	-41.8 to -20.8
	250	0 vs. 20	0.9259, ns	-1.64	-12.1 to 8.87
		0 vs. 20	<0.0001, ****	-28	-40.1 to -19.1
		2 vs. 20	<0.0001, ****	-28	-38.5 to -17.5
	300	0 vs. 20	0.9577, ns	-1.23	-11.7 to 9.28
		0 vs. 20	<0.0001, ****	-23.4	-33.9 to -12.9
		2 vs. 20	<0.0001, ****	-22.1	-32.6 to 11.6
	350	0 vs. 20	0.9779, ns	-0.882	-11.4 to 9.62
		0 vs. 20	0.0003, ***	-18.2	-28.7 to -7.69
		2 vs. 20	0.0006, ***	-17.3	-27.8 to -6.81

Oligo	[ThT]	[Oligo]	Tukey's multiple comparison test		
			p-value	$\overline{x}_2 - \overline{x}_1$	95% CI
WT	400	0 vs. 20	0.9909, ns	-0.565	-11.1 to 9.94
		0 vs. 20	0.0074, **	-13.7	-24.2 to -3.17
		2 vs. 20	0.0107, *	-13.1	-2.36 to -2.61
	450	0 vs. 20	0.9947, ns	-0.43	-10.9 to 10.1
		0 vs. 20	0.0752, ns	-9.73	-20.2 to 0.778
		2 vs. 20	0.0931, ns	-9.3	-19.8 to 1.21
	500	0 vs. 20	0.9989, ns	-0.2	-10.7 to 10.3
		0 vs. 20	0.3196, ns	-6.37	-16.9 to 4.14
		2 vs. 20	0.3425, ns	-6.17	-16.7 to 4.33
Int1	10	0 vs. 20	0.9211, ns	-1.121	-8.081 to 5.839
		0 vs. 20	0.0109, *	-8.667	-15.63 to 1.707
		2 vs. 20	0.0305, *	-7.546	-14.51 to 0.5857
	50	0 vs. 20	0.7666, ns	-2.02	-8.98 to 4.94
		0 vs. 20	<0.0001, ****	-22.27	-29.23 to 15.31
		2 vs. 20	<0.0001, ****	-20.25	-27.21 to 13.29
	100	0 vs. 20	0.8212, ns	-1.738	-8.698 to 5.222
		0 vs. 20	<0.0001, ****	-30.59	-37.55 to 23.63
		2 vs. 20	<0.0001, ****	-28.85	-35.81 to 21.89
	150	0 vs. 20	0.8630, ns	-1.503	-8.463 to 5.4547
		0 vs. 20	<0.0001, ****	-26.48	-33.44 to 19.52
		2 vs. 20	<0.0001, ****	-24.98	-31.94 to 18.02
	200	0 vs. 20	0.8759, ns	-1.425	-8.385 to 5.535
		0 vs. 20	<0.0001, ****	-22.84	-29.8 to -15.88
		2 vs. 20	<0.0001, ****	-21.42	-28.38 to 14.46
	250	0 vs. 20	0.9762, ns	-0.6067	-7.567 to 6.353

Oligo	[ThT]	[Oligo]	Tukey's multiple comparison test		
			p-value	$\overline{x}_2 - \overline{x}_1$	95% CI
Int1	250	0 vs. 20	<0.0001, ****	-19.53	-26.49 to 12.57
		2 vs. 20	<0.0001, ****	-18.93	-25.89 to 11.97
	300	0 vs. 20	0.9968, ns	-0.2213	-7.181 to 6.739
		0 vs. 20	<0.0001, ****	-14.88	-21.84 to 7.922
		2 vs. 20	<0.0001, ****	-14.66	-21.62 to 7.701
	350	0 vs. 20	0.9967, ns	-0.2233	-7.183 to 6.737
		0 vs. 20	0.0011, **	-10.86	-17.82 to 3.898
		2 vs. 20	0.0014, **	-10.63	-17.59 to 3.675
	400	0 vs. 20	0.9969, ns	-0.2193	-7.179 to 6.741
		0 vs. 20	0.0159, *	-8.273	-15.23 to 1.093
		2 vs. 20	0.0194, *	-8.053	-15.01 to 1.093
	450	0 vs. 20	0.9992, ns	-0.108	-7.068 to 6.852
		0 vs. 20	0.1136, ns	-5.993	-12.95 to 0.9669
		2 vs. 20	0.1136, ns	-5.885	-12.84 to 1.075
	500	0 vs. 20	>0.9999, ns	-0.001	-6.961 to 6.959
		0 vs. 20	0.2461, ns	-4.691	-11.65 to 2.269
		2 vs. 20	0.2463, ns	-4.69	-11.65 to 2.27
Int7	10	0 vs. 20	0.9644, ns	-1.04	-10.7 to 8.65
		0 vs. 20	0.0253, *	-10.8	-20.5 to -1.11
		2 vs. 20	0.0477, *	-9.77	-19.5 to -0.0787
	50	0 vs. 20	0.9157, ns	-1.62	-11.3 to 8.07
		0 vs. 20	<0.0001, ****	-22.6	-32.2 to -12.9
		2 vs. 20	<0.0001, ****	-20.9	-30.6 to -11.2
	100	0 vs. 20	0.8454, ns	-2.23	-11.9 to 7.46
		0 vs. 20	<0.0001, ****	-33.6	-43.3 to -23.9
		2 vs. 20	<0.0001, ****	-31.4	-41.1 to -21.7
	150	0 vs. 20	0.8960, ns	-1.81	-11.5 to 7.88
		0 vs. 20	<0.0001, ****	-31.3	-40.9 to -21.6
		2 vs. 20	<0.0001, ****	-29.4	-39.1 to -19.8

Oligo	[ThT]	[Oligo]	Tukey's multiple comparison test		
			p-value	$\overline{x}_2 - \overline{x}_1$	95% CI
Int7	200	0 vs. 20	0.9323, ns	-1.44	-11.1 to 8.25
		0 vs. 20	<0.0001, ns	-25.1	-33.4 to -15.4
		2 vs. 20	<0.0001, ****	-23.7	-33.4 to -14
	250	0 vs. 20	0.9629, ns	-1.06	-10.7 to 8.63
		0 vs. 20	<0.0001, ****	-19.1	-28.8 to -9.42
		2 vs. 20	<0.0001, ****	-18.1	-27.7 to -8.36
	300	0 vs. 20	0.9714, ns	-0.928	-10.6 to 8.76
		0 vs. 20	0.0019, **	-14.4	-24.1 to -4.75
		2 vs. 20	0.0039, **	-13.5	-23.2 to -3.82
	350	0 vs. 20	0.9869, ns	-0.625	-10.3 to 9.07
		0 vs. 20	0.037, *	-10.2	-19.9 to -0.503
		2 vs. 20	0.0537, ns	-9.57	-19.3 to 0.122
	400	0 vs. 20	0.9923	-0.478	-10.2 to 9.21
		0 vs. 20	0.1975, ns	-7.04	-16.7 to 2.65
		2 vs. 20	0.2430, ns	-6.56	16.3 to 3.13
	450	0 vs. 20	0.9978, ns	-0.255	-9.94 to 9.44
		0 vs. 20	0.4735, ns	-4.74	-14.4 to 4.95
		2 vs. 20	0.5115, ns	-4.49	-14.2 to 5.21
	500	0 vs. 20	0.9984, ns	-0.218	-9.91 to 9.47
		0 vs. 20	0.5844, ns	-4.01	-13.7 to 5.68
		2 vs. 20	0.6183, ns	-3.79	-13.5 to 5.9
CD3	10	0 vs. 20	0.9923, ns	-0.338	-7.18 to 6.5
		0 vs. 20	0.8362, ns	-1.63	-8.47 to 5.21
		2 vs. 20	0.8936, ns	-1.29	-8.13 to 5.55
	50	0 vs. 20	0.9559, ns	-0.816	-7.66 to 6.03
		0 vs. 20	0.0816, ns	-6.23	-13.1 to 0.612
		2 vs. 20	0.1475, ns	-5.41	-12.3 to 1.43
	100	0 vs. 20	0.9478, ns	-0.891	-7.73 to 5.95
		0 vs. 20	0.0048, **	-9.33	-16.2 to -2.49

Oligo	[ThT]	[Oligo]	Tukey's multiple comparison test		
			p-value	$\overline{x}_2 - \overline{x}_1$	95% CI
CD3	100	2 vs. 20	0.0118, *	-8.44	-15.3 to -1.6
	150	0 vs. 20	0.9631, ns	-0.746	-7.59 to 6.1
		0 vs. 20	0.0050, **	-9.3	-16.1 to -2.46
		2 vs. 20	0.0106, *	-8.55	-15.4 to -1.71
	200	0 vs. 20	0.9803, ns	-0.543	-7.39 to 6.3
		0 vs. 20	0.0213, *	-7.82	-14.7 to -0.977
		2 vs. 20	0.0346, *	-7.28	-14.1 to -0.435
	250	0 vs. 20	0.9807, ns	-0.536	-7.38 to 6.31
		0 vs. 20	0.0013, **	-10.5	-17.4 to -3.69
		2 vs. 20	0.0024, **	-10	-16.8 to -3.16
	300	0 vs. 20	0.9937, ns	-0.305	-7.15 to 6.54
		0 vs. 20	0.0025, **	-9.94	-16.8 to -3.1
		2 vs. 20	0.0035, **	-9.64	-16.5 to -2.8
	350	0 vs. 20	0.9920, ns	-0.344	-7.19 to 605
		0 vs. 20	0.0103, *	-8.58	-15.4 to -1.74
		2 vs. 20	0.0144, *	-8.24	-15.1 to -1.4
	400	0 vs. 20	0.9940, ns	-0.297	-7.14 to 6.55
		0 vs. 20	0.0275, *	-7.53	-14.4 to -0.692
		2 vs. 20	0.0358, *	-7.24	-14.1 to -0.394
	450	0 vs. 20	0.9798, ns	-0.549	-7.39 to 6.29
		0 vs. 20	0.0789, ns	-6.27	-13.1 to 0.57
		2 vs. 20	0.1188, ns	-5.72	-12.6 to 1.12
	500	0 vs. 20	0.9638, ns	0.738	-7.58 to 6.1
		0 vs. 20	0.1465, ns	-5.42	-12.3 to 1.42
		2 vs. 20	0.2354, ns	-4.69	-11.5 to 2.16
CD4	10	0 vs. 20	0.9997, ns	-0.0443	-4.57 to 4.48
		0 vs. 20	0.3194, ns	-2.74	-7.27 to 1.78
		2 vs. 20	0.3310, ns	-2.7	-7.22 to 1.82

Oligo	[ThT]	[Oligo]	Tukey's multiple comparison test		
			p-value	$\overline{x}_2 - \overline{x}_1$	95% CI
CD4	50	0 vs. 20	0.9702, ns	-0.442	-4.96 to 4.08
		0 vs. 20	0.0001, ***	-8.25	-12.8 to 3.72
		2 vs. 20	0.0003, ***	-7.81	-12.3 to -3.28
	100	0 vs. 20	0.9902, ns	-0.252	-4.77 to 4.27
		0 vs. 20	<0.0001, ****	-13.2	-17.8 to -8.71
		2 vs. 20	<0.0001, ****	-13	-17.5 to -8.46
	150	0 vs. 20	0.9928, ns	-0.217	-4.74 to 4.31
		0 vs. 20	<0.0001, ****	-13.1	-17.6 to -8.56
		2 vs. 20	<0.0001, ****	-12.9	-17.4 to -8.33
	200	0 vs. 20	0.9861, ns	-0.301	-4.82 to 4.22
		0 vs. 20	<0.0001, ****	-12.9	-17.4 to -8.33
		2 vs. 20	<0.0001, ****	-12.6	-17.1 to -8.03
	250	0 vs. 20	0.9944, ns	-0.191	-4.71 to 4.33
		0 vs. 20	<0.0001, ****	-11.3	-15.8 to -6.78
		2 vs. 20	<0.0001, ****	-11.1	-15.6 to -6.59
	300	0 vs. 20	0.9756, ns	-0.399	-4.92 to 4.12
		0 vs. 20	<0.0001, ****	-8.81	-13.3 to -4.29
		2 vs. 20	<0.0001, ****	-8.41	-12.9 to -3.89
	350	0 vs. 20	0.9905, ns	-0.248	-4.77 to 4.27
		0 vs. 20	0.0039, **	-6.29	-10.8 to -1.77
		2 vs. 20	0.0058, **	-6.04	-10.6 to -1.52
	400	0 vs. 20	0.9759, ns	-0.397	-4.92 to 4.13
		0 vs. 20	0.0243, *	-5.07	-9.6 to -0.551
		2 vs. 20	0.0411, *	-4.68	-9.2 to -0.154
	450	0 vs. 20	0.9913, ns	-0.238	-4.76 to 4.28
		0 vs. 20	0.1670, ns	-3.46	-7.98 to1.07
		2 vs. 20	0.2104, ns	-3.22	-7.74 to1.3
	500	0 vs. 20	0.9985, ns	-0.097	-4.62 to 4.43
		0 vs. 20	0.5119, ns	-2.09	-6.61 to 2.43
		2 vs. 20	0.5436, ns	-2	-6.52 to 2.53

Oligo	[ThT]	[Oligo]	Tukey's multiple comparison test		
			p-value	$\overline{x}_2 - \overline{x}_1$	95% CI
cmyc	10	0 vs. 20	0.9986, ns	-0.12	-5.75 to5.51
		0 vs. 20	0.0002, ***	-9.92	-15.5 to -4.29
		2 vs. 20	0.0003, ***	-9.8	-15.4 to -4.17
	50	0 vs. 20	0.9925, ns	-0.275	-5.9 to 5.35
		0 vs. 20	<0.0001, ****	-20	-25.6 to -14.4
		2 vs. 20	<0.0001, ****	-19.7	-25.4 to -14.1
	100	0 vs. 20	0.9818, ns	-0.429	-6.05 to 5.2
		0 vs. 20	<0.0001, ****	-28	-33.6 to -22.4
		2 vs. 20	<0.0001, ****	-27.6	-33.2 to -22
	150	0 vs. 20	0.9953, ns	-0.218	-5.84 to 5.41
		0 vs. 20	<0.0001, ****	-28.3	-34 to -22.7
		2 vs. 20	<0.0001, ****	-28.1	-33.7 to -22.5
	200	0 vs. 20	0.9967, ns	-0.18	-5.81 to 5.45
		0 vs. 20	<0.0001, ****	-23.9	-29.5 to -18.3
		2 vs. 20	<0.0001, ****	-23.7	-29.4 to -18.1
	250	0 vs. 20	0.9920, ns	-0.283	-5.91 to 5.34
		0 vs. 20	<0.0001, ****	-19.7	-25.4 to -14.1
		2 vs. 20	<0.0001, ****	-19.4	-25.1 to -13.8
	300	0 vs. 20	0.9953	-0.216	-5.84 to 5.41
		0 vs. 20	<0.0001	-15.8	-21.4 to -10.1
		2 vs. 20	<0.0001, ****	-15.5	-21.2 to -9.92
	350	0 vs. 20	0.9999, ns	-0.0207	-5.65 to 5.6
		0 vs. 20	<0.0001, ****	-11.7	-17.4 to -6.12
		2 vs. 20	<0.0001, ****	-11.7	-17.3 to -6.1
	400	0 vs. 20	0.9937, ns	-0.251	-5.88 to 5.37
		0 vs. 20	0.0004, ***	-9.54	-15.2 to -3.91
		2 vs. 20	0.0005, ***	-9.54	-15.2 to -3.91
	450	0 vs. 20	0.9984, ns	-0.128	-5.75 to 5.5

Oligo	[ThT]	[Oligo]	Tukey's multiple comparison test		
			p-value	$\bar{x}_2 - \bar{x}_1$	95% CI
cmyc	450	0 vs. 20	0.0058, **	-7.52	-13.1 to -1.9
		2 vs. 20	0.0068, **	-7.39	-13 to -1.77
	500	0 vs. 20	0.9996, ns	-0.062	-5.69 to 5.56
		0 vs. 20	0.1603, ns	-4.35	-9.98 to 1.28
		2 vs. 20	0.1685, ns	-4.29	-9.91 to 1.34
Plas24	10	0 vs. 20	0.9824, ns	-0.496	-7.12 to 6.13
		0 vs. 20	0.0899, ns	-5.91	-12.5 to 0.716
		2 vs. 20	0.1305, ns	-5.41	-12 to 1.21
	50	0 vs. 20	0.8685, ns	-1.4	-8.02 to 5.22
		0 vs. 20	<0.0001, ****	-22.9	-29.6 to -16.3
		2 vs. 20	<0.0001, ****	-21.5	-28.2 to -14.9
	100	0 vs. 20	0.7554, ns	-1.98	-8.6 to 4.65
		0 vs. 20	<0.0001, ****	-29.3	-35.9 to .22.6
		2 vs. 20	<0.0001, ****	-27.3	-33.9 to -20.7
	150	0 vs. 20	0.9024, ns	-1.19	-782 to 5.43
		0 vs. 20	<0.0001, ****	-24.6	-31.2 to -17.9
		2 vs. 20	<0.0001, ****	-23.4	-30 to -16.8
	200	0 vs. 20	0.9422, ns	-0.908	-7.53 to 5.72
		0 vs. 20	<0.0001, ****	-20.4	-27 to -13.8
		2 vs. 20	<0.0001, ****	-19.5	-26.1 to -12.8
	250	0 vs. 20	0.9681, ns	-0.67	-7.29 to 5.95
		0 vs. 20	<0.0001, ****	-14.1	-20.7 to-7.49
		2 vs. 20	<0.0001, ****	-13.4	-20.1 to -6.82
	300	0 vs. 20	0.9737, ns	-0.608	-7.23 to 6.02
		0 vs. 20	0.0011, **	-10.4	-17 to -3.74
		2 vs. 20	0.0022, **	-9.76	-16.4 to -3.14
	350	0 vs. 20	0.9845, ns	-0.465	-7.09 to 6.16
		0 vs. 20	0.0218, *	-7.54	-14.2 to -0.919
		2 vs. 20	0.0335, *	-7.08	-13.7 to -0.454

Oligo	[ThT]	[Oligo]	Tukey's multiple comparison test		
			p-value	$\overline{x}_2 - \overline{x}_1$	95% CI
Plas24	400	0 vs. 20	0.9854, ns	-0.451	-7.07 to 6.17
		0 vs. 20	0.1437, ns	-5.28	-11.9 to 1.35
		2 vs. 20	0.1955, ns	-4.83	-11.5 to 1.8
	450	0 vs. 20	0.9993, ns	-0.099	-6.72 to 6.52
		0 vs. 20	0.2755, ns	-4.28	-10.9 to 2.35
		2 vs. 20	0.2919, ns	-4.18	-10.8 to 2.45
	500	0 vs. 20	0.9991, ns	-0.111	-6.73 to 6.51
		0 vs. 20	0.5581, ns	-2.86	-9.48 to 3.77
		2 vs. 20	0.5832, ns	-2.75	-9.37 to 3.88
Int1+18	10	0 vs. 20	0.8736, ns	-0.544	-3.17 to 2.09
		0 vs. 20	0.0672, ns	-2.49	-5.12 to 0.14
		2 vs. 20	0.1862, ns	-1.95	-4.57 to 0.684
	50	0 vs. 20	0.1802, ns	-1.96	-4.59 to 0.664
		0 vs. 20	<0.0001, ****	-10.1	-12.7 to -7.43
		2 vs. 20	<0.0001, ****	-8.1	-107. To -5.47
	100	0 vs. 20	0.1771, ns	-1.98	-4.6 to 0.654
		0 vs. 20	<0.0001, ****	-14.5	-17.1 to -11.9
		2 vs. 20	<0.0001, ****	-12.5	-15.1 to -9.89
	150	0 vs. 20	0.4235, ns	-1.38	-4.01 to 1.25
		0 vs. 20	<0.0001, ****	-15.5	-18.1 to -12.9
		2 vs. 20	<0.0001, ****	-14.1	-16.7 to -11.5
	200	0 vs. 20	0.3897, ns	-1.45	-4.08 to 1.18
		0 vs. 20	<0.0001, ****	-13.5	-16.1 to -10.9
		2 vs. 20	<0.0001, ****	-12.1	-14.7 to -9.43
	250	0 vs. 20	0.6379, ns	-0.994	-3.62 to 1.63
		0 vs. 20	<0.0001, ****	-11.3	-13.9 to -8.63
		2 vs. 20	<0.0001, ****	-10.3	-12.9 to -7.64
	300	0 vs. 20	0.8186, ns	-0.662	-3.29 to 1.97
		0 vs. 20	<0.0001, ****	-8.95	-11.6 to -6.32

Oligo	[ThT]	[Oligo]	Tukey's multiple comparison test		
			p-value	$\overline{x}_2 - \overline{x}_1$	95% CI
Int1+18	300	2 vs. 20	<0.0001, ****	-8.29	-10.9 to -5.66
	350	0 vs. 20	0.8848, ns	-0.517	-3.15 to 2.11
		0 vs. 20	<0.0001, ****	-6.26	-8.89 to -3.63
		2 vs. 20	<0.0001, ****	-5.74	-8.37 to -3.11
	400	0 vs. 20	0.8852, ns	-0.516	-3.15 to 2.11
		0 vs. 20	<0.0001, ****	-4.96	-7.59 to -2.33
		2 vs. 20	0.0004, ***	-4.45	-7.07 to -1.82
	450	0 vs. 20	0.9869, ns	-0.169	-2.8 to 2.46
		0 vs. 20	0.0112, *	-3.27	-5.89 to -0.636
		2 vs. 20	0.017, *	-3.1	-5.73 to -0.467
	500	0 vs. 20	0.9996, ns	0.0307	-2.6 to 2.66
		0 vs. 20	0.3334, ns	-1.56	-4.19 to 1.07
		2 vs. 20	0.3195, ns	-1.59	-4.22 to 1.03
Int7+20	10	0 vs. 20	0.7915, ns	-0.889	-4.15 to 2.38
		0 vs. 20	0.0091, **	-4.15	-7.42-0.888
		2 vs. 20	0.05, ns	-3.26	-6.53 to 0.000227
	50	0 vs. 20	0.3871, ns	-1.8	-5.07 to 1.46
		0 vs. 20	<0.0001, ****	-14.2	-17.5 to -11
		2 vs. 20	<0.0001, ****	-12.4	-15.7 to 1.37
	100	0 vs. 20	0.3525, ns	-1.89	-5.16 to 1.37
		0 vs. 20	<0.0001, ****	-20	-23.3 to -16.8
		2 vs. 20	<0.0001, ****	-18.1	-21.4 to -14.9
	150	0 vs. 20	0.5988, ns	-1.32	-4.58 to 1.95
		0 vs. 20	<0.0001, ****	-20.9	-24.1 to -17.6
		2 vs. 20	<0.0001, ****	-19.6	-22.8 to -16.3
	200	0 vs. 20	0.6724, ns	-1.16	-4.42 to 2.11
		0 vs. 20	<0.0001, ****	-19	-22.3 to -15.8
		2 vs. 20	<0.0001, ****	-17.9	-21.1 to -14.6
	250	0 vs. 20	0.8146, ns	-0.832	-4.1 to 2.43

Oligo	[ThT]	[Oligo]	Tukey's multiple comparison test		
			p-value	$\overline{x}_2 - \overline{x}_1$	95% CI
Int7+20	250	0 vs. 20	<0.0001, ****	-16.2	-19.5 to -13
		2 vs. 20	<0.0001, ****	-15.4	-18.7 to -12.1
	300	0 vs. 20	0.9374, ns	-0.467	-3.73 to 2.8
		0 vs. 20	<0.0001, ****	-13.4	-16.7 to -10.2
		2 vs. 20	<0.0001, ****	-13	-16.7 to -9.72
	350	0 vs. 20	0.9411, ns	-0.452	-3.72 to 2.81
		0 vs. 20	<0.0001, ****	-10.3	-13.5 to -7.01
		2 vs. 20	<0.0001, ****	-9.82	-13.1 to -6.56
	400	0 vs. 20	0.8564, ns	-0.723	-3.99 to 2.54
		0 vs. 20	<0.0001, ****	-7.75	-11 to -4.48
		2 vs. 20	<0.0001, ****	-7.02	-10.3 to -3.76
	450	0 vs. 20	0.9597, ns	-0.72	-3.64 to 2.89
		0 vs. 20	0.0015, **	-4.97	-8.24 to -1.71
		2 vs. 20	0.0035, **	-4.6	-7.86 to -1.33
	500	0 vs. 20	0.9793, ns	-0.265	-3.53 to 3
		0 vs. 20	0.1173, ns	-2.74	-6 to 0.526
		2 vs. 20	0.1720, ns	-2.47	-5.74 to 0.791
dT22	10	0 vs. 20	0.5238, ns	0.197	-0.236 to 0.629
		0 vs. 20	0.9923, ns	-0.0213	-0.454 to 0.411
		2 vs. 20	0.4527, ns	-0.218	-0.651 to 0.215
	50	0 vs. 20	0.3789, ns	0.242	-0.191 to 0.674
		0 vs. 20	0.0859, ns	-0.39	-0.822 to 0.043
		2 vs. 20	0.0024, **	-0.631	-1.06 to -0.199
	100	0 vs. 20	0.1092, ns	0.369	-0.0634 to 0.802
		0 vs. 20	0.0029, **	-0.619	-1.05 to -0.187
		2 vs. 20	<0.0001, ****	-0.989	-1.42 to -0.556
	150	0 vs. 20	0.1165, ns	0.364	-0.069 to 0.796
		0 vs. 20	<0.0001, ****	-0.866	-1.3 to -0.434
		2 vs. 20	<0.0001, ****	-1.23	-1.66 to -0.797

Oligo	[ThT]	[Oligo]	Tukey's multiple comparison test		
			p-value	$\overline{x}_2 - \overline{x}_1$	95% CI
dT22	200	0 vs. 20	0.2976, ns	0.271	-0.162 to 0.703
		0 vs. 20	0.0006, ***	-0.71	-1.14 to -0.278
		2 vs. 20	<0.0001, ****	-0.981	-1.41 to -0.548
	250	0 vs. 20	0.9384, ns	0.0613	-0.371 to 0.494
		0 vs. 20	<0.0001, ****	-1.07	-1.5 to -0.636
		2 vs. 20	<0.0001, ****	-1.13	-.156 to -0.697
	300	0 vs. 20	0.145, ns	0.344	-0.0887 to 0.777
		0 vs. 20	<0.001, ****	-0.909	-1.34 to -0.476
		2 vs. 20	<0.0001, ****	-1.25	-1.69 to -0.82
	350	0 vs. 20	0.2554, ns	0.288	-0.145 to 0.72
		0 vs. 20	0.0008, ***	-0.694	-1.13 to -0.262
		2 vs. 20	<0.0001, ****	-0.982	-1.41 to 0.549
	400	0 vs. 20	0.9338, ns	0.0637	-0.369 to 0.496
		0 vs. 20	0.0003, ***	-0.739	-1.17 to -0.306
		2 vs. 20	0.0001, ***	-0.803	-1.24 to -0.37
	450	0 vs. 20	0.5397, ns	0.192	-0.241 to 0.625
		0 vs. 20	0.1363, ns	-0.35	-0.782 to 0.083
		2 vs. 20	0.0105, *	-0.542	-0.974 to 0.109
	500	0 vs. 20	0.0532, ns	0.428	-0.00471 to 0.861
		0 vs. 20	0.9911, ns	-0.023	-0.456 to 0.41
		2 vs. 20	0.0392, *	-0.451	-0.884 to 0.0183

Table 22 – Significance of ThT screening for G4 formation *in vitro* in INS intron 1.

Summary of Friedman test performed for the comparison of mean fluorescence intensities of INS intron 1 DNA derived oligos, G4-forming control oligos and sequence-binding properties by ThT, in water (relative to Figure 14).

Friedman test Dunn's test	Rank sum diff.	p-value
WT vs. Int1	3	0.8625, ns
WT vs. Int2	51	0.0032, **
WT vs. Int3	40	0.0209, *
WT vs. Int4	42	0.0153, *
WT vs. Int5	14	0.4189, ns
WT vs. Int6	-3	0.8625, ns
WT vs. Int7	-9	0.6033, ns
WT vs. CD3	39	0.0243, *
WT vs. CD4	31	0.0735, ns
WT vs. IAO21	41	0.0179, *
WT vs. c-myc	-2	0.9081, ns
WT vs. Plas24	2	0.9081, ns
WT vs. 21DNA	10	0.5637, ns
WT vs. dT22	54	0.0018, **
WT vs. DCAF6	25	0.1489, ns
WT vs. CLASP1	48	0.0056, **
WT vs. Gtr1	14	0.4189, ns
WT vs. Gtr2	30	0.0833, ns
WT vs. Gtr3	16	0.3556, ns
WT vs. GA8	-15	0.3865, ns
WT vs. GA12	-12	0.4884, ns
WT vs. GT8	23	0.1842, ns
WT vs. GT12	26	0.1333, ns
Int1 vs. Int2	48	0.0056, **
Int1 vs. Int3	37	0.0327, *
Int1 vs. Int4	39	0.0243, *
Int1 vs. Int5	11	0.5254, ns
Int1 vs. Int6	-6	0.7290, ns
Int1 vs. Int7	-12	0.4884, ns
Int1 vs. CD3	36	0.0377, *
Int1 vs. CD4	28	0.1060, ns
Int1 vs. IAO21	38	0.0282, *
Int1 vs. c-myc	-5	0.7728, ns
Int1 vs. Plas24	-1	0.9540, ns
Int1 vs. 21DNA	7	0.6861, ns
Int1 vs. dT22	51	0.0032, **
Int1 vs. DCAF6	22	0.2040, ns
Int1 vs. CLASP1	45	0.0094, **
Int1 vs. Gtr1	11	0.5254, ns
Int1 vs. Gtr2	27	0.1190, ns
Int1 vs. Gtr3	13	0.4529, ns
Int1 vs. GA8	-18	0.2987, ns
Int1 vs. GA12	-15	0.3865, ns
Int1 vs. GT8	20	0.2482, ns
Int1 vs. GT12	23	0.1842, ns
Int2 vs. Int3	-11	0.5254, ns

Appendix B

Friedman test Dunn's test	Rank sum diff.	p-value
Int2 vs. Int4	-9	0.6033, ns
Int2 vs. Int5	-37	0.0327, *
Int2 vs. Int6	-54	0.0018, **
Int2 vs. Int7	-60	0.0005, ***
Int2 vs. CD3	-12	0.4884, ns
Int2 vs. CD4	-20	0.2482, ns
Int2 vs. IAO21	-10	0.5637, ns
Int2 vs. c-myc	-53	0.0022, **
Int2 vs. Plas24	-49	0.0047, **
Int2 vs. 21DNA	-41	0.0179, *
Int2 vs. dT22	3	0.8625, ns
Int2 vs. DCAF6	-26	0.1333, ns
Int2 vs. CLASP1	-3	0.8625, ns
Int2 vs. Gtr1	-37	0.0327, *
Int2 vs. Gtr2	-21	0.2253, ns
Int2 vs. Gtr3	-35	0.0433, *
Int2 vs. GA8	-66	0.0001, ***
Int2 vs. GA12	-63	0.0003, ***
Int2 vs. GT8	-28	0.1060, ns
Int2 vs. GT12	-25	0.1489, ns
Int3 vs. Int4	2	0.9081, ns
Int3 vs. Int5	-26	0.1333, ns
Int3 vs. Int6	-43	0.0130, *
Int3 vs. Int7	-49	0.0047, **
Int3 vs. CD3	-1	0.9540, ns
Int3 vs. CD4	-9	0.6033, ns

Friedman test Dunn's test	Rank sum diff.	p-value
Int3 vs. IAO21	1	0.9540, ns
Int3 vs. c-myc	-42	0.0153, *
Int3 vs. Plas24	-38	0.0282, *
Int3 vs. 21DNA	-30	0.0833, ns
Int3 vs. dT22	14	0.4189, ns
Int3 vs. DCAF6	-15	0.3865, ns
Int3 vs. CLASP1	8	0.6442, ns
Int3 vs. Gtr1	-26	0.1333, ns
Int3 vs. Gtr2	-10	0.5637, ns
Int3 vs. Gtr3	-24	0.1659, ns
Int3 vs. GA8	-55	0.0015, **
Int3 vs. GA12	-52	0.0027, **
Int3 vs. GT8	-17	0.3263, ns
Int3 vs. GT12	-14	0.4189, ns
Int4 vs. Int5	-28	0.1060, ns
Int4 vs. Int6	-45	0.0094, **
Int4 vs. Int7	-51	0.0032, **
Int4 vs. CD3	-3	0.8625, ns
Int4 vs. CD4	-11	0.5254, ns
Int4 vs. IAO21	-1	0.9540, ns
Int4 vs. c-myc	-44	0.0111, *
Int4 vs. Plas24	-40	0.0209, *
Int4 vs. 21DNA	-32	0.0647, ns
Int4 vs. dT22	12	0.4884, ns
Int4 vs. DCAF6	-17	0.3263, ns
Int4 vs. CLASP1	6	0.7290, ns

Friedman test Dunn's test	Rank sum diff.	p-value
Int4 vs. Gtr1	-28	0.1060, ns
Int4 vs. Gtr2	-12	0.4884, ns
Int4 vs. Gtr3	-26	0.1333, ns
Int4 vs. GA8	-57	0.0010, ***
Int4 vs. GA12	-54	0.0018, **
Int4 vs. GT8	-19	0.2727, ns
Int4 vs. GT12	-16	0.3556, ns
Int5 vs. Int6	-17	0.3263, ns
Int5 vs. Int7	-23	0.1842, ns
Int5 vs. CD3	25	0.1489, ns
Int5 vs. CD4	17	0.3263, ns
Int5 vs. IAO21	27	0.1190, ns
Int5 vs. c-myc	-16	0.3556, ns
Int5 vs. Plas24	-12	0.4884, ns
Int5 vs. 21DNA	-4	0.8174, ns
Int5 vs. dT22	40	0.0209, *
Int5 vs. DCAF6	11	0.5254, ns
Int5 vs. CLASP1	34	0.0496, *
Int5 vs. Gtr1	0	>0.9999, ns
Int5 vs. Gtr2	16	0.3556, ns
Int5 vs. Gtr3	2	0.9081, ns
Int5 vs. GA8	-29	0.0941, ns
Int5 vs. GA12	-26	0.1333, ns
Int5 vs. GT8	9	0.6033, ns
Int5 vs. GT12	12	0.4884, ns
Int6 vs. Int7	-6	0.7290, ns

Friedman test Dunn's test	Rank sum diff.	p-value
Int6 vs. CD3	42	0.0153, *
Int6 vs. CD4	34	0.0496, *
Int6 vs. IAO21	44	0.0111, *
Int6 vs. c-myc	1	0.9540, ns
Int6 vs. Plas24	5	0.7728, ns
Int6 vs. 21DNA	13	0.4529, ns
Int6 vs. dT22	57	0.0010, ***
Int6 vs. DCAF6	28	0.1060, ns
Int6 vs. CLASP1	51	0.0032, **
Int6 vs. Gtr1	17	0.3263, ns
Int6 vs. Gtr2	33	0.0567, ns
Int6 vs. Gtr3	19	0.2727, ns
Int6 vs. GA8	-12	0.4884, ns
Int6 vs. GA12	-9	0.6033, ns
Int6 vs. GT8	26	0.1333, ns
Int6 vs. GT12	29	0.0941, ns
Int7 vs. CD3	48	0.0056, **
Int7 vs. CD4	40	0.0209, *
Int7 vs. IAO21	50	0.0039, n**
Int7 vs. c-myc	7	0.6861, ns
Int7 vs. Plas24	11	0.5254, ns
Int7 vs. 21DNA	19	0.2727, ns
Int7 vs. dT22	63	0.0003, ***
Int7 vs. DCAF6	34	0.0496, *
Int7 vs. CLASP1	57	0.0010, ***
Int7 vs. Gtr1	23	0.1842, ns

Appendix B

Friedman test Dunn's test	Rank sum diff.	p-value
Int7 vs. Gtr2	39	0.0243, *
Int7 vs. Gtr3	25	0.1489, ns
Int7 vs. GA8	-6	0.7290, ns
Int7 vs. GA12	-3	0.8625, ns
Int7 vs. GT8	32	0.0647, ns
Int7 vs. GT12	35	0.0433, *
CD3 vs. CD4	-8	0.6442, ns
CD3 vs. IAO21	2	0.9081, ns
CD3 vs. c-myc	-41	0.0179, *
CD3 vs. Plas24	-37	0.0327, *
CD3 vs. 21DNA	-29	0.0941, ns
CD3 vs. dT22	15	0.3865, ns
CD3 vs. DCAF6	-14	0.4189, ns
CD3 vs. CLASP1	9	0.6033, ns
CD3 vs. Gtr1	-25	0.1489, ns
CD3 vs. Gtr2	-9	0.6033, ns
CD3 vs. Gtr3	-23	0.1842, ns
CD3 vs. GA8	-54	0.0018, **
CD3 vs. GA12	-51	0.0032, **
CD3 vs. GT8	-16	0.3556, ns
CD3 vs. GT12	-13	0.4529, ns
CD4 vs. IAO21	10	0.5637, ns
CD4 vs. c-myc	-33	0.0567, ns
CD4 vs. Plas24	-29	0.0941, ns
CD4 vs. 21DNA	-21	0.2253, ns
CD4 vs. dT22	23	0.1842, ns

Friedman test Dunn's test	Rank sum diff.	p-value
CD4 vs. DCAF6	-6	0.7290, ns
CD4 vs. CLASP1	17	0.3263, ns
CD4 vs. Gtr1	-17	0.3263, ns
CD4 vs. Gtr2	-1	0.9540, ns
CD4 vs. Gtr3	-15	0.3865, ns
CD4 vs. GA8	-46	0.0079, **
CD4 vs. GA12	-43	0.0130, *
CD4 vs. GT8	-8	0.6442, ns
CD4 vs. GT12	-5	0.7728, ns
IAO21 vs. c-myc	-43	0.0130, *
IAO21 vs. Plas24	-39	0.0243, *
IAO21 vs. 21DNA	-31	0.0735, ns
IAO21 vs. dT22	13	0.4529, ns
IAO21 vs. DCAF6	-16	0.3556, ns
IAO21 vs. CLASP1	7	0.6861, ns
IAO21 vs. Gtr1	-27	0.1190, ns
IAO21 vs. Gtr2	-11	0.5254, ns
IAO21 vs. Gtr3	-25	0.1489, ns
IAO21 vs. GA8	-56	0.0012, **
IAO21 vs. GA12	-53	0.0022, **
IAO21 vs. GT8	-18	0.2987, ns
IAO21 vs. GT12	-15	0.3865, ns
c-myc vs. Plas24	4	0.8174, ns
c-myc vs. 21DNA	12	0.4884, ns
c-myc vs. dT22	56	0.0012, **
c-myc vs. DCAF6	27	0.1190, ns

Friedman test Dunn's test	Rank sum diff.	p-value
c-myc vs. CLASP1	50	0.0039, **
c-myc vs. Gtr1	16	0.3556, ns
c-myc vs. Gtr2	32	0.0647, ns
c-myc vs. Gtr3	18	0.2987, ns
c-myc vs. GA8	-13	0.4529, ns
c-myc vs. GA12	-10	0.5637, ns
c-myc vs. GT8	25	0.1489, ns
c-myc vs. GT12	28	0.1060, ns
Plas24 vs. 21DNA	8	0.6442, ns
Plas24 vs. dT22	52	0.0027, **
Plas24 vs. DCAF6	23	0.1842, ns
Plas24 vs. CLASP1	46	0.0079, **
Plas24 vs. Gtr1	12	0.4884, ns
Plas24 vs. Gtr2	28	0.1060, ns
Plas24 vs. Gtr3	14	0.4189, ns
Plas24 vs. GA8	-17	0.3263, ns
Plas24 vs. GA12	-14	0.4189, ns
Plas24 vs. GT8	21	0.2253, ns
Plas24 vs. GT12	24	0.1659, ns
21DNA vs. dT22	44	0.0111, *
21DNA vs. DCAF6	15	0.3865, ns
21DNA vs. CLASP1	38	0.0282, *
21DNA vs. Gtr1	4	0.8174, ns
21DNA vs. Gtr2	20	0.2482, ns
21DNA vs. Gtr3	6	0.7290, ns
21DNA vs. GA8	-25	0.1489, ns

Friedman test Dunn's test	Rank sum diff.	p-value
21DNA vs. GA12	-22	0.2040, ns
21DNA vs. GT8	13	0.4529, ns
21DNA vs. GT12	16	0.3556, ns
dT22 vs. DCAF6	-29	0.0941, ns
dT22 vs. CLASP1	-6	0.7290, ns
dT22 vs. Gtr1	-40	0.0209, *
dT22 vs. Gtr2	-24	0.1659, ns
dT22 vs. Gtr3	-38	0.0282, *
dT22 vs. GA8	-69	<0.0001, ****
dT22 vs. GA12	-66	0.0001, ***
dT22 vs. GT8	-31	0.0735, ns
dT22 vs. GT12	-28	0.1060, ns
DCAF6 vs. CLASP1	23	0.1842, ns
DCAF6 vs. Gtr1	-11	0.5254, ns
DCAF6 vs. Gtr2	5	0.7728, ns
DCAF6 vs. Gtr3	-9	0.6033, ns
DCAF6 vs. GA8	-40	0.0209, *
DCAF6 vs. GA12	-37	0.0327, *
DCAF6 vs. GT8	-2	0.9081, ns
DCAF6 vs. GT12	1	0.9540, ns
CLASP1 vs. Gtr1	-34	0.0496, *
CLASP1 vs. Gtr2	-18	0.2987, ns
CLASP1 vs. Gtr3	-32	0.0647, ns
CLASP1 vs. GA8	-63	0.0003, ***
CLASP1 vs. GA12	-60	0.0005, ***
CLASP1 vs. GT8	-25	0.1489, ns

Appendix B

Friedman test Dunn's test	Rank sum diff.	p-value
CLASP1 vs. GT12	-22	0.2040, ns
Gtr1 vs. Gtr2	16	0.3556, ns
Gtr1 vs. Gtr3	2	0.9081, ns
Gtr1 vs. GA8	-29	0.0941, ns
Gtr1 vs. GA12	-26	0.1333, ns
Gtr1 vs. GT8	9	0.6033, ns
Gtr1 vs. GT12	12	0.4884, ns
Gtr2 vs. Gtr3	-14	0.4189, ns
Gtr2 vs. GA8	-45	0.0094, **
Gtr2 vs. GA12	-42	0.0153, *
Gtr2 vs. GT8	-7	0.6861, ns

Friedman test Dunn's test	Rank sum diff.	p-value
Gtr2 vs. GT12	-4	0.8174, ns
Gtr3 vs. GA8	-31	0.0735, ns
Gtr3 vs. GA12	-28	0.1060, ns
Gtr3 vs. GT8	7	0.6861, ns
Gtr3 vs. GT12	10	0.5637, ns
GA8 vs. GA12	3	0.8625, ns
GA8 vs. GT8	38	0.0282, *
GA8 vs. GT12	41	0.0179, *
GA12 vs. GT8	35	0.0433, *
GA12 vs. GT12	38	0.0282, *
GT8 vs. GT12	3	0.8625, ns

Table 23 - Significance of fluorescence variation of ThT in the presence of INS intron 1-derived Int1+.

Summary of Fisher's LSD multiple comparison test was performed for the comparison of mean fluorescence intensities of Int1+ oligos (relative to Figure 15). For each pair of oligos, difference between means ($\bar{x}_2 - \bar{x}_1$), and 95% confidence interval (CI) and p-value and its summary, respectively, are shown.

Fisher's LSD	$\bar{x}_2 - \bar{x}_1$	95% CI	p-value
Int1 vs. Int1+2	4108	1198 to 7018	0.0261, *
Int1 vs. Int1+4	929.7	-1735 to 3594	0.2721, ns
Int1 vs. Int1+6	1832	234.6 to 3429	0.0387, *
Int1 vs. Int1+8	-279.7	-2536 to 1977	0.6472, ns
Int1 vs. Int1+10	2420	-522.5 to 5362	0.0714, ns
Int1 vs. Int1+12	2475	151.4 to 4799	0.0445, *
Int1 vs. Int1+14	2058	356.7 to 3759	0.0350, *
Int1 vs. Int1+16	2716	1496 to 3937	0.0107, *
Int1 vs. Int1+18	2448	1420 to 3477	0.0094, **
Int1+2 vs. Int1+4	-3178	-4729 to -1628	0.0126, *
Int1+2 vs. Int1+6	-2276	-4059 to -493.4	0.0316, *
Int1+2 vs. Int1+8	-4388	-5108 to -3668	0.0015, **
Int1+2 vs. Int1+10	-1688	-2211 to -1166	0.0051, **
Int1+2 vs. Int1+12	-1633	-3468 to 202.5	0.0620, ns
Int1+2 vs. Int1+14	-2050	-3265 to -835.8	0.0184, *
Int1+2 vs. Int1+16	-1392	-3114 to 330.3	0.0737, ns
Int1+2 vs. Int1+18	-1660	-3669 to 350.1	0.0709, ns
Int1+4 vs. Int1+6	902	-165.5 to 1969	0.0680, ns
Int1+4 vs. Int1+8	-1209	-2352 to -66.22	0.0450, *
Int1+4 vs. Int1+10	1490	400.7 to 2579	0.0277, *
Int1+4 vs. Int1+12	1546	-1363 to 4455	0.1496, ns
Int1+4 vs. Int1+14	1128	-308.9 to 2565	0.0776, ns
Int1+4 vs. Int1+16	1787	-150.5 to 3724	0.0580, ns

Fisher's LSD	$\overline{x}_2 - \overline{x}_1$	95% CI	p-value
Int1+4 vs. Int1+18	1519	-134.6 to 3172	0.0585, ns
Int1+6 vs. Int1+8	-2111	-3183 to -1039	0.0136, *
Int1+6 vs. Int1+10	588	-996.1 to 2172	0.2513, ns
Int1+6 vs. Int1+12	643.7	-1723 to 3010	0.3625, ns
Int1+6 vs. Int1+14	226	-621.8 to 1074	0.3701, ns
Int1+6 vs. Int1+16	884.7	-195.9 to 1965	0.0720, ns
Int1+6 vs. Int1+18	616.7	14.37 to 1219	0.0479, *
Int1+8 vs. Int1+10	2699	1996 to 3403	0.0036, **
Int1+8 vs. Int1+12	2755	970.9 to 4539	0.0219, *
Int1+8 vs. Int1+14	2337	1766 to 2908	0.0032, **
Int1+8 vs. Int1+16	2996	1852 to 4140	0.0078, **
Int1+8 vs. Int1+18	2728	1422 to 4034	0.0122, *
Int1+10 vs. Int1+12	55.67	-2211 to 2322	0.9255, ns
Int1+10 vs. Int1+14	-362	-1636 to 911.6	0.3459, ns
Int1+10 vs. Int1+16	296.7	-1550 to 2143	0.5609, ns
Int1+10 vs. Int1+18	28.67	-1927 to 1984	0.9554, ns
Int1+12 vs. Int1+14	-417.7	-1972 to 1137	0.3671, ns
Int1+12 vs. Int1+16	241	-1148 to 1630	0.5332, ns
Int1+12 vs. Int1+18	-27	-2091 to 2037	0.9602, ns
Int1+14 vs. Int1+16	658.7	78.3 to 1239	0.0395, *
Int1+14 vs. Int1+18	390.7	-432 to 1213	0.1778, ns
Int1+16 vs. Int1+18	-268	-943.7 to 407.7	0.2300, ns

Table 24 - Significance of fluorescence variation of ThT in the presence of INS intron 1-derived Int7+.

Summary of Friedman multiple comparison test was performed for the comparison of mean fluorescence intensities of Int1+ oligos (relative to Figure 15). For each pair of oligos, differences between rank sums and the p-value and its summary, respectively, are shown.

Friedman test Dunn's test	Rank sum diff.	p-value	Friedman test Dunn's test	Rank sum diff.	p-value
Int7 vs. Int7+2	-3	0.7119, ns	Int7+4 vs. Int7+12	-11	0.1757, ns
Int7 vs. Int7+4	14	0.0848, ns	Int7+4 vs. Int7+14	6	0.4602, ns
Int7 vs. Int7+6	16	0.0489, *	Int7+4 vs. Int7+16	10	0.2184, ns
Int7 vs. Int7+8	21	0.0097, **	Int7+4 vs. Int7+18	4	0.6225, ns
Int7 vs. Int710	6	0.4602, ns	Int7+4 vs. Int7+20	-1	0.9020, ns
Int7 vs. Int7+12	3	0.7119, ns	Int7+6 vs. Int7+8	5	0.5383, ns
Int7 vs. Int7+14	20	0.0138, *	Int7+6 vs. Int7+10	-10	0.2184, ns
Int7 vs. Int7+16	24	0.0031, **	Int7+6 vs. Int7+12	-13	0.1096, ns
Int7 vs. Int7+18	18	0.0267, *	Int7+6 vs. Int7+14	4	0.6225, ns
Int7 vs. Int7+20	13	0.1096, ns	Int7+6 vs. Int7+16	8	0.3248, ns
Int7+2 vs. Int7+4	17	0.0364, *	Int7+6 vs. Int7+18	2	0.8055, ns
Int7+2 vs. Int7+6	19	0.0193, *	Int7+6 vs. Int7+20	-3	0.7119, ns
Int7+2 vs. Int7+8	24	0.0031, **	Int7+8 vs. Int1+10	-15	0.0648, ns
Int7+2 vs. Int7+10	9	0.2679, ns	Int7+8 vs. Int7+12	-18	0.0267, *
Int7+2 vs. Int7+12	6	0.4602, ns	Int7+8 vs. Int7+14	-1	0.9020, ns
Int7+2 vs. Int7+14	23	0.0046, **	Int7+8 vs. Int7+16	3	0.7119, ns
Int7+2 vs. Int7+16	27	0.0009, ***	Int7+8 vs. Int7+18	-3	0.7119, ns
Int7+2 vs. Int7+18	21	0.0097, **	Int7+8 vs. Int7+20	-8	0.3248, ns
Int7+2 vs. Int7+20	16	0.0489, *	Int7+10 vs. Int7+12	-3	0.7119, ns
Int7+4 vs. Int7+6	2	0.8055, ns	Int7+10 vs. Int7+14	14	0.0848, ns
Int7+4 vs. Int7+8	7	0.3889, ns	Int7+10 vs. Int7+16	18	0.0267, *
Int7+4 vs. Int1+10	-8	0.3248, ns	Int7+10 vs. Int7+18	12	0.1396, ns

Appendix B

Friedman test Dunn's test	Rank sum diff.	p-value
Int7+10 vs. Int7+20	7	0.3889, ns
Int7+12 vs. Int7+14	17	0.0364, *
Int7+12 vs. Int7+16	21	0.0097, **
Int7+12 vs. Int7+18	15	0.0648, ns
Int7+12 vs. Int7+20	10	0.2184, ns
Int7+14 vs. Int7+16	4	0.6225, ns
Int7+14 vs. Int7+18	-2	0.8055, ns
Int7+14 vs. Int7+20	-7	0.3889, ns
Int7+16 vs. Int7+18	-6	0.4602, ns
Int7+16 vs. Int7+20	-11	0.1757, ns
Int7+18 vs. Int7+20	-5	0.5383, ns

Table 25 – Significance of fluorescence variation of *INS* intron 1 DNA-derived oligos in the presence of different solvents at neutral pH conditions.
Summary of Welch's-corrected unpaired t-test, performed to mean fluorescence in the presence of *INS* DNA-derived oligos in water or buffer at pH 7.2 (relative to Figure 17). For each pair of compared solvents, p-value and its summary, t and degrees of freedom, means difference ($\bar{x}_2 - \bar{x}_1$), and 95% confidence interval (CI), respectively, are shown.

Oligo	Solvents	Unpaired t-test with Welch's correction			
		p-value	t, df	$\bar{x}_2 - \bar{x}_1$	95% CI
Int1	H2O vs Licac	0.0394, *	t=4.72 df=2.07	1820 ± 386	212 to 3429
	H2O vs Licac+KCl	0.2526, ns	t=1.56 df=2.11	605 ± 387	-984 to 2194
	H2O vs Licac+LiCl	0.1627, ns	t=1.72 df=3.89	1022 ± 594	-647 to 2691
	Licac vs Licac+KCl	0.0002, ***	t=15.2 df=3.8	-1215 ± 79.8	-1442 to -989
	Licac vs Licac+LiCl	0.2202, ns	t=1.74 df=2.05	-798 ± 458	-2724 to 1127
	Licac+KCl vs Licac+LiCl	0.4566, ns	t=0.9082 df=2.076	417 ± 459.2	-1491 to 2325
Int7	H2O vs Licac	0.0218, *	t=5.21 df=2.48	3122 ± 600	964 to 5280
	H2O vs Licac+KCl	0.0208, *	t=4.33 df=3.13	2806 ± 648	791 to 4821
	H2O vs Licac+LiCl	0.0101, *	t=5.09 df=3.49	3466 ± 681	1460 to 5471
	Licac vs Licac+KCl	0.4522, ns	t=0.849 df=3.35	-316 ± 372	-1433 to 801
	Licac vs Licac+LiCl	0.4788, ns	t=0.806 df=3.01	344 ± 426	-1009 to 1696
	Licac+KCl vs Licac+LiCl	0.2534, ns	t=1.34 df=3.88	660 ± 492	-725 to 2044
CD3	H2O vs Licac	0.1366, ns	t=2.24 df=2.32	300 ± 134	-206 to 805
	H2O vs Licac+KCl	0.2958, ns	t=1.39 df=2.05	456 ± 328	-922 to 1834
	H2O vs Licac+LiCl	0.6332, ns	t=0.552 df=2.14	110 ± 199	-696 to 916
	Licac vs Licac+KCl	0.6897, ns	t=0.446 df=2.61	156 ± 350	-1059 to 1371
	Licac vs Licac+LiCl	0.4704, ns	t=0.809 df=3.45	-190 ± 234	-883 to 504
	Licac+KCl vs Licac+LiCl	0.4245, ns	t=0.91 df=3.28	-346 ± 380	-1499 to 807
CD4	H2O vs Licac	0.4126**, ns**	t=1.03 df=2	411 ± 400	-1309 to 2131
	H2O vs Licac+KCl	0.8292, ns	t=0.242 df=2.25	9 ± 37.2	-135 to 153
	H2O vs Licac+LiCl	0.0136, *	t=7.56 df=2.17	-341 ± 45.1	-521 to -161
	Licac vs Licac+KCl	0.4212, ns	t=1 df=2.03	-402 ± 402	-2104 to 1300
	Licac vs Licac+LiCl	0.1997, ns	t=1.87 df=2.05	-752 ± 402	-2444 to 941
	Licac+KCl vs Licac+LiCl	0.0041, **	t=6.13 df=3.85	-350 ± 57.1	-511 to -189

Oligo	Solvents	Unpaired t-test with Welch's correction			
		p-value	t, df	$\overline{x}_2 - \overline{x}_1$	95% CI
Plas24	H2O vs Licac	0.2203, ns	t=1.5 df=3.36	1376 ± 915	-1368 to 4120
	H2O vs Licac+KCl	0.5098, ns	t=0.757 df=2.69	637 ± 842	-2225 to 3500
	H2O vs Licac+LiCl	0.1061, ns	t=2.37 df=2.76	2011 ± 849	-828 to 4850
	Licac vs Licac+KCl	0.2850, ns	t=1.26 df=3.5	-738 ± 586	-2460 to 983
	Licac vs Licac+LiCl	0.3522, ns	t=1.07 df=3.61	636 ± 596	-1092 to 2364
	Licac+KCl vs Licac+LiCl	0.0447, *	t=2.89 df=3.99	1374 ± 475	52.6 to 2695
dT22	H2O vs Licac	0.9839, ns	t=0.0215 df=3.95	1 ± 46.6	-129 to 131
	H2O vs Licac+KCl	0.1580, ns	t=1.76 df=3.71	-76.7 ± 43.5	-201 to 47.8
	H2O vs Licac+LiCl	0.1930, ns	t=1.62 df=3.37	-106 ± 65.1	-301 to 89.2
	Licac vs Licac+KCl	0.1303, ns	t=1.91 df=3.88	-77.7 ± 40.6	-192 to 36.3
	Licac vs Licac+LiCl	0.1857, ns	t=1.69 df=3.16	-107 ± 63.2	-302 to 89.1
	Licac+KCl vs Licac+LiCl	0.6683, ns	t=0.476 df=2.86	-29 ± 61	-229 to 171

Table 26 – Significance of fluorescence variation of *INS* intron 1 DNA-derived oligos in the presence of different solvents at acidic pH conditions.

Summary of Welch's-corrected unpaired t-test, performed to mean fluorescence in the presence of *INS* DNA-derived oligos in water or buffer at pH 5.8 (relative to Figure 17). For each pair of compared solvents, p-value and its summary, t and degrees of freedom, means difference ($\bar{x}_2 - \bar{x}_1$), and 95% confidence interval (CI), respectively, are shown.

Oligo	Solvents	Unpaired t-test with Welch's correction			
		p-value	t, df	$\bar{x}_2 - \bar{x}_1$	95% CI
Int1	H2O vs Licac	0.2260, ns	t=1.68 df=2.16	1991 ± 1187	-2763 to 6745
	H2O vs Licac+KCl	0.1543, ns	t=1.79 df=3.7	-525 ± 294	-1368 to 318
	H2O vs Licac+LiCl	0.6538, ns	t=0.494 df=3.12	-241 ± 487	-1757 to 1276
	Licac vs Licac+KCl	0.1603, ns	t=2.14 df=2.09	-2516 ± 1177	-7373 to 2341
	Licac vs Licac+LiCl	0.1864, ns	t=1.8 df=2.53	-2231 ± 1239	-6626 to 2164
	Licac+KCl vs Licac+LiCl	0.5856, ns	t=0.618 df=2.66	285 ± 461	-1294 to 1863
Int7	H2O vs Licac	0.0595, ns	t=2.66 df=3.79	2004 ± 753	-132 to 4139
	H2O vs Licac+KCl	0.3890, ns	t=0.998 df=3.13	955 ± 957	-2019 to 3929
	H2O vs Licac+LiCl	0.1032, ns	t=2.39 df=2.79	2693 ± 1127	-1050 to 6436
	Licac vs Licac+KCl	0.3696, ns	t=1.02 df=3.6	-1049 ± 1024	-4020 to 1923
	Licac vs Licac+LiCl	0.5990, ns	t=0.582 df=3.2	689 ± 1184	-2952 to 4330
	Licac+KCl vs Licac+LiCl	0.2620, ns	t=1.31 df=3.84	1738 ± 1323	-1996 to 5472
CD3	H2O vs Licac	0.0465, *	t=4.17 df=2.15	680 ± 163	24.4 to 1336
	H2O vs Licac+KCl	0.2003, ns	t=1.87 df=2.03	713 ± 381	-905 to 2331
	H2O vs Licac+LiCl	0.6455, ns	t=0.535 df=2.02	220 ± 412	-1531 to 1972
	Licac vs Licac+KCl	0.9411, ns	t=0.08092 df=2.689	33.33 ± 411.9	-1368 to 1435
	Licac vs Licac+LiCl	0.3840, ns	t=1.04 df=2.59	-460 ± 440	-1994 to 1075
	Licac+KCl vs Licac+LiCl	0.4279, ns	t=0.882 df=3.98	-493 ± 559	-2049 to 1063
CD4	H2O vs Licac	0.2052, ns	t=1.53 df=3.76	228 ± 149	-196 to 652
	H2O vs Licac+KCl	0.2488, ns	t=1.53 df=2.31	523 ± 341	-773 to 1818
	H2O vs Licac+LiCl	0.5602, ns	t=0.655 df=2.92	-66.7 ± 102	-396 to 262
	Licac vs Licac+KCl	0.4715, ns	t=0.844 df=2.51	295 ± 349	-951 to 1540
	Licac vs Licac+LiCl	0.1162, ns	t=2.34 df=2.57	-295 ± 126	-737 to 148
	Licac+KCl vs Licac+LiCl	0.2130, ns	t=1.78 df=2.07	-589 ± 332	-1968 to 789

Appendix B

Oligo	Solvents	Unpaired t-test with Welch's correction			
		p-value	t, df	$\overline{x}_2 - \overline{x}_1$	95% CI
Plas24	H2O vs Licac	0.2949, ns	t=1.41 df=2	512 ± 365	-1054 to 2078
	H2O vs Licac+KCl	0.0467, *	t=4.41 df=2.03	-600 ± 136	-1178 to -21.2
	H2O vs Licac+LiCl	0.1086, ns	t=2.78 df=2	1142 ± 411	-624 to 2908
	Licac vs Licac+KCl	0.0785, ns	t=2.86 df=2.54	-1112 ± 389	-2485 to 261
	Licac vs Licac+LiCl	0.3161, ns	t=1.15 df=3.94	630 ± 549	-903 to 2163
	Licac+KCl vs Licac+LiCl	0.0404, *	t=4.03 df=2.43	1742 ± 433	163 to 3321
dT22	H2O vs Licac	0.3340, ns	t=1.1 df=4	62 ± 56.5	-94.9 to 219
	H2O vs Licac+KCl	0.8838, ns	t=0.156 df=3.99	-8.67 ± 55.6	-163 to 146
	H2O vs Licac+LiCl	0.5076, ns	t=0.797 df=2.04	305 ± 383	-1310 to 1920
	Licac vs Licac+KCl	0.2689, ns	t=1.28 df=4	-70.7 ± 55.1	-224 to 82.3
	Licac vs Licac+LiCl	0.5892, ns	t=0.635 df=2.04	243 ± 383	-1373 to 1859
	Licac+KCl vs Licac+LiCl	0.4971, ns	t=0.82 df=2.04	314 ± 383	-1303 to 1931

Table 27 – Significance of RNA fluorescence intensity compared to DNA.
Comparison of mean fluorescence intensity enhancement in RNA oligos at 2, 10 and 20 µM to DNA oligos at the same concentrations (relative to Figure 18). The Welch's-corrected unpaired t-test was performed for the comparison of RNA oligos to their DNA counterparts at the same concentration. Tukey's multiple comparison test compared the variation of fluorescence intensity of increasing oligo concentrations.

DNA vs. RNA		Unpaired t-test with Welch's correction			
Oligo	**[Oligo]**	**p-value**	**t, df**	$\overline{x}_2 - \overline{x}_1$	**95% CI**
Int1	**2**	0.0354, *	4.842; 2.128	867 ± 179.1	139.1 to 1595
	10	0.0041, **	15.31; 2.01	9483 ± 619.4	6831 to 12135
	20	0.0051, **	6.298; 3.487	7153 ± 1136	3808 to 10499
Int7	**2**	0.0830, ns	3.097; 2.139	392 ± 126.6	-119.9 to 904
	10	0.0469, *	3.668; 2.511	3576 ± 974.9	101.5 to 7050
	20	0.0335, *	5.227; 2.033	3658 ± 699.8	693.1 to 6623
Plas24	**2**	0.002, **	11.96; 2.578	1061 ± 88.72	750.2 to 1371
	10	0.0016, **	11.42; 2.935	6119 ± 535.6	4393 to 7845
	20	0.0195, *	4.673; 2.928	5219 ± 1117	1614 to 8823
dT22/AV3	**2**	0.2262, ns	1.431; 3.972	64.67 ± 45.19	-61.15 to 190.5
	10	0.0688, ns	3.28; 2.271	368 ± 112.2	-63.55 to 799.5
	20	0.0609, ns	3.692; 2.112	630 ± 170.6	-68.15 to 1328

			Tukey's multiple comparison test		
Oligo	**Nucleic acid**	**[Oligo]**	**p-value**	$\overline{x}_2 - \overline{x}_1$	**95% CI**
Int1	**DNA**	2 vs. 10	>0.9999, ns	0 ± 772.2	-2369 to 2369
		2 vs. 20	0.0006, ***	-5955 ± 772.2	-8325 to -3586
		10vs. 20	0.0006, ***	-5955 ± 772.2	-8325 to -3586
	RNA	2 vs. 10	0.0039, **	-5088 ± 938.5	-7968 to -2209
		2 vs. 20	<0.0001, ****	-12242 ± 938.5	-15121 to -9362
		10vs. 20	0.0007, ***	-7153 ± 938.5	-1003 to -4274
Int7	**DNA**	2 vs. 10	0.0248, *	-2304 ± 630.1	-4237 to -370.2
		2 vs. 20	0.0002, ***	-5879 ± 630.1	-7812 to -3694
		10vs. 20	0.0031, **	-3575 ± 630.1	-5509 to -1642
	RNA	2 vs. 10	0.0009, ***	.5487 ± 757.5	-7811 to -3163
		2 vs. 20	<0.0001, ****	-9145 ± 757.5	-11469 to -6821
		10vs. 20	0.007, **	-3658 ± 757.5	-5982 to -1334

Plas24	**DNA**	2 vs. 10	0.0037, **	-2476 ± 450.5	-3858 to -1093
		2 vs. 20	<0.0001, ****	-5321 ± 450.5	-6703 to -3938
		10vs. 20	0.0018, **	-2845 ± 450.5	-4227 to -1463
	RNA	2 vs. 10	0.0004, ***	-7534 ± 908.4	-10321 to -4746
		2 vs. 20	0.0001, ***	-9478 ± 908.4	-12266 to -6691
		10vs. 20	0.1614, ns	-1945 ± 908.4	-4732 to 842.4
dT22/AV3	**DNA**	2 vs. 10	0.1350, ns	-93.67 ± 41.06	-219.7 to 32.33
		2 vs. 20	0.0128, *	-174.3 ± 41.06	-300.3 to -48.33
		10vs. 20	0.2019, ns	-80.66 ± 41.06	-206.7 to 45.34
	RNA	2 vs. 10	0.1167, ns	-397 ± 165.8	-905.6 to 111.6
		2 vs. 20	0.0101, *	-739.7 ± 165.8	-1248 to -231.1
		10vs. 20	0.1722, ns	-342.7 ± 165.8	-851 to 165.9

Table 28 – Significance of fluorescence variation of *INS* intron 1 RNA-derived oligos in the presence of different solvents at neutral pH conditions.

Summary of Welch's-corrected unpaired t-test, performed to mean fluorescence in the presence of *INS* RNA-derived oligos in water or buffer at pH 7.2 (relative to Figure 20). For each pair of compared solvents, p-value and its summary, t and degrees of freedom, means difference ($\bar{x}_2 - \bar{x}_1$), and 95% confidence interval (CI), respectively, are shown.

Oligo	Solvents	Unpaired t-test with Welch's correction			
		p-value	t, df	$\bar{x}_2 - \bar{x}_1$	95% CI
Int1	H2O vs Licac	0.7084, ns	0.4018; 4	-943.7 ± 2349	-7465 to 5577
	H2O vs Licac+KCl	0.1613, ns	1.746; 3.707	-3603 ± 2064	-9516 to 2309
	H2O vs Licac+LiCl	0.0258, *	3.464; 3.997	-7976 ± 2302	-14370 to -1582
	Licac vs Licac+KCl	0.2752, ns	1.28; 3.687	-2660 ± 2078	-8628 to 3309
	Licac vs Licac+LiCl	0.0386, *	3.037; 3.994	-7032 ± 2315	-13465 to -599.1
	Licac+KCl vs Licac+LiCl	0.1015, ns	2.158; 3.758	-4372 ± 2026	-10143 to 1398
Int7	H2O vs Licac	0.4334, ns	0.8704; 3.984	-1238 ± 1423	-5195 to 2718
	H2O vs Licac+KCl	0.0065, **	7.437; 2.781	-8465 ± 1138	-12254 to -4676
	H2O vs Licac+LiCl	0.0227. *	5.016; 2.529	-5544 ± 1105	-9463 to -1625
	Licac vs Licac+KCl	0.0078, **	6.691; 2.878	-7227 ± 1080	-10749 to -3705
	Licac vs Licac+LiCl	0.0340, *	4.12; 2.597	-4306 ± 1045	-7944 to -668.1
	Licac+KCl vs Licac+LiCl	0.0093, **	4.842; 3.84	2921 ± 603.2	1218 to 4624
CD3	H2O vs Licac	0.0360, *	3.261; 3.615	866 ± 265.6	96.67 to 1635
	H2O vs Licac+KCl	0.0208, *	3.762; 3.889	758.7 ± 201.7	192.4 to 1325
	H2O vs Licac+LiCl	0.1797, ns	1.871; 2.42	-303.3 ± 162.1	-896.8 to 290.2
	Licac vs Licac+KCl	0.6970, ns	0.4254; 3.279	-107.3 ± 252.3	-873.1 to 658.4
	Licac vs Licac+LiCl	0.0274, *	5.267; 2.215	-1169 ± 222	-2041 to -297.7
	Licac+KCl vs Licac+LiCl	0.0078, **	7.619; 2.584	-1062 ± 139.4	-1549 to -575.1
Plas24	H2O vs Licac	0.2533, ns	1.368; 3.46	1546 ± 1129	-1793 to 4884
	H2O vs Licac+KCl	0.0460, *	3.589; 2.621	-3645 ± 1016	-7158 to -132.3
	H2O vs Licac+LiCl	0.1022, ns	2.255; 3.264	-2477 ± 1098	-5818 to 863.8
	Licac vs Licac+KCl	0.0041, **	7.146; 3.294	-5191 ± 726.4	-7390 to -2992
	Licac vs Licac+LiCl	0.0089, **	4.799; 3.962	-4023 ± 838.3	-6359 to -1687
	Licac+KCl vs Licac+LiCl	0.1700, ns	1.725; 3.491	1168 ± 677.2	-825.3 to 3161

Appendix B

Oligo	Solvents	Unpaired t-test with Welch's correction			
		p-value	t, df	$\overline{x}_2 - \overline{x}_1$	95% CI
AV3	H2O vs Licac	0.2494, ns	1.553; 2.203	-182 ± 117.2	-644.3 to 280.3
	H2O vs Licac+KCl	0.1449, ns	2.142; 2.376	-256.3 ± 119.6	-700.4 to 187.7
	H2O vs Licac+LiCl	0.1308, ns	2.422; 2.095	-280.2 ± 115.7	-757 to 196.6
	Licac vs Licac+KCl	0.1704, ns	1.702; 3.667	-74.33 ± 43.67	-200 to 51.38
	Licac vs Licac+LiCl	0.0413, *	3.141; 3.53	-98.17 ± 31.25	-189.7 to -6.658
	Licac+KCl vs Licac+LiCl	0.5886, ns	0.6052; 2.941	-23.83 ± 39.38	-150.6 to 102.9

Table 29 - Significance of fluorescence variation of *INS* intron 1 RNA-derived oligos in the presence of different solvents at acidic pH conditions.

Summary of Welch's-corrected unpaired t-test, performed to mean fluorescence in the presence of *INS* RNA-derived oligos in water or buffer at pH 5.8 (relative to Figure 20). For each pair of compared solvents, p-value and its summary, t and degrees of freedom, means difference ($\bar{x}_2 - \bar{x}_1$), and 95% confidence interval (CI), respectively, are shown.

Oligo	Solvents	Unpaired t-test with Welch's correction			
		p-value	t, df	$\bar{x}_2 - \bar{x}_1$	95% CI
Int1	H2O vs Licac	0.1272, ns	2.072; 3.092	3033 ± 1464	-1547 to 7614
	H2O vs Licac+KCl	0.2460, ns	1.376; 3.721	-1207 ± 877.7	-3718 to 1303
	H2O vs Licac+LiCl	0.0264, *	5.46; 2.178	-3909 ± 716	-6760 to -1058
	Licac vs Licac+KCl	0.0647, ns	3.052; 2.659	-4241 ± 1390	-9003 to 521.3
	Licac vs Licac+LiCl	0.0312, *	5.367; 2.053	-6942 ± 1294	-12373 to -1512
	Licac+KCl vs Licac+LiCl	0.0288, *	4.919; 2.312	-2702 ± 549.2	-4784 to -619.2
Int7	H2O vs Licac	0.3664, ns	1.024; 3.816	-1974 ± 1928	-7431 to 3483
	H2O vs Licac+KCl	0.0596, ns	3.832; 2.046	-5804 ± 1514	-12180 to 572.9
	H2O vs Licac+LiCl	0.1434, ns	2.21; 2.252	-3431 ± 1553	-9444 to 2582
	Licac vs Licac+KCl	0.0838, ns	3.151; 2.073	-3830 ± 1215	-8888 to 1228
	Licac vs Licac+LiCl	0.3509, ns	1.154; 2.391	-1457 ± 1263	-6121 to 3207
	Licac+KCl vs Licac+LiCl	0.0136, *	5.761; 2.711	2373 ± 411.9	979.5 to 3767
CD3	H2O vs Licac	0.0189, *	4.442; 3.166	296.3 ± 66.71	90.2 to 502.5
	H2O vs Licac+KCl	0.0093, **	5.276; 3.448	317 ± 60.08	139.1 to 494.9
	H2O vs Licac+LiCl	0.0010, ***	9.037; 3.873	-387 ± 42.83	-507.5 to -266.5
	Licac vs Licac+KCl	0.8013, ns	0.2692; 3.92	20.67 ± 76.77	-194.2 to 235.5
	Licac vs Licac+LiCl	0.0022, **	10.65; 2.85	-683.3 ± 64.17	-893.8 to -472.9
	Licac+KCl vs Licac+LiCl	0.0010, ***	12.3; 3.092	-704 ± 57.25	-883.2 to -524.8
Plas24	H2O vs Licac	0.5423, ns	0.727; 2.015	1219 ± 1676	-5942 to 8380
	H2O vs Licac+KCl	0.0007, ***	12.77; 3.249	-1529 ± 119.8	-1895 to -1164
	H2O vs Licac+LiCl	0.0690, ns	3.309; 2.237	-1441 ± 435.4	-3137 to 254.7
	Licac vs Licac+KCl	0.2421, ns	1.641; 2.005	-2748 ± 1674	-9934 to 4438
	Licac vs Licac+LiCl	0.2494, ns	1.541; 2.255	-2660 ± 1726	-9337 to 4018
	Licac+KCl vs Licac+LiCl	0.8547, ns	0.2067; 2.083	88.33 ± 427.4	-1682 to 1859

Appendix B

Oligo	Solvents	Unpaired t-test with Welch's correction			
		p-value	t, df	$\bar{x}_2 - \bar{x}_1$	95% CI
AV3	H2O vs Licac	0.8344, ns	0.2281; 2.966	8.467 ± 37.12	-110.4 to 127.4
	H2O vs Licac+KCl	0.4028, ns	0.9411; 3.779	-39.53 ± 42.01	-158.9 to 79.84
	H2O vs Licac+LiCl	0.1792, ns	1.827; 2.597	-64.93 ± 35.54	-188.7 to 58.79
	Licac vs Licac+KCl	0.2061, ns	1.556; 3.433	-48 ± 30.84	-139.5 to 43.51
	Licac vs Licac+LiCl	0.0285, *	3.462; 3.754	-73.4 ± 21.2	-133.8 to -12.98
	Licac+KCl vs Licac+LiCl	0.4456, ns	0.8783; 2.941	-25.4 ± 28.92	-118.5 to 67.68

Table 30 – Significance of fluorescence variation in the presence of RNA-derived oligos at neutral and acidic pH conditions.

The unpaired Welch's-corrected t-test was performed for the comparison of INS intron 1-derived oligos at neutral and acidic pH conditions, in water or buffer (relative to Figure 20). For each pair of compared pH condition in water or buffer, the p-value and its summary, Welch-corrected t and degrees of freedom, difference between means ($\bar{x}_2 - \bar{x}_1$), and 95% confidence interval (CI), respectively, are indicated.

Oligo	Solvent	Unpaired t-test with Welch's correction			
		p-value	t, df	$\bar{x}_2 - \bar{x}_1$	95% CI
Int1	H2O	0.0719, ns	2.885; 2.697	-5175 ± 1794	-11264 to 914.7
	Licac	0.6020, ns	0.5684; 3.754	-1198 ± 2107	-7202 to 4807
	Licac+KCl	0.1406, ns	2.065; 2.707	-2779 ± 1346	-7335 to 1778
	Licac+LiCl	0.5616, ns	0.6878; 2.034	-1108 ± 1611	-7929 to 5713
Int7	H2O	0.1444, ns	1.866; 3.55	-3413 ± 1829	-8754 to 1928
	Licac	0.0579, ns	2.679; 3.831	-4149 ± 1549	-8524 to 227.2
	Licac+KCl	0.2450, ns	1.517; 2.474	-751.3 ± 495.4	-2535 to 1033
	Licac+LiCl	0.0727, ns	2.42; 4	-1299 ± 536.8	-2790 to 191.1
CD3	H2O	0.6986, ns	0.4418; 2.182	-69.63 ± 157.6	-696.4 to 557.1
	Licac	0.0891, ns	2.855; 2.286	-639.3 ± 223.9	-1496 to 217.2
	Licac+KCl	0.0448, *	3.668; 2.585	-511.3 ± 139.4	-998.1 to -24.49
	Licac+LiCl	0.0726, ns	2.68; 3.094	-153.3 ± 57.2	-332.2 to 25.65
Plas24	H2O	0.1190, ns	2.596; 2.048	-2463 ± 948.9	-6456 to 1530
	Licac	0.2318, ns	1.563; 2.541	-2790 ± 1785	-9097 to 3517
	Licac+KCl	0.4545, ns	0.9106; 2.105	-347.3 ± 381.4	-1912 to 1218
	Licac+LiCl	0.1181, ns	2.027; 3.713	-1427 ± 704.1	-3443 to 589
AV3	H2O	0.1960, ns	1.796; 2.333	-213.8 ± 119	-661.9 to 234.4
	Licac	0.4979, ns	0.7565; 3.437	-23.3 ± 30.8	-114.6 to 68.04
	Licac+KCl	0.9483, ns	0.06941; 3.671	3.033 ± 43.70	-122.7 to 128.8
	Licac+LiCl	0.9500, ns	0.06712; 3.671	1.467 ± 21.85	-61.41 to 64.34

Table 31 - Significance of fluorescence intensity of *INS* intron 1 RNA-derived oligos in the presence of increasing potassium (K) concentrations.

Comparison of mean fluorescence of G4 formation in RNA oligos in the presence of increasing potassium concentrations (mM), using unpaired t-tests with Welch's correction (relative to Figure 21). For each pair of compared concentrations, p-value and its summary, t and degrees of freedom, means difference ($\bar{x}_2 - \bar{x}_1$), and 95% confidence interval (CI), respectively, are shown.

Oligo	Solvents	Unpaired t-test with Welch's correction			
		p-value	t, df	$\bar{x}_2 - \bar{x}_1$	95% CI
Int1	Licac vs. Licac+1 K	0.5156, ns	0.712; 4	-1475 ± 2070	-7222 to 4273
	Licac vs. Licac+3 K	0.4420, ns	0.853; 3.99	-1722 ± 2019	-7334 to 3890
	Licac vs. Licac+10 K	0.1372, ns	2.11; 2.65	-3335 ± 1580	-8761 to 2091
	Licac vs. Licac+30 K	0.0453, *	3.9; 2.37	-5959 ± 1529	-11646 to -272
	Licac vs. Licac+100 K	0.0212, *	6.23; 2.13	-9263 ± 1487	-15295 to -3232
	Licac vs. Licac+150 K	0.0212, *	6.7; 2.01	-9822 ± 1465	-16087 to -3556
	Licac vs. Licac+300 K	0.0205, *	6.84; 2.01	-10018 ± 1464	-16297 to -3739
	Licac vs. Licac+500 K	0.0200, *	6.94; 2.01	-10165 ± 1464	-16446 to -3885
Int7	Licac vs. Licac+1 K	0.2171, ns	1.67; 2.38	-3578 ± 2146	-11530 to 4374
	Licac vs. Licac+3 K	0.0991, ns	2.75; 2.21	-5792 ± 2103	-14069 to 2486
	Licac vs. Licac+10 K	0.0570, ns	3.989; 2.011	-8188 ± 2053	-16975 to 598.5
	Licac vs. Licac+30 K	0.0433, *	4.639; 2.005	-9515 ± 2051	-18320 to -710.5
	Licac vs. Licac+100 K	0.0366, *	4.906; 2.066	-10140 ± 2067	-18766 to -1514
	Licac vs. Licac+150 K	0.0389, *	4.901; 2.008	-10058 ± 2052	-18853 to -1262
	Licac vs. Licac+300 K	0.0377, *	5; 2.001	-10249 ± 2050	-19068 to -1431
	Licac vs. Licac+500 K	0.0361, *	5.106; 2.004	-10472 ± 2051	-19281 to -1663
CD3	Licac vs. Licac+1 K	0.6087, ns	0.5646; 3.274	-239 ± 423.3	-1525 to 1047
	Licac vs. Licac+3 K	0.5893, ns	0.6122; 2.623	-239.3 ± 390.9	-1591 to 1112
	Licac vs. Licac+10 K	0.2877, ns	1.37;2.332	-517.7 ± 377.9	-1941 to 905.3
	Licac vs. Licac+30 K	0.1395, ns	2.256; 2.231	-842.3 ± 373.4	-2300 to 615
	Licac vs. Licac+100 K	0.0562, ns	4.012; 2.015	-1459 ± 363.7	-3013 to 95.06
	Licac vs. Licac+150 K	0.0466, *	4.428; 2.018	-1611 ± 363.9	-3163 to -59.34
	Licac vs. Licac+300 K	0.0391, *	4.775; 2.053	-1745 ± 365.4	-3279 to -210.5
	Licac vs. Licac+500 K	0.0380, *	4.888; 2.036	-1782 ± 364.7	-3325 to -239.8

Oligo	Solvents	Unpaired t-test with Welch's correction			
		p-value	t, df	$\bar{x}_2 - \bar{x}_1$	95% CI
Plas24	Licac vs. Licac+1 K	0.3876, ns	0.9712; 3.913	-2023 ± 2083	-7858 to 3812
	Licac vs. Licac+3 K	0.1494, ns	2.158; 2.249	-3512 ± 1628	-9823 to 2798
	Licac vs. Licac+10 K	0.0893, ns	2.838; 2.307	-4651 ± 1639	-10876 to 1574
	Licac vs. Licac+30 K	0.0635, ns	3.581; 2.134	-5749 ± 1606	-12257 to 758.7
	Licac vs. Licac+100 K	0.0494, *	4.239; 2.045	-6732 ± 1588	-13423 to -42.02
	Licac vs. Licac+150 K	0.0448, *	4.306; 2.126	-6906 ± 1604	-13430 to -381.6
	Licac vs. Licac+300 K	0.0399, *	4.52; 2.146	-7267 ± 1608	-13753 to -781.7
	Licac vs. Licac+500 K	0.0403, *	4.761; 2.028	-7545 ± 1585	-14275 to -816
AV3	Licac vs. Licac+1 K	0.6112, ns	0.551; 3.93	-47.3 ± 85.8	-287 to 193
	Licac vs. Licac+3 K	0.2283, ns	1.42; 3.99	-116 ± 81.4	-342 to 110
	Licac vs. Licac+10 K	0.1400, ns	1.89; 3.59	-130 ± 69	-331 to 70.2
	Licac vs. Licac+30 K	0.0373, *	4.08; 2.5	-245 ± 59.9	-459 to -30.4
	Licac vs. Licac+100 K	0.0224, *	5.87; 2.19	-339 ± 57.8	-568 to -110
	Licac vs. Licac+150 K	0.0203, *	5.82; 2.3	-340 ± 58.5	-563 to -117
	Licac vs. Licac+300 K	0.0126, *	6.3; 2.57	-381 ± 60.4	-592 to -169
	Licac vs. Licac+500 K	0.0152, *	7.29; 2.14	-419 ± 57.4	-651 to -186

Table 32 - Significance of fluorescence intensity of *INS* intron 1 RNA-derived oligos in the presence of increasing magnesium (Mg) concentrations.

Comparison of mean fluorescence intensity of G4 formation in RNA oligos in the presence of increasing magnesium concentrations (mM), using unpaired t-tests with Welch's correction (relative to Figure 22). For each pair of compared concentrations, the p-value and its summary, Welch-corrected t and degrees of freedom, difference between means ($\bar{x}_2 - \bar{x}_1$), and 95% confidence interval (CI), respectively, are shown.

Oligo	Solvents	Unpaired t-test with Welch's correction			
		p-value	t, df	$\bar{x}_2 - \bar{x}_1$	95% CI
Int1	Licac vs. Licac+0.01 Mg	0.6204, ns	0.5367; 3.931	-1040 ± 1937	-6455 to 4376
	Licac vs. Licac+0.03 Mg	0.6383, ns	0.5287; 2.633	-831 ± 1572	-6252 to 4590
	Licac vs. Licac+0.1 Mg	0.1539, ns	2.083; 2.339	-3164 ± 1519	-8870 to 2542
	Licac vs. Licac+0.3 Mg	0.0599, ns	3.463; 2.321	-5247 ± 1515	-10976 to 481.8
	Licac vs. Licac+1 Mg	0.0442, *	4.515; 2.037	-6612 ± 1464	-12805 to -418.2
	Licac vs. Licac+3 Mg	0.0389, *	4.9; 2.008	-7150 ± 1459	-13406 to -895.1
	Licac vs. Licac+10 Mg	0.0368, *	5.049; 2.006	-7365 ± 1459	-13625 to -1106
Int7	Licac vs. Licac+0.01 Mg	0.4001, ns	1.05; 2.083	936.7 ± 892	-2758 to 4631
	Licac vs. Licac+0.03 Mg	0.5441, ns	0.6799; 3.084	-1259 ± 1851	-7061 to 4544
	Licac vs. Licac+0.1 Mg	0.3032, ns	1.181; 4	-1475 ± 1249	-4943 to 1993
	Licac vs. Licac+0.3 Mg	0.1321, ns	2.464; 2.009	-2178 ± 883.9	-5964 to 1608
	Licac vs. Licac+1 Mg	0.0192, *	6.56; 2.127	-5883 ± 896.8	-9529 to -2237
	Licac vs. Licac+3 Mg	0.0090, **	9.029; 2.189	-8158 ± 903.6	-11741 to -4576
	Licac vs. Licac+10 Mg	0.0093, **	10.29; 2.002	-9084 ± 883.1	-12880 to -5288
CD3	Licac vs. Licac+0.01 Mg	0.7441, ns	0.3529; 3.542	-89 ± 252.2	-826.4 to 648.4
	Licac vs. Licac+0.03 Mg	0.5122, ns	0.7201; 3.911	197.3 ± 274.1	-570.5 to 965.1
	Licac vs. Licac+0.1 Mg	0.3381, ns	1.162; 2.682	-262 ± 225.5	-1030 to 506.1
	Licac vs. Licac+0.3 Mg	0.1540, ns	2.191; 2.094	-461 ± 210.4	-1328 to 406.2
	Licac vs. Licac+1 Mg	0.0820, ns	3.139; 2.118	-662.3 ± 211	-1523 to 198.5
	Licac vs. Licac+3 Mg	0.0644, ns	3.64; 2.072	-763.7 ± 209.8	-1637 to 109.6
	Licac vs. Licac+10 Mg	0.0578, ns	3.899; 2.046	-815.3 ± 209.1	-1696 to 65.46

Oligo	Solvents	Unpaired t-test with Welch's correction			
		p-value	t, df	$\bar{x}_2 - \bar{x}_1$	95% CI
Plas24	Licac vs. Licac+0.01 Mg	0.3740, ns	1.113; 2.162	-649.7 ± 583.6	-2989 to 1690
	Licac vs. Licac+0.03 Mg	0.9009, ns	0.1358; 2.886	-86.33 ± 635.5	-2155 to 1982
	Licac vs. Licac+0.1 Mg	0.2293, ns	1.429; 3.83	-1051 ± 735.5	-3129 to 1028
	Licac vs. Licac+0.3 Mg	0.0162, *	5.119; 2.859	-3243 ± 633.4	-5316 to -1169
	Licac vs. Licac+1 Mg	0.0056, **	9.612; 2.405	-5774 ± 600.7	-7983 to -3565
	Licac vs. Licac+3 Mg	0.0044, **	13.62; 2.1	-7889 ± 579.3	-10272 to -5507
	Licac vs. Licac+10 Mg	0.0028, **	15.86; 2.159	-9254 ± 583.4	-11595 to -6913
AV3	Licac vs. Licac+0.01 Mg	0.4167, ns	1.009; 2.058	142 ± 140.8	-447.5 to 731.5
	Licac vs. Licac+0.03 Mg	0.0894, ns	2.527; 2.87	47.33 ± 18.73	-13.83 to 108.5
	Licac vs. Licac+0.1 Mg	0.8294, ns	0.23; 3.986	-5.667 ± 24.63	-74.15 to 62.82
	Licac vs. Licac+0.3 Mg	0.0957, ns	2.479; 2.791	-101.3 ± 40.88	-237.1 to 34.46
	Licac vs. Licac+1 Mg	0.0014, **	9.195; 3.494	-187 ± 20.34	-246.8 to -127.2
	Licac vs. Licac+3 Mg	0.0003, ***	11.34; 4	-270.7 ± 23.87	-336.9 to -204.4
	Licac vs. Licac+10 Mg	0.0041, **	7.015; 3.343	-224.7 ± 32.03	-320.9 to -128.4

Table 33 - Significance of fluorescence intensity of *INS* intron 1 RNA-derived oligos in the presence of combined potassium (K) and magnesium (Mg) concentrations.

Comparison of mean fluorescence intensity of G4 formation in RNA oligos in the presence of combined concentrations of potassium (K) and magnesium (mM), using unpaired t-tests with Welch's correction (relative to Figure 23). For each pair of compared concentrations, the p-value and its summary, Welch-corrected t and degrees of freedom, difference between means ($\bar{x}_2 - \bar{x}_1$), and 95% confidence interval (CI), respectively, are shown.

Oligo	Solvents	Unpaired t-test with Welch's correction			
		p-value	t, df	$\bar{x}_2 - \bar{x}_1$	95% CI
Int1	1 K vs. Licac+150 K	0.0018, **	23.24; 2.017	-6474 ± 278.5	-7662 to -5285
	1 K vs. 0.03 Mg	0.0739, ns	2.875; 2.651	-2111 ± 734.4	-4633 to 410.1
	1 K vs. 1 Mg	0.0003, ***	20.49; 2.97	-6389 ± 311.8	-7387 to -5391
	1 K vs. 1 K+0.03 Mg	0.0200, *	3.76; 3.974	-1421 ± 378	-2474 to -369
	1 K vs.1 K+1 Mg	0.0014, **	23.51; 2.109	-6623 ± 281.7	-7776 to -5469
	1 K vs. 150 K+0.03 Mg	0.0012, **	22.71; 2.205	-6470 ± 285	-7593 to -5347
	1 K vs. 150 K+1 Mg	0.0014, **	23.84; 2.096	-6705 ± 281.2	-7863 to -5547
	0.03 Mg vs. 150 K	0.0234, *	6.415; 2.003	4362 ± 680	1441 to 7284
	0.03 Mg vs. 1 Mg	0.0207, *	6.161; 2.173	-4277 ± 694.3	-7048 to -1506
	0.03 Mg vs. 1 K+0.03 Mg	0.4231, ns	0.9498; 2.557	690 ± 726.4	-1866 to 3246
	0.03 Mg vs. 1 K+1 Mg	0.0215, *	6.622; 2.018	-4511 ± 681.3	-7417 to -1605
	0.03 Mg vs. 150 K+0.03 Mg	0.0227, *	6.385; 2.034	-4359 ± 682.6	-7249 to -1469
	0.03 Mg vs. 150 K+1 Mg	0.0208, *	6.744; 2.016	-4594 ± 681.1	-7502 to -1685
	1K+0.03 Mg vs. 150 K	0.0025, **	19.67; 2.02	5052 ± 256.9	3957 to 6147
	1 K+0.03 Mg vs. 1 Mg	0.0004, ***	16.97; 3.114	4967 ± 292.7	4055 to 5880
	1 K+0.03 Mg vs. 1 K+1 Mg	0.0019, **	19.98; 2.128	-5201 ± 260.4	-6259 to -4143
	1 K+0.03 Mg vs. 150 K+0.03 Mg	0.0016, **	19.13; 2.241	-5049 ± 263.9	-6075 to -4023
	1 K+0.03 Mg vs. 150 K+1 Mg	0.0018, **	20.33; 2.113	-5284 ± 259.9	-6346 to -4221
Int7	1 K vs. Licac+150 K	0.0042, **	14.4; 2.061	-4479 ± 311	-5780 to -3178
	1 K vs. 0.03 Mg	0.0045, **	5.983; 3.829	-2373 ± 396.6	-3494 to -1252
	1 K vs. 1 Mg	0.0055, **	11.85; 2.14	-3721 ± 314	-4991 to -2451
	1 K vs. 1 K+0.03 Mg	0.5247, ns	0.7196; 2.94	-497 ± 690.6	-2720 to 1726
	1 K vs.1 K+1 Mg	0.0043, **	13.23; 2.14	-4156 ± 314	-5426 to -2886

Oligo	Solvents	Unpaired t-test with Welch's correction			
		p-value	t, df	$\bar{x}_2 - \bar{x}_1$	95% CI
Int7	1 K vs. 150 K+0.03 Mg	0.0037, **	14.25; 2.141	-4476 ± 314.1	-5746 to -3206
	1 K vs. 150 K+1 Mg	0.0037, **	14.82; 2.096	-4630 ± 312.4	-5917 to -3343
	0.03 Mg vs. 150 K	0.0122, *	8.361; 2.094	2106 ± 251.9	1068 to 3145
	0.03 Mg vs. 1 Mg	0.0274, *	5.272; 2.214	-1348 ± 255.6	-2352 to -343.7
	0.03 Mg vs. 1 K+0.03 Mg	0.0778, ns	2.816; 2.633	1876 ± 666.1	-421.1 to 4173
	0.03 Mg vs. 1 K+1 Mg	0.0151, *	6.973; 2.215	-1783 ± 255.7	-2786 to -778.9
	0.03 Mg vs. 150 K+0.03 Mg	0.0106, *	8.225; 2.216	-2103 ± 255.7	-3107 to -1099
	0.03 Mg vs. 150 K+1 Mg	0.0099, **	8.9; 2.147	-2257 ± 253.6	-3279 to -1235
	1K+0.03 Mg vs. 150 K	0.0229, *	6.434; 2.015	3982 ± 619	1338 to 6626
	1 K+0.03 Mg vs. 1 Mg	0.0339, *	5.195; 2.035	3224 ± 620.5	597.3 to 5850
	1 K+0.03 Mg vs. 1 K+1 Mg	0.0265, *	5.896; 2.035	-3659 ± 620.5	-6285 to -1032
	1 K+0.03 Mg vs. 150 K+0.03 Mg	0.0225, *	6.412; 2.035	-3979 ± 620.5	-6605 to -1353
	1 K+0.03 Mg vs. 150 K+1 Mg	0.0211, *	6.67; 2.024	-4133 ± 619.7	-6769 to -1497
CD3	1 K vs. Licac+150 K	0.0011, **	11.03; 3.25	-1145 ± 103.9	-1462 to -828.8
	1 K vs. 0.03 Mg	0.0102, *	3.825; 5.508	-483 ± 126.3	-798.8 to -167.2
	1 K vs. 1 Mg	0.0004, ***	10.16; 4.278	-1144 ± 112.6	-1448 to -839
	1 K vs. 1 K+0.03 Mg	0.0428, *	2.821; 4.4	-320.7 ± 113.6	-625.2 to -16.1
	1 K vs.1 K+1 Mg	0.0012, **	10.2; 3.361	-1069 ± 104.8	-1383 to -754.6
	1 K vs. 150 K+0.03 Mg	0.0012, **	12.01; 3.047	-1227 ± 102.1	-1549 to -904.8
	1 K vs. 150 K+1 Mg	0.0010, **	12.75; 3.014	-1298 ± 101.9	-1622 to -975
	0.03 Mg vs. 150 K	0.0019, **	8.535; 3.461	662.3 ± 77.6	433 to 891.7
	0.03 Mg vs. 1 Mg	0.0006, ***	7.43; 5.122	-660.7 ± 88.91	-887.6 to -433.7
	0.03 Mg vs. 1 K+0.03 Mg	0.1291, ns	1.798; 5.273	162.4 ± 90.29	-66.18 to 390.9
	0.03 Mg vs. 1 K+1 Mg	0.0025, **	7.429; 3.662	-585.7 ± 78.83	-812.7 to -358.6
	0.03 Mg vs. 150 K+0.03 Mg	0.0020, **	9.88; 3.088	-744 ± 75.31	-979.9 to -508.1
	0.03 Mg vs. 150 K+1 Mg	0.0016, **	10.88; 3.025	-815.3 ± 74.92	-1053 to -578
	1K+0.03 Mg vs. 150 K	0.0001, ***	15.07; 3.984	824.7 ± 54.73	672.5 to 976.9

Oligo	Solvents	Unpaired t-test with Welch's correction			
		p-value	t, df	$\bar{x}_2 - \bar{x}_1$	95% CI
CD3	1 K+0.03 Mg vs. 1 Mg	<0.0001, ****	11.78; 5.985	823 ± 69.85	652 to 994
	1 K+0.03 Mg vs. 1 K+1 Mg	0.0001, ***	13.25; 4.38	-748 ± 56.46	-899.5 to -596.5
	1 K+0.03 Mg vs. 150 K+0.03 Mg	0.0003, ***	17.62; 3.191	-906.4 ± 51.43	-1065 to -748.1
	1 K+0.03 Mg vs. 150 K+1 Mg	0.0003, ***	19.22; 3.056	-977.7 ± 50.86	-1138 to -817.5
Plas24	1 K vs. Licac+150 K	0.0192, *	6.635; 2.105	-3338 ± 503.1	-5402 to -1274
	1 K vs. 0.03 Mg	0.7734, ns	0.3119; 3.369	183 ± 586.6	-1574 to 1940
	1 K vs. 1 Mg	0.0641, ns	3.16; 2.53	-1672 ± 529	-3547 to 203.5
	1 K vs. 1 K+0.03 Mg	0.8787, ns	0.1652; 3.197	94.67 ± 573.2	-1667 to 1857
	1 K vs.1 K+1 Mg	0.0491, *	3.807; 2.327	-1967 ± 516.6	-3915 to -17.94
	1 K vs. 150 K+0.03 Mg	0.0228, *	6.484; 2.006	-3222 ± 496.9	-5354 to -1090
	1 K vs. 150 K+1 Mg	0.0213, *	6.63; 2.026	-3303 ± 498.2	-5420 to -1185
	0.03 Mg vs. 150 K	0.0053, **	10.91; 2.265	3521 ± 322.6	2277 to 4764
	0.03 Mg vs. 1 Mg	0.0120, *	5.128; 3.221	-1855 ± 361.7	-2962 to -747
	0.03 Mg vs. 1 K+0.03 Mg	0.8451, ns	0.2085; 3.97	-88.33 ± 423.7	-1268 to 1092
	0.03 Mg vs. 1 K+1 Mg	0.0101, *	6.262; 2.797	-2150 ± 343.3	-3288 to -1011
	0.03 Mg vs. 150 K+0.03 Mg	0.0081, **	10.88; 2.015	-3405 ± 313	-4742 to -2068
	0.03 Mg vs. 150 K+1 Mg	0.0072, **	11.07; 2.065	-3486 ± 314.9	-4800 to -2171
	1K+0.03 Mg vs. 150 K	0.0043, **	11.54; 2.316	3432 ± 297.4	2306 to 4559
	1 K+0.03 Mg vs. 1 Mg	0.0101, *	5.204; 3.394	1766 ± 339.4	753.7 to 2779
	1 K+0.03 Mg vs. 1 K+1 Mg	0.0081, **	6.447; 2.933	-2061 ± 319.7	-3092 to -1031
	1 K+0.03 Mg vs. 150 K+0.03 Mg	0.0072, **	11.56; 2.018	-3317 ± 286.9	-4541 to -2093
	1 K+0.03 Mg vs. 150 K+1 Mg	0.0062, **	11.75; 2.078	-3397 ± 289	-4597 to -2197
AV3	1 K vs. Licac+150 K	0.0089, **	5.071; 3.674	-156.3 ± 30.83	-245 to -67.66
	1 K vs. 0.03 Mg	0.3786, ns	1.003; 3.587	-43.33 ± 43.2	-168.9 to 82.26
	1 K vs. 1 Mg	0.0105, *	4.633; 3.887	-178.7 ± 38.56	-287 to -70.36
	1 K vs. 1 K+0.03 Mg	0.1158, ns	2.003; 3.997	-69.33 ± 34.62	-165.5 to 26.81
	1 K vs.1 K+1 Mg	0.0060, **	5.363; 3.955	-199.3 ± 37.17	-303 to -95.67

Oligo	Solvents	Unpaired t-test with Welch's correction			
		p-value	t, df	$\bar{x}_2 - \bar{x}_1$	95% CI
AV3	1 K vs. 150 K+0.03 Mg	0.0068, **	6.418; 3.113	-182 ± 28.36	-270.4 to -93.57
	1 K vs. 150 K+1 Mg	0.0025, **	6.978; 3.856	-224.3 ± 32.15	-314.9 to -133.7
	0.03 Mg vs. 150 K	0.0657, ns	2.84; 2.997	113 ± 39.79	-13.71 to 239.7
	0.03 Mg vs. 1 Mg	0.0441, *	2.939; 3.876	-135.3 ± 46.04	-264.8 to -5.862
	0.03 Mg vs. 1 K+0.03 Mg	0.5804, ns	0.6076; 3.53	-26 ± 42.79	-151.3 to 99.32
	0.03 Mg vs. 1 K+1 Mg	0.0279, *	3.476; 3.781	-156 ± 44.88	-283.5 to -28.48
	0.03 Mg vs. 150 K+0.03 Mg	0.0450, *	3.658; 2.587	-138.7 ± 37.91	-271 to -6.345
	0.03 Mg vs. 150 K+1 Mg	0.0186, *	4.434; 3.2	-181 ± 40.82	-306.4 to -55.57
	1K+0.03 Mg vs. 150 K	0.0492, *	2.876; 3.727	87 ± 30.25	0.5229 to 173.5
	1 K+0.03 Mg vs. 1 Mg	0.0476, *	2.869; 3.848	109.3 ± 38.1	1.872 to 216.8
	1 K+0.03 Mg vs. 1 K+1 Mg	0.0247, *	3.543; 3.927	-130 ± 36.69	-232.6 to -27.38
	1 K+0.03 Mg vs. 150 K+0.03 Mg	0.0242, *	4.063; 3.168	-112.7 ± 27.73	-198.3 to -27.01
	1 K+0.03 Mg vs. 150 K+1 Mg	0.0086, **	4.906; 3.894	-155 ± 31.59	-243.7 to -66.33

Table 34 – Proteins bound to *INS* WT transcript in pull-down assay, identified by mass spectrometry

Entry name	Protein name/Function (UniProtKB)	Organism	Gene	Protein mass	Peptide sequence	Peptide mass
TBB5_Human	Tubulin beta chain/Major constituent of microtubules; GTPase activity (P07437)	HS	TUBB	49639	TAVCDIPPR	1027,5121
					YLTVAAVFR	1038,5862
					LAVNMVPFPR	1142,627
					ISEQFTAMFR	1228,591
					ISVYYNEATGGK	1300,6299
					EVDEQMLNVQNK	1445,682
					AILVDLEPGTMDSVR	1614,8287
					LHFFMPGFAPLTSR	1619,8283
					ALTVPELTQQVFDAK	1658,8879
					NSSYFVEWIPNNVK	1695,8257
					MAVTFIGNSTAIQELFK	1868,9706
					GHYTEGAELVDSVLDVVR	1957,9745
					GHYTEGAELVDSVLDVVRK	2086,0695
					LTTPTYGDLNHLVSATMSGVTTCLR	2707,331
SEPT7_HUMAN	Septin-7/Filament-forming cytoskeletal GTPase (Q16181)	HS	SEPT7	50648	VNIIPLIAK	979,643
					LKDSEAELQR	1187,6146
					FEDYLNAESR	1242,5517
					LAAVTYNGVDNNK	1377,6888
					DVTNNVHYENYR	1522,6801
					LPLAVVGSNTIIEVNGK	1722,988
					NLEGYVGFANLPNQVYR	1952,9744
					STLINSLFLTDLYSPEYPGPSHR	2606,3017

Entry name	Protein name/Function (UniProtKB)	Organism	Gene	Protein mass	Peptide sequence
HNRH1_HUMAN	Heterogeneous nuclear ribonucleoprotein/pre-mRNA alternative splicing regulation; binds poly(RG) (P31943)	HS	HNRNPH1	49198	IQNGAQGIR VHIEIGPDGR SNNVEMDWVLK GLPWSCSADEVQR DLNYCFSGMSDHR HTGPNSPDTANDGFVR STGEAFVQFASQEIAEK ATENDIYNFFSPLNPVR EGRPSGEAFVELESEDEVK YVELFLNSTAGASGGAYEHR VTGEADVEFATHEDAVAAMSK
HNRH2_HUMAN	Heterogeneous nuclear ribonucleoprotein H2/pre-mRNA alternative splicing regulation; binds poly(RG) (P55795)	HS	HNRNPH2	49232	VHIEIGPDGR GLPWSCSADEVMR DLNYCFSGMSDHR HTGPNSPDTANDGFVR STGEAFVQFASQEIAEK ATENDIYNFFSPLNPMR YGDGGSSFQSTTGHCVHMR VTGEADVEFATHEDAVAAMAK
SEP11_HUMAN	Septin-11/Filament-forming cytoskeletal GTPase (Q9NVA2)	HS	SEPT11	49367	VNIIPIIAK SLFNYHDTR SYELQESNVR STLMDTLFNTK FESDPATHNEPGVR LTIVDTVGFGDQINK AAAQLLQSQAQQSGAQQTK STSQGFCFNILCVGETGIGK
SEP10_HUMAN	Septin-10/Filament-forming cytoskeletal GTPase (Q9P0V9)	HS	SEPT10	52560	ADTVSKTELQK LLEEEIIAFSK AQTYELQESNVQLK ATSEIFHSQSFLATGSNLR LMSELVSNGVQIYQFPTDDDTIAK

Appendix B

Entry name	Protein name/Function (UniProtKB)	Organism	Gene	Protein mass	Peptide sequence	Peptide mass
TBB3_HUMAN	Tubulin beta-3 chain/Major constituent of microtubules; GTPase activity (Q13509)	HS	TUBB3	50400	LAVNMVPFPR	1142,627
					ISEQFTAMFR	1228,591
					AILVDLEPGTMDSVR	1614,8287
					NSSYFVEWIPNNVK	1695,8257
					GHYTEGAELVDSVLDVVR	1957,9745
					GHYTEGAELVDSVLDVVRK	2086,0695
					ECENCDCLQGFQLTHSLGGGTGSGMGTLLISK	3312,4883
TBA1B_HUMAN	Tubulin alpha-1B chain/Major constituent of microtubules; GTPase activity (P68363)	HS	TUBA1B	50120	SIQFVDWCPTGFK	1583,7443
					AVFVDLEPTVIDEVR	1700,8985
					VGINYQPPTVVPGGDLAK	1823,9782
					TIGGGDDSFNTFFSETGAGK	2006,8858
HNRPF_HUMAN	Heterogeneous nuclear ribonucleoprotein F/pre-mRNA alternative splicing regulation; binds poly(RG) (P52597)	HS	HNRNPF	45643	VHIEIGPDGR	1091,5724
					ITGEAFVQFASQELAEK	1866,9363
					ATENDIYNFFSPLNPVR	1995,969
CSTF1_HUMAN	Cleavage stimulation factor subunit 1/Polyadenylation and 3'end cleavage of mammalian pre-mRNAs (Q05048)	HS	CSTF1	48327	YTGAGLSGR	880,4403
					LGMENDDTAVQYAIGR	1751,8148
					TQAVFNHTEDYVLLPDER	2146,0331
					TLYDHVDEVTCLAFHPTEQILASGSR	2958,4182
LA_HUMAN	Lupus La protein/Exonuclease protection, folding and maturation regulation of RNA pol III	HS	SSB	46808	IIEDQQESLNK	1315,6619
					GSIFVVFDSIESAK	1497,7715
PDIA6_HUMAN	Protein disulfide-isomerase A6/Inhibition of misfolded/unfolded protein aggregation and	HS	PDIA6	48091	TGEAIVDAALSALR	1385,7514
					LAAVDATVNQVLASR	1526,8416
PDIP3_HUMAN	Polymerase delta-interacting protein 3/Translation regulation (Q9BY77)	HS	POLDIP3	46060	VGIQQGLLSQSTR	1385,7627
DX39B_HUMAN	Spliceosome RNA helicase DDX39B/Nuclear export of (un)spliced mRNA (Q13838)	HS	DDX39B	48960	ILVATNLFGR	1102,6499
RUVB2_HUMAN	RuvB-like 2/ATP-dependent DNA helicase (5' to 3') (Q9Y230)	HS	RUVBL2	51125	LLIVSTTPYSEK	1349,7442
SRSF6_HUMAN	Serine/arginine-rich splicing factor 6/Constitutive splicing and regulation of the selection of alternative splice sites (Q13247)	HS	SRSF6	39563	QAGEVTYADAHKER	1573,7485

Table 35 - Proteins bound to *INS* del5 transcript in pull-down assay, identified by mass spectrometry

Entry name	Protein name/Function (UniProtKB)	Organism	Gene	Protein mass	Peptide sequence	Peptide mass
SEPT7_HUMAN	Septin-7	HS	SEPT7	50648	VNIIPLIAK	979,643
					ILEQQNSSR	1073,5465
					FEDYLNAESR	1242,5517
					LAAVTYNGVDNNK	1377,6888
					KLAAVTYNGVDNNK	1505,7838
					DVTNNVHYENYR	1522,6801
					MEMEMEQVFEMK	1560,6332
					LPLAVVGSNTIIEVNGK	1722,988
					QFEDEKANWEAQQR	1777,8019
					LPLAVVGSNTIIEVNGKR	1879,0891
					NLEGYVGFANLPNQVYR	1952,9744
					DRLPLAVVGSNTIIEVNGK	1994,116
					IYEFPETDDEEENKLVK	2096,979
					STLINSLFLTDLYSPEYPGPSHR	2606,3017
IF4A1_HUMAN	Eukaryotic initiation factor 4A-I	HS	EIF4A1	46125	VLITTDLLAR	1113,6758
					KEELTLEGIR	1186,6557
					GYDVIAQAQSGTGK	1393,6838
					MFVLDEADEMLSR	1554,7058
					GIYAYGFEKPSAIQQR	1826,9315
HNRH1_HUMAN	Heterogeneous nuclear ribonucleoprotein H	HS	HNRNPH1	49198	VHIEIGPDGR	1091,5724
					STGEAFVQFASQEIAEK	1840,8843
					ATENDIYNFFSPLNPVR	1995,969
					VTGEADVEFATHEDAVAAMSK	2192,9896

Entry name	Protein name/Function (UniProtKB)	Organism	Gene	Protein mass	Peptide sequence	Peptide mass
ACTB_HUMAN	Actin, cytoplasmic 1	HS	ACTB	41710	AGFAGDDAPR	975,441
					DLTDYLMK	997,479
					EITALAPSTMK	1160,6111
					DSYVGDEAQSK	1197,515
					DSYVGDEAQSKR	1353,6161
					QEYDESGPSIVHR	1515,6954
					SYELPDGQVITIGNER	1789,8846
					DLYANTVLSGGTTMYPGIADR	2214,0627
					LCYVALDFEQEMATAASSSSLEK	2549,1665
					TTGIVMDSGDGVTHTVPIYEGYALPHAILR	3182,6071
ACTG_HUMAN	Actin, cytoplasmic 2	HS	ACTG1	41766	AGFAGDDAPR	975,441
					DLTDYLMK	997,479
					EITALAPSTMK	1160,6111
					DSYVGDEAQSK	1197,515
					DSYVGDEAQSKR	1353,6161
					QEYDESGPSIVHR	1515,6954
					SYELPDGQVITIGNER	1789,8846
					DLYANTVLSGGTTMYPGIADR	2214,0627
					LCYVALDFEQEMATAASSSSLEK	2549,1665
					TTGIVMDSGDGVTHTVPIYEGYALPHAILR	3182,6071
HNRPF_HUMAN	Heterogeneous nuclear ribonucleoprotein F	HS	HNRNPF	45643	VHIEIGPDGR	1091,5724
					DLSYCLSGMYDHR	1615,6759
					HSGPNSADSANDGFVR	1629,7132
					QSGEAFVELGSEDDVK	1708,7792
					ITGEAFVQFASQELAEK	1866,9363
					ATENDIYNFFSPLNPVR	1995,969
					VTGEADVEFATHEEAVAAMSK	2191,0103

Entry name	Protein name/Function (UniProtKB)	Organism	Gene	Protein mass	Peptide sequence	Peptide mass
EF1A1_HUMAN	Elongation factor 1-alpha 1	HS	EEF1A1	50109	QLIVGVNK	869,5334
					QTVAVGVIK	913,5597
					LPLQDVYK	974,5437
					IGGIGTVPVGR	1024,603
					STTTGHLIYK	1119,5924
					EHALLAYTLGVK	1313,7343
					YYVTIIDAPGHR	1403,7197
					VETGVLKPGMVVTFAPVNVTTEVK	2514,3768
					SGDAAIVDMVPGKPMCVESFSDYPPLGR	2994,3926
EF1A3_HUMAN	Putative elongation factor 1-alpha-like 3		EEF1A1P5	50153	QLIVGVNK	869,5334
					QTVAVGVIK	913,5597
					LPLQDVYK	974,5437
					IGGIGTVPVGR	1024,603
					STTTGHLIYK	1119,5924
					EHALLAYTLGVK	1313,7343
					YYVTIIDAPGHR	1403,7197
					VETGVLKPGMVVTFAPVNVTTEVK	2530,3717
					SGDAAIVDMVPGKPMCVESFSDYPPLGR	2994,3926

Entry name	Protein name/Function (UniProtKB)	Organism	Gene	Protein mass	Peptide sequence	Peptide mass
IF4A3_HUMAN	Eukaryotic initiation factor 4A-III	HS	EIF4A3	46841	GRDVIAQSQSGTGK	1402,7165
					MLVLDEADEMLNK	1519,7262
					GIYAYGFEKPSAIQQR	1826,9315
PLIN3_HUMAN	Perilipin-3	HS	PLIN3	47046	SVVTGGVQSVMGSR	1362,6926
					LGQMVLSGVDTVLGK	1515,8331
					TLTAAAVSGAQPILSK	1526,8668
VAT1_HUMAN	Synaptic vesicle membrane protein VAT-1 homolog	HS	VAT1	41893	VLLVPGPEKEN	1193,6656
					VVTYGMANLLTGPK	1462,7854
DAZP1_HUMAN	DAZ-associated protein 1	HS	DAZAP1	43356	SQAPGQPGASQWGSR	1512,707
DC8L2_HUMAN	DDB1- and CUL4-associated factor 8-like protein 2	HS	DCAF8L2	67869	LASSGDDLK	904,4502

Table 36 - Proteins bound to beads in pull-down assay, identified by mass spectrometry

Entry name	Protein name/Function (UniProtKB)	Organism	Gene	Protein mass	Peptide sequence	Peptide mass
VIME_HUMAN	Vimentin	HS	VIM	53619	FANYIDK	869,4283
					GTNESLER	904,425
					SYVTTSTR	913,4505
					QQYESVAAK	1022,5033
					QVDQLTNDK	1059,5197
					DNLAEDIMR	1075,4968
					QDVDNASLAR	1087,5258
					FADLSEAANR	1092,52
					VELQELNDR	1114,5618
					LQDEIQNMK	1117,5437
					EYQDLLNVK	1120,5764
					ILLAELEQLK	1168,7067
					RQVDQLTNDK	1215,6208
					LGDLYEEEMR	1253,5598
					MALDIEIATYR	1294,6591
					EEAENTLQSFR	1322,6102
					SLYASSPGGVYATR	1427,7045
					QVQSLTCEVDALK	1489,7446
					MFGGPGTASRPSSSR	1509,6994
					KVESLQEEIAFLK	1532,845
					ILLAELEQLKGQGK	1538,9032
					ISLPLPNFSSLNLR	1569,8878
					TNEKVELQELNDR	1586,79
					ETNLDSLPLVDTHSK	1667,8366
					VEVERDNLAEDIMR	1687,8199
					LQDEIQNMKEEMAR	1733,8076
					ETNLDSLPLVDTHSKR	1823,9377
					LLQDSVDFSLADAINTEFK	2125,0579
					EMEENFAVEAANYQDTIGR	2185,9586
					QVQSLTCEVDALKGTNESLER	2376,1591

Entry name	Protein name/Function (UniProtKB)	Organism	Gene	Protein mass	Peptide sequence	Peptide mass
TBB5_HUMAN	Tubulin beta chain	HS	TUBB	49639	TAVCDIPPR	1027,5121
					YLTVAAVFR	1038,5862
					NMMAACDPR	1064,4201
					FPGQLNADLR	1129,588
					LAVNMVPFPR	1142,627
					ISEQFTAMFR	1228,591
					ISVYYNEATGGK	1300,6299
					IMNTFSVVPSPK	1318,6955
					EVDEQMLNVQNK	1445,682
					AILVDLEPGTMDSVR	1614,8287
					LHFFMPGFAPLTSR	1619,8283
					ALTVPELTQQVFDAK	1658,8879
					NSSYFVEWIPNNVK	1695,8257
					EIVHIQAGQCGNQIGAK	1821,9156
					MAVTFIGNSTAIQELFK	1868,9706
					GHYTEGAELVDSVLDVVR	1957,9745
					LTTPTYGDLNHLVSATMSGVTTCLR	2707,331
					SGPFGQIFRPDNFVFGQSGAGNNWAK	2797,3361
ATPA_HUMAN	ATP synthase subunit alpha, mitochondria	HS	ATP5A1	59714	VVDALGNAIDGK	1170,6245
					HALIIYDDLSK	1286,687
					TSIAIDTIINQK	1315,7347
					TGTAEMSSILEER	1422,666
					TGAIVDVPVGEELLGR	1623,8832
G6PD_HUMAN	Glucose-6-phosphate 1-dehydrogenase	HS	G6PD	59219	VGFQYEGTYK	1190,5608
					DGLLPENTFIVGYAR	1663,857
DHE3_HUMAN	Glutamate dehydrogenase 1, mitochondrial	HS	GLUD1	61359	TAAYVNAIEK	1078,5658
TRXR1_HUMAN	Thioredoxin reductase 1, cytoplasmic	HS	TXNRD1	70862	VVGFHVLGPNAGEVTQGFAAALK	2281,2219

Entry name	Protein name/Function (UniProtKB)	Organism	Gene	Protein mass	Peptide sequence	Peptide mass
TBA1B_HUMAN	Tubulin alpha-1B	HS	TUBA1B	50120	FDLMYAK	886,4259
					EDMAALEK	905,4164
					LSVDYGKK	908,4967
					DVNAAIATIK	1014,5709
					EIIDLVLDR	1084,6128
					QLFHPEQLITGK	1409,7667
					LISQIVSSITASLR	1486,8719
					SIQFVDWCPTGFK	1583,7443
					AVFVDLEPTVIDEVR	1700,8985
					IHFPLATYAPVISAEK	1755,9559
					VGINYQPPTVVPGGDLAK	1823,9782
					AVCMLSNTTAIAEAWAR	1863,8971
					AVCMLSNTTAIAEAWAR	1863,8971
					TIGGGDDSFNTFFSETGAGK	2006,8858
					FDGALNVDLTEFQTNLVPYPR	2408,2012
					FDGALNVDLTEFQTNLVPYPR	2408,2012
					QLFHPEQLITGKEDAANNYAR	2414,1978
					AYHEQLSVAEITNACFEPANQMVK	2749,284
TBB3_HUMAN	Tubulin beta-3 chain	HS	TUBB3	50400	NMMAACDPR	1064,4201
					FPGQLNADLR	1129,588
					LAVNMVPFPR	1142,627
					ISEQFTAMFR	1228,591
					IMNTFSVVPSPK	1334,6904
					EVDEQMLAIQSK	1389,681
					AILVDLEPGTMDSVR	1614,8287
					ALTVPELTQQMFDAK	1690,86
					NSSYFVEWIPNNVK	1695,8257
					EIVHIQAGQCGNQIGAK	1821,9156
					MSSTFIGNSTAIQELFK	1872,9291
					GHYTEGAELVDSVLDVVR	1957,9745
					ECENCDCLQGFQLTHSLGGGTGSGMGTLLISK	3312,4883

Entry name	Protein name/Function (UniProtKB)	Organism	Gene	Protein mass	Peptide sequence	Peptide mass
TBB2A_HUMAN	Tubulin beta-2A chain	HS	TUBB2A	49875	TAVCDIPPR	1027,5121
					NMMAACDPR	1064,4201
					FPGQLNADLR	1129,588
					LAVNMVPFPR	1142,627
					ISEQFTAMFR	1228,591
					IMNTFSVMPSPK	1350,6676
					INVYYNEAAGNK	1354,6517
					EVDEQMLNVQNK	1445,682
					AILVDLEPGTMDSVR	1614,8287
					LHFFMPGFAPLTSR	1619,8283
					NSSYFVEWIPNNVK	1695,8257
					EIVHIQAGQCGNQIGAK	1821,9156
					MSATFIGNSTAIQELFK	1872,9291
					GHYTEGAELVDSVLDVVR	1957,9745
					LTTPTYGDLNHLVSATMSGVTTCLR	2707,331
					SGPFGQIFRPDNFVFGQSGAGNNWAK	2797,3361
TBA1A_HUMAN	Tubulin alpha-1A chain	HS	TUBA1A	50104	FDLMYAK	886,4259
					EDMAALEK	905,4164
					LSVDYGKK	908,4967
					DVNAAIATIK	1014,5709
					EIIDLVLDR	1084,6128
					QLFHPEQLITGK	1409,7667
					TIQFVDWCPTGFK	1597,7599
					AVFVDLEPTVIDEVR	1700,8985
					IHFPLATYAPVISAEK	1755,9559
					VGINYQPPTVVPGGDLAK	1823,9782
					AVCMLSNTTAIAEAWAR	1863,8971
					TIGGGDDSFNTFFSETGAGK	2006,8858
					FDGALNVDLTEFQTNLVPYPR	2408,2012
					QLFHPEQLITGKEDAANNYAR	2414,1978
					AYHEQLSVAEITNACFEPANQMVK	2749,284

Entry name	Protein name/Function (UniProtKB)	Organism	Gene	Protein mass	Peptide sequence	Peptide mass
TBB4B_HUMAN	Tubulin beta-4B chain	HS	TUBB4B	49799	TAVCDIPPR	1027,5121
					NMMAACDPR	1064,4201
					FPGQLNADLR	1129,588
					LAVNMVPFPR	1142,627
					ISEQFTAMFR	1228,591
					IMNTFSVVPSPK	1318,6955
					INVYYNEATGGK	1327,6408
					IMNTFSVVPSPK	1334,6904
					EVDEQMLNVQNK	1445,682
					AVLVDLEPGTMDSVR	1600,8131
					LHFFMPGFAPLTSR	1619,8283
					ALTVPELTQQMFDAK	1690,86
					NSSYFVEWIPNNVK	1695,8257
					EIVHLQAGQCGNQIGAK	1821,9156
					MSATFIGNSTAIQELFK	1872,9291
					GHYTEGAELVDSVLDVVR	1957,9745
					LTTPTYGDLNHLVSATMSGVTTCLR	2707,331
					SGPFGQIFRPDNFVFGQSGAGNNWAK	2797,3361

Table 37 – Significance of transfection efficiencies of human and primates' *INS* 5' UTRs.
Comparison of *INS* 5'UTR-dependent fluc expression from human and primates. Dunnett's test was performed for the comparison of luciferase expression levels of each higher primate construct to the empty pICtest (pIC) vector (relative to Figure 31). Tukey's multiple comparison test was used for three sets of luciferase expression comparison: WT INS 5'UTR of primates' vs. human; multiple comparison of constructs mutated at the 3'ss; and multiple comparison of human constructs. Welch's-corrected unpaired t-test for the comparison WT construct of each primate to the mutated 3'ss construct.

Constructs	Dunnett's multiple comparison test		
	p-value	$\overline{x}_2 - \overline{x}_1$	95% CI
pIC vs. Hs4	0.9916, ns	0.335	-0.989 to 1.66
pIC vs. Hs6	0.0001, ****	3.53	2.21 to 4.85
pIC vs. Hs6 ATG 3'ss	0.0002, ***	2.25	0.928 to 3.58
pIC vs. Hs6 3'ss	0.0001, ****	3.16	1.83 to 4.48
pIC vs. PP	0.0351, *	1.39	0.067 to 2.71
pIC vs. PP 3'ss	0.0107, *	1.6	0.277 to 2.93
pIC vs. PM	0.0001, ****	2.59	1.27 to 3.92
pIC vs. PM 3'ss	0.0002, ***	2.25	0.921 to 3.57
pIC vs. PC	0.0002, ***	2.28	0.952 to 3.6
pIC vs. PC 3'ss	0.0001, ***	2.29	0.971 to 3.62
pIC vs. PS	0.0001, ****	2.98	1.66 to 4.31
pIC vs. PS 3'ss	0.0001, ****	2.64	1.31 to 3.96

Constructs	Tukey's multiple comparison test		
	p-value	$\overline{x}_2 - \overline{x}_1$	95% CI
Hs6 vs. PP	0.0001, ****	-2.14	-3.01 to -1.27
Hs6 vs. PM	0.0331, *	-0.937	-1.81 to -0.068
Hs6 vs. PC	0.0047, **	-1.25	-2.12 to -0.384
Hs6 vs. PS	0.2957, ns	-0.545	-1.41 to 0.325

Constructs	Tukey's multiple comparison test		
	p-value	$\overline{x}_2 - \overline{x}_1$	95% CI
Hs6 3'ss vs. PP 3'ss	0.0164, *	-1.55	-2.86 to -0.247
Hs6 3'ss vs. PM 3'ss	0.2504, ns	-0.91	-2.22 to 0.397
Hs6 3'ss vs. PC 3'ss	0.2974, ns	-0.861	-2.17 to 0.446
Hs6 3'ss vs. PS 3'ss	0.7398, ns	-0.517	-1.82 to 0.79
PP 3'ss vs. PM 3'ss	0.5652, ns	0.644	-0.663 to 1.95
PP 3'ss vs. PC 3'ss	0.4976, ns	0.693	-0.614 to 2
PP 3'ss vs. PS 3'ss	0.1552, ns	1.04	-0.27 to 2.34
PM 3'ss vs. PC 3'ss	>0.9999, ns	0.0493	-1.26 to 1.36
PM 3'ss vs. PS 3'ss	0.8812, ns	0.393	-0.914 to 1.7
PC 3'ss vs. PS 3'ss	0.9227, ns	0.344	-0.963 to 1.65

Constructs	Tukey's multiple comparison test		
	p-value	$\overline{x}_2 - \overline{x}_1$	95% CI
Hs4 vs. Hs6	<0.0001, ****	3.19	2.22 to 4.17
Hs4 vs. Hs6 ATG 3'ss	0.0004, ***	1.92	0.944 to 2.89
Hs4 vs. Hs6 3'ss	<0.0001, ****	2.82	1.85 to 3.79
Hs6 vs. Hs6 ATG 3'ss	0.0098, **	-1.28	-2.25 to -0.305
Hs6 vs. Hs6 3'ss	0.6721, ns	-0.374	-1.35 to 0.599
Hs6 ATG 3'ss vs. Hs6 3'ss	0.0717, ns	0.904	-0.0691 to 1.88

Constructs	Welch's corrected unpaired t test			
	p-value	t, df	$\overline{x}_2 - \overline{x}_1$	95% CI
PP vs. PP 3'ss	0.7432, ns	0.343; 5.98	-0.21 ± 0.613	-1.71 to 1.29
PM vs. PM 3'ss	0.5254, ns	0.697; 3.88	0.347 ± 0.498	-1.05 to 1.75
PC vs. PC 3'ss	0.9298, ns	0.092; 5.75	-0.0182 ± 0.198	-0.507 to 0.47
PS vs. PS 3'ss	0.1111, ns	2.06; 3.86	0.346 ± 0.168	-0.127 to 0.82

Appendix C Publications

Nucleic Acids Research Advance Access published June 17, 2014

Nucleic Acids Research, 2014 **1**
doi: 10.1093/nar/gku507

Optimal antisense target reducing *INS* intron 1 retention is adjacent to a parallel G quadruplex

Jana Kralovicova[1], Ana Lages[1], Alpa Patel[2], Ashish Dhir[3], Emanuele Buratti[3], Mark Searle[2] and Igor Vorechovsky[1,*]

[1]University of Southampton, Faculty of Medicine, Southampton SO16 6YD, UK, [2]University of Nottingham, School of Chemistry, Centre for Biomolecular Sciences, Nottingham NG7 2RD, UK and [3]ICGEB, Padriciano 99, 34149 Trieste, Italy

Received March 26, 2014; Revised May 14, 2014; Accepted May 20, 2014

ABSTRACT

Splice-switching oligonucleotides (SSOs) have been widely used to inhibit exon usage but antisense strategies that promote removal of entire introns to increase splicing-mediated gene expression have not been developed. Here we show reduction of *INS* intron 1 retention by SSOs that bind transcripts derived from a human haplotype expressing low levels of proinsulin. This haplotype is tagged by a polypyrimidine tract variant *rs689* that decreases the efficiency of intron 1 splicing and increases the relative abundance of mRNAs with extended 5′ untranslated region (5′UTR), which curtails translation. Co-expression of haplotype-specific reporter constructs with SSOs bound to splicing regulatory motifs and decoy splice sites in primary transcripts revealed a motif that significantly reduced intron 1-containing mRNAs. Using an antisense microwalk at a single nucleotide resolution, the optimal target was mapped to a splicing silencer containing two pseudoacceptor sites sandwiched between predicted RNA guanine (G) quadruplex structures. Circular dichroism spectroscopy and nuclear magnetic resonance of synthetic G-rich oligoribonucleotide tracts derived from this region showed formation of a stable parallel 2-quartet G-quadruplex on the 3′ side of the antisense retention target and an equilibrium between quadruplexes and stable hairpin-loop structures bound by optimal SSOs. This region interacts with heterogeneous nuclear ribonucleoproteins F and H that may interfere with conformational transitions involving the antisense target. The SSO-assisted promotion of weak intron removal from the 5′UTR through competing noncanonical and canonical RNA structures may facilitate development of novel strategies to enhance gene expression.

INTRODUCTION

Most eukaryotic genes contain intervening sequences or introns that must be accurately removed from primary transcripts to create functional mRNAs capable of encoding proteins (1). This process modifies mRNP composition in a highly dynamic manner, employing interdependent interactions of five small nuclear RNAs and a large number of proteins with conserved but degenerate sequences in the pre-mRNA (2). Intron splicing generally promotes mRNA accumulation and protein expression across species (3–5). This process can be altered by intronic mutations or variants that may also impair coupled gene expression pathways, including transcription, mRNA export and translation. This is best exemplified by introns in the 5′ untranslated region (5′UTR) where natural variants or mutations modifying intron retention alter the relative abundance of transcripts with upstream open reading frames (uORFs) or other regulatory motifs and dramatically influence translation (6,7). However, successful sequence-specific strategies to normalize gene expression in such situations have not been developed.

Splice-switching oligonucleotides (SSOs) are antisense reagents that modulate intron splicing by binding splice-site recognition or regulatory sequences and competing with *cis*- and *trans*-acting factors for their targets (8). They have been shown to restore aberrant splicing, modify the relative expression of existing mRNAs or produce novel splice variants that are not normally expressed (8). Improved stability of targeted SSO-RNA duplexes by a number of SSO modifications, such as 2′-*O*-methyl and 2′-*O*-methoxyethyl ribose, facilitated studies exploring their therapeutic potential for a growing number of human disease genes, including *DMD* in muscular dystrophy (9,10), *SMN2* in spinal muscular atrophy (11), *ATM* in ataxia-telangiectasia (12) and *BTK* in X-linked agammaglobulinemia (13). Although such approaches are close to achieving their clinical potential for

*To whom correspondence should be addressed. Tel: +44 2381 206425; Fax: +44 2381 204264; Email: igvo@soton.ac.uk

a restricted number of diseases (8), >300 Mendelian disorders resulting from mutation-induced aberrant splicing (14) and a growing number of complex traits may be amenable to SSO-mediated correction of gene expression.

Etiology of type 1 diabetes has a strong genetic component conferred by human leukocyte antigens (HLA) and a number of modifying non-HLA loci (15). The strongest modifier was identified in the proinsulin gene (*INS*) region on chromosome 11 (termed IDDM2) (15). Further mapping of this area suggested that *INS* is the most likely IDDM2 target (16), consistent with a critical role of this autoantigen in pathogenesis (17). Genetic risk to this disease at IDDM2 has been attributed to differential steady-state RNA levels from predisposing and protective *INS* haplotypes, potentially involving a minisatellite DNA sequence upstream of this gene (18,19). However, systematic examination of naturally occurring *INS* polymorphisms revealed haplotype-specific proinsulin expression levels in reporter constructs devoid of the minisatellite sequence, resulting from two variants in intron 1 (7), termed IVS1+5ins4 (also known as *rs3842740* or INS-69) and IVS1–6A/T (*rs689*, INS-27 or *Hph*I+/−) (16,20). The former variant activates a cryptic 5′ splice site of intron 1 whereas adenine (A) at the latter variant, which resides 6 nucleotides upstream of the 3′ splice site (3′ss), promotes intron retention, expanding the relative abundance of transcripts with extended 5′UTR (21). As compared to thymine (T), the A allele at IVS1–6A/T decreases affinity to pyrimidine-binding proteins *in vitro* and renders the 3′ss more dependent on the auxiliary factor of U2 small nuclear ribonucleoprotein (U2AF) (7), a heterodimer required for U2 binding, spliceosome assembly and 3′ss selection (22). Intron 1-containing transcripts are overrepresented in IVS1-6A-derived cDNA libraries prepared from insulin producing tissues (21), are exported from the nucleus (23) and contain a short, *Homininae*-specific uORF that co-evolved with relaxation of the 3′ss of intron 1 in higher primates (7). The lower proinsulin expression conferred by the A allele may lead to suboptimal presentation of proinsulin peptides in the foetal thymus and inadequate negative selection of autoreactive T cells, culminating in autoimmune destruction of insulin-producing β cells in the pancreas (7). However, no attempts have been made to correct the low efficiency of *INS* intron 1 removal from the IVS1-6A-containing pre-mRNAs and reduce intron retention to the levels observed for the disease-protective T allele.

In this study, we set out to search for SSOs that increase the efficiency of *INS* intron 1 splicing and repress splicing silencers or decoy splice sites in the pre-mRNA to enhance proinsulin expression. We report identification of SSOs reducing the relative abundance of intron 1-retaining transcripts, delineation of the optimized antisense target at a single-nucleotide resolution, evidence for formation of a parallel G-quadruplex adjacent to the antisense target sequence and identification of proteins that bind to this region.

MATERIALS AND METHODS

Antisense oligonucleotides

SSOs were purchased from the MWG Biotech (Germany). All SSOs and scrambled controls had a full-length phosphorothioate backbone with 2′-*O*-methyl ribonucleotides at the second ribose position. Apart from *INS* SSOs and their scrambled versions, we employed SSOs that target other human genes as additional controls, as described (13). Location of each SSO is shown in Figure 1A and their sequences in Supplementary Table S1.

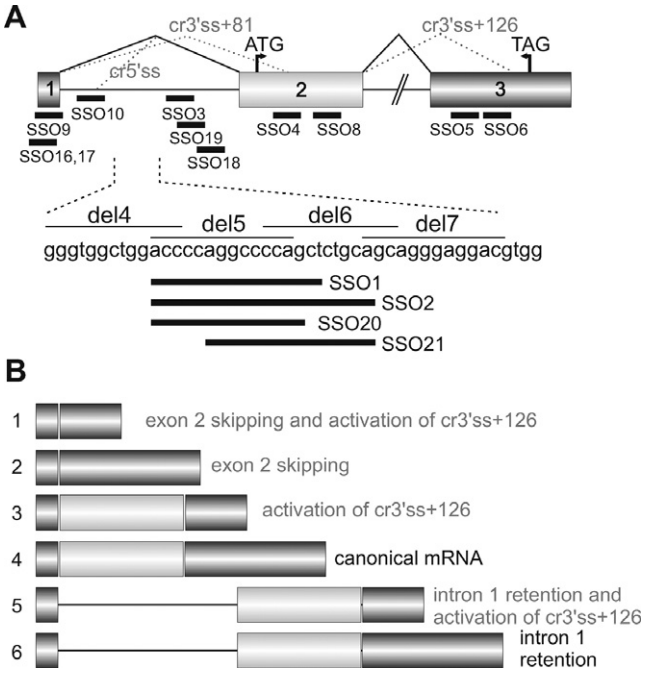

Figure 1. Location of SSOs in the human proinsulin gene. (**A**) Schematics of the *INS* reporter and its mRNA products. SSOs are shown as black horizontal bars below exons (numbered boxes) and below intron 1 (line); their sequences are in Supplementary Table S1. Start and stop codons are denoted by arrowheads. Canonical (solid lines) and cryptic (dotted lines) splicing is shown above the primary transcript; designation of cryptic splice sites is in grey. SSOs targeting intron 1 segments del4-del7 are shown in the lower panel. (**B**) mRNA isoforms (numbered 1–6) generated by the *INS* reporter construct. Description of isoforms that do not produce proinsulin is in grey.

Splicing reporter constructs

The wild-type splicing reporter carrying the type 1 diabetes-associated haplotype termed IC was reported previously (7,21). Each construct contains all *INS* exons and unabridged introns but differ in the length of the last exon. The IC reporters were cloned using primers D-C, D-F and D-B; IC D-B lacks the cryptic 3′ss of intron 2. The relative abundance of isoforms spliced to this site is lower for IC D-F than for IC D-C (7,21). To test SSOs targeting the cryptic 5′ splice site of intron 1, the IC construct was modified by a 4-nt insertion at *rs3842740* to create a reporter termed IC-IVS1+5ins4. *TSC2* and *F9* constructs were reported previously (24). Plasmids were propagated in the *E. coli* strain DH5α and plasmid DNA was extracted using the Wizard Plus SV Miniprep kit (Promega, USA). Their inserts were completely sequenced to confirm the identity of each of the 14 intragenic natural variants and to exclude undesired mutations.

Cell cultures and transfections

Human embryonic kidney 293 (HEK293), human hepatocellular liver carcinoma HepG2 and African green monkey COS7 cells were cultured in Dulbecco's modified Eagle medium, 10% fetal calf serum and penicillin/streptomycin (Life technologies, USA). Transient transfections were carried out as described (13), using jetPRIME (Polyplus, USA) according to manufacturer's recommendations. Downregulation of U2AF35 by RNA interference (RNAi) to induce cryptic 3′ss of intron 1 was performed with two hits of small interfering RNA (siRNA) U2AF35ab, as reported earlier (7,25); siRNA duplex targeting DHX36 was as described (26). The second hit was applied 24 h before the addition of SSOs and/or reporter. Cell cultures were harvested 24 h after addition of reporter constructs.

Analysis of spliced products

Total RNA was extracted with TRI Reagent and treated with DNase (Life technologies, USA). The first-strand cDNA was reverse transcribed using oligo-$(dT)_{15}$ primers and Moloney murine virus reverse transcriptase (Promega, USA). Polymerase chain reaction (PCR) was carried out with a combination of a vector-specific primer PL3 and primer E targeting the 3′UTR, as reported previously (7). PCR products were separated on polyacrylamide gels and their signal intensity was measured as described (27). The identity of each mRNA isoform was confirmed by Sanger nucleotide sequencing.

Circular dichroism and nuclear magnetic resonance spectroscopy

Oligoribonucleotides for circular dichroism (CD) and nuclear magnetic resonance (NMR) were purchased from Thermo Scientific, deprotected according to manufacturer's instructions, lyophilized and stored at −20°C. Stock solutions were prepared from the desalted, lyophilized samples by resuspending in milliQ water or KCl buffer (100 mM KCl, 10 mM K_2HPO_4/KH_2PO_4, pH 7.0, milliQ water) to a final concentration of 2–4 μM.

CD spectra were acquired using a PiStar-180 spectrophotometer (Applied Photophysics Ltd, Surrey, UK), equipped with a LTD6G circulating water bath (Grant Instruments, UK) and thermoelectric temperature controller (Melcor, USA). Samples were heated in the cell to 95°C for a total period of 15 min, samples were then annealed by allowing to cool to room temperature for a minimum period of 4 h. CD spectra were recorded over a wavelength range of 215–340 nm using a 1 cm path length strain-free quartz cuvette and at the temperatures indicated. Data points recorded at 1 nm intervals. A bandwidth of 3 nm was used and 5000 counts acquired at each point with adaptive sampling enabled. Each trace is shown as the mean of three scans (±SD). CD temperature ramps were acquired at 265 nm corresponding to the band maxima of the folded quadruplex species. Ranges between 5 and 99°C were used, with points acquired at 0.5°C intervals with a 120–180 s time-step between 0.5°C increments. Points were acquired with 10 000 counts and adaptive sampling enabled. Heating and cooling studies were compared to check for hysteresis and overall reversibility.

NMR spectra (^1H) were collected at 800 MHz using a Bruker Avance III spectrometer with a triple resonance cryoprobe. Standard Bruker acquisition parameters were used. Data were collected using Topspin (v. 3.0) and processed in CCPN Analysis (v. 2.1).

Pull-down assays and western blotting

In vitro transcription was carried out using MEGAshortscript™ T7 (LifeTechnologies, USA) and T7-tagged PCR products amplified with primers 5′-ATTAATACGACTCACTATAGGGCTCAGGGTTCCAGG and 5′-TGCAGCAGGGAGGACG, and DNA of the indicated plasmids as a template. Indicated synthetic RNAs were purchased from Eurofins UK. Five hundred pmols of each RNA was treated with 5 mM sodium *m*-periodate and bound to adipic acid dihydrazide agarose beads (Sigma, USA). Beads with bound RNAs were washed three times in 2 ml of 2 M NaCl and three times in buffer D (20 mM HEPES–KOH, pH 7, 6.5% v/v glycerol, 100 m M KCl, 0.2 mM EDTA, 0.5 mM dithiothreitol), incubated with HeLa nuclear extracts and buffer D with heparin at a final concentration of 0.5 mg/ml. Unbound proteins were washed five times with buffer D. Bound proteins were separated on 10% sodium dodecyl sulphate-polyacrylamide gel electrophoresis, stained by Coomassie blue and/or blotted on to nitrocellulose membranes.

Western blotting was carried out as described (7). Antibodies were purchased from Sigma (hnRNP E1/E2, product number R4155, U2AF65, product number U4758 and SFRS2, product number S2320), Abcam (DHX36, product number ab70269) and Millipore (SC35, clone 1SC-4F11). Antiserum against hnRNP F and hnRNP H was a generous gift of Prof. Douglas Black, UCLA.

Mass spectrometry analysis

Following trypsin digestion, samples were freeze dried and resuspended with 25 ul of 5% ACN/0.1% formic acid for mass spectrometry (MS). Peptides were analysed by LC/MS/MS using a Surveyor LC system and LCQ Deca XP Plus (ThermoScientific). The raw data files were converted into mascot generic files using the MassMatrix File Conversion Tool (Version 2.0; http://www.massmatrix.net) for input into the Mascot searching algorithm (Matrix Science).

Enzymatic structural probing

RNA secondary structure determination with the use of limited V1 RNAse (Ambion), T1 RNAse (Ambion) and S1 nuclease (Fermentas) digestion has been described in detail elsewhere (28). Briefly, 1 μg aliquots of RNAs from the insertion (ins) and deletion (del) pre-mRNAs were digested with 0.002 U of RNAse V1, 0.05 U of RNAse T1 and 19 U of S1 nuclease in a 100 μl at 30°C for 10 min. An enzyme-free aliquot was used as a control (C). The cleaved RNAs were retrotranscribed according to standard protocols using antisense primers labeled with [^{32}P]-ATP at the 5′ end.

RESULTS

Antisense oligonucleotides that promote pre-mRNA splicing of a weak intron in 5′UTR

To identify SSOs capable of reducing retention of *INS* intron 1 and increase splicing-mediated translational enhancement, we designed a series of 2′-*O*-methyl-modifed phosphorothioate SSOs, individually co-expressed each SSO with a splicing reporter construct carrying haplotype IC in HEK293 cells and examined the relative abundance of exogenous mRNA products (Figure 1A and B). The IC haplotype in the reporter was devoid of the minisatellite sequence and contained a total of 14 polymorphic sites (7,20), including the A allele at *rs689*. This allele inhibits intron 1 splicing and yields lower proinsulin levels as compared to the more common T allele (21). SSOs targeting intron 1 and exon 2 were chosen in regions that showed the most prominent alterations of exon inclusion or intron retention in previous systematic deletion analyses of these sequences (7). SSOs in exon 3 were located between authentic 3′ss of intron 2 and a strong competing cryptic 3′ss 126 nt downstream to identify pre-mRNA motifs that modify their usage (Figure 1A).

Of the initial set of 15 *INS* SSOs tested in HEK293 cells, 11 showed reproducible alterations in the relative abundance of mRNA isoforms (Supplementary Table S1). Intron 1 retention was significantly reduced by a single oligoribonucleotide SSO21 ($P < 0.01$, Mann-Whitney rank sum test; Figure 2A). SSO21 targeted intron 1 positions 59–74, encompassing a motif (termed del5) previously found to confer the largest reduction of intron retention upon deletion (7). The decrease in intron retention levels induced by SSO21 was dose-dependent (Figure 2A) and was also observed in HepG2 cells (Supplementary Figure S1) and *Chlorocebus aethiops* COS7 cells (data not shown), consistent with ubiquitous expression and a high degree of evolutionary conservation of spliceosome components that employ auxiliary splicing sequences (1,2).

In addition to reducing intron 1 retention, SSO21 promoted cryptic 3′ss of intron 2 (Figure 2A). However, this effect was also seen for other *INS* SSOs and for scrambled controls (Figure 3 and Supplementary Table S1), suggesting non-specific interactions. To confirm that the SSO21-induced enhancement of intron 1 splicing is not facilitated by the cryptic 3′ss of intron 2, we cotransfected this SSO with a shorter reporter lacking this site and retaining only the first 89 nucleotides of exon 3. Figure 2B shows that SSO21 was capable of promoting intron 1 splicing to the same extent as the reporter with longer exon 3. In contrast, the SSO21-induced decrease of intron retention was not observed for the reporter lacking the del5 segment (data not shown).

Apart from intron retention, we observed an increase of exon 2 skipping for five SSOs, including SSO8 that bound downstream of the cryptic 3′ss of intron 1 (cr3′ss+81; Figures 1 and 3C, Supplementary Table S1). This cryptic 3′ss was induced by RNAi-mediated depletion of the small subunit of U2AF (U2AF35) and was not reversed by a bridging oligoribonucleotide (SSO4) in cells lacking U2AF35; instead we observed exon 2 skipping (Figure 3C). Depletion of U2AF35 also repressed the cryptic 3′ss of intron 2. Taken together, we identified a single SSO that reduced *INS* intron 1 retention in several primate cell lines, consistent with a high degree of evolutionary conservation of spliceosome components that recognize auxiliary splicing sequences.

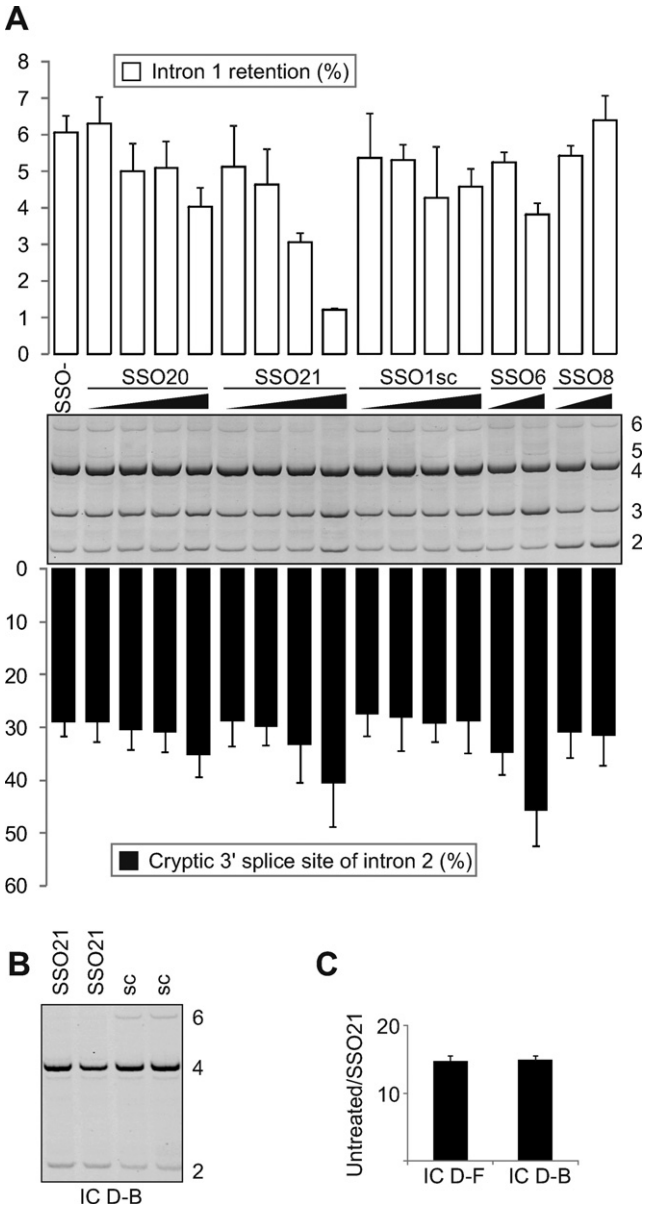

Figure 2. SSO-induced inhibition of *INS* intron 1 retention. (**A**) Cotransfection of the *INS* reporter construct (IC D-F) with the indicated SSOs into HEK293 cells. Spliced products described in Figure 1B are shown to the right. Bars represent percentage of intron 1-containing isoforms relative to natural transcripts (upper panel) or percentage of splicing to the cryptic 3′ splice site of intron 2 relative to the total (lower panel). Error bars denote SD; sc, scrambled control; SSO-, 'no SSO' control. Final concentration of SSOs was 1, 3, 10 and 30 nM, except for SSO6 and SSO8 (10 and 30 nM). (**B**) SSO21-mediated promotion of intron 1 splicing in clones lacking the cryptic 3′ss of intron 2. RNA products are to the right. (**C**) A fold change in SSO21-induced intron 1 retention in transcripts containing and lacking the cryptic 3′ss of intron 2. The final concentration of SSO21 was 30 nM in duplicate transfection. Designation of the reporter constructs is at the bottom.

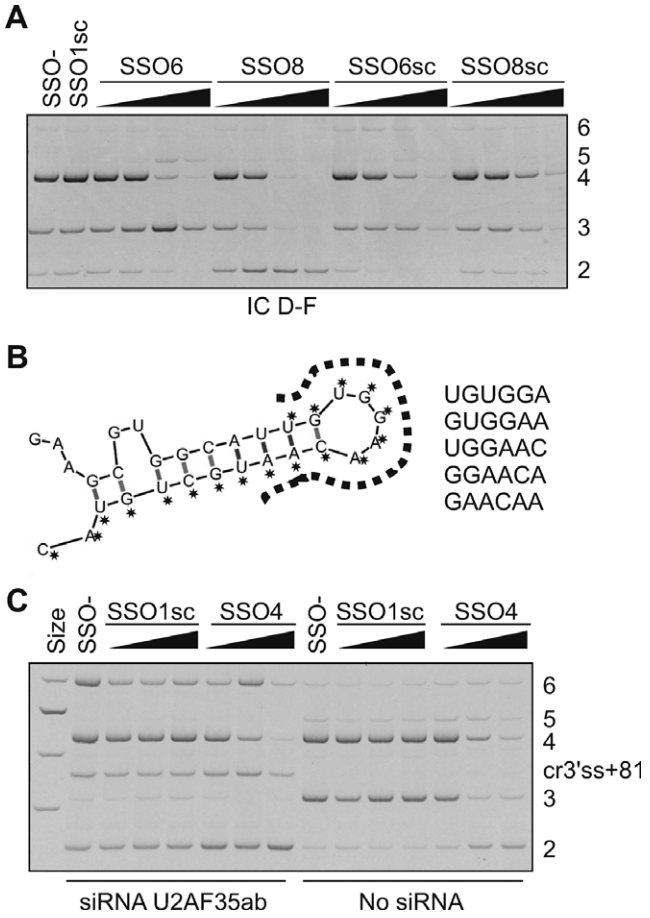

Figure 3. *INS* SSOs targeting cryptic 3′ splice sites. (**A**) Activation of cryptic 3′ss of intron 2 (cr3′ss+126; Figure 1A) by SSO6 and promotion of exon 2 skipping by SSO8. Concentration of each SSO was 2, 10, 50 and 250 nM. SSOs are shown at the top, spliced products to the right, reporter at the bottom. (**B**) A predicted stable hairpin between the authentic and cryptic 3′ss of *INS* intron 2. Bases targeted by SSO6 are denoted by asterisks and predicted splicing enhancer hexamers (listed to the right) are denoted by a dotted line. (**C**) SSO4 does not prevent activation of cryptic 3′ss 81 base pairs downstream of its authentic counterpart (cr3′ss+81) in cells depleted of U2AF35 but induces exon skipping. The final concentration of each SSO in COS7 cells was 5, 20 and 80 nM. The final concentration of the siRNA duplex U2AF35ab (29) was 70 nM. The reporter was the same as in panel A.

Optimization of the intron retention target at the single-nucleotide level

Interestingly, other SSOs designed to target the del5 segment did not reduce intron 1 retention, except for a small effect of SSO20 (Figures 1A and 2A). To test the importance of nucleotides flanking SSO21 and to map the optimal target at a single-base resolution, we carried out a detailed antisense microwalk in this region. We individually co-transfected the *INS* reporter with additional eighteen 16-mers bound 1–9 nucleotides 5′ and 3′ of SSO21 into HEK293 cells and examined their RNA products. Intron 1 retention was most repressed by SSO21 and by SSOs that were shifted by 1–2 nucleotides in each direction (Figure 4). In agreement with the initial screen, SSOs targeting more than one cytosine in the upstream run of four Cs (C4, see SSO1 and SSO2, Figure 1A) were not effective (SSO21–3r through SSO21–10r, Figure 4). In the opposite direction, SSOs targeting consecutive Gs, which are often found in intronic splicing enhancers (30–32), increased intron retention. Thus, the optimal antisense target for reducing retention of *INS* intron 1 was mapped at a single nucleotide resolution to a region previously identified as the most repressive by a systematic deletion analysis of the entire intron (7).

Antisense target for intron retention is adjacent to a parallel RNA quadruplex

We noticed that the target was sandwiched between two intronic segments predicted to form stable RNA guanine (G) quadruplexes (intron 1 nucleotides 36–61 and 78–93; highlighted in Figure 4A). These structures are produced by stacking G-quartets that consist of four Gs organized in a cyclic Hoogsteen hydrogen bonding arrangement (33) and have been implicated in important cellular processes, including replication, recombination, transcription, translation (34,35) and RNA processing (36–40). To test if they are formed *in vitro*, we employed synthetic ribonucleotides derived from this region in CD spectroscopy that has been used widely to characterize DNA and RNA quadruplex structures (41–44). The CD spectrum of a downstream 19-mer (termed CD1) recorded between 215 and 330 nm at 25°C revealed strong positive ellipticity at 265 nm with negative intensity at around 240 nm, indicative of a parallel quadruplex (Figure 5A). To confirm the presence of a quadruplex, rather than other stable secondary structure motifs, we recorded UV absorbance spectra at 5°C and 95°C. The UV absorbance difference spectrum at the two temperatures (below and above the melting transition point) showed the characteristic hyperchromic shift at ∼295 nm (data not shown) and a double maximum at 240 nm and 280 nm, providing evidence for formation of a stable parallel-stranded RNA quadruplex *in vitro.* This was confirmed by ^{1}H NMR studies of CD1 (Figure 5B) which showed a characteristic envelope of signals between 10 and 12 ppm corresponding to Hoogsteen H-bonded Gs within G-tetrad structures. Thermal stability measurements by CD produced a highly reversible sigmoidal co-operative unfolding transition with a $T_m = 56.8 \pm 0.2$°C (Figure 5C). Figure 5D (upper panel) shows a possible arrangement of the 19-mer into two stacked G-tetrads connected by relatively short loop sequences of 1–4 nucleotides.

Conformational transition model for splicing inhibitory sequences in *INS* intron 1

CD of a synthetic 20-mer derived from a region upstream of the antisense target (termed CD2) also showed evidence of stable structure formation, giving a broader absorption envelope centered around 270 nm and a sigmoidal thermal unfolding transition ($T_m = 69.0 \pm 0.45$°C; Figure 5A). Unlike the downstream oligo CD1, no hyperchromic shift in the UV was found in the thermal difference spectrum (data not shown). However, a well-defined set of sharp signals in the ^{1}H NMR spectrum between 12 and 14 ppm that differed from those for CD1 showed the formation of Watson–Crick H-bonded base pairs characteristic of double-stranded RNA (Figure 5B). Secondary

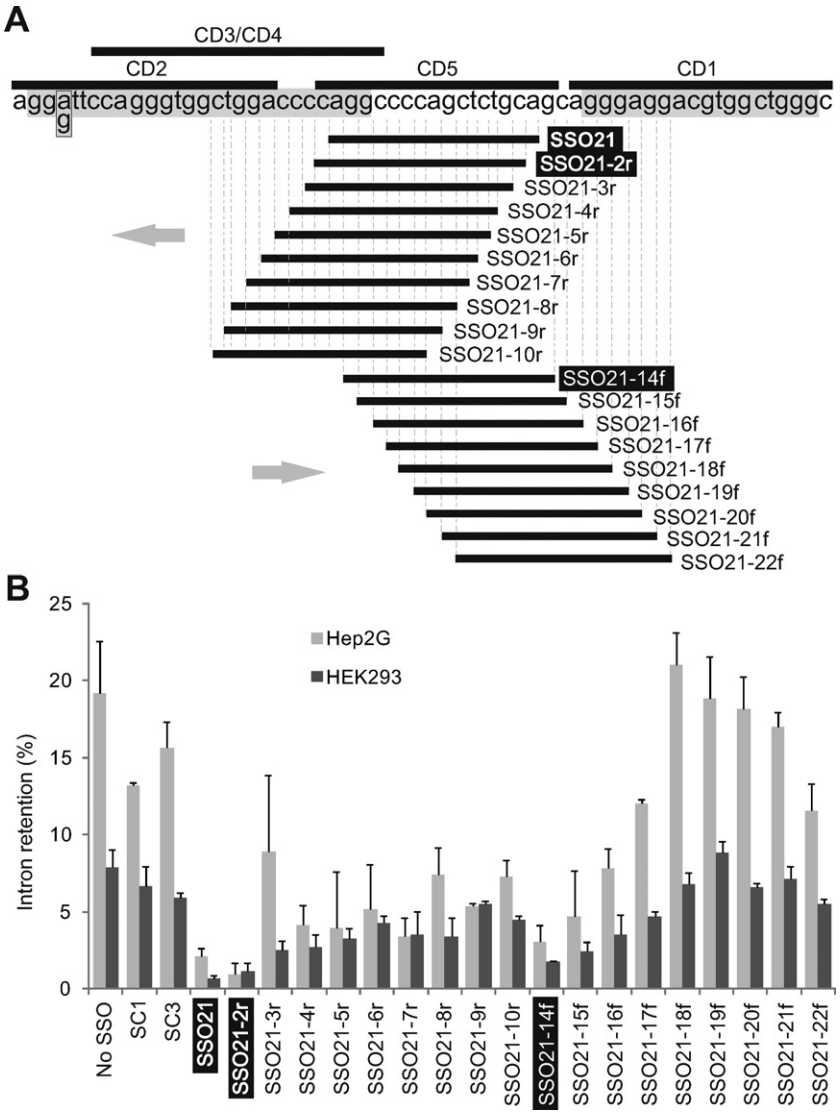

Figure 4. Optimization of the intron retention target by antisense microwalk at a single-nucleotide resolution. (**A**) Location of oligoribonucletoides. Microwalk SSOs and oligos used for CD/NMR are represented by horizontal black bars below and above the primary transcript, respectively. Intron 1 sequences predicted to form RNA G-quadruplexes are highlighted in grey. Microwalk direction is shown by grey arrows; winner oligos are highlighted in black. A box denotes a single nucleotide polymorphism reported previously (20). (**B**) Intron retention levels of each microwalk SSO in two cell lines. Error bars denote SDs obtained from two independent cotransfections with reporter IC D-F.

structure predictions of overlapping intronic segments using Mfold suggested that the pre-mRNA forms stable local stem-loops; one of them was further stabilized by a G→C mutation (termed G2; Figure 5D, lower panel) that increased intron 1 retention (7). Another G→C substitution (termed G3) located further downstream and destabilizing the quadruplex structure (Figure 5D, upper panel) also repressed intron splicing (7). Finally, CD2 oligonucleotides containing either A or G at a single-nucleotide polymorphism (Figure 4A and (20) exhibited very similar CD spectra with well-defined melting transitions and T_m values (data not shown), suggesting that the G and A alleles form the same structure.

To test further the importance of a tentative equilibrium between canonical and noncanonical structures in intron splicing, we used a combination of CD, NMR and mutagenesis experiments (Figure 6). We synthesized an oligoribonucleotide CD3 encompassing the 5′ end of the intron retention target and predicted stem-loops/quadruplex (Figures 4A and 6A). We also synthesised a mutated version CD4, which carried two C→U transitions destabilizing the hairpin but maintaining stability of the quadruplex. The same mutation was also introduced in our IC reporter construct transfected into HEK293 cells.

The NMR spectrum of CD3 revealed the co-existence of signals for both G-tetrad and canonical base-paired hairpin structures (termed H1 and H2) in equilibrium (Figure 6B and C). We investigated the effects of Mg^{2+} on the conformational equilibrium between quadruplex and hairpin by adding 2 mM and then 6 mM $MgCl_2$ to the buffered solution containing 100 mM KCl. As reported by Bugaut *et al.* (45), the conformational equilibrium was not sig-

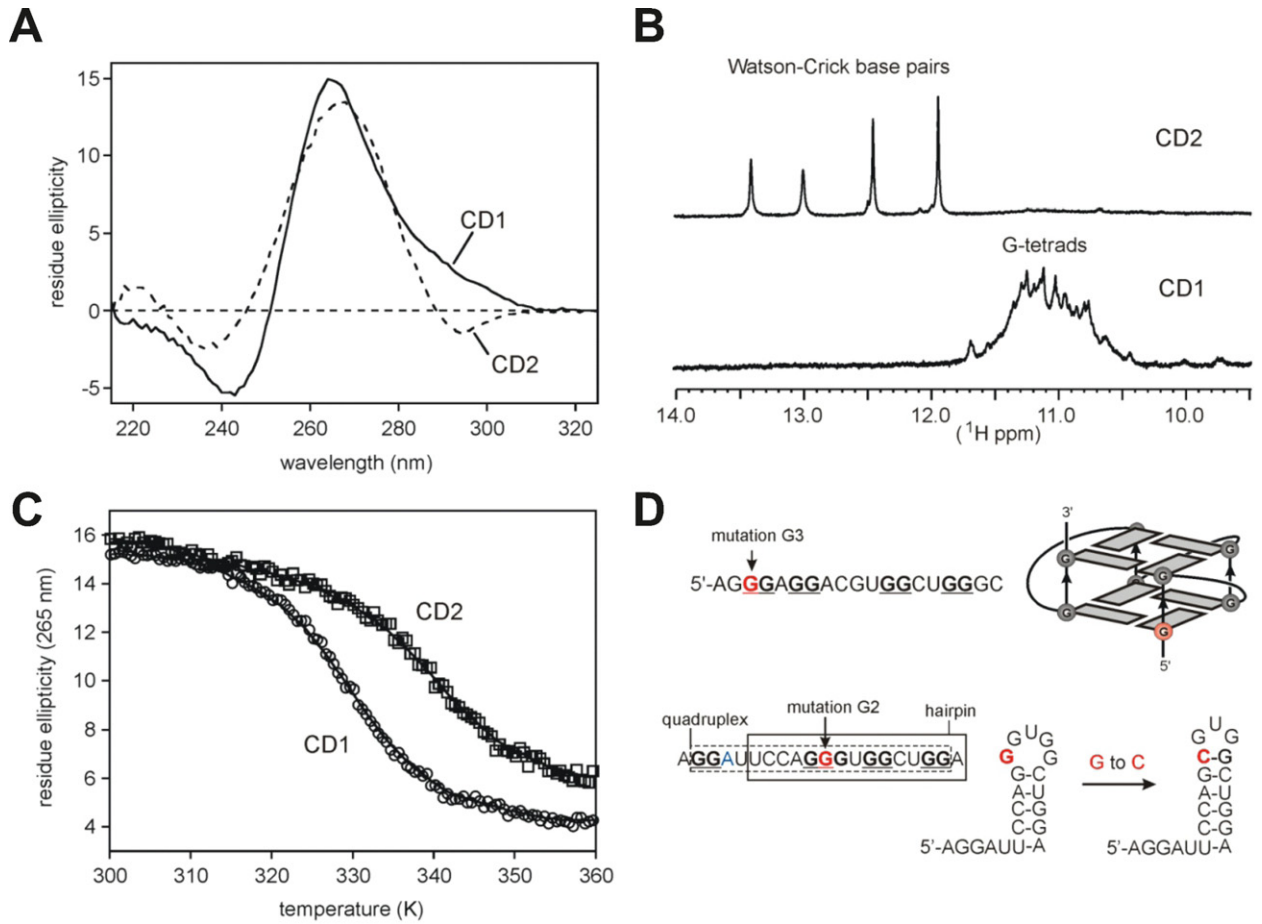

Figure 5. Biophysical characterization of RNA secondary structure formation. (**A**) Far-UV CD spectrum at 25°C for CD1 (19-mer) and CD2 (20-mer) RNAs, revealing ellipticity maximum at 265 and 270 nm, respectively. (**B**) ^{1}H NMR spectra of CD1 and CD2 recorded at 800 MHz and 298 K showing characteristic groups of resonances from H-bonded G bases. (**C**) Sigmoidal CD melting curves for the two RNAs showing a transition mid-point at 56.8 ± 0.2°C and 69.0 ± 0.45°C, respectively. The two curves have been displaced slightly from each other for clarity. (**D**) The proposed parallel quadruplex structure with two stacked G-tetrads connected by short loop sequences for CD1 (top panel). Predicted hairpin structures for CD2 are shown at the bottom panel. G→C mutations are in red.

nificantly perturbed by the addition of Mg^{2+} in the presence of KCl. Thus, we observed formation of the RNA hairpin and quadruplex structures in an environment that mimics the cellular context where both K^{+} and Mg^{2+} ions were present at high concentrations. The CD melting curve showed a broad transition (T_m = 79.9°C), consistent with multiple conformational states with different stabilities. The CC→UU mutation in CD4 resulted in the loss of NMR signals for H1 (Figure 6B) and a reduction in the T_m by 13°C, consistent with the selective destabilization of the more stable hairpin H1, leading to an increase in the population of H2 in equilibrium with the quadruplex. Transient transfections showed that the CC→UU mutation improved intron 1 splicing while a mutation termed M1 predicted to destabilize both the quadruplex and the hairpin had only a small effect (Figure 6D, Supplementary Table S2).

To explore how the equilibrium of these structures affects intron splicing more systematically, we prepared a series of mutated constructs to destabilize/maintain predicted quadruplex, H1/H2 structures and two cytosine runs (Supplementary Table S2). Their transcripts showed significant differences in intron retention levels (Figure 7; $P = 0.0001$, Kruskal–Wallis one-way ANOVA on ranks). First, elimination of the G-quadruplex increased intron 1 retention, which was further enhanced by removing each cytosine run (cf. mutations 4–6 with the wild-type, $P = 0.0004$). These mutations appeared to have additive effects on intron retention (cf. wild-type versus mutations 1 or 9; 3 versus 2 and 4 versus 5). Second, the increased intron retention in the absence of the G-quadruplex was not altered by removing H1 and H2, but their elimination enhanced exon skipping (cf. isoform 2 for mutations 4 versus 6). Third, when only one of the two C4 runs was present, removal of H1 somewhat improved intron 1 splicing (cf. 8 versus 9), consistent with a statistically significant correlation between intron retention and predicted stability of tested RNAs (Figure 7B). The efficiency of intron splicing was thus controlled by conformational transitions between canonical and noncanonical structures in equilibrium.

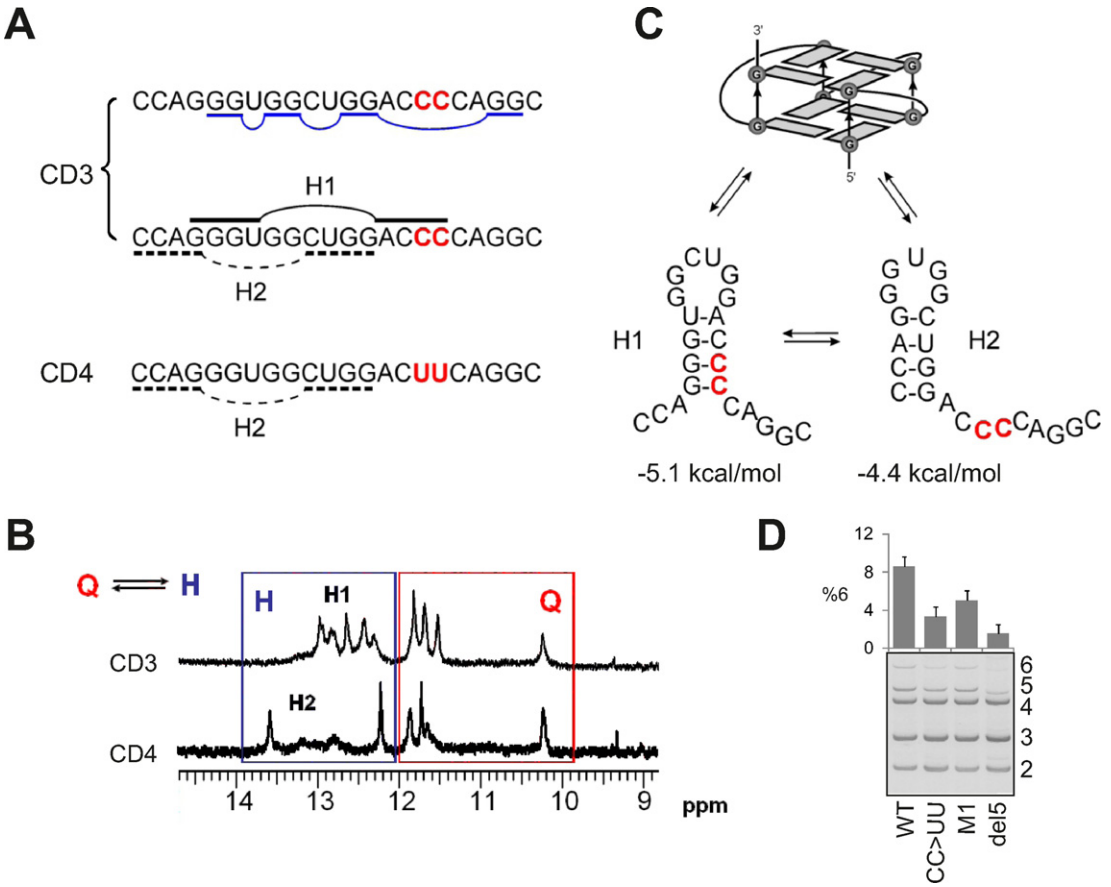

Figure 6. Conformational quadruplex/hairpin transitions involving the antisense target. (**A**) Schematic equilibrium between hairpin (black) and quadruplex (dark blue) structures proposed to form within the G-rich motif encompassing oligoribonucleotide CD3. CD4 contains a CC→UU mutation (in red). (**B**) The NMR spectrum in the 9–15 ppm region reveals imino proton signals corresponding to hydrogen bonded bases. The signals between 10 and 12 ppm are characteristic of Hoogsteen hydrogen bonded Gs within a G-tetrad (red box), while signals > 12 ppm are indicative of Watson–Crick A-U and G-C base pairs within hairpin structures (black box). In CD3, hairpin H1 is significantly populated, but mutations in CD4 destabilize H1 making H2 the major species, with both in equilibrium with the quadruplex structure. (**C**) Mfold predictions of two possible hairpins, consistent with the NMR data. (**D**) Reduction of intron retention upon destabilization of the hairpin structure by the CC→UU mutation. Error bars denote SD of a duplicate experiment with reporter IC D-C. Del5, the IC D-C reporter lacking segment del5 (Figure 1A); M1, a reporter containing two substitutions (Supplementary Table S2) to destabilize both the G-quadruplex and the stem-loop.

Protein–RNA interactions in the region targeted by winner SSOs

To identify proteins that interact with RNAs encompassing the antisense target and/or associated canonical and non-canonical structures, we carried out pull-down assays using wild type and del5 RNAs transcribed from T7-tagged PCR products, a synthetic RNA (CD5) representing the target sequence, and a control oligo containing a 3′ss CAG, termed AV3. Western blotting showed that both wild type and del5 transcripts bound hnRNPs F/H but this binding was absent for CD5 (Figure 7C). These proteins were also detected by MS/MS analysis of differentially stained fragments from pull down gels with wild type and del5 RNAs as compared to beads-only controls (data not shown). Two antibodies against SRSF2, which showed the highest score for putative binding activity among several SR proteins (Supplementary Figure S2), failed to detect any specific interaction (Figure 7C). Although the signal from hnRNP E1/E2, which constitute a major poly(C) binding activity in mammalian cells (46), was above background for del5 (Figure 7C), we observed no change in intron retention in cells lacking hnRNP E1/E2 (data not shown).

Splicing pattern of G-rich and G-poor reporters upon DHX36 depletion

RNA G-quadruplexes bind helicase DHX36, which is capable of converting quadruplex RNA to a stable duplex and is a major source of quadruplex-resolving activity in HeLa cells (26,47). DHX36 was crosslinked to an intronic splicing enhancer in the *ATM* pre-mRNA (48) and could unwind the quadruplex structure within the 5′ region of *TERC* (26). To test if DHX36 depletion can influence *INS* splicing, we transiently transfected G-quadruplex-poor and -rich reporters (Figure 8A, Table 1) into depleted cells. Control constructs were chosen to give approximately equal representation of spliced products, which was achieved by weakening the branch site (24), thus providing a sensitive *ex vivo* splicing assay. However, despite efficient DHX36 depletion (Figure 8B), we did not see statistically significant alterations of *INS* intron 1 retention in either short or long

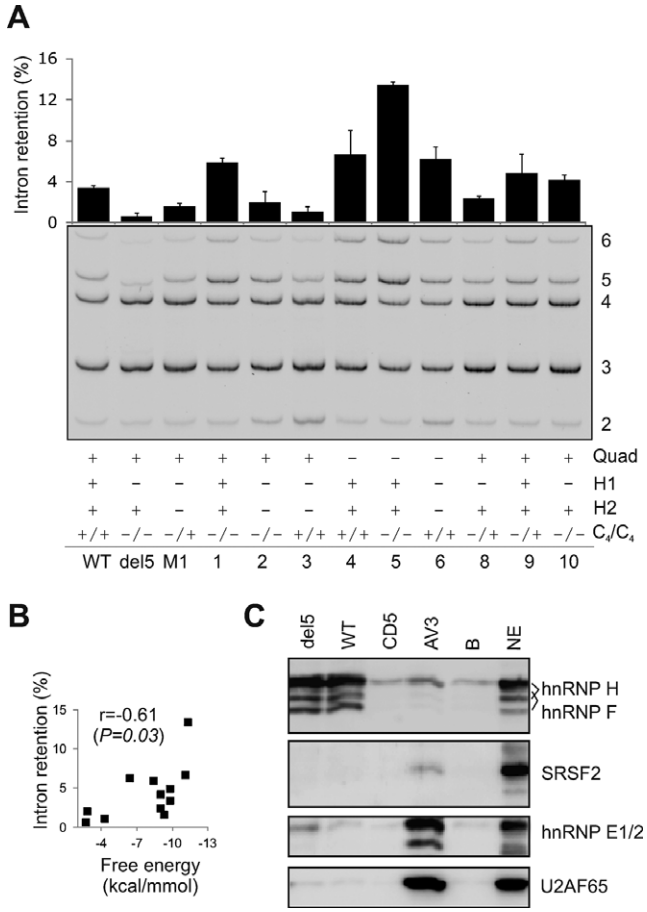

Figure 7. Identification of proteins that interact with pre-mRNAs encompassing the antisense target for intron retention. (**A**) Intron retention levels for wild type and mutated reporter constructs (IC D-C) following transient transfections into HEK293T cells. Mutations are shown in Supplementary Table S2. RNA products are to the right. The presence of predicted RNA quadruplexes, hairpins H1/H2 and the upstream and downstream C_4 run are indicated below the gel figure. Error bars denote SDs obtained from two replicate experiments. (**B**) Intron retention levels of tested RNAs correlate with their predicted stabilities across the antisense target. (**C**) Western blot analysis of a pull-down assay with antibodies indicated to the right. NE, nuclear extracts; B, beads-only control; AV3, control RNA oligo containing a cytosine run and a 3′ss AG (7). The sequence of CD5 RNA is shown in Figure 4A.

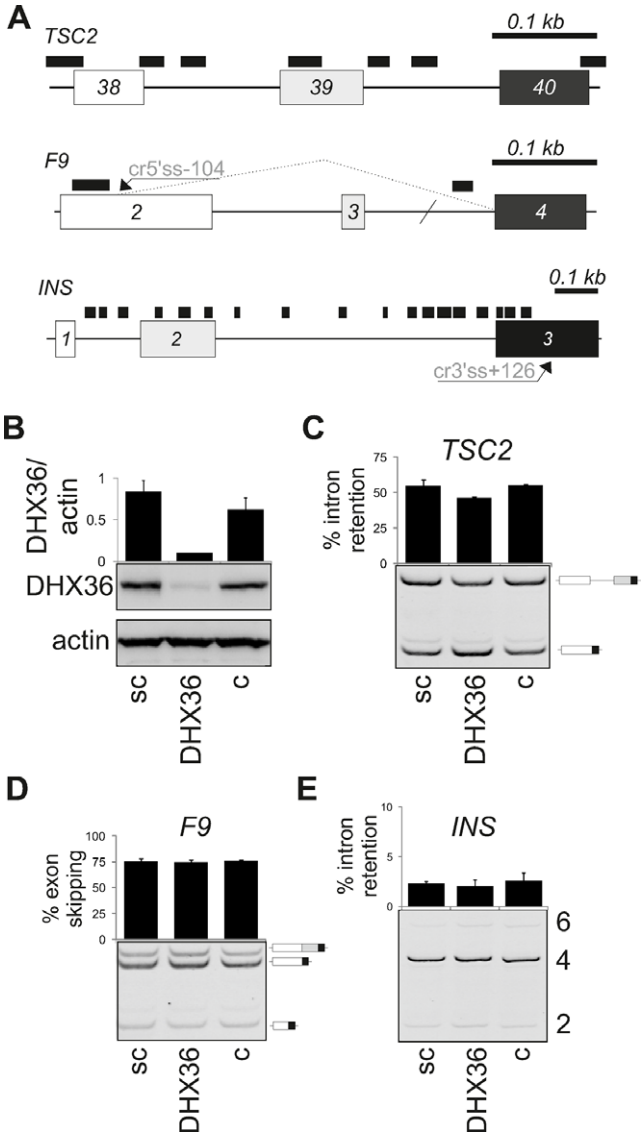

Figure 8. Splicing pattern of quadruplex-rich and -poor minigenes upon DHX36 depletion. (**A**) Schematics of reporter constructs. Predicted quadruplexes are denoted by black rectangles; their densities are shown in Table 1. Exons (boxes) are numbered; forward slash denotes shortening of *F9* intron 3 (24). The *F9* and *TSC2* minigenes contain branch point substitutions c.253–25C and c.5069–18C, respectively, that impair splicing (24). Cr5′ss-104; cryptic 5′ss 104 upstream of authentic 5′ss of intron 2. (**B**) Immunoblot with antibodies against DHX36. sc, scrambled siRNA; c, untreated cells. Error bars are SDs of two transfection experiments. (**C**–**E**) Intron retention and exon skipping of the indicated reporters. The final concentration of DHX36 siRNA was 50 nM. RNA products are shown schematically to the right. Error bars are SDs of two transfection experiments.

constructs, nor did we observe major changes in G-poor and G-rich controls (Figure 8C–E and data not shown). These results are in agreement with a previous lack of significant enrichment of quadruplex sequences among transcripts downregulated in DHX36-depleted cells (49) and with the absence of *ATM* response to the knockdown (48).

SSO-induced repression of a population-specific cryptic 5′ splice site of *INS* intron 1

In addition to *rs689, INS* intron 1 splicing is influenced by a polymorphic TTGC insertion at *rs3842740* located in the vicinity of the natural 5′ss (21). This insertion is present in a quarter of all African chromosomes but is absent on Caucasian IC haplotypes (20). The insertion activates a downstream cryptic 5′ss (Figure 1A), extending the 5′UTR of the resulting mRNAs by further 26 nucleotides and repressing proinsulin expression (7,21). To test if the new 5′ss can be efficiently inhibited by SSOs, we introduced the same insertion in our IC construct and co-expressed the wild type and mutated reporters with a bridging oligoribonucleotide termed SSO10. Although the cryptic splicing was inhibited, canonical splicing of intron 1 was not completely restored even at high SSO10 concentrations (Supplementary Figure S3 and data not shown), most likely as a result of subopti-

Table 1. Density of predicted RNA G-quadruplexes in reporter constructs

Reporter	TSC2	F9	INS
G-quadruplexes per nucleotide[a]	0.25	0.05	0.27
G score per nucleotide[a]	0.20	0.04	0.22

[a]The length of non-overlapping quadruplex sequences and their G scores were computed as described (50).

mal recognition of the authentic 5′ss weakened by the insertion.

To gain initial insights into folding of 5′UTR sequences in the presence and absence of the insertion, we carried out enzymatic structural probing using partial RNA digestion with single- and double-strand specific RNAses (Supplementary Figure S4). The overall cleavage positions and intensities detected for the wild-type RNA were broadly consistent with mfold predictions, in which two major stem-loop regions (SL1 and SL2) were interrupted by several internal bulges. Both the structural probing and mfold predictions suggested that the insertion at *rs3842740* extended the central bulge in SL1 as the number of T1 and S1 cleavages in this region increased in contrast to the remaining portions of SL1 and in SL2 (Supplementary Figure S5). Finally, transcripts were not digested by RNase V1 in regions showing quadruplex formation *in vitro*.

DISCUSSION

Antisense intron retention target in a splicing silencer of *INS* intron 1

Here we demonstrate the first use of antisense technology to reduce retention of the entire intron in mature transcripts and to modify the haplotype-dependent *INS* expression using SSOs. Identification of winner SSOs that compensate the adverse impact of the A allele at *rs689* on efficient RNA processing was facilitated by systematic mutagenesis of intron 1 (7), and by our macro- (Figure 1) and micro-walk (Figure 4) strategies. A similar approach was used previously for fine-mapping sequences that influence inclusion of *SMN2* exon 7 in the mRNA (51). Interestingly, the target sequence contains a tandem CAG(G/C) motif, which resembles a 3′ss consensus (Figure 4). Such 'pseudo-acceptors' were previously implicated in splice-site repression experimentally (27) and are overrepresented in splicing silencers. For example, the two tetramers are more common among high-confidence 102 intronic splicing silencers (52) and are depleted in 109 enhancers (53) identified by fluorescence activated screen of random 10-mers. The YAG motifs were also more frequent than expected among QUEPASA splicing silencers (54), suggesting that they are important functional components of the retention target. The intervening cytosine tract may also play an important role as the frequency of C_4 runs among QUEPASA silencers is ∼2 times higher than expected. We also found these motifs in 4% of intronic splicing regulatory elements identified by a systematic screening of sequences inserted at positions –62/–51 relative to a tested 3′ss (55). This study identified an element termed ISS22 (AAATAGAGGCCCCAG) that shared a 3′ nonamer (underlined) with the optimal intron retention target. However, unlike an optimal 3′ss recognition sequence of AV3, our pull-down assay coupled with western blotting revealed only a very weak binding if any to U2AF65 (Figure 7C).

Conformational transition between quadruplex and hairpins in RNA processing control

The antisense target was identified just upstream of a potential G-quadruplex forming RNA whose structure was subsequently confirmed by CD and NMR analysis (Figures 1A and 5). RNA quadruplexes are more stable than their DNA counterparts, have been increasingly implicated in regulation of RNA metabolism (34–35,42–43) and offer unique avenues for drug development (56). The 2-quartet quadruplexes are thermodynamically less stable than their 3- or 4-quartet counterparts and are probably kinetically more labile, yet they still display pronounced stability and may serve as more compliant and dynamic switches between quadruplex and non-quadruplex structures in response to cellular environment (57–59). The winner SSOs may block interactions with *trans*-acting factors, alter higher-order structures, the rate of RNA–protein complex formation or impair conformational transition between the 2-quartet quadruplex and H1/H2 (Figure 5). A similar transition has been recently described for a quadruplex not predicted *ab initio* (45), raising a possibility that additional sequences in the G-rich intron 1 may participate in the equilibria near the antisense target, possibly involving multiple quadruplex motifs and competing stem-loops.

Our binding (Figure 7C) and functional experiments showing the increased intron 1 retention upon hnRNP F/H depletion and the opposite effect upon hnRNP F/H overexpression (7) indicate that these proteins interact with key splicing auxiliary sequences in this intron. In contrast to a previous report concluding that hnRNP F binds directly to the RNA quadruplex (60), hnRNP F has been shown to prevent formation of RNA quadruplexes by binding exclusively single-stranded G-tracts (61). Although preliminary predictions based on primate genomes suggest that the majority of putative quadruplexes are likely to fold into canonical structures (62), future studies will be required to explain how decreased pre-mRNA occupancy by these proteins, presumably promoting quadruplex formation (61), can reduce splicing efficiency.

RNA quadruplexes in coupled splicing and translational gene expression control

RNA quadruplexes were predicted in ∼8.0% of 5′UTR and were proposed to act as general inhibitors of translation (62,63). *INS* intron 1 is weakly spliced and U2AF35-dependent (7) and a significant fraction of intron 1-containing transcripts is exported from the nucleus (23). This suggests that the RNA G-quadruplex formed by CD1

could influence translation of these mRNAs, which contain a three-amino acid uORF specific for *Hominidae* (7). This uORF markedly inhibits proinsulin expression and is located just a few base-pairs downstream, prompting a speculation that the G-quadruplexes can promote translation by sequestering uORFs. As functional 2-quartet quadruplexes are required for activity of internal ribosomal entry sites (57), future studies should also explore the importance of these structures in cap-independent translation of proinsulin transcripts (64).

Antisense strategies for dependencies in splice-site selection

Apart from canonical mRNA isoform 4, isoforms 2, 3 and 6 (Figure 1B) have been found in expressed sequence tag databases derived from cDNA libraries from insulin-producing tissues (21). This suggests that cryptic splice sites produced by our reporter construct are recognized *in vivo* and that our haplotype-dependent reporter system recapitulates these events accurately in cultured cells no matter whether the cells express or not endogenous insulin. Apart from repressing intron 1-retaining transcripts, optimal SSOs increased utilization of cryptic 3′ss of exon 3 (Figure 2). This undesired effect could be explained by coordination of splicing of adjacent exons and introns, which was observed previously for individual genes and globally (65–69). Also, G-richness downstream transcription start sites have been associated with RNA polymerase II pausing sites (70). Although the two robustly competing 3′ss of intron 2 are likely to respond to non-specific signals that influence RNA folding (Figure 3, Supplementary Table S1), it might be possible to alleviate the observed dependencies and reduce cryptic 3′ss activation using SSO combinations at linked splice sites and examine their synergisms or antagonisms, benefiting from the use of full-gene constructs as opposed to minigenes.

Multifunctional antisense oligonucleotides to reduce *INS* intron 1 retention

Since the first use of 2′-*O*-methyl-phosphorothioate SSOs (71), this type of chemical modification has been successfully exploited for many *in vitro* and *in vivo* applications (9–10,72). To further fine-tune expression of mRNA isoforms, optimized SSOs can be designed to tether suitable *trans*-acting splicing factors to their target sequences (11,73). An obvious candidate for our system is U2AF35 because intron 1 is weak as a result of relaxation of the 3′ss in higher primates and is further undermined by the A allele at *rs689*, which renders this intron highly U2AF35-dependent (Figure 3) (7). Apart from U2AF35, future bi- or multifunctional antisense strategies can employ binding platforms for splicing factors previously shown to influence *INS* intron 1 and exon 2 splicing, such as Tra2β or SRSF3 (7). Tra2β is likely to bind the SSO6 target which forms a predicted stable hairpin structure with a potent GAA splicing enhancer in a terminal loop (Figure 3B). SRSF3 is required for repression of the cryptic 3′ss of intron 2 (7) and binds pyrimidine-rich sequence with a consensus (A/U)C(A/U)(A/U)C (74). The CAUC motif, which interacts with the RNA-recognition motif of SRSF3 (75), is present just upstream of the cryptic 3′ss.

Normalizing intron retention levels in human genetic disease

Our results provide an opportunity to use non-genetic means to compensate less efficient splicing and lower *INS* expression from haplotypes predisposing to type 1 diabetes. Common variants such as *rs689* contribute to a great extent to the heritability of complex traits, including autoimmune diseases (76), but their functional and structural consequences are largely unknown. If optimized *INS* SSOs can be safely and efficiently introduced into the developing thymus, this approach may offer a novel preventive approach to promote tolerance to the principal self-antigen in type 1 diabetes. The most obvious candidates for such intervention are mothers who had an affected child homozygous for disease-predisposing alleles at both HLA and *INS* loci. Such genotypes were associated with an extremely high disease risk for siblings (77). Apart from primary prevention of type 1 diabetes, future SSO-based therapeutics might be applicable to patients with significant residual β-cell activity at diagnosis and to those who are eligible to receive β-cell transplants and may benefit from increased intron-mediated enhancement of proinsulin expression from transplanted cells. It is also possible to envisage use of this therapeutic modality for other patients with diabetes through a more dramatic enhancement of intron splicing and proinsulin expression by targeting multiple splicing regulatory motifs with multifunctional SSOs. Future studies should therefore examine utility of our SSOs in thymic epithelial cells and β-cells that may provide a more natural system for testing their impact on both exo- and endogenous proinsulin expression. Finally, similar antisense strategies may help reduce pervasive intron retention in cancer cells resulting from somatic mutations of splicing factor genes, as illustrated by specific substitutions in the zinc finger domain of U2AF35 in myeloproliferative diseases (78).

SUPPLEMENTARY MATERIAL

Supplementary Data are available Online.

ACKNOWLEDGEMENTS

We thank Huw Williams (University of Nottingham), Omar Jallow (University of London) and Joe Rogers (University of Southampton) for technical help, Alex Cousins (University of Nottingham) for preliminary CD studies, Mike Gait (University of Cambridge) for useful discussions and Chris Proud (University of Southampton) and Ian Eperon (University of Leicester) for manuscript comments. We also thank Prof. Douglas Black, UCLA, for a generous gift of antibodies.

FUNDING

Juvenile Diabetes Research Foundation International [1-2008-047 to I.V.]; Diabetes UK [09/3962 to I.V.]. Open access charge shared with co-authors.
Conflict of interest. None.

REFERENCES

1. Smith,C.W. and Valcarcel,J. (2000) Alternative pre-mRNA splicing: the logic of combinatorial control. *Trends Biochem. Sci.*, **25**, 381–388.

2. Wahl,M.C., Will,C.L. and Luhrmann,R. (2009) The spliceosome: design principles of a dynamic RNP machine. *Cell*, **136**, 701–718.
3. Callis,J., Fromm,M. and Walbot,V. (1987) Introns increase gene expression in cultured maize cells. *Genes Dev.*, **1**, 1183–1200.
4. Buchman,A.R. and Berg,P. (1988) Comparison of intron-dependent and intron-independent gene expression. *Mol. Cell. Biol.*, **8**, 4395–4405.
5. Le Hir,H., Nott,A. and Moore,M.J. (2003) How introns influence and enhance eukaryotic gene expression. *Trends Biochem. Sci.*, **28**, 215–220.
6. Cazzola,M. and Skoda,R.C. (2000) Translational pathophysiology: a novel molecular mechanism of human disease. *Blood*, **95**, 3280–3288.
7. Kralovicova,J. and Vorechovsky,I. (2010) Allele-dependent recognition of the 3′ splice site of *INS* intron 1. *Hum. Genet.*, **128**, 383–400.
8. Kole,R., Krainer,A.R. and Altman,S. (2012) RNA therapeutics: beyond RNA interference and antisense oligonucleotides. *Nat. Rev. Drug Discov.*, **11**, 125–140.
9. Aartsma-Rus,A. and van Ommen,G.J. (2007) Antisense-mediated exon skipping: a versatile tool with therapeutic and research applications. *RNA*, **13**, 1609–1624.
10. Goyenvalle,A., Seto,J.T., Davies,K.E. and Chamberlain,J. (2012) Therapeutic approaches to muscular dystrophy. *Hum. Mol. Genet.*, **20**, R69–78.
11. Hua,Y., Sahashi,K., Hung,G., Rigo,F., Passini,M.A., Bennett,C.F. and Krainer,A.R. (2010) Antisense correction of SMN2 splicing in the CNS rescues necrosis in a type III SMA mouse model. *Genes Dev.*, **24**, 1634–1644.
12. Du,L., Pollard,J.M. and Gatti,R.A. (2007) Correction of prototypic ATM splicing mutations and aberrant ATM function with antisense morpholino oligonucleotides. *Proc. Natl Acad. Sci. U.S.A.*, **104**, 6007–6012.
13. Kralovicova,J., Hwang,G., Asplund,A.C., Churbanov,A., Smith,C.I. and Vorechovsky,I. (2011) Compensatory signals associated with the activation of human GC 5′ splice sites. *Nucleic Acids Res.*, **39**, 7077–7091.
14. Buratti,E., Chivers,M.C., Hwang,G. and Vorechovsky,I. (2011) DBASS3 and DBASS5: databases of aberrant 3′ and 5′ splice sites in human disease genes. *Nucleic Acids Res.*, **39**, D86–D91.
15. Davies,J.L., Kawaguchi,Y., Bennett,S.T., Copeman,J.B., Cordell,H.J., Pritchard,L.E., Reed,P.W., Gough,S.C., Jenkins,S.C., Palmer,S.M. *et al.* (1994) A genome-wide search for human type 1 diabetes susceptibility genes. *Nature*, **371**, 130–136.
16. Barratt,B.J., Payne,F., Lowe,C.E., Hermann,R., Healy,B.C., Harold,D., Concannon,P., Gharani,N., McCarthy,M.I., Olavesen,M.G. *et al.* (2004) Remapping the insulin gene/IDDM2 locus in type 1 diabetes. *Diabetes*, **53**, 1884–1889.
17. Zhang,L., Nakayama,M. and Eisenbarth,G.S. (2008) Insulin as an autoantigen in NOD/human diabetes. *Curr. Opin. Immunol.*, **20**, 111–118.
18. Vafiadis,P., Bennett,S.T., Todd,J.A., Nadeau,J., Grabs,R., Goodyer,C.G., Wickramasinghe,S., Colle,E. and Polychronakos,C. (1997) Insulin expression in human thymus is modulated by *INS* VNTR alleles at the IDDM2 locus. *Nat. Genet.*, **15**, 289–292.
19. Pugliese,A., Zeller,M., Fernandez,A. Jr, Zalcberg,L.J., Bartlett,R.J., Ricordi,C., Pietropaolo,M., Eisenbarth,G.S., Bennett,S.T. and Patel,D.D. (1997) The insulin gene is transcribed in the human thymus and transcription levels correlated with allelic variation at the INS VNTR-IDDM2 susceptibility locus for type 1 diabetes. *Nat. Genet.*, **15**, 293–297.
20. Stead,J.D., Hurles,M.E. and Jeffreys,A.J. (2003) Global haplotype diversity in the human insulin gene region. *Genome Res.*, **13**, 2101–2111.
21. Kralovicova,J., Gaunt,T.R., Rodriguez,S., Wood,P.J., Day,I.N.M. and Vorechovsky,I. (2006) Variants in the human insulin gene that affect pre-mRNA splicing: is -23*Hph*I a functional single nucleotide polymorphism at *IDDM2*? *Diabetes*, **55**, 260–264.
22. Ruskin,B., Zamore,P.D. and Green,M.R. (1988) A factor, U2AF, is required for U2 snRNP binding and splicing complex assembly. *Cell*, **52**, 207–219.
23. Wang,J., Shen,L., Najafi,H., Kolberg,J., Matschinsky,F.M., Urdea,M. and German,M. (1997) Regulation of insulin preRNA splicing by glucose. *Proc. Natl Acad. Sci. U.S.A.*, **94**, 4360–4365.
24. Kralovicova,J., Haixin,L. and Vorechovsky,I. (2006) Phenotypic consequences of branchpoint substitutions. *Hum. Mutat.*, **27**, 803–813.
25. Pacheco,T.R., Gomes,A.Q., Barbosa-Morais,N.L., Benes,V., Ansorge,W., Wollerton,M., Smith,C.W., Valcarcel,J. and Carmo-Fonseca,M. (2004) Diversity of vertebrate splicing factor U2AF35: identification of alternatively spliced U2AF1 mRNAS. *J. Biol. Chem.*, **279**, 27 039–27 049.
26. Booy,E.P., Meier,M., Okun,N., Novakowski,S.K., Xiong,S., Stetefeld,J. and McKenna,S.A. (2012) The RNA helicase RHAU (DHX36) unwinds a G4-quadruplex in human telomerase RNA and promotes the formation of the P1 helix template boundary. *Nucleic Acids Res.*, **40**, 4110–4124.
27. Lei,H. and Vorechovsky,I. (2005) Identification of splicing silencers and enhancers in sense *Alu*s: a role for pseudo-acceptors in splice site repression. *Mol. Cell. Biol.*, **25**, 6912–6920.
28. Buratti,E., Muro,A.F., Giombi,M., Gherbassi,D., Iaconcig,A. and Baralle,F.E. (2004) RNA folding affects the recruitment of SR proteins by mouse and human polypurinic enhancer elements in the fibronectin EDA exon. *Mol. Cell. Biol.*, **24**, 1387–1400.
29. Pacheco,T.R., Moita,L.F., Gomes,A.Q., Hacohen,N. and Carmo-Fonseca,M. (2006) RNA interference knockdown of hU2AF35 impairs cell cycle progression and modulates alternative splicing of Cdc25 transcripts. *Mol. Biol. Cell*, **17**, 4187–4199.
30. Nussinov,R. (1988) Conserved quartets near 5′ intron junctions in primate nuclear pre-mRNA. *J. Theor. Biol.*, **133**, 73–84.
31. Sirand-Pugnet,P., Durosay,P., Brody,E. and Marie,J. (1995) An intronic (A/U)GGG repeat enhances the splicing of an alternative intron of the chicken beta-tropomyosin pre-mRNA. *Nucleic Acids Res.*, **23**, 3501–3507.
32. Kralovicova,J. and Vorechovsky,I. (2006) Position-dependent repression and promotion of DQB1 intron 3 splicing by GGGG motifs. *J. Immunol.*, **176**, 2381–2388.
33. Neidle,S. and Balasubramanian,S. (2006) *Quadruplex Nucleic Acids*. RSC Biomolecular Sciences, Cambridge, UK.
34. Bugaut,A. and Balasubramanian,S. (2012) 5′-UTR RNA G-quadruplexes: translation regulation and targeting. *Nucleic Acids Res.*, **40**, 4727–4741.
35. Millevoi,S., Moine,H. and Vagner,S. (2012) G-quadruplexes in RNA biology. *Wiley Interdiscip. Rev. RNA*, **3**, 495–507.
36. Gomez,D., Lemarteleur,T., Lacroix,L., Mailliet,P., Mergny,J.L. and Riou,J.F. (2004) Telomerase downregulation induced by the G-quadruplex ligand 12459 in A549 cells is mediated by hTERT RNA alternative splicing. *Nucleic Acids Res.*, **32**, 371–379.
37. Didiot,M.C., Tian,Z., Schaeffer,C., Subramanian,M., Mandel,J.L. and Moine,H. (2008) The G-quartet containing FMRP binding site in FMR1 mRNA is a potent exonic splicing enhancer. *Nucleic Acids Res.*, **36**, 4902–4912.
38. Hai,Y., Cao,W., Liu,G., Hong,S.P., Elela,S.A., Klinck,R., Chu,J. and Xie,J. (2008) A G-tract element in apoptotic agents-induced alternative splicing. *Nucleic Acids Res.*, **36**, 3320–3331.
39. Marcel,V., Tran,P.L., Sagne,C., Martel-Planche,G., Vaslin,L., Teulade-Fichou,M.P., Hall,J., Mergny,J.L., Hainaut,P. and Van Dyck,E. (2011) G-quadruplex structures in TP53 intron 3: role in alternative splicing and in production of p53 mRNA isoforms. *Carcinogenesis*, **32**, 271–278.
40. Melko,M., Douguet,D., Bensaid,M., Zongaro,S., Verheggen,C., Gecz,J. and Bardoni,B. (2011) Functional characterization of the AFF (AF4/FMR2) family of RNA-binding proteins: insights into the molecular pathology of FRAXE intellectual disability. *Hum. Mol. Genet.*, **20**, 1873–1885.
41. Balagurumoorthy,P., Brahmachari,S.K., Mohanty,D., Bansal,M. and Sasisekharan,V. (1992) Hairpin and parallel quartet structures for telomeric sequences. *Nucleic Acids Res.*, **20**, 4061–4067.
42. Derecka,K., Balkwill,G.D., Garner,T.P., Hodgman,C., Flint,A.P. and Searle,M.S. (2010) Occurrence of a quadruplex motif in a unique insert within exon C of the bovine estrogen receptor alpha gene (ESR1). *Biochemistry.* **49**, 7625–7633.
43. Balkwill,G.D., Derecka,K., Garner,T.P., Hodgman,C., Flint,A.P. and Searle,M.S. (2009) Repression of translation of human estrogen receptor alpha by G-quadruplex formation. *Biochemistry.* **48**, 11487–11495.
44. Garner,T.P., Williams,H.E., Gluszyk,K.I., Roe,S., Oldham,N.J., Stevens,M.F., Moses,J.E. and Searle,M.S. (2009) Selectivity of small

molecule ligands for parallel and anti-parallel DNA G-quadruplex structures. *Org. Biomol. Chem.*, **7**, 4194–4200.
45. Bugaut,A., Murat,P. and Balasubramanian,S. (2012) An RNA hairpin to g-quadruplex conformational transition. *J. Am. Chem. Soc.*, **134**, 19953–19956.
46. Thisted,T., Lyakhov,D.L. and Liebhaber,S.A. (2001) Optimized RNA targets of two closely related triple KH domain proteins, heterogeneous nuclear ribonucleoprotein K and alphaCP-2KL, suggest Distinct modes of RNA recognition. *J. Biol. Chem.*, **276**, 17484–17496.
47. Creacy,S.D., Routh,E.D., Iwamoto,F., Nagamine,Y., Akman,S.A. and Vaughn,J.P. (2008) G4 resolvase 1 binds both DNA and RNA tetramolecular quadruplex with high affinity and is the major source of tetramolecular quadruplex G4-DNA and G4-RNA resolving activity in HeLa cell lysates. *J. Biol. Chem.*, **283**, 34626–34634.
48. Pastor,T. and Pagani,F. (2011) Interaction of hnRNPA1/A2 and DAZAP1 with an Alu-derived intronic splicing enhancer regulates ATM aberrant splicing. *PLoS One*, **6**, e23349.
49. Iwamoto,F., Stadler,M., Chalupnikova,K., Oakeley,E. and Nagamine,Y. (2008) Transcription-dependent nucleolar cap localization and possible nuclear function of DExH RNA helicase RHAU. *Exp. Cell Res.*, **314**, 1378–1391.
50. Kikin,O., D′Antonio,L. and Bagga,P.S. (2006) QGRS Mapper: a web-based server for predicting G-quadruplexes in nucleotide sequences. *Nucleic Acids Res.*, **34**, W676–W682.
51. Singh,N.N., Hollinger,K., Bhattacharya,D. and Singh,R.N. (2010) An antisense microwalk reveals critical role of an intronic position linked to a unique long-distance interaction in pre-mRNA splicing. *RNA*, **16**, 1167–1181.
52. Wang,Y., Xiao,X., Zhang,J., Choudhury,R., Robertson,A., Li,K., Ma,M., Burge,C.B. and Wang,Z. (2012) A complex network of factors with overlapping affinities represses splicing through intronic elements. *Nat. Struct. Mol. Biol.*, **20**, 36–45.
53. Wang,Y., Ma,M., Xiao,X. and Wang,Z. (2012) Intronic splicing enhancers, cognate splicing factors and context-dependent regulation rules. *Nat. Struct. Mol. Biol.*, **19**, 1044–1052.
54. Ke,S., Shang,S., Kalachikov,S.M., Morozova,I., Yu,L., Russo,J.J., Ju,J. and Chasin,L.A. (2011) Quantitative evaluation of all hexamers as exonic splicing elements. *Genome Res.*, **21**, 1360 –1374.
55. Culler,S.J., Hoff,K.G., Voelker,R.B., Berglund,J.A. and Smolke,C.D. (2010) Functional selection and systematic analysis of intronic splicing elements identify active sequence motifs and associated splicing factors. *Nucleic Acids Res.*, **38**, 5152–5165.
56. Collie,G.W. and Parkinson,G.N. (2011) The application of DNA and RNA G-quadruplexes to therapeutic medicines. *Chem. Soc. Rev.*, **40**, 5867–5892.
57. Morris,M.J., Negishi,Y., Pazsint,C., Schonhoft,J.D. and Basu,S. (2010) An RNA G-quadruplex is essential for cap-independent translation initiation in human VEGF IRES. *J. Am. Chem. Soc.*, **132**, 17831–17839.
58. Wieland,M. and Hartig,J.S. (2007) RNA quadruplex-based modulation of gene expression. *Chem. Biol.*, **14**, 757–763.
59. Zhang,A.Y. and Balasubramanian,S. (2012) The kinetics and folding pathways of intramolecular g-quadruplex nucleic acids. *J. Am. Chem. Soc.*, **134**, 19297–19308.
60. Decorsiere,A., Cayrel,A., Vagner,S. and Millevoi,S. (2011) Essential role for the interaction between hnRNP H/F and a G quadruplex in maintaining p53 pre-mRNA 3′-end processing and function during DNA damage. *Genes Dev.*, **25**, 220–225.
61. Samatanga,B., Dominguez,C., Jelesarov,I. and Allain,F.H. (2013) The high kinetic stability of a G-quadruplex limits hnRNP F qRRM3 binding to G-tract RNA. *Nucleic Acids Res.*, **41**, 2505–2516.
62. Lorenz,R., Bernhart,S.H., Qin,J., Honer,Zu, Siederdissen,C., Tanzer,A., Amman,F., Hofacker,I.L. and Stadler,P.F. (2013) 2D meets 4G: G-quadruplexes in RNA secondary structure prediction. *IEEE/ACM Trans. Comput. Biol. Bioinform.* **10**, 832–844.
63. Beaudoin,J.D. and Perreault,J.P. (2010) 5′-UTR G-quadruplex structures acting as translational repressors. *Nucleic Acids Res.*, **38**, 7022–7036.
64. Fred,R.G., Sandberg,M., Pelletier,J. and Welsh,N. (2011) The human insulin mRNA is partly translated via a cap- and eIF4A-independent mechanism. *Biochem. Biophys. Res. Commun.*, **412**, 693–698.
65. Schwarze,U., Starman,B.J. and Byers,P.H. (1999) Redefinition of exon 7 in the *COL1A1* gene of type I collagen by an intron 8 splice-donor-site mutation in a form of osteogenesis imperfecta: influence of intron splice order on outcome of splice-site mutation. *Am. J. Hum. Genet.*, **65**, 336–344.
66. Xing,Y., Resch,A. and Lee,C. (2004) The multiassembly problem: reconstructing multiple transcript isoforms from EST fragment mixtures. *Genome Res.*, **14**, 426–441.
67. Fededa,J.P., Petrillo,E., Gelfand,M.S., Neverov,A.D., Kadener,S., Nogues,G., Pelisch,F., Baralle,F.E., Muro,A.F. and Kornblihtt,A.R. (2005) A polar mechanism coordinates different regions of alternative splicing within a single gene. *Mol. Cell*, **19**, 393–404.
68. Emerick,M.C., Parmigiani,G. and Agnew,W.S. (2007) Multivariate analysis and visualization of splicing correlations in single-gene transcriptomes. *BMC Bioinformatics*, **8**, 16.
69. Peng,T., Xue,C., Bi,J., Li,T., Wang,X., Zhang,X. and Li,Y. (2008) Functional importance of different patterns of correlation between adjacent cassette exons in human and mouse. *BMC Genomics*, **9**, 191.
70. Eddy,J., Vallur,A.C., Varma,S., Liu,H., Reinhold,W.C., Pommier,Y. and Maizels,N. (2011) G4 motifs correlate with promoter-proximal transcriptional pausing in human genes. *Nucleic Acids Res.*, **39**, 4975–4983.
71. Mayeda,A., Hayase,Y., Inoue,H., Ohtsuka,E. and Ohshima,Y. (1990) Surveying *cis*-acting sequences of pre-mRNA by adding antisense 2′-O-methyl oligoribonucleotides to a splicing reaction. *J. Biochem.*, **108**, 399–405.
72. Dominski,Z. and Kole,R. (1993) Restoration of correct splicing in thalassemic pre-mRNA by antisense oligonucleotides. *Proc. Natl Acad. Sci. U.S.A.*, **90**, 8673–8677.
73. Baughan,T.D., Dickson,A., Osman,E.Y. and Lorson,C.L. (2009) Delivery of bifunctional RNAs that target an intronic repressor and increase SMN levels in an animal model of spinal muscular atrophy. *Hum. Mol. Genet.*, **18**, 1600–1611.
74. Cavaloc,Y., Bourgeois,C.F., Kister,L. and Stevenin,J. (1999) The splicing factors 9G8 and SRp20 transactivate splicing through different and specific enhancers. *RNA*, **5**, 468–483.
75. Hargous,Y., Hautbergue,G.M., Tintaru,A.M., Skrisovska,L., Golovanov,A.P., Stevenin,J., Lian,L.Y., Wilson,S.A. and Allain,F.H. (2006) Molecular basis of RNA recognition and TAP binding by the SR proteins SRp20 and 9G8. *EMBO J.*, **25**, 5126–5137.
76. Hunt,K.A., Mistry,V., Bockett,N.A., Ahmad,T., Ban,M., Barker,J.N., Barrett,J.C., Blackburn,H., Brand,O., Burren,O. *et al.* (2013) Negligible impact of rare autoimmune-locus coding-region variants on missing heritability. *Nature*, **498**, 232–235.
77. Aly,T.A., Ide,A., Jahromi,M.M., Barker,J.M., Fernando,M.S., Babu,S.R., Yu,L., Miao,D., Erlich,H.A., Fain,P.R. *et al.* (2006) Extreme genetic risk for type 1A diabetes. *Proc. Natl Acad. Sci. U.S.A.*, **103**, 14074–14079.
78. Yoshida,K., Sanada,M., Shiraishi,Y., Nowak,D., Nagata,Y., Yamamoto,R., Sato,Y., Sato-Otsubo,A., Kon,A., Nagasaki,M. *et al.* (2011) Frequent pathway mutations of splicing machinery in myelodysplasia. *Nature*, **478**, 64–69.

SUPPLEMENTARY DATA

Figures S1-S5

Tables S1 and S2

Optimal antisense target reducing *INS* intron 1 retention is adjacent to a parallel G quadruplex

Jana Kralovicova[1], Ana Lages[1], Alpa Patel[2], Ashish Dhir[3],

Emanuele Buratti[3], Mark Searle[2], Igor Vorechovsky[1]

[1]University of Southampton
Faculty of Medicine
Southampton SO16 6YD
United Kingdom

[2]University of Nottingham
School of Chemistry
Centre for Biomolecular Sciences
Nottingham NG7 2RD
United Kingdom

[3]ICGEB,
Padriciano 99,
34149 Trieste,
Italy

FIGURE S1 SSO21-induced decrease of *INS* intron 1 retention in HepG2 cells

Legend: Final SSO concentrations were the same as in Fig. 2A. SCm, scrambled controls, SSO-, no-SSO control.

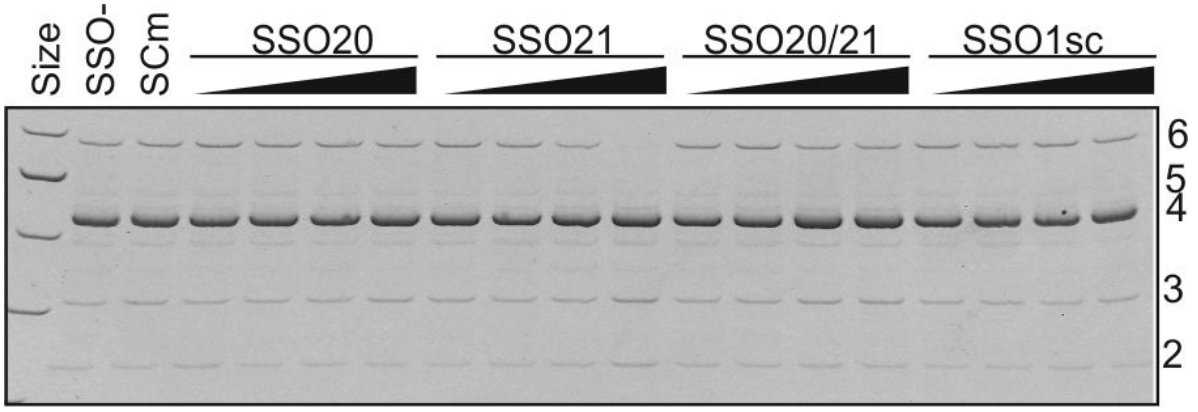

FIGURE S2 Prediction of putative enhancer binding sites of SR proteins in the region surrounding the intron 1 antisense target

Legend: The prediction was carried out by ESEFinder using default score matrices (1). SRSF1/SRSF1(IgM-BRCA1) sites are shown in red/purple, SRSF2 in blue, SRSF5 in green and SRSF6 in yellow. The SSO21 target sequence is shown by a box.

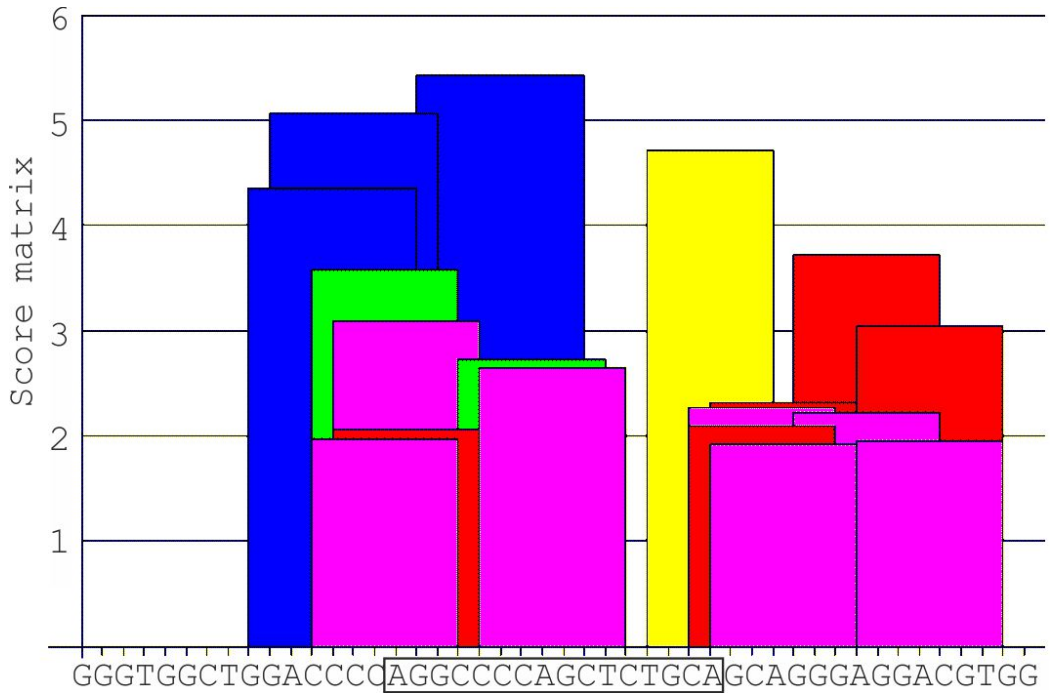

FIGURE S3 A partial restoration of authentic 5' splice site of *INS* intron 1

Legend: RNA products are shown to the right, the reporter at the bottom. SSOs are shown at the top, the final concentration of SSO10 in transfections wells were 10, 30 and 90 nM.

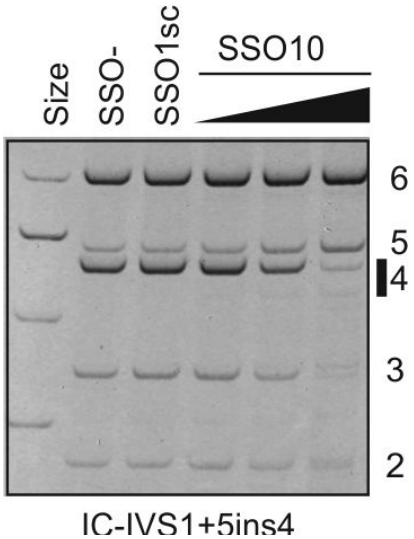

FIGURE S4 Enzymatic probing of *INS* 5'UTR

Legend: *In vitro* transcribed RNA enzymatically digested with S1 nuclease, T1 and V1 RNases. No enzyme was added to the RNA in a control reaction mixture (lane C).The cleaved fragments were detected by an RT reaction with an isotopically labelled oligonucleotides. The RT products were separated on a denaturing 6% polyacrylamide gel. A sequencing reaction performed with the same RT primer was run in parallel (lanes g, a, t and c). Squares, circles and triangles indicate S1, T1 and V1 cleavage sites. Black and white symbols indicate high and low cleavage intensity, respectively. The positions of the splice sites are indicated by arrows and their intrinsic strength by Shapiro-Senapathy scores (2). Secondary structure predictions were carried out using mfold (3).

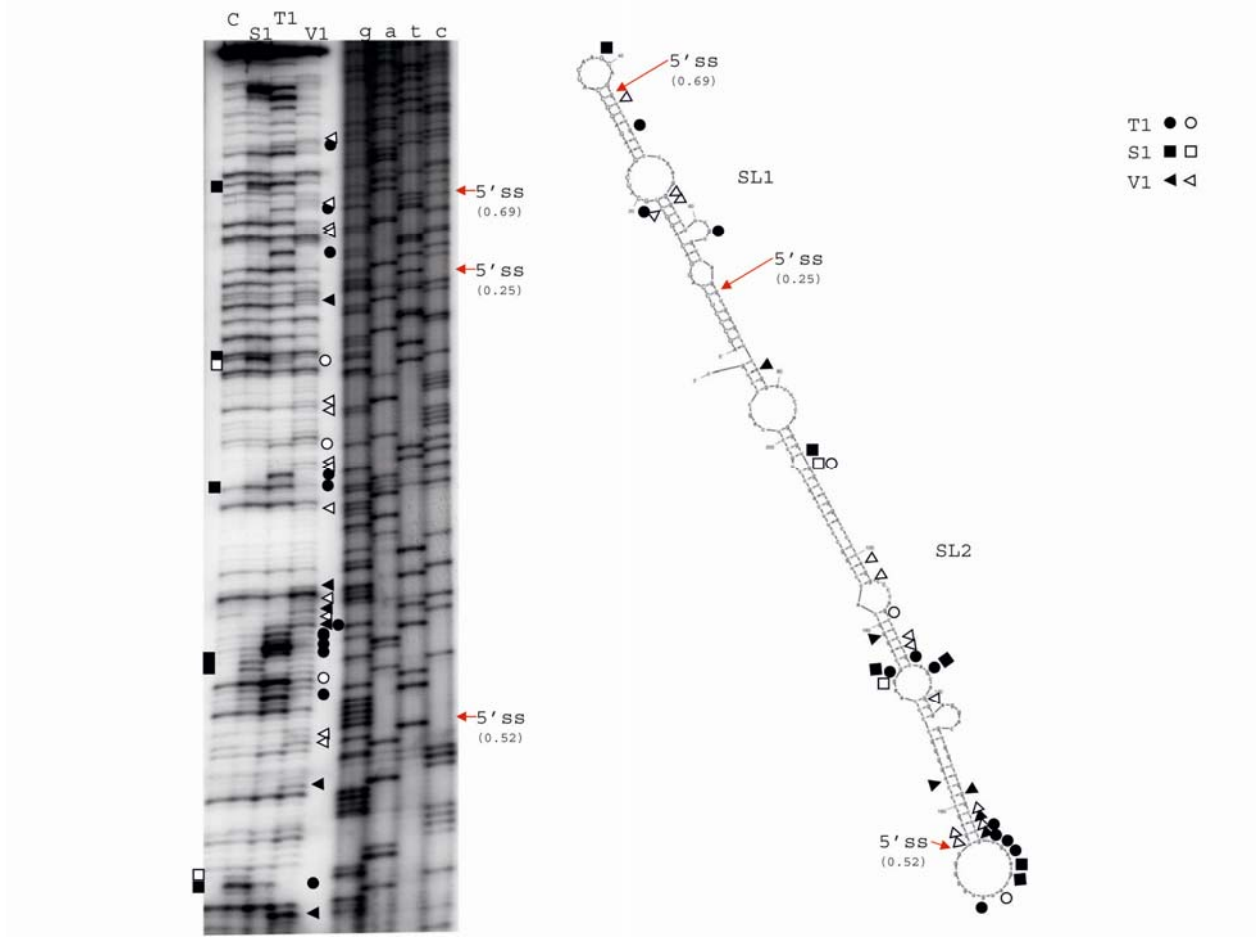

FIGURE S5 Structural probing of ins/del RNAs at *rs3842740*

For legend, see Figure S4.

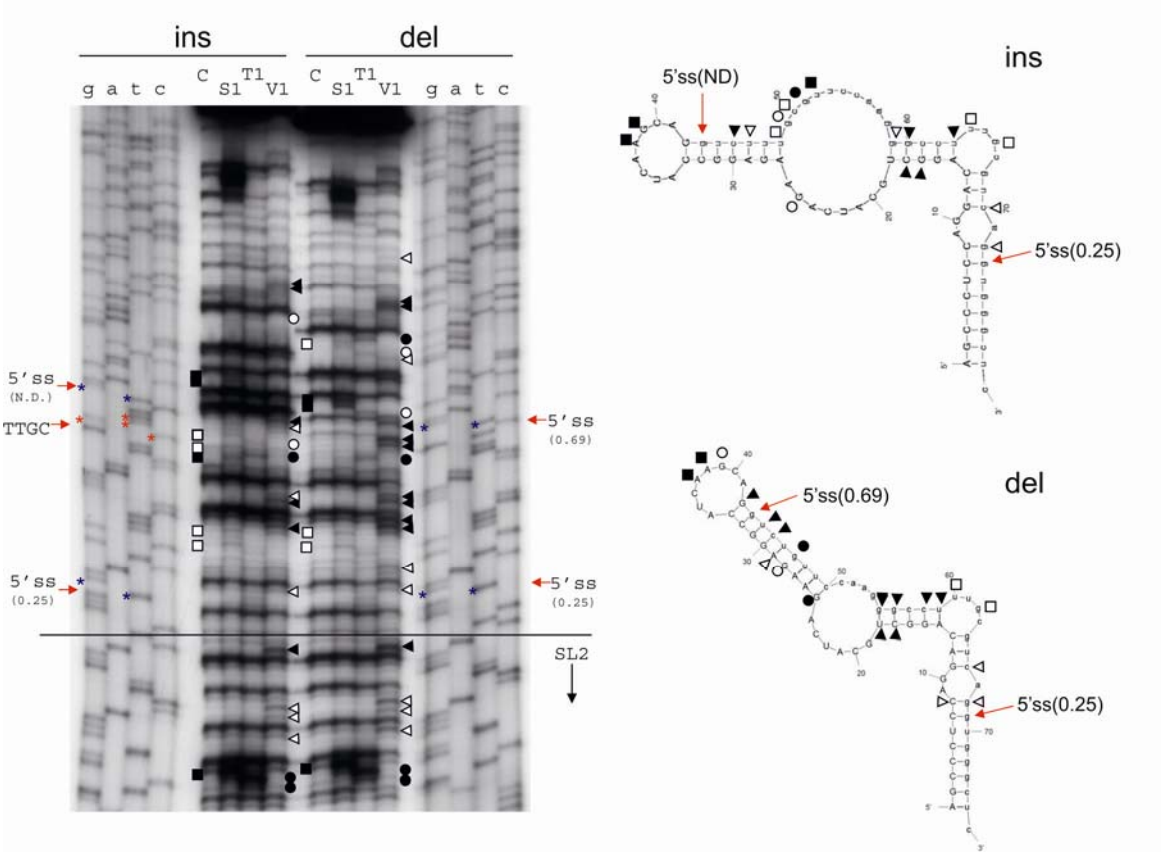

TABLE S1 Splice-switching oligonucleotides targeting proinsulin pre-mRNAs

SSO	Location[1]	Sequence (5'-3')	Effects on the relative abundance of *INS* mRNA isoforms
1	Intron 1 (del5, del6)	AGCUGGGGCCUGGGGU	Activation of the cryptic 3'ss of intron 2
2	Intron 1 (del5, del6)	UGCAGAGCUGGGGCCUGGGGU	Activation of the cryptic 3'ss of intron 2
3	Intron 1 (del8, del9)	CAUGCUUCACGAGCCCAGCC	Increased exon 2 skipping
4	Exon 2 (cryptic 3'ss +81, del8, del9)	AAGGCUGCGGCUGGGUC	Increased exon 2 skipping
5	Exon 3	UGGUAGAGGGAGCAGAUGCUG	Decreased efficiency of intron 2 splicing; Activation of the cryptic 3'ss of intron 2
6	Exon 3	UGGUACAGCAUUGUUCCACA	Activation of the cryptic 3'ss of intron 2 at high concentration
8	Exon 2 (del13-15)	CGCACACUAGGUAGAGAGC	Increased exon 2 skipping
9	Exon 1	GAUGCAGCCUGUCCUGGAG	None
10	Intron 1 (del1, del2, cryptic 5' splice site +30)	GAGCCCACCUGACGCAAAGGC	Partial restoration of authentic 5' splice site
16	Exon 1	UGGAGGGCUGAGGGCUGCU	None
17	Exon 1	AUGGCCUCUUCUGAUGCA	None
18	Intron 1 (del9, del10)	UCACCCCCACAUGCUUC	Increased exon 2 skipping
19	Intron 1 (del9)	ACAUGCUUCACGAG	Increased exon 2 skipping
20	Intron 1 (del5)	CUGGGGCCUGGGGU	Minor reduction of intron 1 retention; activation of the cryptic 3'ss of intron 2
21	Intron 1 (del5, del6)	UGCAGAGCUGGGGCCU	Reduction of intron 1 retention; activation of the cryptic 3'ss of intron 2
1sc	Scrambled control	AGGUGCUCGCGGGUGG	None
2sc	Scrambled control	GGGUGGAAGCGUCCGGUCGUG	Stimulation of the cryptic 3'ss of intron 2
3sc	Scrambled control	ACACACUGUGCCUCGCCAGC	None
6sc	Scrambled control	GACUCACUUGCCGUAGUUAA	Stimulation of the cryptic 3'ss of intron 2
8sc	Scrambled control	CACGCUCAGUAGAGAAGGC	None

[1], sequence of deleted segments (del) is shown in Fig. 2 and Supplemental Fig. 13 of our previous study (4).

TABLE S2 ***INS*** **intron 1 mutatons altering predicted RNA G quadruplexes, stem loops and two cytosines runs in plasmid constructs**

Mutation	Input sequence for computation predictions[1]	Predicted RNA quadruplex	H2	H1	C runs	The most stable RNA structure	Free energy (kcal/mmol)
Wildtype sequence	GGAUUCCAGGGUGGCUGGACCCCAGGCCCC	+	+	+	+	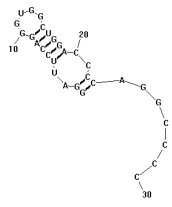	-9.8
Del5	GGAUUCCAGGGUGGCUGG----------	+	+	-	-		-2.7
M1	GGAUUCCAGGGUGGCUGCACGCCAGGCCCC	+	-	-	-	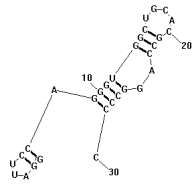	-9.3
1	GGAUUCCAGGGUGGCUGGACCCGAGGCGCC	+	+	+	-	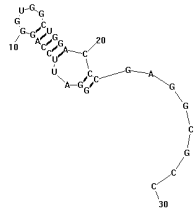	-8.4
2	GGAUUCCAGGAUGGUAGGACCCGAGGCGCC	+	-	-	-	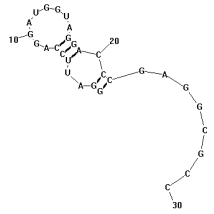	-2.8
3	GGAUUCCAGGAUGGUAGGACCCCAGGCCCC	+	-	-	+	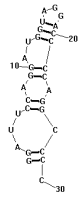	-4.3
4	GGAUUCCAGGGUUGCUGGACCCCAGUCCCC	-	+	+	+	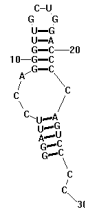	-11.1
5	GGAUUCCAGGGUUGCUGGACCCGAGUCGCC	-	+	+	-	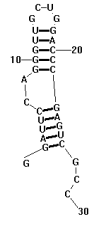	-11.3

6	GGAUUCCAGGAUUGUAGGACCCCAGUCCCC	-	-	-	+	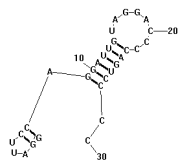	-6.4
8	GGAUUCCAGGGUGGCUGGACUUCAGGCCCC	+	+	-	-	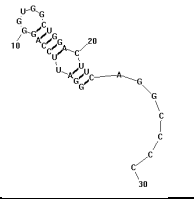	-9.0
9	GGAUUCCAGGGUGGCUGGACCCCAGGCUUC	+	+	+	-	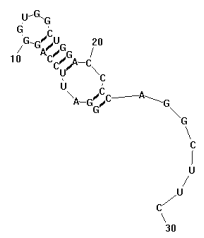	-9.8
10	GGAUUCCAGGGUGGCUGGACUUCAGGCUUC	+	+	-	-	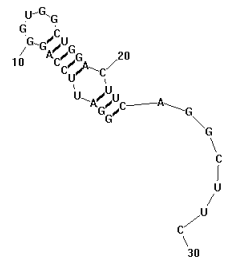	-9.0

[1]sequences that form H1 (strikethrough) and H2 (underlined) stems are highlighted. Guanines contributing to predicted quadruplex formation are in yellow; mutations are in red. RNA secondary structures/free energy were predicted by RNAStructure (v.5.2) (5).

References to supplementary data

1 Cartegni, L., Wang, J., Zhu, Z., Zhang, M.Q. and Krainer, A.R. (2003) ESEfinder: a web resource to identify exonic splicing enhancers. Nucleic Acids Res., 31, 3568-3571.

2 Shapiro, M.B. and Senapathy, P. (1987) RNA splice junctions of different classes of eukaryotes: sequence statistics and functional implications in gene expression. Nucleic Acids Res., 15, 7155-7174.

3 Zuker, M. (2003) Mfold web server for nucleic acid folding and hybridization prediction. Nucleic Acids Res., 31, 3406-3415.

4 Kralovicova, J. and Vorechovsky, I. (2010) Allele-dependent recognition of the 3' splice site of INS intron 1. Hum. Genet., 128, 383-400.

5 Reuter, J.S. and Mathews, D.H. (2010) RNAstructure: software for RNA secondary structure prediction and analysis. BMC Bioinformatics, 11, 129.